School of Civil and Mechanical Engineering
Faculty of Science and Engineering

Experimental Characterisation and Modelling of Sustainable Multiscaled Bionanocomposites

Mohanad Hashim Mousa

This thesis is presented for the degree of

Doctor of Philosophy

of
Curtin University

August 2018

Declaration

I declare that, this thesis contains no material previously published any other person expect where due acknowledgment has been made.

This thesis contains no material which has been accepted for the award of any other degree or diploma in any university.

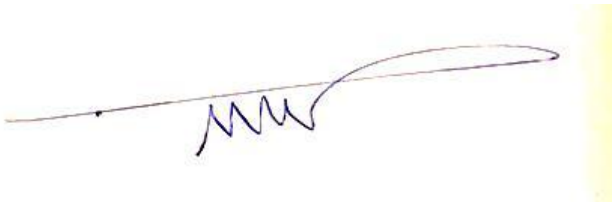

Signature

Date: 19 / 08 / 2018

Acknowledgements

First of all, I would like to express my deepest appreciation and gratitude to my primary supervisor Dr. Yu (Roger) Dong, without whose encouragement and enthusiasm, this thesis would not have been completed so successfully. It has always been wonderful experience to be his student. I would like to express my warm gratitude to my co-supervisor A/Prof. Ian J. Davies for his countless guidances and supports during my PhD study. I would also like to extend my sincere appreciation to my associate supervisor Associate Professor Chunsheng Lu.

My research would not have been completed without tremendous supports from technical staff. I would also like to extend my sincere appreciation to Mr. David Collier, Mr. Graeme Watson, and Mr. Andreas Viereckl from Mechanical Engineering Department laboratories for their continued technical assistance. Ms. Elaine Miller and Ms. Veronica Avery from the Department of Imaging & Applied Physic for their valuable supports of SEM and XRD analyses. I would also like to express my sincere gratitude to Dr. Thomas Becker from Nanochemistry Research Institute, Curtin University for his technical support in PFQNM measurements.

My acknowledgement also goes to my sponsor Higher Committee For Education Development (HCED) in Iraq for offering a full PhD Scholarship for my PhD study at Curtin University.

Last but not least, I would like to thank my parents, my wife and Dr. Ahmed Alketife for their unlimited supports and great patience.

Dedication

To my God, Allah

To my Parents

To my Family

Abstract

Biopolymers have gained significant attention due to the ever-increasing levels of synthetic polymers accumulated in various environments. Polyvinyl alcohol (PVA), considered as one of popular water-soluble and eco-friendly biopolymers owing to its characteristic such as recyclability and bio-tribological properties to make it widely used in biotechnological applications. However, such biopolymers possess insufficient thermal and mechanical properties to compete with synthetic polymers. Different nanofillers such as carbon nanotubes (CNTs), graphene sheets and nanoclays are incorporated within PVA matrices in nanocomposite systems to improve overall material performance. Carbon-based nanofillers like CNTs are considered as more effective reinforcements because of their unique structures and properties. However, the use of such nanofillers can be hindered due to their nanotoxicity and high material cost. Bamboo charcoals (BCs) are ecofriendly and sustainable carbon-based particles, which possess good affinity with PVA to achieve excellent properties of PVA/BC nanocomposites. In particular, porous structures of BC particles enable the easy penetration of polymeric molecules along with the strong filler-matrix internal bonding.

In this study, solvent casting method is employed to prepare novel and strong PVA/ BC bionanocomposite films as well as PVA/ HNT nanocomposite and PVA/ Cloisite30B nanocomposite films. This work holistically investigates the effect of different nanofiller sizes, contents, shapes and structures on the material performance of their corresponding nanocomposite films.

Initially, particle size effect has been investigated using two different types of BC particles, namely microdiameter bamboo charcoals (MBCs) and nanodiameter bamboo charcoals (NBCs). The addition of NBCs yields increasingly higher mechanical properties of PVA/BC nanocomposites compared with the incorporation of MBCs. The maximum increases in tensile moduli of nanocomposites were achieved up to 123% and 100% with the inclusion of 10 wt% NBCs and MBCs, respectively. Whereas, corresponding tensile strengths were enhanced by 110% and 72% when filled with 3 wt% NBCs and MBCs accordingly, as compared with those of PVA. In a similar manner, glass transition temperatures (T_g) and maximum degradation temperatures (T_d) for PVA/NBC nanocomposites are higher than those of PVA/MBC counterparts. Such improvements are associated with particle dispersion states within PVA matrices, as well as interfacial interactions between BCs and PVA matrices in nanocomposite systems.

In view of the impact of different particle shapes and structures, NBCs are generally considered as 3D nanoparticles while HNTs and Cloisite 30B clays are well known to be 2D and 1D nanoparticles, respectively. The incorporation of NBCs within PVA matrices reveals better dispersion and morphological structures than the addition of HNTs and Cloisite 30B clays in PVA nanocomposites, as evidenced by highest mechanical and thermal properties obtained for PVA/NBC nanocomposites.

This study also demonstrates for first time a novel approach to measured 3D interphase dimensions and properties between different nanofillers and PVA matrices via peak force quantitative nanomechanical tapping mode (PFQNM). More significantly, different mechanical properties of nanointerphases are revealed as opposed to those of individual nanofillers and PVA matrices. Non-uniform and

irregular three-dimensional structures and shapes of nanointerphases are manifested around individual nanofillers, which can be greatly influenced by nanoparticle size, shape and roughness, as well as nanoparticle dispersion and distribution. Interphase elastic moduli between NBCs and PVA phase are higher than those between HNTs and PVA, as well as between Cloisite 30B clays and PVA in PVA nanocomposites. Such a finding is ascribed to a higher ratio of interphase volume over particle volume for PVA/NBC nanocomposites as opposed to PVA/HNT nanocomposites and PVA/Cloisite 30B clay nanocomposites. Experimentally determined tensile moduli of PVA nanocomposites have been predicted by Halpin-Tsai model and combined Mori-Tanaka model and laminate theory in well-aligned and randomly oriented states of nanofillers, which suggests that the implementation of effective volume fractions of randomly oriented nanofillers gives rise to the better modulus estimation. Moreover, this work has developed a theoretical approach to estimate effective volume fraction of nanoparticles based on interphase volume and volume fraction. Besides, the use of effective volume fraction of nanoparticles in Halpin-Tsai model and Mori-Tanaka model reveals much better agreement with experimental data for higher accuracy.

Considering significantly high mechanical properties of PVA/NBC nanocomposites determined in this study, as well as cost effectiveness and availability of BCs, it is worthwhile to apply them on a wider scale to replace conventional carbon-based nanofillers for developing more economical and eco-friendly nanocomposites, which potentially leads to widespread applications in material packaging and biomedical engineering.

List of Publications

Journal Papers

1. **M. Mousa** and Y. Dong, "Strong Poly (Vinyl Alcohol) (PVA)/Bamboo Charcoal (BC) Nanocomposite Films with Particle Size Effect," *ACS Sustainable Chemistry & Engineering*, vol. 6, no. 1, pp. 467-479, 2017 **Impact Factor = 6.14**

2. **M. Mousa** and Y. Dong, Novel Three-Dimensional Interphase Characterisation of Polymer Nanocomposites Using Nanoscaled Topography, *Nanotechnology*, vol. 29, no. 38, 385701, 2018. **Impact Factor = 3.446**.

3. **M. H. Mousa**, Y. Dong, and I. J. Davies, "Recent Advances in Bionanocomposites: Preparation, Properties, and Applications," *International Journal of Polymeric Materials and Polymeric Biomaterials*, vol. 65, no. 5, pp. 225-254, 2016. **Impact Factor = 2.127**

4. **M. Mousa**, Y. Dong, and I. J. Davies, "Eco-friendly Polyvinyl Alcohol (PVA)/Bamboo Charcoal (BC) Nanocomposites with Superior Mechanical and Thermal Properties," *Advanced Composite Materials*, vol. 27, pp. 499-509, 2018 **Impact Factor =1.124**

5. **M. Mousa,** and Y. Dong, "Elastic Behavior of Nanophases in Polyvinyl Alcohol (PVA)/Bamboo Charcoal (BC) Nanocomposite Films,". *Frontiers in Materials.* Vol. 5, 44. **Impact Factor =2.1**

6. **M. Mousa,** and Y. Dong, Role of Nanoparticle Shape and Structure in the Material Characterisation of Poly(vinyl) Alcohol (PVA) Bionanocomposites," in preparation.

Book

7. **M. Mousa**, and Y. Dong Multiscaled PVA bionanocomposite films: Characterization and nanoscale modelling, Springer Nature, in preparation

Book Chapter

8. **M. Mousa**, and Y. Dong, A Critical Role of Interphase Properties and Features on Mechanical Properties of Poly(vinyl) Alcohol (PVA) Bionanocomposites: Nanoscaled Characterisation and Modelling, accepted.

9. **M. Mousa**, and Y. Dong, Polymeric materials as bionanocomposites: Green Synthesis and Applications, accepted

International Conference papers

10. **M. Mousa**, M. and Y. Dong, Nanomechanical Mapping of Polyvinyl Alcohol (PVA)/Bamboo Charcoal Nanoparticle (NBCs) Composites. The 26 International Conference on Processing and Fabrication of Advanced materials (PFAM-XXVI) October 16 - 21, 2017, Jeonju, South Korea. (**Oral presentation**).

11. **M. Mousa,** and Y. Dong, Eco-friendly Polyvinyl Alcohol (PVA)/ Bamboo Charcoal (BC) Nanocomposites with Superior Mechanical and Thermal

Properties, the 10th Asian-Australasian Conference on Composite Materials (ACCM-10). Busan, South Korea. October 16 – 19. (**Keynote presentation**)

Table of Contents

List of Figures

List of Tables

Nomenclatures

θ	Measured diffraction angle
$W_{\text{iInterphase}}$	Interphase width scanning along the *i*th transverse plane
d_{001}	The interlayer spacing from (001) basal reflection peak
$L_{\text{j Interphase}}$	Interphase length along the *j*th longitudinal plane
$H_{\text{k Interphase}}$	Interphase height along *k*th height plane
$SA_{\text{outer Interface}}$	Outer interface area
$SA_{\text{inner Interface}i}$	Inner interface area
$V_{\text{p/Interphase}}$	Interphase / nanoparticle volume
V_{p}	The nanoparticles volume
$V_{\text{Interphase}}$	The interphase volume
E_{random}	Elastic moduli of nanocomposites at randomly oriented nanofillers
$E_{parallel}$	Elastic moduli of nanocomposites at well-aligned nanofillers
E_m	Young's moduli of polymer matrices
E_p	Young's moduli of nanoparticles
E_{11}	Longitudinal elastic moduli of polymer nanocomposites
E_{22}	Transverse elastic moduli of polymer nanocomposites
E_c	Elastic modulusof nanocomposites
α	Aspect ratio of nanofillers
l_f	length of nanofillers
t_f	Thickness of nanofillers
$\emptyset'_p$	Nominal volume fraction of nanofillers
$\emptyset'_p$	Effective volume fraction of nanofillers

W_p	Weight fraction of nanofillers
v_m	The Poisson's ratio of polymer matrices
A_T	The specific surface area of nanofillers
η_T	$\eta_T = \frac{(E_p/E_m) - 1}{(E_{fp}/E_m) + 2}$
η_L	$\eta_L = \frac{(E_p/E_m) - 1}{(E_p/E_m) + \xi}$
ξ	$\xi = \frac{2\alpha}{3} = \frac{2\iota_p}{3t_p}$
ρ_p	The density of nanofillers
P_m	The density of polymer matrices
t	The thickness of plymer adsorbed layers
Rg	The radius of gyration of polymer matrices
kx	$kx = \frac{E_m}{E_p}\left(\frac{t}{Rg}\right)$
d_{002}	The interlayer spacing from (002) basal reflection peak
W'_p	The weight fraction of clay platelets within organoclays
W_p^1	The weight fraction of intercalated clay structures
S	$S = (1 - W_p^1)/W_p^1$
N	The average layer number per stack of platelets
h	The thickness of platelets
$e_v(r)$	The expected void fraction in a two-phase nanocomposite system
ρ	Density of isotropic particles
η	$\eta = \rho\langle V\rangle = \rho\frac{\pi^{3/2}\langle R^3\rangle}{\Gamma(1+3/2)} = \frac{4\pi}{3}\,\rho\,\langle R^3\rangle$
e	$e = \frac{\langle S\rangle}{\pi(1-\eta)}$

d	$d = \frac{4\langle R \rangle}{1-\eta} + \frac{\rho\langle R^2 \rangle}{2\pi(1-\eta)^2}$
g	$g = \frac{4}{3(1-\eta)} + \frac{4\rho\langle R \rangle\langle S \rangle}{3(1-\eta)^2} + \frac{m\rho^2\langle S \rangle^3}{27\pi(1-\eta)^3}$
$\langle S \rangle$	The average area of rigid particles
(N_V)	The number density of anisotropic particles
D_{eq}	The equivalent diameter of anisotropic particles
$F_V(D)$	The cumulative volume percentage of isotopic particles
$\langle D_{eq}^k \rangle$	$\langle D_{eq}^k \rangle = \int_{D_{\min eq}}^{D_{\max eq}} D_{eq}^k \, fn(D_{eq}) dD_{eq}$
$D_{\max eq}$	The maximum equivalent diameter of anisotropic particles
$D_{\min eq}$	The minimum equivalent diameter of anisotropic particles
EVF	equal volume fraction graduations
T_m	Melting temperature
T_c	Crystallisation temperature
T_g	Glass transition temperature
$\chi_C(\%)$	The degree of crystallinity
F_{Lc}	The load force on the cantilever
F_{adh}	The adhesion force
E^*	The reduced Young's modulus
E_{tip}	Elastic modulus of AFM tip
E_s	Elastic modulus of sample
$z - z_o$	The difference between current piezo position z and orginal position z_0
W	The energy dissipation in a cycle of interaction
$\bar{F}$	Interaction force vector
$d\bar{z}$	Displacement vector

λ	Geometric size factor of anisotropic particles
λo	Lame first constant

Chapter 1.

Introduction

1.1. Background

Advances in material science have led to increasing annual production of synthetic polymers. To date 8.3 billion metric tons of synthetic polymers have been produced [1], among which 6.3 billion metric tons becomes typical wastes. In between, about 9% have been recycled while 12% have been incinerated. The other 79% of plastic wastes are stored in landfills or directly released into the environment [1]. The majority of such plastics are petro-based synthetic polymers such as polypropylene (PP), polyethylene (PE) and polystyrene (PS) [2-5]. For example, the annual production of PE and PP only are more than 70 and 50 million metric tons, respectively [6]. Such polymers are generally regarded as non-degradable wastes after the consumption, and are often disposed of directly in the environment to cause severe pollution like marine plastic pollution. It has been reported that about 5.25 trillion plastic particles (weighing 269,000 tons) are floating on the sea [7]. such ubiquitous plastic particles in the marine environment could result in the entanglement of species by marine debris including marine mammals and other species in net fragment litter [7].

Moreover, proposed solutions such as waste accumulation in landfill are unsatisfactory on the long term because of the limitation of landfill sites in continuous urban development. In addition, the incineration of plastic wastes produces a large amount of carbon dioxide and hazardous emission such as dioxins, resulting in the detrimental effect to our ecosystem. On the other hand, recycling plastic wastes is often non-economical with insufficient processing infrastructures being available whilst the quality of recycled plastics is lower than that of virgin materials. In response to these concerns, the development of biopolymers has become an increasing priority for material scientists and engineers. Such polymers

would not involve the use of toxic gases in their manufacture, and thus can easily degrade in the environment. According to different manufacturing routes, biodegradable polymers can be classified as (i) agro-polymers based on the biomass of agro-resources as raw materials (e.g., starch and cellulose), (ii) polymers based on microbial production (e.g., polyhydroxyalkanoates), (iii) polymers that are chemically synthesised using biomass based monomers (e.g., poly (lactic acid) (PLA)) and (iv) polymers that are produced from the chemical synthesis of petroleum resources [4, 8]. Among those categories, polyvinyl alcohol (PVA) as one of most popular water soluble polymers has practically received considerable attention due to its favourable mechanical properties, thermal resistance, excellent flexibility [9] and recyclability, and bio-tribological properties [10]. Furthermore, its biotechnological applications comprise tissue engineering, drug delivery, articular cartilage and biosensors [11].

In recent years, the incorporation of nanofillers such as montmorillonite (MMT) clays [12, 13], halloysite nanotubes (HNTs) [14-16], carbon nanotubes (CNTs) [17, 18], graphene sheets [19, 20], cellulose nanocrystals [21, 22], laponite [23] and nanodiamond [24] into PVA matrices in nanocomposite systems have drawn great attention in order to significantly improve mechanical and thermal properties as well as biodegradability of PVA nanocomposites.

CNTs are considered as effective reinforcements widely used in polymer nanocomposites. In addition to their high material cost, nanotoxicity is deemed as the significant drawback to CNTs due to their accumulation in cytoplasm with their resulting ability to destroy human cells under certain inhalational conditions [25]. On the other hand, graphene sheets have also experienced limited use owing to their

tendency to form agglomerates [26]. More recently, bamboo charcoals (BCs), as newly used carbon-based particles, employed as effective reinforcements with unique eco-friendly and environmentally sustainable material features. Such BC particles are generally produced from carbonised bamboo and bamboo residues at a typical temperature of 1000˚C under nitrogen atmosphere [27], which results in the formation of significant amounts of lengthwise and crosswise pores within BC structures [27, 28]. More impressively, their volumetric porosity, mineral constituents and absorption efficiency are approximately 5, 8 and 10 times more than those of wood charcoals [27]. Besides, inner surface areas of BCs are typically in range from 250-390 m^2/g as opposed to 10 m^2/g for wood charcoals [29, 30]. Due to aforementioned remarkable characteristics, the use of BCs have led to widespread applications such as negative ion supply [31], humidity regulators [32], water purification [33], oxidation prevention, anti-bacterial [34] and anti-fungal features, as well as breathability [30]. The ability of BCs to regulate humidity has enabled them to inhibit the growth of bacteria and fungi with well-maintained freshness of food [34], which is a key requirement for food packaging industries in order to increase the shelf life of products. Additionally, BCs are also capable of absorbing significant levels of infrared energies from the environment, which can then be emitted to support cell activation for efficient human blood circulation [35]. Elemental inclusions within BCs such as calcium, potassium, sodium and iron have also been employed for the purposes of food cooking, baking and storage [36, 37].

Apart from bamboo charcoals, several types of clays have been used in nanocomposite system like kaolin [38], mica [39], sepiolite [40], and montmorillonite (MMT) [12]. Among them, (MMT) is most popular clay fillers owing to their layered silicate structures with exchangeable cations and reactive -OH

groups on MMT layer surfaces [25], as well as high strength and stiffness, large aspect ratio with natural abundance , and readily available in large quantities [25, 41]. MMT is capable of forming stable suspensions in water while its hydrophilic characteristic also promotes the dispersion of these inorganic crystalline layers in water soluble polymers, such as PVA [12]. Moreover, layered silicates in their pristine state has high ion exchange capacity, which allows for the modification of interlayer spacing in order to achieve better compatibility with base polymer [25]. Modified MMTs such as Closite 30B clays, containing 90 meq/100 g of a methyl, tallow, bis-2-hydroxyethyl ammonium chloride surfactant [42], has been employed in many studies for the preparation of bionanocomposites. For instance, Closite 30B clays contain –OH groups to be more compatible with base polymer when compared with Na^{+}MMTs and Closite 15A counterparts [43]. Moreover, Closite 30B clays have much larger *d*-spacing value as opposed to those of other modified clays such as Closite 15A, Closite 20A and Closite 25A clays [44].

Hallysite nanotubes (HNTs) as the alternative aluminosilicate clays [$Al_2Si_2O_5(OH)_4 \cdot nH_2O$] has received great attention owing to their novel 2D natural hollow nanotubular structures resembling that of multi-walled CNTs [45]. In addition, HNTs have high aspect ratios, good functionality and biocompatibility, as well as high mechanical strength [45]. These aforementioned material characteristics warrant the wide use of HNTs in biological/medical applications such as bioreactors [45], drug delivery [45] and nanocoating [45]. Moreover, HNT surfaces contain alumina and silica groups to facilitate hydrogen-bonding interactions between HNTs and PVA matrices, which make HNTs an ideal nanofiller candidate for PVA bionanocomposite films [45]

1.2. Research Significance and Objectives

1.2.1. Significance

- Most previous studies have been carried out in relation to bionanocomposites based on biopolymers such as PCL, PLA and PVA, as well as nanofillers like CNTs and GOs in order to achieve significant property enhancement. However, the cost and nanotoxic issues of CNTs as well as GO agglomeration problems are of a major concern for their potentially widespread large-scaled applications. The current study aims to develop a new ecofriendly nanocomposite system based on PVA as biopolymer matrices and BCs as nanofillers, and investigate the possibility of taking BCs as cheap, widely abundant and sustainable non-toxic nanofiller alternatives to carbon based nanofillers in comparison with clay-based nanofillers including MMT and HNTs. In a nanocomposite system, BC morphology displays a wide range of pore distribution from less than 1 nm to 1 μm [46]. The walls of the basic units within BCs, known as parenchyma, are very rough despite their smooth outer surfaces, which makes entire particles quite hard. With a large number of roughly walled pores inside BCs, polymeric chains tend to easily penetrate into internal BC pores [47] to form strong mechanical bonding in addition to the hydrogen bonding of pores. Hence, mechanical properties of resulting nanocomposites improved accordingly owing to effective interfacial bonding between nanofillers and polymer matrices. Nevertheless, the selection of polymer matrices also plays a leading role in the preparation of nanocomposites in addition to the inclusion of BCs. Polymeric behaviour in a porous medium is associated with capillary forces, enabling to prevent polymeric chains from entering into internal pores [47]. According to the Laplace theory [47, 48], the strength of capillary forces is dependent on

surface chemistry and physical properties of polymers. When hydrophilic media are selected, applied positive capillary pressures drive polymeric chains into BC pores to form both effective mechanical and chemical bondings, which is the reason why PVA has been chosen in this study. On the contrary, the surfaces of hydrophobic media generate negative capillary pressures to hinder the entry of polymeric chains into BC pores, leading to typical phase separation in a nanocomposite system. Such a mechanism can be interpreted as the debonding effect in polymer/BC composites including polylactic acid (PLA)/BC composites [31], ultra-high molecular weight polyethylene (UHMWPE)/BC composites [49] and polyaniline (PANI)/BC composites [50].

- Modified MMT has been used widely to enhance material performance of bionanocomposites. Among different types of modified MMTs, Cloisite 30B clays are of particular interest due to their structures containing –OH groups for better compatibility with water-soluble polymers like PVA as compared with those of pristine MMTs and other modified MMTs such as Cloisite 20A, Cloisite 25A and Cloisite 10A clays [44]. Moreover, Cloisite 30B clays also possess superior antimicrobial features to other nanofillers consisting of Cloisite Na^+ and Cloisite 20A clays [51] when blended with PLA. On the other hand, HNTs represent 2D novel nanofillers with the combination of tubular structures and high aspect ratios when considering the sizes of HNTs varying from 500-1000 nm in length and 15-100 nm in diameter from different sources [45]. Besides, alumina and silica groups are located on HNT surfaces, especially observed at their crystal edges for the purpose of facilitating hydrogen bonding with more active interactions with base polymeric molecules [45]. Due to the complexity

and difficulty in the experimental measurement of interphase properties and features, widely used micromechanical models such as Halpin-Tsai model [52] and Mori-Tanaka model [53] are generally employed without considering interphase features and properties between fillers and matrices for simplicity. As a result, mechanical properties of polymer nanocomposites can be either overestimated based on such conventional composite theoretical models for polymer/carbon nanotube (CNT) composites [54] and silk fibroin/graphene oxide nanocomposites [55], or underpredicted for polyamide 66 (PA66)/calcium carbonate ($CaCO_3$) nanocomposites [56]. Such drawbacks in modelling work for polymer nanocomposites are inevitably associated with the absent interphase features. Many recent attempts have been made by incorporating interphase regions as the third phase for available micromechanical models like Mori-Tanaka model [57] and Maxwell model [58] with little success. This can be attributed to a simple assumption that the interphase is one-dimensional transitional material phase surrounding nanofillers with uniform interphase thickness and regular shapes. Whereas, it is evident in reality that irregular-shape interphase with non-uniform thickness genrally occurs in the material morphology of composites [59-62]. In order to consider the benefit of real interphase effect in nanocomposite modelling work, interphase volume fraction is one of key interphase material parameters to be predetermined. Lewis [63] reported that with the inclusion of mondispersed spherical nanoparticles with the particle diameter being less than 5 nm and interphase thickness of 0.5 nm, the interphase volume fraction could be as high as 50% when compared with that of nanoparticles [63]. However, a full understanding for the effect of interphase volume fraction on elastic modulus of bulk nanocomposites still remains

challenging owing to complex interphase network structures and an overlapping potential for neighbouring interfacial layers [64, 65] The accurate experimental determination of interphase volume fraction appears to be practically inapplicable. In addition, complicated geometric configurations of nanoparticles or nanofillers give rise to a widespread variation of interphase properties and dimensions. In this study, It is aimed to develop a new modelling approach by incorporating actual interphase volume fractions, properties and dimensions into conventional composite theoretical models such as Halpin-Tsai model and Miro-Tanaka model in order to achieve more accurate prediction of elastic moduli of polymer nanocomposites.

1.2.2. Objectives

The main objective in this study is to successfully synthesise eco-friendly PVA nanocomposite films reinforced with BCs, Cloisite 30B clays and HNTs with significant enhancements of mechanical and thermal properties. The detailed steps are given as follows:

- Process and manufacture eco-friendly PVA bionanocomposite films reinforced with BCs, Cloisite 30B clays and HNTs.
- Characterise PVA based nanocomposites in terms of nanoparticle shapes, contents and structures along with the determination of material properties.
- Study 3D interphase properties in PVA based nanocomposites in order to evaluate the interphase dimensions and properties between matrices and nanofillers.
- Apply theoretical modelling to predict mechanical properties of PVA based nanocomposites using modified composite theoretical models including

interphase properties and volume fractions to achieve better agreement between the constituents and overall macroscopic behaviour of nanocomposites.

1.3. Thesis Structure

This thesis is divided into totally eight chapters as outline below (also shown in Figure1.1):

- **Chapter 1** presents the background for the development of bionanocomposites and PVA based nanocomposite films. In addition, this chapter also demonstrates research significance and objectives, as well as brief thesis outline.

- **Chapter 2** covers in details literature review about biopolymers, bionanocomposites, with a particular focus on PVA based nanocomposites reinforced with BCs, Cloisite 30B clays and HNTs. This chapter also demonstrates nanocomposite fabrication and various properties including mechanical and thermal properties as well as interphase nanomechanical properties. Moreover, this chapter also involves the recent development in micromechanical modelling approach implemented in predicting mechanical properties of nanocomposites as well as nanocomposite applications.

- **Chapter 3** reports the material selection for PVA, BCs, Cloisite 30B clays and HNTs as well as manufacturing processes and material characterisation techniques employed according to selected material formulations in this study.

- **Chapter 4** covers the initial investigation, which is pertinent to detect BC material characteristics. Moreover, it also demonstrates the effect of BC particle

sizes and contents on material characterisation, mechanical properties, nanomechanical properties and thermal properties of nanocomposite films in order to develop newly eco-friendly and super strong PVA/BC nanocomposite films. This chapter also reports a directly experimental measurement of Young's modulus of BCs via atomic force microscopy (AFM) for the first time.

- **Chapter 5** presents a holistic study in relation to the effect of different nanofiller shapes, structures and contents on material characterisation, mechanical properties, nanomechanical properties and thermal properties of bionanocomposite films. BCs are used to represent 3D irregular-shape particles while HNTs and Cloisite 30B clays are employed to represent 2D tubular nanofillers and 1D platelet-like nanofillers.

- **Chapter 6** introduces a novel approach to measure 3D interphase properties and dimensions in nanocomposite systems in terms of interphase surface area and interphase volume.

- **Chapter 7** undertakes micromechanical modelling to predict the elastic modulus of PVA based nanocomposites with the estimated results being compared with those obtained from experimental work. Moreover, micromechanical models developed to consider the incorporation of 3D interphases in nanocomposite systems in terms of interphase surface area and interphase volume. A more reliable agreement occurs between experimental data and theoretical modelling results based on interphase properties and effective volume fraction of nanoparticles.

Chapter 8 summaries main conclusions for the entire research work, as well as the recommendations and future work for consideration.

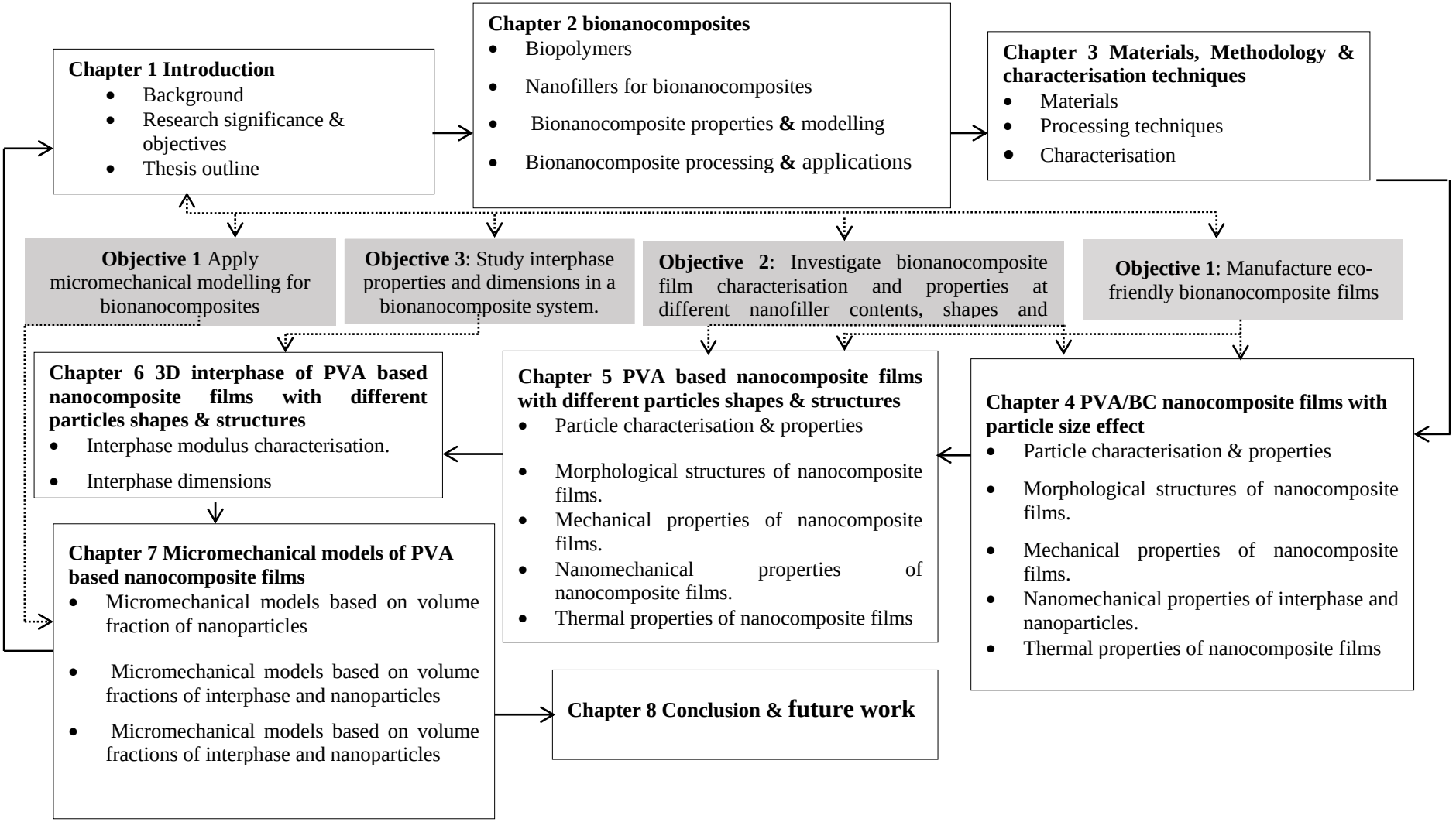

Figure 1.1 Thesis structure.

Chapter 2.

Literature Review

2.1. Biopolymers

Biodegradable polymers or biopolymers are defined as those polymeric materials that can degrade in a bioactive environment via the enzymatic action of microorganisms such as bacteria, fungi, and algae. Moreover, some polymeric chains may also undergo a scission-down by nonenzymatic processes like chemical hydrolysis. Among different types of biopolymers, poly lactide or poly lactic acid (PLA) is regarded as one of the most widely produced bioplastics [66]. It is a linear thermoplastic polymer mainly derived from renewable resources such as corns or sugar beets [66]. Fully biodegradable and non-toxic PLA is produced from lactic acid that possesses a chiral molecule in the dextrorotatory form as L-(+)-lactic acid or else in the levorotatory form as D-(-)-lactic acid. The insufficient properties of some PLA in relation to thermal stability, impact resistance and flexibility can be improved by their blending with other polymers like poly(ethylene oxide) (PEO) or by using a plasticiser such as oligomer lactic acid (OLA), citrate ester or low-molecular-weight polyethylene glycol (PEG) [8, 67]. Moreover, it is worth noting that the processing temperature of PLA should exceed thermal degradation temperature at 200°C. However, microbial degradation of PLA seems still challenging because PLA requires the temperature level above its glass transition temperature (T_g=55-62°C) for the onset of PLA hydrolysis, which makes its degradation difficult at ambient temperatures. Additionally, the degradation rate of PLA depends on its molecular weight. In general, high-molecular-weight PLA is mechanically stronger, and less susceptible to biodegradation [68].

Polyhydroxyalkanoates (PHA) as another biopolymer belongs to a family of naturally occurring hydrophobic, biocompatible and biodegradable polyesters [69, 70]. It is available in a wide variety of forms, and used for carbon or energy storage

in microorganism in the form of light refracting granules inside the cells. According to their chain length, PHA can be divided into three major types, namely short chain length (scI PHA with carbon number range of C3-C5), medium chain length (msI PHA with carbon number range of C6-C14) and long chain length (IcI PHA with carbon number greater than C14) [71]. Polyhydroxybutyrate (PHB) and poly (hydroxybutyrate-cohydroxyvalerate) (PHBV) are the two most common PHA based polymers with a wide range of microorganisms used to accumulate PHB. However, the genetic manipulation is essential for the large-scaled production of PHB. Whereas, alcaligenes eutrophus is the most common microorganism used in the biosynthesis of PHA [67, 69-71]. PHB is comparable to polypropylene (PP) due to their several similar physical properties such as melting point, degree of crystallinity and glass transition temperature. Nevertheless, PHA exhibits higher stiffness, lower toughness, lower solvent resistance and higher natural resistance to ultraviolet radiation when compared with PP [69]. The main disadvantage of PHA lies in its narrow processing window since it starts to degrade under the condition of high shear and high temperature.

Poly (ε-caprolactone) (PCL) is a linear polyester synthesised via the ring-opening polymerisation of ε-caprolactone in the presence of metal alkoxides [2]. It possesses good flexibility and high elongation at break, which makes it attractive for various applications such as PVC plasticisation, drug release control and soft compostable packaging [2]. The main drawback of PCL is its low melting point at 65°C, which can be alleviated by polymer blending [72, 73] or by modifications such as cross-linking [74]. PCL biodegradability can be assessed in the presence of fungi, which is ready for enzymatic degradation [74]. Such similar effect is also achieved in bacteria and yeast [75]. The low hydrolysis rate of PCL homopolymer [76, 77], has been

shown to be improved significantly when blended with starch [72]. However, high production cost remains its main material demerit.

In contrast to above-mentioned biopolymers, water-soluble polymers have a broad range of applications in various fields such as food and pharmaceutical use, detergent builders, scale inhibitors, adhesives and so on [78]. A majority of water-soluble polymers are prepared from acrylic acid, maleic anhydride, methacrylic acid, and various combinations of these monomers. Except their oligomers, these polymers are commonly non-biodegradable. Therefore, conventional water-soluble polymers persist in water depositories such as oceans and lakes and their effects are harder to be recognised by consumers with potential problems [78]. Water-soluble biopolymers could be synthesised via the modification of starch and cellulose such as carboxymethyl cellulose (CMC) and hydroxyethyl cellulose (HEC). However, the biodegradability of such polysaccharide-derived polymer decreases when a high level of cellulose modification is used. Moreover, many of these polymers have not yet been studied by standard testing methods to determine their biodegradability [78, 79] .

Poly (amino acids) with free carboxylic groups, such as poly (aspartic acid) and poly-(glutamic acid), are considered as suitable material candidates for water-soluble biopolymers. As such, those polymers based on aspartic acid can lead to greater commercial success. Poly (aspartic acid)s (thermal polyaspartate, TPAs) are functionally equivalent to poly(acrylic acid), and become fully biodegradable when they are highly linear in chemical structures [78, 80]. TPAs used in a wide range of applications such as performance chemicals, diapers, and agriculture. Poly (malic

acid)s, the polyester equivalent of poly(aspartic acid)s, may be useful polymers for biodegradable detergents despite their hydrolytically unstable characteristic [78].

To date, poly (vinyl alcohol) or PVA is the only water-soluble polymer with exclusively carbon atoms in main chains with good biodegradability. It is currently used in textiles, paper and packaging industries as paper coatings, adhesives and films [78].

2.1.1. Poly (Vinyl Alcohol) (PVA)

PVA is a water-soluble polymer with 1, 3-diol units or 1, 2-diol units, which depends on the hydrolysis of poly (vinyl acetate). In addition, the content of 1, 2-diol units reduced when the temperature of vinyl acetate polymerisation decreases. The chemical structures of PVA and viny alcohol are shown in Figure 2. 1. PVA has been synthesised by several routes such as the polyaldol condensation of acetaldehyde despite its little success until now [81]. In addition, the polymerisation of metal compounds, followed by the saponification process, produces low-molecular-weight PVA. However, the synthesis of PVA by the polymerisation of vinyl ester or ethers, further subjected to the saponification or esterification, is regarded as the most popular method [13, 81, 82]. In this technique, vinyl ester or other derivatives such as vinyl mono and dichloroacetate are usually used as base materials for manufacturing PVA. Moreover, PVA characteristics like molecular weight and residual content of acetyl groups can be controlled by optimising processing parameters such as polymerisation temperature, vinyl acetate/methoanol ratio and polymerisation conversion [83]. It has been reported that the decrease in polymerisation temperature with a suitable proportion of methonal and conversion leads to an increase in the molecular weight of final PVA [83]. In addition, PVA

should be free from monomeric vinyl acetate to avoid the cosaponification [81]. The conversion process of PVAc to PVA is usually carried out in the solution, suspension, or emulsion in the presence alkaline or acidic catalysts. As such, the most recommended process is the transesterification in the methanol using a proper amount of sodium methoxide as the catalysts. The residual content of acetyl groups can be controlled by manipulating the catalyst content, reaction temperature and reaction time. Moreover, the types of catalysts and solvents used are selected based on the distribution nature of acetyl groups in the partial saponification of PVA. For example, acetyl groups are distributed in a blockwise manner in case of alkaline saponification while they distributed statistically in case of acidic saponification [83].

PVA properties are determined from molecular weight and degree of hydrolysis, as depicted in Figure 2.2. When these two parameters are increased, the water resistance, tensile strength, block resistance and solvent resistance increase while solubility, flexibility and water sensitivity diminish accordingly [84]. Remarkable PVA properties such as its resistance against organic solvents, water solubility (even in cold water), low cost, good mechanical properties and excellent barrier properties [78] make it an excellent biopolymer candidate for various applications ranging from food packaging, textile products, paper coating, finishing adhesives to medical devices [13, 82, 84]. The biocompatibility of PVA has been widely investigated with its apparent non-toxic characteristic. For example, it has been reported that subcutaneous and intramuscular implantation of PVA hydrogel into rabbits did not induce any adverse effects on the surrounding tissues [82]. Similarly, the injection of PVA hydrogel into the eyes of crab-eating macaques did not show any evidence, even after three-month tissue loss, as compared to the change in opthalmoscopic finding or increase in intraocular pressure [78]. In addition, after the investigation of

PVA biocompatibility by the food industry, PVA is recommended as a safe biopolymer product [13, 82, 84].

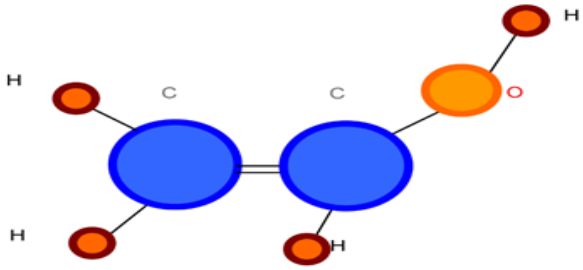

(a) Vinyl alcohol

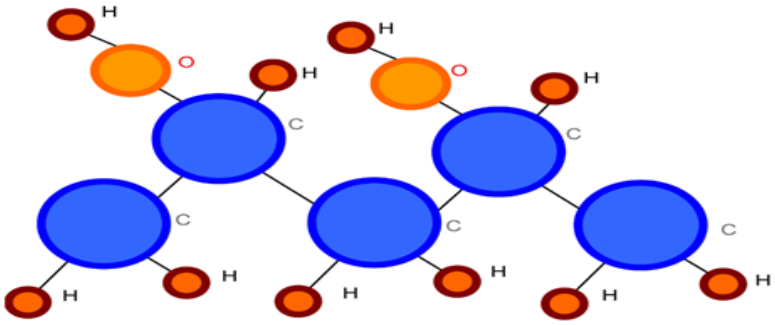

(b) Poly vinyl alcohol

Figure 2.1 Chemical structures: (a) viny alcohol and (b) poly vinyl alcohol (PVA) [78].

2.1.1.1. PVA solubility and Viscosity in Water

In general, PVA is used after being dissolved in water. Such a polymer can be dissolved in water when the entire strength of solute-solvent hydrogen bonding exceeds that of PVA inter-molecular hydrogen bonding [85]. As a result, PVA solubility in water is mainly determined by the degree of hydrolysis. It is noted that the solubility of PVA with a partial degree of hydrolysis is higher than that of full hydrolysis crystalline counterpart [85]. This could be attributed to strong inter-

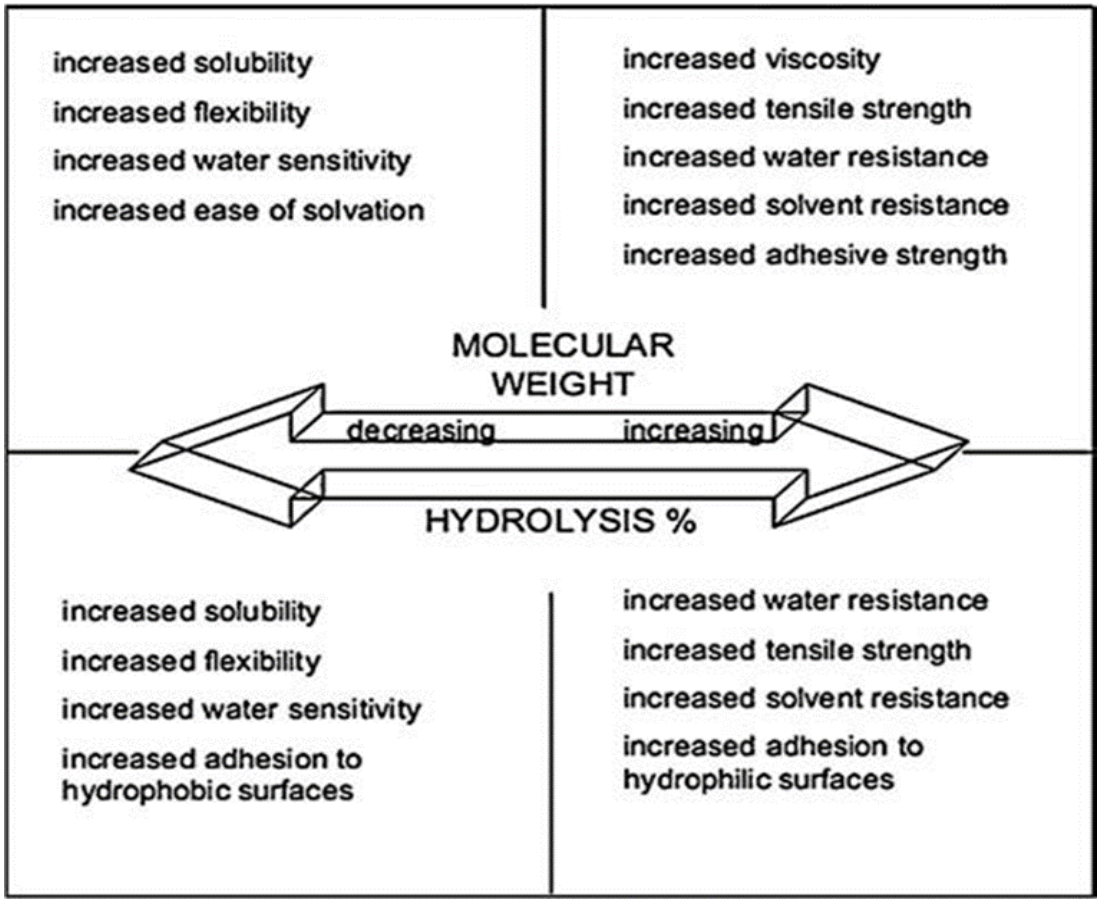

Figure 2.2 Effect of degree of hydrolysis and molecular weight on PVA properties [86].

molecular hydrogen bonding in the case of full hydrolysis when compared with partial hydrolysis, as shown in Figure 2.3 [87]. In addition, to ensure that PVA has been completely dissolved in water, the preparation temperature must exceed 80°C over an acceptable time period [87]. It is believed that the inter- and intrachain hydrogen bonding of PVA is disrupted by thermal energy. Moreover, the interaction between PVA chains leads to the increase in solution viscosity, and may further result in phase separation, depending on its degree of hydrolysis, solid content and storage modulus [88, 89]. On the other hand, PVA with the partial hydrolysis can be dissolved in water at room temperature more readily than that with a full degree of hydrolysis [90]. Moreover, the viscosity of PVA demonstrates a marginal change with the storage time, which is ascribed to more acetyl groups in PVA with the

partial hydrolysis to be responsible for disrupting inter- and intrachain hydrogen bondings, thus resulting in the increase of polymer solubility in water [90].

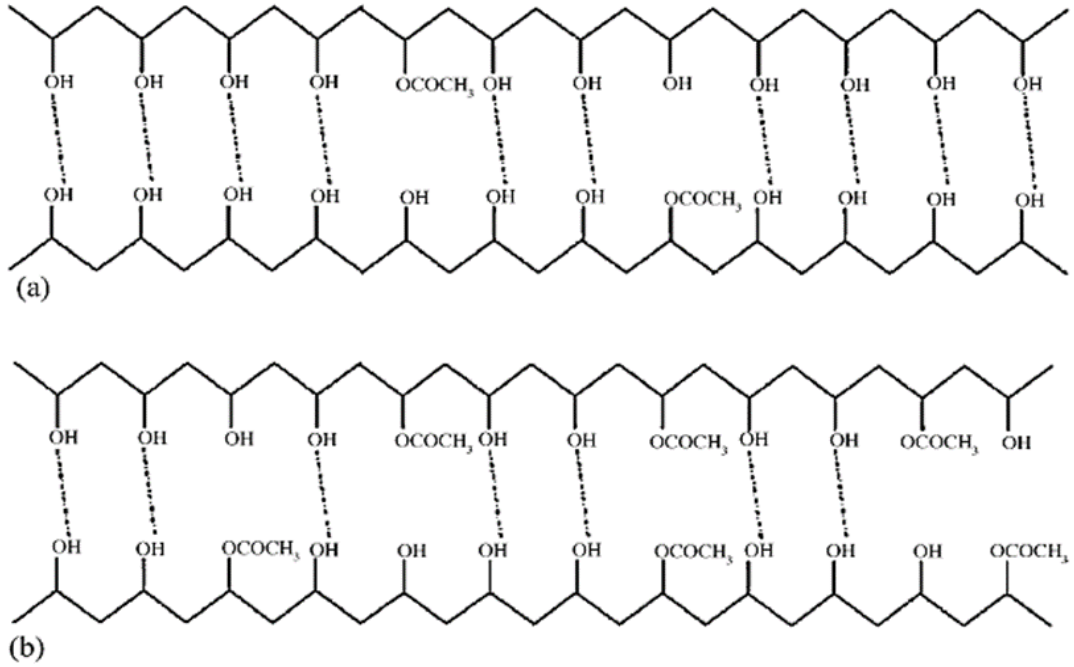

Figure 2.3 Inter-molecular hydrogen bonding for different types of PVA containing (a) full-hydrolysis molecules and (b) partial- hydrolysis molecules [87].

The molecular weight (MW) of PVA is also considered as an important factor in controlling solubility. In case of full-hydrolysis PVA, the solubility decreases with increasing the molecular weight, which is because the increase in PVA molecular weight leads to the higher possibility of intramolecular hydrogen bonding between hydroxyl groups in side branches [90]. As such, these types of bonds make PVA difficult to dissolve in water. For example, Chang et al. [87] noted that full-hydrolysis PVA with MW = 22,000 dalton (Da) was higher than that of full-hydrolysis PVA with MW= 74,800 dalton (Da). However, partial-hydrolysis PVA demonstrates different solubility behaviour. The solubility of PVA increases with increasing its molecular weight, which is attributed to a small number of hydroxyl groups in partial-hydrolysis PVA, which is insufficient to build up the intra-molecular hydrogen bonding [90]. In addition to molecular weight effect, electrolyte

impact on hydrogen bonding in a water soluble system has also been investigated [91]. It is believed that the use of electrolyte can disrupt hydrogen bonding between polymeric chains with an decrease in the viscosity of polymer solutions [91]. In case of PVA, The additional NaCl can induce the disruption of inter- and intrachains for hydrogen bonding. That is why it is essential to enhance both PVA solubility and viscosity in water. Nevertheless, the further addition of NaCl leads to the disruption of solute-solvent hydrogen bonding with decreasing the solution viscosity [92].

2.2. Nanofillers for Bionanocomposites

2.2.1. Layered Silicates

Natural or synthetic mineral-layered silicates have gained great popularity as effective reinforcements for nanocomposite systems. These types of fillers comprise stacks of layers separated by van der Waals interactions with gallery spacing. Each layer is typically 1 nm in thickness and 30 nm to several microns in length [93, 94]. Depending on clay sources, silicate types and synthesis techniques, these layers can be bound together with counter ions. Each layer comprises a tetrahedral sheet containing a silicon atom surrounded by four oxygen atoms and an octahedral sheet in which metals such as aluminium or magnesium hydroxide are surrounded by eight oxygen atoms. For instance, kaolinite 1:1 layered structure consists of a silicon tetrahedral sheet and aluminium octahedral sheet that share a common plane of oxygen atoms [93]. In comparison to this, the crystal structure for 2:1 phyllosilicates has two tetrahedral sheets with a central octahedral sheet of alumina (Figure 2. 4) [95, 96]. Pyrophyllite is formed in a 2:1 crystal structure containing silicon in tetrahedral sheets and aluminium in an octahedral sheet without any partial or complete replacement of atoms. Pyrophyllite layers do not expand in water and

possess only outer surface areas. When the substitution takes place between the silicon in tetrahedral sheets and aluminium in octahedral sheets, the final structure is known as mica. Any negative hole resulting from mineral substitution is counter balanced by potassium cations located in the gallery. Mica has a similar behaviour to pyrophyllite in that it does not expand in water and only possesses external surface areas. This is attributed to the potassium cation occupying the holes resulting from Si/Al replacement. On the other hand, a partial substitution between $Al^{3+}$and Mg^{2+} is required in order to ensure that layered silicates possess the ability to swell in water and hydrophilic polymers. Such a clay type is known as montmorillonite (MMT). Additionally, the negative charge is balanced by sodium or calcium ions that fit the gap leading to the weak bonding between the layers. Thus, it explains why MMTs are commonly used as fillers in polymer nanocomposites. Apart from MMTs, hectorite and sponite are also attractive fillers owing to their high aspect ratios and good dispersibility, as well as their easy surface modification using organic or inorganic surface cations [96, 97]. Chemical formulae for these nanoclays are given in Table 2.1 The pristine form of layered silicates containing sodium and calcium ions alone is only miscible with hydrophilic polymers such as PVA [98] and PEO [99]. In order to make nanoclays miscible with hydrophobic polymers, their surface condition must be modified from hydrophilic to organophilic using ion-exchange reactions based on the typical method in which alkali-cation ions are substituted for organic compounds like alkylammonium ions, sulfonium and phosphonium (Figure 2.5) [99, 100].

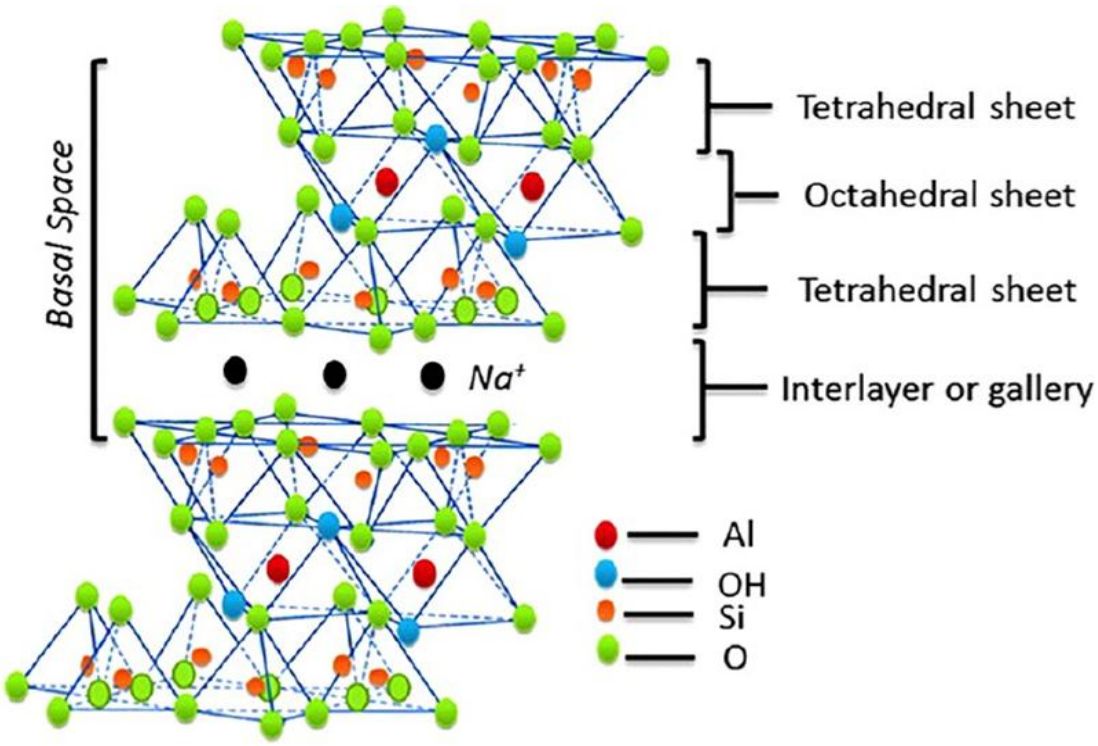

Figure 2.4 Crystal structure of 2:1 layered silicates [101].

These organic surfactants can minimise the surface energy of inorganic host and enhance clay wettability by using hydrophobic polymers with increasing the interlayer spacing. In addition, functional groups of organic compounds have also been utilised to improve the bonding between layered silicates and polymers [100, 102]. The chain length of surfactants and charge density of clays are known to play an important role in controlling the interlayer spacing between clays. In general, the use of a long molecular chain in combination with high charge density tends to increase the interlayer spacing (Figure 2.6) [103, 104].

Table 2.1 Chemical structures of commonly used 2:1 phyllosilicates [97].

2:1 Phyllosilicate	General formula
Montmorillonite	$M_x (Al_{4-x}Mg_x) Si_8O_{20}(OH)_4$
Hectorite	$M_x (Mg_{6-x}Li_x) Si_8O_{20}(OH)_4$
Saponite	$M_x Mg_6(Si_{8-x}Al_x) O_{20}(OH)_4$

Wang *et al.* [105] prepared organoclays with different chain lengths of alkylammonium and they achieved an increase in interlayer spacing values with

increasing the length of alkylammonium. It was reported that the interlayer spacing of MMT modified with octadecylammonium was increased from 1.36 to 2.47 nm.

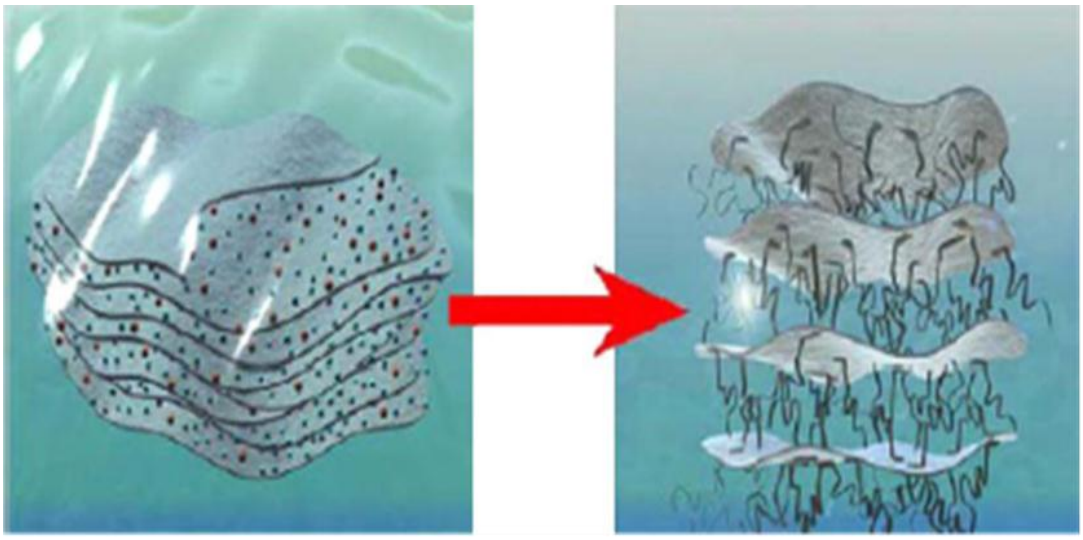

Figure 2.5 Schematic diagram of the modification of layered silicates by ion–exchange reactions [103].

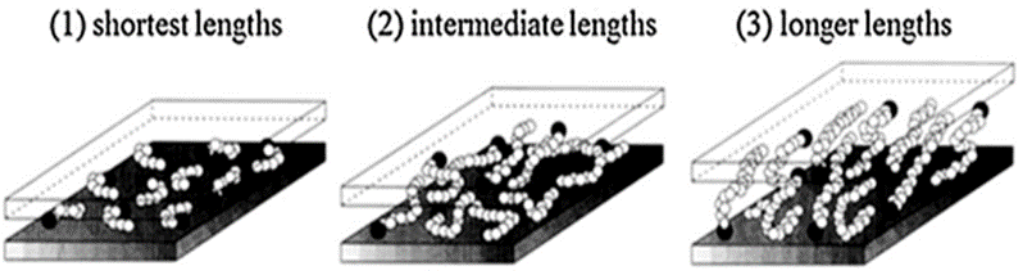

Figure 2.6 Alkylammonium chain aggregation models [25].

2.2.2. Halloysite Nanotubes (HNTs)

Halloysite nanotubes (HNTs) are a type of tubular clays that occur naturally as a result of hydrothermal change in alumino-silicate minerals [45, 106]. HNTs were named after Omalius d'Halloy who discovered such a mineral material in 1826. The HNT crystal structure comprises tetrahedral sheets with corner shared SiO_4 and octahedral sheets with edge shared AlO_6, as depicted in Figure 2.7. HNTs (chemical formula: $Al_2Si_2O_5(OH)_4 \cdot nH_2O$) can be classified as hydrated or dehydrated halloysite depending on the value of n. In the case of $n = 2$, hydrated halloysite is formed with a 10 Å interlayer space while dehydrated halloysite is formed when $n = 0$ [107, 108]. A

second scenario can take place when HNTs are heated to 30-110°C, leading to the removal of water molecules located in their interlayer areas [45]. Halloysite can be observed in different forms such as tubular, spheroidal and platy halloysite depending on the geological and crystallisation conditions, among which the tubular form is the most common one [109]. HNT surfaces contain low hydroxyl groups in addition to siloxane groups (Si-O-Si) while the interlayer region contains intensive hydroxyl groups with Al-OH. The main feature of having low numbers of hydroxyl groups on HNT surfaces is to minimise the tube-tube interaction, and thus promote their miscibility with polymers or other solvents [110-113]. The main advantages of HNTs include their wide availability [45], cost-effectiveness, environmental friendliness [114], high aspect ratio [115] and high heat resistance in addition to their good mechanical properties, as shown in Table 2.2. HNTs are widely used for nanoreactors [109], sorbent for contaminants and drug delivery [107]. Most raw halloysite contains impurities such as illite, feldspar, perlite and metal ions to be removed prior to use. However, previous studies [16, 116] have shown that pure HNTs can be obtained after stirring 10 wt% HNTs in distilled water with gradually improved HNT dispersion up to 60°C. This step is followed by centrifugation and washing three times by using distilled water before being dried in air at 60°C for 12 h. Sodiumhexametaphosphate [116] and Tween 80 [16] can be added to the suspension in order to improve the stability of HNTs within the suspension. In nanocomposite systems, HNTs are considered as promising nanoreinforcements due to their outstanding material performance, demonstrating overall performance improvement of thermoplastics or their blends such as polyamide, PP/PCL and polybutylene terephthalate (PBT) via melt compounding without any modification [45, 109]. However, the surface functionalisation of HNTs is required to increase

their compatibility with polymers in order to ensure maximum stress transfer from polymer matrices to HNTs in nanocomposites [45, 109]. Two approaches exist for HNT modification, namely covalent modification and non-covalent modification [45]. Covalent modification uses the reaction between a covalent agent and hydroxyl groups on HNT surfaces to increase their interfacial adhesion.

Table 2.2 Typical properties of HNTs.

Type of property	Description	Ref.
Chemical formula	$Al_2Si_2O_5(OH)_4 \cdot nH_2O$	[45, 107]
Aluminium (%)	20.9	[106]
Silicon (%)	21.76	[106]
Hydrogen (%)	1.56	[106]
Length	100-2000 nm	[109]
Internal diameter	30-50 nm	[109]
External diameter	1-30 nm	[109]
Aspect ratio	10-50	[45]
Elastic modulus (theoretical value)	140 GPa (230-340 GPa)	[117, 118]
Mean particle size in aqueous solution	143 nm	[119]
Particle size range in aqueous solution	50-400 nm	[119]
BET surface area	22.1-81.6 m^2g^{-1}	[120]
Lumen space	11-39%	[45]
Density	2.14-2.59 $g \cdot cm^{-3}$	[45]
Structure water release temperature	400-600 ◦C	[45]

This has been achieved by grafting HNTs with silane coupling agents such as γ-lycidoxypropyltrimethoxysilane (GPTS) [121], 3-aminopropyltrimethoxysilane

(APS) [122], (3-aminopropyl) triethoxysilane (APTES) [123] or 3-(trimethoxysilyl)propyl methacrylate (MAPTS) [124] in the presence of toluene or water/alcohol mixture. This method can also be used as a pre-treatment before applying surface graft polymerisation as another HNT surface modification process [108]. The second method involves the grafting of HNTs by compatible polymeric chains such as poly (butylenes adipate) (PBA). It has been found that 3 wt% PBA-grafted HNTs could significantly increase the interfacial bonding between HNTs and polyvinylchloride [125]. The other study indicates that grafting HNTs with poly (methyl methacrylate) (PMMA) can increase the contact angle of water, decrease the polarity of HNTs, and enhance toughness and wear resistance for resulting nanocomposites [126]. Phosphonic acid grafting is another method of covalent modification to result in significant increases in interlayer spacing for HNTs (i.e., increasing from 7 to 15.1 Å), which induces improved HNT dispersion and better performance for final nanocomposites [127]. Figure 2.8 illustrates an example of HNTs before and after modification. Though covalent modification results in some improvements to nanocomposite performance, a relatively low number of hydroxyl groups existing on HNT surfaces offers limited reaction sites for covalent modification, which makes this method generally unsatisfactory for HNT modification [45]. Fortunately, the presence of metallic atoms such as Al and Fe without occupied orbital can render suitable opportunities to modify HNTs through an electron transfer interaction (*i.e.*, non-covalent approach) [128]. During this process, chemical compounds with the ability to donate electrons such as 2,5-bis (2-benzoxazolyl) thiophene (BBT) [116] and 2,2-(1,2-ethene diyldi-4,1-phenylene) bisbenzoxazole (EPB) [129] are mechanically mixed with HNTs to form fibril structures within continuous polymer matrices.

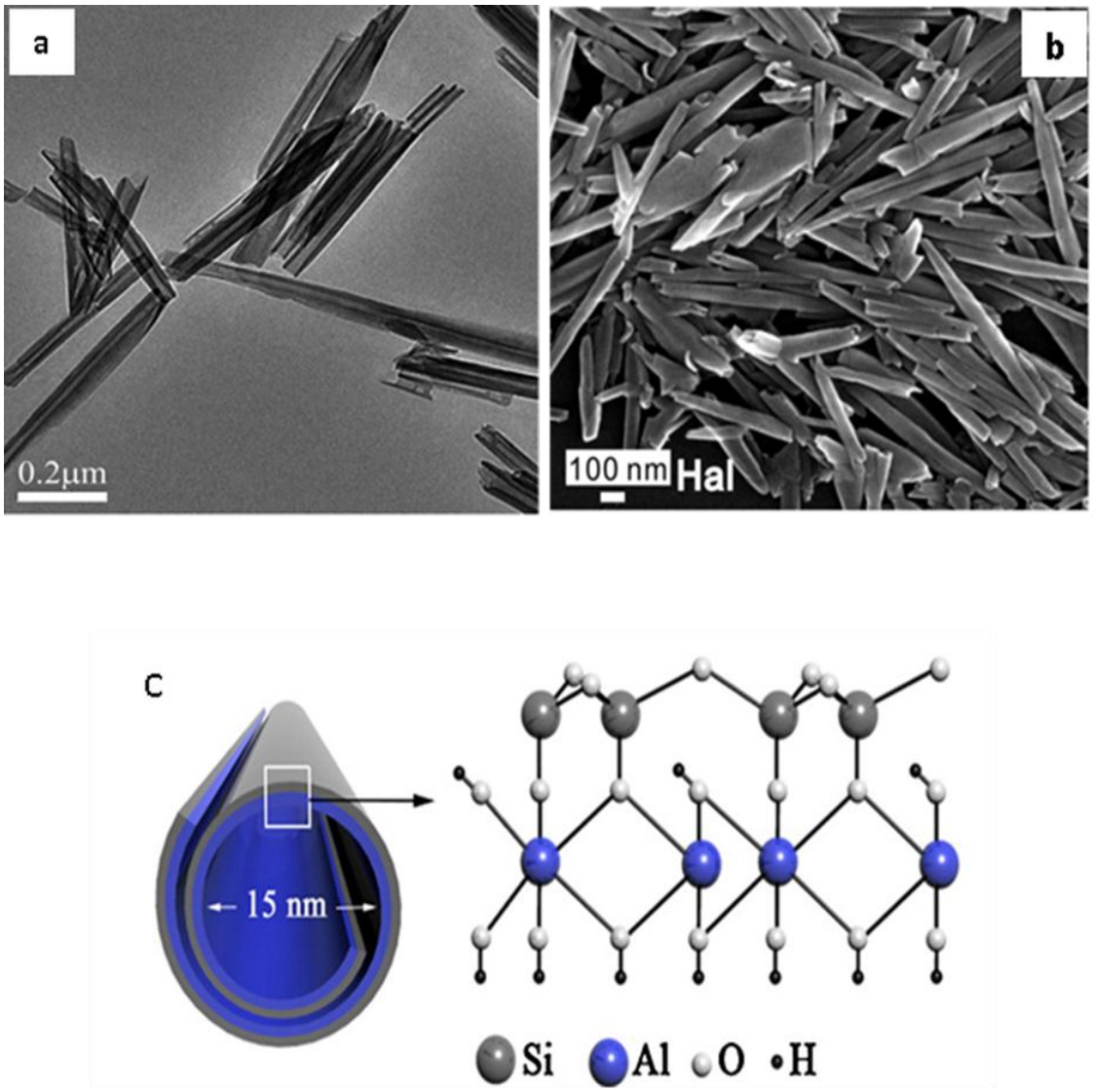

Figure 2.7 Halloysite shape and structure: (a) transmission electron micrograph (b) scanning electron micrograph [112] and (c) chemical structure of halloysite [45].

This enhances the crystallinity level and mechanical performance of final nanocomposites [45]. Hydrogen bonding interaction is a second non-covalent modification technique in which organic compounds involving melamine (MEL), melamine cyanurate (MCA) or diphenylguanidine (DPG) are attached to HNTs by hydrogen bonding to create filler networks within polymer matrices [130]. It has been reported that HNT/MEL based nanocomposites possess increased flexural modulus of 3.65 GPa and flexural strength of 109.1 MPa when compared with those of unfilled polymer (1.93 GPa and 79.7 MPa, respectively) [131].

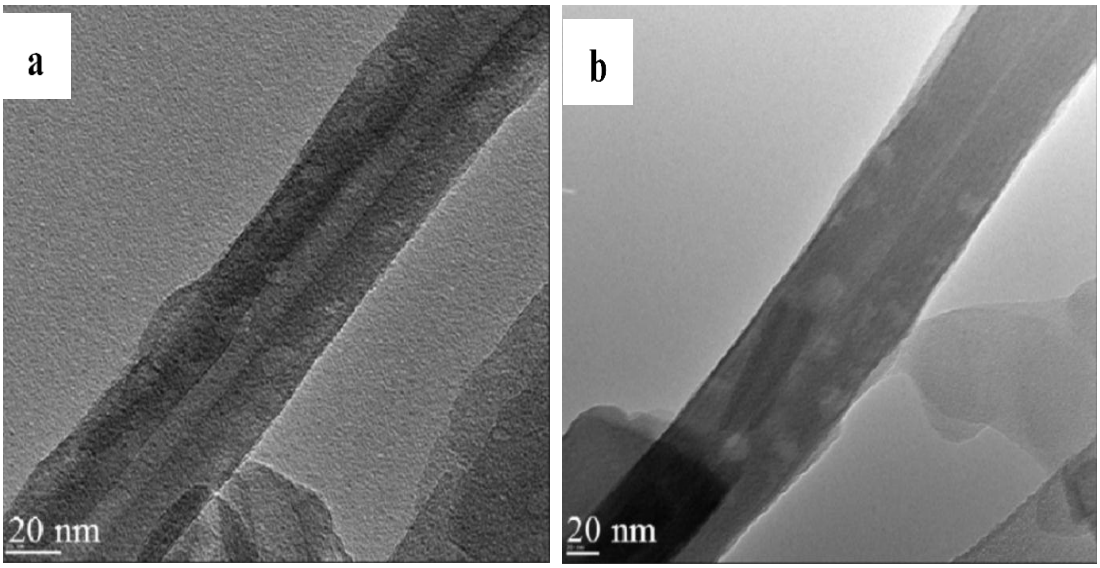

Figure 2.8 Transmission electron micrographs of halloysite: (a) pristine HNT and (b) octadecylphosphonic acid treated HNT [129].

2.2.3. Bamboo Charcoals (BCs)

Bamboos as naturally grown plants are usually discovered in East Asia, but currently grow worldwide, especially in subtropical regions [46]. Moreover, bamboo forests cover approximately 22 million hectares, which is equivalent to 1% of total global forest areas [46]. Bamboos are also considered as inexpensive and eco-friendly materials because they do not required fertilisers, or pesticides for their growth. Bamboos can be converted into widely used charcoals with typical porous structures when they are carbonised or pyrolysed. The carbonisation is carried out at inert atmosphere and temperature above 700ºC, during which bamboos start to release the water content and organic gases, followed by the reconstruction of carbon structures [132]. Although the volume of bamboo can shrink significantly during the carbonisation, their tubular structures still well remain. Figure 2.9 presents morphological structures for cross-sectional and lateral views of bamboo charcoals carbonised at 1000 ºC, which confirms apparent existing porous nature of original bamboos [46].

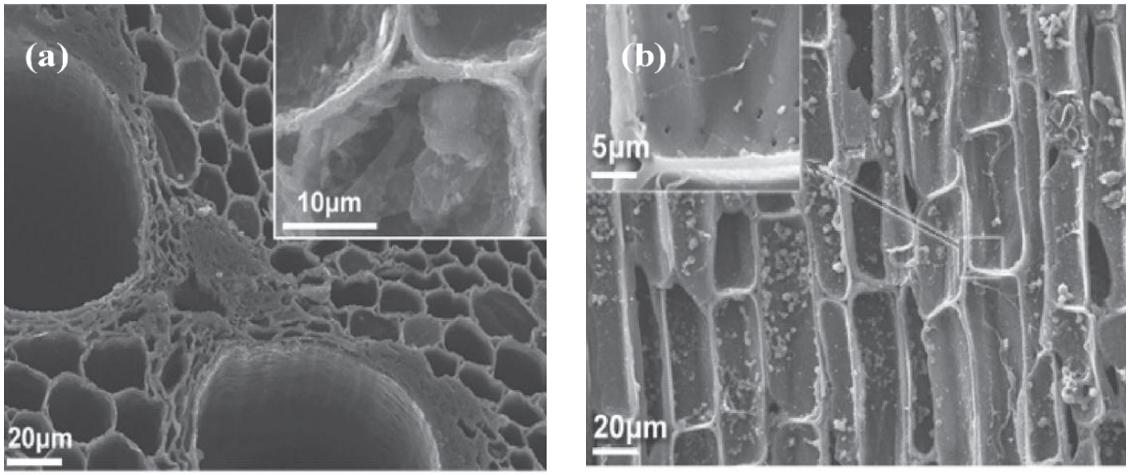

Figure 2.9 scanning electron micrograph of raw bamboo biotemplate after pyrolysis: (a) cross-sectional view and (b) lateral view [46].

In previous work [133], morphological structures and the shrinkage of bamboo charcoals were investigated at different carbonisation temperatures, which showed that the scaffolding of bamboo charcoals was similar to that of original bamboos despite a slight change of bamboo microstructures during the shrinkage. Furthermore, the shrinkage ratios of bamboo carbonised at 500, 750, and 1000 ºC were found to be about 21, 38, and 40%, respectively. Zhu et al. [134] confirmed that morphological structures of bamboo charcoals pyrolysed at 1000-1500ºC possessed the same porous features of fresh bamboos as well as exhibited a wide range of pore distributions from 1 nm to 1 μm in size. On the other hand, rough walls of basic units inside bamboo charcoals, namely parenchyma, along with their smooth outer surfaces can make entire charcoals very hard. This is because bamboo charcoals consist of carbons with a small amount of minerals. Chen et al. [135], as seen in Figure 2.10, investigated the graphitisation behaviour of bamboo charcoals treated in temperature range from 2100-3000ºC by using X-ray diffraction (XRD) analysis. In general, XRD result for BC showed the existence of two broad bands at 22 and 43º corresponding to the C_{0002} and C_{0004} reflections of carbon, respectively. Moreover, it

was clearly revealed that increasing the graphitisation temperature led to a decreasing d_{002} spacing of bamboo charcoals while corresponding graphite crystallite size L_c increased instead.

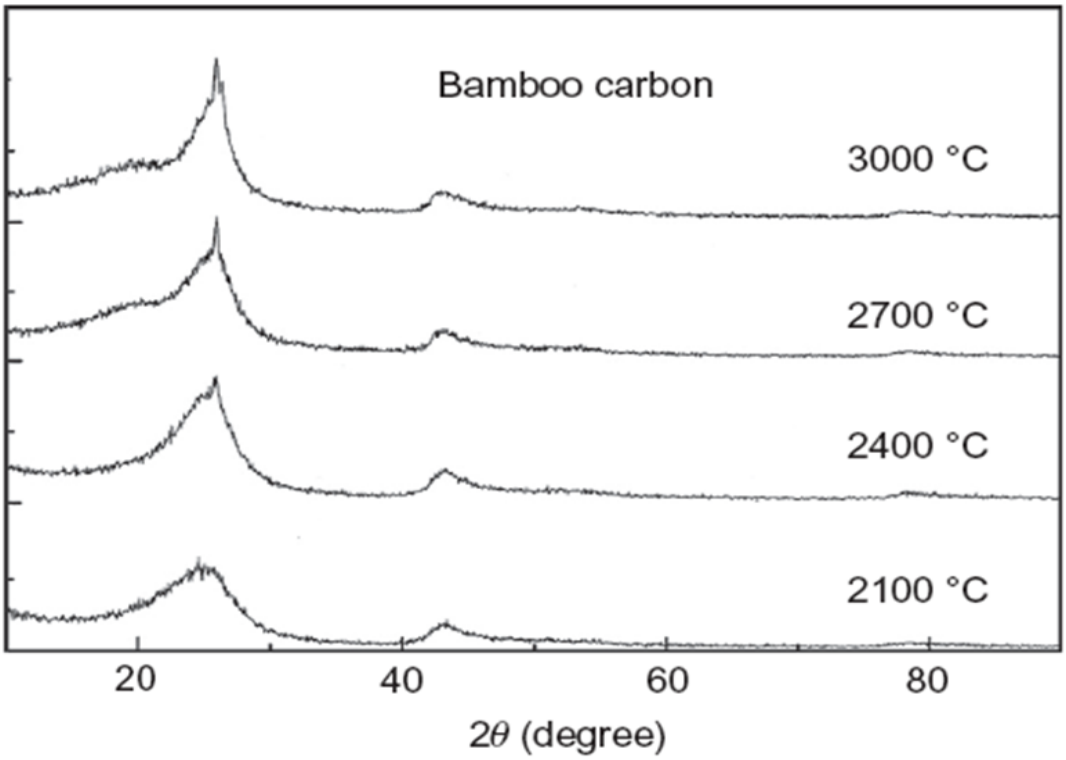

Figure 2.10 XRD profiles of bamboo charcoals after the carbonisation at different temperatures [135].

The amount of minerals inside bamboo charcoals is usually less than 10 wt%, and the amount and type of such minerals depend on the carbnisation temperature as well as geological vegetation source. For example, the bamboos 'phyllostachys edulis' obtained from Fujian province, China contain many additional elements, such as Si, N, P, K, Mg, Al in addition to C, O and H [46]. As mentioned above, carbon represents the main element of bamboo charcoals. This kind of biocarbon with special structures attracts the considerable attention for a wide range of applications such as the adsorption of harmful gases in air and the disposal of heavy metal ions in

sewage water treatment [136]. Bamboo charcoals have high volumetric porosity and large surface areas of approximately 250-390 m^2/g as opposed to 10 m^2/g for wood charcoals, thus they can strongly absorb toxic gases in the environment [136]. Asada et al. [137] reported that the adsorption ability of bamboo charcoals to benzene, toluene and skatole increased with increasing the carbonisation temperature. Additionally, bamboo charcoals are also capable of emitting infrared waves that can be absorbed by human bodies. As a result, they can improve human microcirculation system, stimulate bodies' acupuncture meridians, promote metabolism and balance the body pH level and so on [136].

Bamboo charcoals (BCs) due to their carbon content also possess certain electrical conductivity and magnetic properties [136]. Electromagnetic pollution becomes a critical issue owing to the excessive application of electronic technology. It has been reported that in range of 10-1000 MHz, composite materials reinforced with BCs (thickness: 3 mm) have electromagnetic shielding effect of 45-75 dB [136]. Additionally, BCs have a special feature to prevent them from electromagnetic radiation, which can motivate manufacturers to develop man-made boards for IT applications. BCs are also considered as good materials in manufacturing super capacitors and lithium-ion batteries [136]. In a nanocomposite system, the BC morphology displays a wide range of pore distributions from less than 1 nm to 1 μm [46]. BC structure comprises parenchyma, which is the basic unit inside bamboo and specified with rough wall surfaces, With a large number of rough walled pores inside BCs, polymeric chains tend to easily penetrate into internal BC pores [47] to form strong mechanical bonding in addition to the hydrogen bonding of pores. Hence, mechanical properties of resulting nanocomposites can be improved accordingly owing to the effective interfacial bonding between fillers and polymer matrices.

Nevertheless, the selection of polymer matrices also plays a leading role in the preparation of nanocomposites in addition to BCs. Polymeric behaviour in a porous medium is associated with capillary forces, which enables to prevent polymeric chains from entering into internal pores [47]. According to the Laplace theory [47, 48], the strength of capillary forces is dependent on surface chemistry and physical properties of polymers. When hydrophilic media are selected, applied positive capillary pressures drive polymeric chains into BC pores to form both mechanical and chemical bondings, which is why PVA has been chosen in this study. On the contrary, the surfaces of hydrophobic media generate negative capillary pressures, and thus hinder the entry of polymeric chains into BC pores, leading to typical phase separation in a nanocomposite system. Such a mechanism can be interpreted as the debonding effect in polymer/BC composites including PLA/BC composites [31], ultra-high molecular weight polyethylene (UHMWPE)/BC composites [49] and polyaniline (PANI)/BC composites [50].

2.2.4. Other Popular Nanofillers

Other nanofillers worth mentioning include CNTs, nanocellulose and graphene oxides (GOs). CNTs are one of the most interesting carbon allotropes in the form of cylinders arranged by rolling graphene sheets [138], which results in the deformation of their sp^2 hybrid orbitals with the formation of a б-л rehybridisation structure [138]. The main feature of the rehybridisation structure is that the confinement of л electrons offers unique and extraordinary properties of CNTs such as high Young's modulus at 1200 GPa and tensile strength at 150 GPa [139]. A great deal of interest has been shown for CNTs owing to their diverse potential for supercapacitors [140], actuators in robotic manufacturing [141] and storage energy (e.g., hydrogen storage) [142]. In a nanocomposites system, CNTs have the capability to improve mechanical

and thermal properties as well fire retardancy, moisture resistance and barrier properties due to their high-performance functionality [143]. It is worth noting that CNTs possess the ability to reinforce both thermosets and thermoplastics [144] in order to produce good mechanical properties and good affinity to chemical compounds [145]. Nevertheless, the critical issue currently being encountered is typical CNT agglomeration in the form of bundles when polymer/CNT nanocomposites are prepared. Such a phenomenon arises from the high aspect ratio of CNTs together with their strong van der Waals interaction, particularly at the high CNT loadings.

Nanocellulose is the other popular nanofillers, which exhibits several excellent properties such as high aspect ratio, low density at 1.6 $g \cdot cm^{-3}$, very low coefficient of thermal expansion and high tensile strength about 500 MPa [146], leading to numerous applications including antimicrobial films, transparent films, drug delivery, fibres and textiles, supercapacitors and batteries [146]. Cellulose can be classified as microfibrillated celluloses (MFCs), nanofibrillated celluloses (NFCs) and cellulose nanocrystals (CNCs). However, the hydrophilic nature of nanocellulose can limit its use as the reinforcements in nanocomposite systems, in which hydrophobic polymers are generally employed as matrices. This is because blending nanocelluloses with hydrophobic polymers can lead to weak interfacial bonding between polymer matrices and nanofillers, resulting in increased water uptake and filler aggregation due to hydrogen bonding [147].

Graphene oxides (GOs) are two-dimensional nanomaterials synthesised from natural graphite. Such nanosheets can be easily prepared from graphite flakes by the thermal oxidation as recommended by Hummers [55]. GOs possess high mechanical

properties (e.g. elastic modulus = 0.25 TPa), binding potential, high aspect ratio, high flexibility, and superior processibility [148]. Moreover, due to their good hydrophilic characteristic, GOs can be easily exfoliated into monolayer nanosheets stably dispersed in water, primarily due to plenty of hydrophilic oxygenated groups [149]. These functional groups play a significant role in the improvement of GO dispersion in solvents or within polymer matrices through covalent or non-covalent bonding [149]. However, a high tendency of GO agglomeration can limit their use at high nanofiller content levels. Recently, Chang et al. [150] examined the toxicity and biocompatibility of GOs on A549 cells. It was reported that GOs gave rise to the oxidative stress and a slight decrease in cell viability at the high GO content.

2.3. Processing of Bionanocomposites

One of most common methods used for bionanocomposite preparation is solution casting. Its first step involves the dispersion of nanoparticles in either water or organic solvents by stirring or ultrasonic treatment, after which polymer and nanoparticles are mixed and stirred together in a solution. The final step is then to evaporate the solvents in order to produce final nanocomposites. Solution casting has been successfully employed in the manufacture of various bionanocomposites such as PVA/HNT nanocomposites [151] and PVA/MMT nanocomposites [13, 152-155]. The main advantage of this method is that intercalated clay structures in nanocomposites can be formed even for low-polar or non-polar polymers notwithstanding that it has been mostly employed for water soluble polymers such as PVA [156]. The reaggregation of nanoparticles such as HNTs in polymer matrices may practically occur during a drying process, particularly after the solvent evaporation. At that stage, the polymer may start to precipitate rather than adhere to HNT surfaces. Hence the use of coagulation method can improve the HNT

dispersion within polymer matrices following solvent evaporation, as observed in Figure 2.11 [157].

The second method is *in situ* polymerisation, in which layered silicates are swollen in liquid monomers or monomer solutions. The monomers start to migrate to layered silicate galleries so that the polymerisation occurs between intercalated sheets. Heat and radiation can then be used to initiate the reaction by diffusing appropriate initiators or by fixing an organic initiator or catalyst via the cation exchange prior to the swelling of layered silicates. This technique gives rise to the formation of long

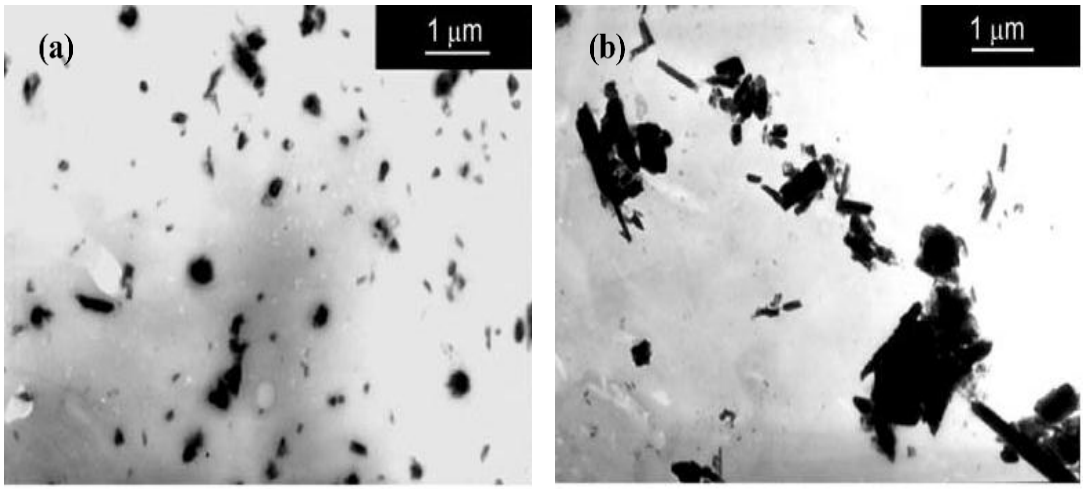

Figure 2.11 TEM micrographs of PVA /HNT nanocomposites prepared by solution casting process using (a) coagulation and (b) as-cast [157].

polymeric chains within clay galleries [158-160]. Toyota research group was the first to report the synthesis of MMT nanocomposites based on ε-caprolactam monomers at 100°C and Na^+-MMT. Similarly, other research groups also successfully utilised *in situ* polymerisation for thermoplastics such as PMMA [161], PS [162], polybenzoxale (PBO) [163] and polyolefins like PP and PE [164]. One of major drawbacks from this method is a time-consuming preparation route owing to the fact that the polymerisation can take over a day to complete. The other is the instability of

thermodynamic state of exfoliated structures, which may result in the reaggregation of layered silicates [165]. Moreover, *In situ* polymerisation is also widely used for the preparation of HNT based nanocomposites., it is proven that the application of such a method can generate covalent bonding between HNTs and polymer matrices [45]. Various HNT based nanocomposites have been prepared using this method such as the emulsion polymerisation of styrene with HNTs in the presence of SDS as an emulsifier (Figure 2.12) [166]. Direct melt intercalation is likely to be the most popular method to disperse nanoparticles into polymer matrices for nanocomposite systems owing to its environmental friendliness and cost-effectiveness with the absence of solvents. This technique involves heating mixture of polymer pellets and nanoparticles to the melting temperature for semi-crystalline polymers or above the glass transition temperature for amorphous polymers [167, 168]. Using this process, nanofillers such as HNTs can be mixed with a molten polymer under high shear forces with a variety of mixing devices. At this stage, the molten polymeric chains start to interact with HNTs due to mechanical shearing mechanism, leading to interfacial compatibility, with the aid of compression moulding, injection moulding and screw extrusion to manufacture final polymer/HNT nanocomposites. Nonetheless, the combination of high-processing temperature and high shear forces often results in polymer oxidation and degradation leading to decreased polymer properties [45].

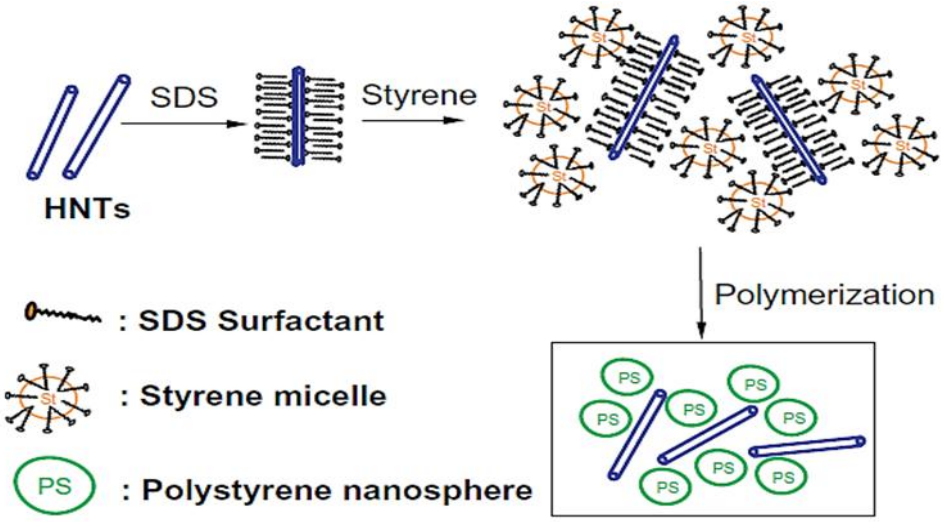

Figure 2.12 Schematic diagram for the in-situ polymerisation of styrene in the presence of HNTs [166].

Moreover, A variety of nanocomposites based on thermoplastics have been successfully fabricated using this method such as PLA/BC composites [31],wood plastic (WP)/BC composites [34] PCL/MMT composites [169] and PLA/MMT composites [170]. The characteristics of resulting nanocomposite structures are known to be influenced by factors such as the type and nature of polymers and modified layered silicates in terms of surfactants, chain length and packing density [171].

The fourth method for the fabrication of bionanocomposites is electrospinning. As previously mentioned, it involves the application of a high-voltage electrical field into polymer solutions with the provision of the formation of continuous micro/nanofibres. These fibres can be used to produce fabric networks with high porosity, small pore sizes and high surface-to-volume ratios. The electrospinning method has been successfully implemented to various nanocomposites systems such as PVA/HNT nanocomposite fibres [157, 172] and PVA/BC composite fibres [173]. In recent years, electrophoretic deposition (EPD) method has gained a particular

attention for the deposition of composite films with HNT inclusions. EPD involves the motion of charged particles in suspension to an electrode leading to the formation of a deposit on the electrode surface under uniform electrical-field effect [174]. The main advantage of this method includes its potential to produce uniform films with controlled thickness as well as for the deposition on substrates with a complex shape and high deposition rate. Such a procedure has been successfully used to fabricate chitosan/HNT nanocomposites [175, 176].

2.4. Bionanocomposite Properties and Characterisation

2.4.1. Morphological Structure

It should be emphasised that mixing a polymer and inorganic nanofillers together does not necessarily produce a nanocomposite. In an immiscible system, poor interfacial bonding between organic and inorganic components leads to the separation of nanocomposite constituents into discrete phases in final structures. This separation induces the same properties in nanocomposites as those of microcomposites [158]. In the case of a miscible system, two types of nanocomposites, namely intercalated and exfoliated (*i.e.*, delaminated) nanocomposites can be achieved, as shown in Figure 2.13. The determination of final nanocomposite type in terms of intercalated or exfoliated structures depends primarily on the synthetic technique and chemical nature of nanocomposite constituents. In addition, intercalated structures are formed when polymeric chains are penetrated into silicate layers, resulting in a multilayered structure of polymer matrices and inorganic fillers. In this case, polymeric chains expand the interlayer spacing of layered silicates by 20-30 Å. In contrast, exfoliated structures occur when layered silicates are peeled apart and individually separated with an increase in

interlayer spacing up to 80-100 Å or more, which is mostly related to the radius of gyration for polymers [158, 177, 178]. Exfoliated structures are generally more favourable because clay dispersibility is significantly enhanced as individual particles/fillers leading to greatly enhanced mechanical properties of final nanocomposites. However, it is more difficult to achieve such an ideal structure since the majority of nanocomposites reported in the literatures possess either intercalated or a mix of intercalated and exfoliated structures [152-154, 156]. The reason for this is that layered silicates are highly anisotropic with lateral dimensions of 100-1000 nm. As a result, even when separated by the high interlayer spacing, silicate layers cannot be completely and randomly dispersed within polymer matrices [178]. X-ray diffraction (XRD) and transmission electron microscopy (TEM) are the most common techniques used to characterise final structures of nanocomposites [158, 177]. XRD analysis allows for the calculation of the distance between silicate layers in nanocomposite structures based on Bragg's law. For example, in an immiscible polymer/OML composite system, the characteristics of the OML basal reflection remain unchanged (Figure 2.4). However, in a miscible system, the formation of an intercalated structure leads to an increase in interlayer spacing, as evidenced by the XRD peak shift to lower diffraction angles. On the other hand, the relatively large interlayer spacing for exfoliated structures generally results in a featureless diffraction pattern and disappearance of diffraction peaks from XRD spectra. This phenomenon takes place because the large interlayer spacing between silicate layers in such a nanocomposite system tends to result in well-dispersed OMLs with the random orientation [158, 179]. Only XRD analysis would be insufficient for determining final nanocomposite structures. As a result, other techniques such as TEM should be employed in order to offer a visual understanding of morphological

structures in nanocomposites. Layered silicates contain heavier elements such as Al, Si and O when compared to surrounding polymeric chains with only C, H and N. Accordingly, much heavier elements produce the dark appearance for layered silicates in a bright field of TEM images, as illustrated in Figure 2.15 [158, 177, 179].

2.4.2. Mechanical Properties

The mechanism that explains the reinforcement effect of nanofillers in nanocomposites is the assumption that soft polymer matrices adjacent to much stiffer nanofillers become mechanically constrained, as illustrated in Figure 2.16. This mechanism enables nanofillers to carry a disproportionately high fraction of an applied load provided that the interfacial bonding between polymer matrices and fillers is sufficient

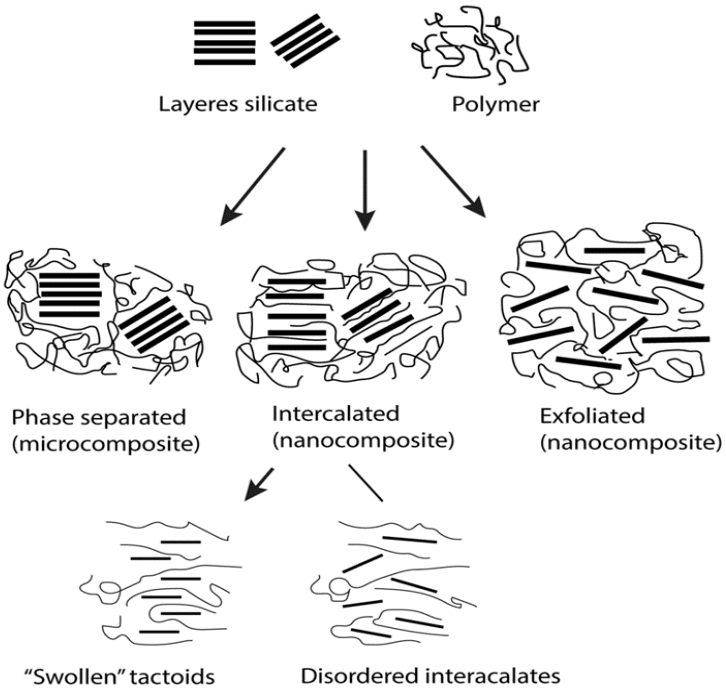

Figure 2.13 Schematic diagram illustrating different clay structures of polymer/layered silicate nanocomposites [180].

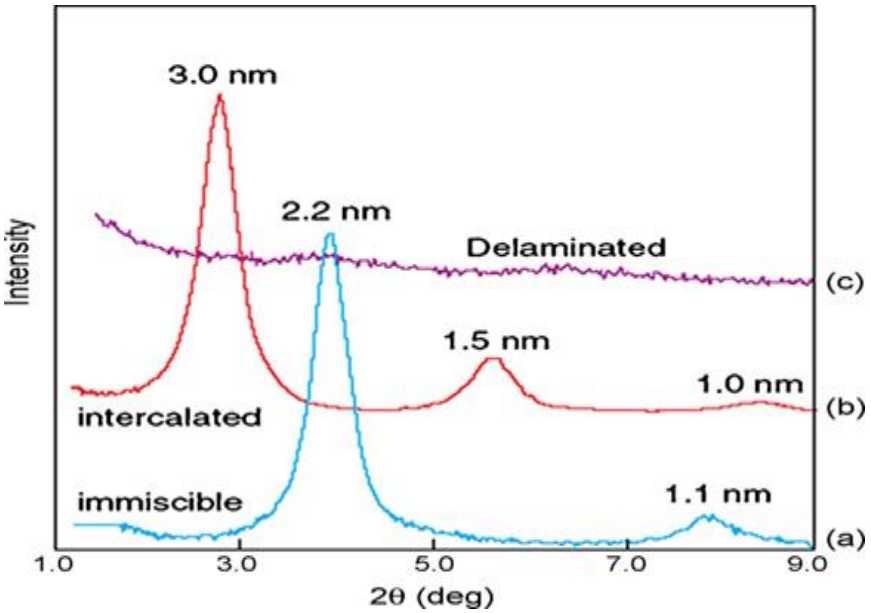

Figure 2.14 Typical XRD patterns for polymer/layered silicate composites: (a) immiscible structure, (b) intercalated structure and (c) exfoliated structure [158].

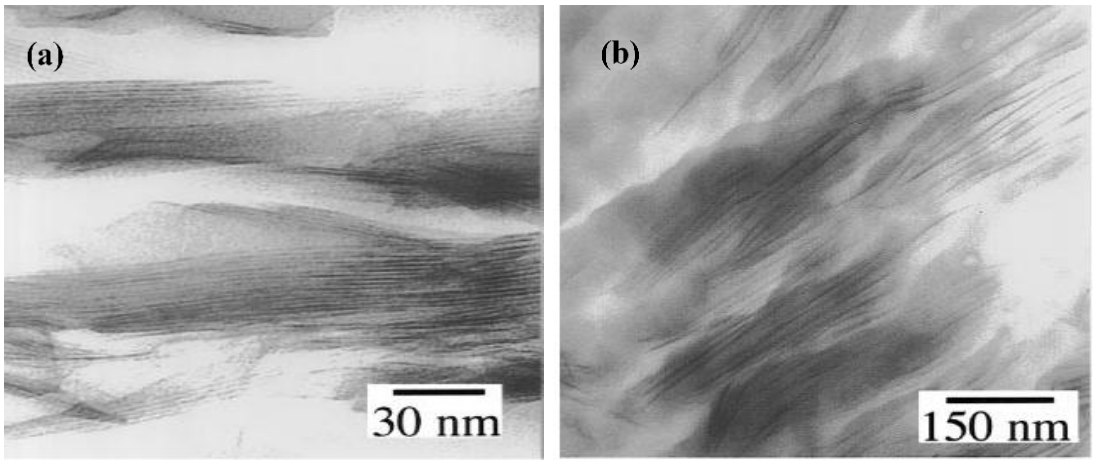

Figure 2.15 TEM micrographs: (a) intercalated structure and (b) exfoliated structure [158, 181].

Furthermore, it can be postulated that much greater reinforcement effect can be achieved by using fillers with large specific surface areas. In a polymer/layered silicate nanocomposite system, Young's modulus can increase significantly with the inclusion of OMLS into continuous polymer matrices, For example, the Young's modulus increased from 1900 MPa for neat PVA to 3200 MPa for PVA/ 5 wt% MMT nanocomposites [182]. In a similar manner, the other study reported an

increase from 1780 MPa for neat PVA to 2650 MPa for PVA/4 wt% MMT nanocomposites [183].

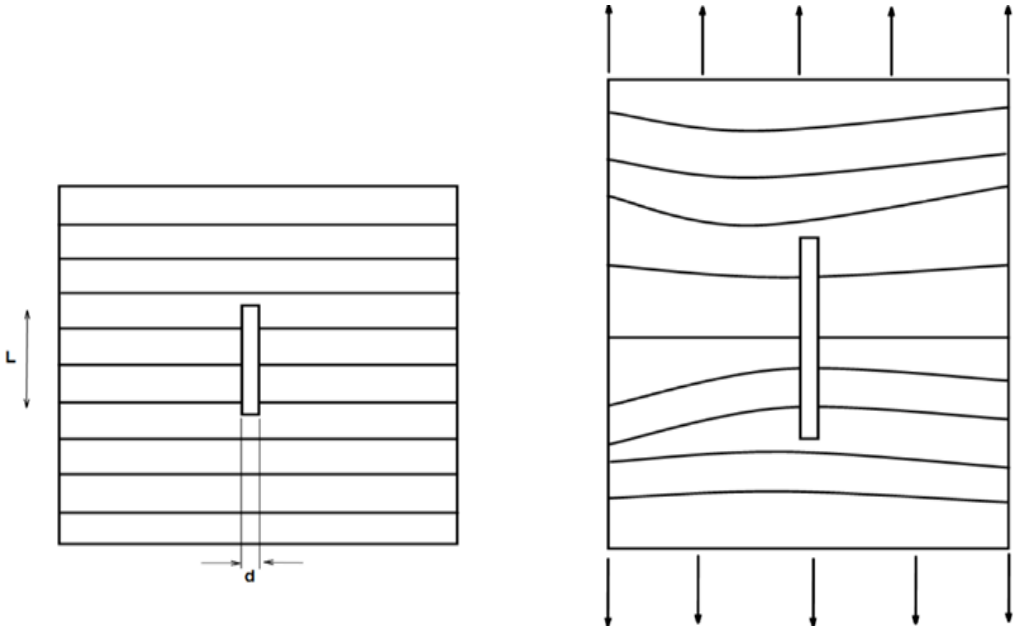

Figure 2.16 Schematic diagram illustrating the reinforcement mechanism in a composite material: (a) before loading and (b) after loading [158].

As can be clearly seen in Table 2.4, the Young's modulus of nanocomposites is a function of clay content. However, any further increase in the clay content appears to make a declining effect on Young's modulus. Based on XRD and TEM observations, this trend is attributed to the change of clay dispersion states from fully exfoliation, partial exfoliation and intercalation to clay agglomeration for the clay content of 10 wt% or above [158, 159].

Table 2.3 Structures and mechanical properties of different polymer/layered silicate nanocomposites.

Polymer	Process	Filler type and content (wt%)	Young's modulus (MPa)	Tensile strength (MPa)	Ref.
PVA	Solvent intercalation	MMT (0) MMT (3) MMT (5)	1900 3100 3200	65.1 98.9 91.6	[182]

PVA	Solvent intercalation	Na-MMT (0) Na-MMT (4) Na-MMT (8)	1470 2160 2690	52.25 63.36 54.95	[183]
PVA/starch	Melt intercalation	Na-MMT (0) Na-MMT (5) Na-MMT (10) Na-MMT (15) Na-MMT (20)	9.65 23.76 30.58 39.17 47.67	11 13.3 14.7 16.17 14.47	[184]
PVA/PVP	Solvent intercalation	Na-MMT (0) Na-MMT (4) Na-MMT (8)	1780 2650 4580	42.4 48.9 52.3	[183]
GS/PVA	Solvent intercalation	MMT (0) MMT (5) MMT (10) MMT (15) MMT (20)	197.8 265 315 331.2 225.5	38.5 48 57.5 60.2 42.3	[185]
PVA	Solvent intercalation	MMT (0) MMT (1.84) MMT (5.44) MMT (17.3)	2064 3640 2966 5055	50 99.6 73.3 95.9	[186]
GS/PVA	Solvent intercalation	HNT (0) HNT (0.25) HNT (0.5) HNT (3) HNT (5)	990 1300 1560 1700 1860	40 46 51 32 29	[15]
PVA- MA		HNT (0) HNT (5) HNT (10) HNT (20)	1023 1105 1185 1244	46.6 42.1 38.8 36.1	[16]

Apart from the change in Young's modulus, the incorporation of organoclays into polymer matrices also causes the increase in tensile strength of nanocomposites. Wang *et al*. [182] reported that the tensile strength of PVA nanocomposites increased by 52% at the MMT loading of 3 wt % relative to that of neat polymer. Similarly,

the other study [186] reported that the tensile strength increased from 50 MPa for neat PVA to 95.9 MPa for PVA based nanocomposites at the clay loading of 17.3 wt%. Nonetheless, it should be clearly stated that the reduction in tensile strength for nanocomposites has also been noted, Table 2.3. This result can be ascribed to clay agglomeration resulting from increasing the clay content generally over 5 wt% associated with non-uniform clay dispersion. Those clay aggregates act as typical defects of stress-concentration sites for the crack initiation [158].

The molecular weight of polymer matrices also has an impact on reinforcement efficiency and tensile strength of nanocomposites. It has been reported that the modulus and yield strength of nanocomposites were substantially enhanced with increasing the molecular weight of polymer matrices [158]. This finding suggests that increasing the molecular weight of polymer matrices induces the higher shear stress to break up large clay particles into exfoliated platelets. The higher degree of exfoliation inevitably results in the effective stress transfer from polymer matrices to nanofillers with their stronger interfacial bonding.

Other factors to play a key role in the enhancement of Young's modulus and tensile strength of nanocomposites are organic modification of layer silicates and the use of compatibilisers to polymer matrices. Hotta and Paul [187] indicated that increasing the number of alkali tails for organoclays from one tail to two tails enhanced Young's modulus and tensile strength of nanocomposites. Pavlidou and Papaspyrides [158] also demonstrated that increasing the amount of CAB-MA compatibiliser in cellulose acetate butyrate (CAB)/CAB-MA based nanocomposites from 0 to 5 wt% improved Young's modulus from 3600 to 3700 MPa [158].

In polymer/HNT nanocomposite systems, the improvements of elastic modulus and tensile strength depend primarily on the HNT loading, HNT dispersion and interfacial adhesion between HNTs and polymer matrices. As indicated in Table 2.4, increasing the HNT loading generally results in higher reinforcement efficiency as well as greater tensile strength of nanocomposites. However, these trends are not always observed due to the influence of HNT dispersion within polymer matrices. Although HNTs are more easily dispersed when compared to natural silica and CNTs, their dispersion can still be challenging, particularly for non-polar polymers [188, 189]. Qiu *al*. [16] reported that the tensile strength of PVA/HNT nanocomposites decreased by 14.2% when their loading increased from 5 to 10 wt% due to the HNT agglomeration at 10 wt%. Better dispersion using surface pre-treatment, including the grafting of silanes or polymers, can lead to the improvement of interfacial bonding (*i.e.*, hydrogen bonding) between HNTs and polymer matrices. It was shown that the modulus of PVA/HNT nanocomposites increased by 21% when using modified HNTs as opposed to unmodified HNTs [14].

2.4.3. Nanomechanical Properties of Nanocomposites

Nanocomposites represent a homogenous material system at the macroscaled level despite their heterogeneity on the micro- or nanoscale. In general, polymers react with nanoparticles during the mixing process to yield multiple phases including partially or fully reacted composites, unreacted components of raw materials and interphase zones, which have different mechanical properties and chemical properties [190]. The properties and amount of each phase relative to entire nanocomposites strongly affect properties of bulk materials [63]. Therefore, only using conventional mechanical testing is insufficient to evaluate the real

reinforcement effect of nanoparticles on polymer matrices, as well as detect localised reinforcement and deformation.

Additionally, even the results of conventional mechanical testing is directly based on a fundamental concept that the chain mobility of soft matrices is constrained by much stiffer nanoparticles [25]. As a consequence, an effective load transfer occurs from matrices to fillers such as nanoparticles to carry a disproportionally high fraction of applied loads, thus leading to an increase in load resistance [25]. This phenomenon is well known to be associated with the level of interfacial bonding between nanoparticles and polymer matrices in terms of interphase existence, dimensions, structures and compositions [191]. Hence, the crack initiation or propagation may take place in a nanocomposite system, resulting from the lack of effective load transfer owing to the weak interfacial bonding.

Interfaces are described as a material boundary between two or more phases with distinct chemical/physical properties and morphological structures. Furthermore, a material volume influenced by the interfacial interaction can be named ‘interphase’[192]. Interphase regions start from the interfacial boundary of nanofillers with different properties from those of bulk nanofillers and end where they are in connection with polymer matrices whose properties also vary from bulk matrices [193]. The material performance of nanocomposites is primarily impacted by the interphase regions where structural and chemical changes such as crosslinking density and crystalline phases result in a major alteration to composite bulk properties [192]. It is also worth mentioning that the alteration in the mobility of polymeric chains plays an important role in mechanical and dielectric properties of nanocomposites [63]. Due to large interfacial-area-to-volume ratios in

nanocomposites, interfacial regions consist of a significant portion of bulk nanocomposites. For instance, with the addition of 5 vol% monodispersed spherical nanoparticles (particle diameter of 10 nm and interphase thickness of 0.5 nm), the volume fraction of interphases can be as high as 25 vol% [63]. More impressively, when particle diameter is reduced to less than 5 nm, the volume fraction of interphases increased by over 50 vol% as compared to that of particles [63]. The characterisation of existing interphases and their associated properties is generally difficult to undertake as interphases for nanocomposites are generally on a nanoscaled level, and thus researchers have had to make most experimental efforts in an uncrosslinked state as the indirect evidence [194]. For example, chain mobility near interphase regions can be less than those of polymer matrices in a nanocomposite system [194]. As a result, Litvinov and Steeman [195] employed proton, low resolution T2 nuclear magnetic resonance (NMR) relaxation technique to detect existing interphases between ethylene propylene dine monomers (EPDMs) and carbon blacks. It was indicative of a significant difference in the chain mobility of EPDMs near carbon black surfaces, at which the generated layer sizes of immobilised EPDMs were estimated in range of 1-2 of the unit diameter of monomers [195]. Pompe and Mäder [196] identified interphases according to differential scanning calorimetry (DSC) in polypropylene/glass fibre composites, which, however, was limited to semicrystalline polymers as matrices in composite materials at only high glass fibre contents. Brown et al. [197] studied a relationship between nanoparticle diameter and interphase thickness based on molecular dynamic (MD) simulations, which implied that the interphase thickness appeared to be relatively insensitive to nanoparticle diameters and contents. Li et al. [198] reported that the volume fraction of interphases could be size-independent by using a

modified hierarchical multi-interphase model (MHMM). However, the interphase thickness might be influenced by the reinforcing efficiency of nanoparticles when their lengths were over 40 nm. On the contrary, Gu et al. [59] and other co-workers [61, 62] inferred that the interphase thickness could be non-constant in nanocomposites systems. So far, nanointerphase properties and features have not been explicitly quantified in a systematic manner by means of direct topography of nanomechanical characterisation. As a matter of fact, nanomechanical techniques using tip-sample interactions such as atomic force microscopy (AFM) [199], nanoindentation and nanoscratch tests [200, 201] are vital as effective and relatively straightforward approaches to determine nanomechanical properties of interphases. In addition, interphase dimensions and sizes can be clearly specified due to their distinct mechanical properties from those of bulk materials. The interphase width of glass fibres coated with coupling agents was previously revealed to be around several microns [200, 202]. Nonetheless, a quantitative analysis of interphase dimensions associated with nanomechanical properties still undergoes limited lateral resolutions and positioning capability of indenter probe used in nanoindentation, and nanoscratch techniques. In particular, interphase regions of thermosetting polymer/glass fibre composites are much thinner than those of individual fibre and matrix components [203]. Plastic deformation usually takes place under a high fraction of applied load, thus resulting in an increase in the minimum allowable distance between tow indentation spots, as well as the reduction of lateral resolutions of such tests [202, 204]. The peak force quantitative nanomechanical mapping (PFQNM) becomes a relatively new and powerful technique to quantitatively measure nanomechanical properties of materials such as the stiffness and adhesion of nanocomposites along with corresponding acquired dimensions [205, 206]. The use

of PFQNM greatly supports the measurement of material elastic properties based on tip-sample force curves and acquisition of topographic images simultaneously. Moreover, other critical properties, consisting of tip-surface adhesion and surface deformation, can also be obtained by avoiding the difficulty associated with lateral forces. Such a technique is believed not only to sophisticatedly distinguish between nanofillers, nanointerphases and polymer matrices, but also to accurately quantify dimensions and nanomechanical properties of interphases.

Nanomechcanical properties of PVA and PVA nanocomposites are completely different from those of their bulk material counterparts. It is worth noting that average elastic modulus of bulk PVA films is approximately 2.064 GPa at a macroscopic level [186], which is far less in magnitude when compared with local nanophases such as 9.9 GPa for PVA/ 10 wt% poly(acrylic acid) (PAA) blends [207]. Moreovere, in case of PVA-PAA based nanocomposites reinforced with cellulose 10 wt% nanocrystals (CNCs) [207], their average elastic modulus in the interphase was found to vary from 12.8 GPa at the interface of CNCs to 9.9 GPa in PVA-PPA matrices. On the contrary, PVA nanocomposites reinforced with 10 wt% CNCs demonstrated the highest elastic modulus of only 1.9 GPa in their bulk properties [208]. Such a modulus variation phenomenon between nanomechanical properties and bulk properties is not limited to PVA alone, but can be applied to different polymers or composites. For instance, the storage modulus of epoxy was measured to be 17 GPa via nanomechanical measurement as opposed to 3-4 GPa for their bulk composites obtained by tensile tests [59]. Moreover, elastic modulus of bulk poly (ether sulfone) (PESU) membrane substrates was found to be only 151.7± 7.9 MPa [209] when compared to 3.2 ±0.3 GPa for PESU films at a nanoscaled level [210].

2.4.4. Thermal Properties

The thermal properties of polymeric materials can be quantified by several techniques. Among these, thermogravimetric analysis (TGA) and DSC are the most popular characterisation techniques. TGA is used to measure the weight loss resulting from the formation of volatile products or chemical reactions as a function of temperature and/or time. Whereas, DSC is employed to measure the glass transition temperature (T_g), crystallisation temperature (T_c) and melting temperature (T_m) of polymeric materials. In a polymer/clay nanocomposite system, the inclusion of layered silicates within polymer matrices can improve the thermal stability by acting as an insulator and mass transport barrier to volatile products that are generated through the degradation process [25]. For instance, the decomposition temperature of PVA/5wt% MMT nanocomposites has increased to 354°C as opposed to 337°C for pure PVA [13]. Moreover, the T_g of PVA also increased from 34 °C to 60 °C when MMT content increased up to 10 wt%. Such a finding was related to uniform dispersion of MMTs, which scattered the applied heat through the polymer and thus led to the improvement of heat resistance for final nanocomposites [13]. In addition, Mallakpour *et al*. [155] reported that the degradation of PVA was enhanced with the inclusion of fluorohectorite or MMTs. The char yield of PVA at 800°C also increased from 6% to 19% in case of PVA/5 wt% MMT nanocomposites, implying the improvement of thermal stability at the higher temperature [155]. Another study showed that the thermal decomposition temperature of PVA/OMLS nanocomposites shifted to a marginally higher temperature compared with that of pure PVA [211], This phenomenon could be explained according to Stawhecker and Manias [156] that PVA could supply oxygen by itself to initiate the thermal decomposition. Conversely, the reduction in the thermal stability of nanocomposites is also noted as

stack-layered silicates can accumulate the heat at the early stages of decomposition [158]. Alkali ammonium cations existing in OMLS may experience subsequent decomposition by Hofmann elimination leading to the acceleration of polymer degradation [4, 158]. Katti *et al*. [212] indicated that the addition of MMTs and hydroxyapatite (HAP) to chitosan improved the thermal stability of such new nanocomposites with even higher onset temperature and the percentage residue left at 500°C when compared to chitosan/MMT nanocomposites.

In case of polymer/HNT nanocomposite system, thermal properties may be significantly improved compared to polymer matrices due to the following reasons: (i) The thermal stability of HNTs is much higher than that of polymer matrices with typical initial degradation taking place at ~400°C; (ii) Excellent HNT dispersion in polymer matrices leads to better barrier effect towards mass and heat transport, and (iii) Polymer chains and volatile products can enter HNT lumens leading to a delay of mass transport with the further improvement of thermal stability. Swapna et al. [213] found that the inclusion of HNTs improved thermal stability of PVA due to the heat-barrier effect of inorganic fillers. However, T_g and crystallinity decreased with the inclusion of HNTs, which could be related to the plasticisation effect of hydrophilic HNT fillers [213]. Qiu et al. [16] stated that decomposition temperatures at the weight loss of 30 and 50% appeared to increase by 3-5°C for PVA/HNT nanocomposite films when compared with neat PVA despite being no change of T_g. This phenomenon was mainly dependent on the uniform dispersion of HNTs within PVA matrices for better thermal stability. Similarly, other studies have also indicated a critical role of HNTs in improving thermal properties of different types of biopolymers such as PVA [16], PEG [214] and starch [215].

2.5. Modelling

Mixing polymer matrices with nanofillers could create nanocomposites, which synergistically combine the properties of polymer matrices and nanofillers. The material performance of nanocomposites depends primarily on filler-matrix interfacial bonding, as well as nanoparticle dispersion status within polymer matrices.

The prediction of mechanical properties of nanocomposites is essential in composite modelling work, which, however, is constrained by a few simple parameters such as nanofiller volume fraction and constituent properties of matrices and nanofillers only. Conventional composite models such as Halpin-Tsai model and Mori-Tanaka model [53, 216] have been well implemented for nanocomposite systems despite the neglect of important interphase features for simplicity. As such, mechanical properties of nanocomposites can be either overestimated based on such conventional models for polymer/CNT composites [58] and silk fibroin/graphene oxide nanocomposites [55], or underpredicted for polyamide 66 (PA66)/calcium carbonate ($CaCO_3$) nanocomposites [56]. De Villoria and Miravete [217] reported that there was evident non-agreement taking place between modelling results and experimental data in predicting the mechanical properties of epoxy/SWCNT composites arising from poor CNT dispersion in epoxy matrices, as confirmed from SEM micrographs. They developed a new micromechanical model (dilute suspension of clusters model) as presented by equations (2.1)-(2.3) by considering the CNT agglomeration, which displays good agreement with experimental data obtained from the mechanical tests.

$$\boldsymbol{E_{dsc} = \frac{9K_{dsc}\mu_{dsc}}{3K_{dsc} + \mu_{dsc}}} \quad (2.1)$$

$$K_{dsc} = K_m + \frac{(K_{Cluster} - K_m)C_C}{1 + \frac{(K_{Cluster} - K_m)}{(K_m + \frac{4}{3}\mu_m)}} \quad (2.2)$$

$$\mu_{dsc} = \mu_m \left[1 - \frac{15(1 - v_m)(1 - \frac{\mu_{Cluster}}{\mu_m})C_C}{7 - 5v_m + 2(4 - 5v_m)\frac{\mu_{Cluster}}{\mu_m}} \right] \quad (2.3)$$

Where E_{dsc} and K_{dsc} are effective Young's modulus and effective bulk modulus for a dilute elastic suspension of spherical clusters, respectively. $K_{Cluster}$ is effective bulk modulus of cluster and μ_{dsc} is effective shear modulus for a dilute elastic suspension of spherical clusters. μ_m is the shear modulus of matrices, C_C is volume fraction of spherical clusters in the composite and v_m is Poisson's ratio of matrices. However, micromechanical models underestimated mechanical properties of nanocomposites because the interphase features and properties were not supplemented as a typical drawback. Many recent attempts have been made by incorporating interphase regions as the third phase within available micromechanical models. Zare [57] developed a simple approach to considering interphase volume fraction, as described by equation (2.4) based on Tando-Weng solution of Mori-Tanaka model. Such a approach led to limited success because its application to polyamide (PA66)/ calcium carbonate ($CaCO_3$) nanocomposites revealed a relative underestimation as opposed to the overprediction for PP/$CaCO_3$ nanocomposites in the same fasion. The major issue is that the interphase was assumed as an uniform layer surrounding nanofillers and nanoparticles/nanofillers were treated with regular shapes and sizes.

$$\phi_i = \phi_f \left[\left(\frac{r + r_i}{r} \right)^3 - 1 \right] \quad (2.4)$$

Where ϕ_i and ϕ_f are interphase volume fraction and nanofiller volume fraction, respectively. *r* and r_i are nanoparticle size and interphase thickness, respectively.

Hu et al [55]. suggested a simple model for predicting the elastic modulus of silk fibroin/graphene oxide nanocomposite film based on interphase modulus gradient reported by Kovalev et al. [218] as follows:

$$\boldsymbol{E^*(t) = \frac{\Delta E}{1 + exp\left[\eta\left(\frac{t}{\tau} - 1\right)\right]} + E_{sf}} \quad 2.5)$$

$E^*(t)$ is the current composite modulus at a distance t from GO/silk fibroin (SF) interface; $\Delta E = E_{GO} - E_{SF}$, where E_{GO} and E_{SF} are the Young's moduli of graphene oxide and silk fibroin, respectively. η is a shape factor, which is proportional to the relative interfacial strength. τ is the effective thickness at which the modulus decays by 50%. In this model, η remains a characteristic constant if the nature of interactions remains unchanged. Such a model demonstrated certain success in predicting the elastic modulus of nanocomposite films. Nonethless, a constant modulus profile at the interphase zone and only effective interphase thickness were hypothesised while the modulus actually varied along the interphase zone instead. In general, a simple assumption that the interphase is regarded as one-dimensional transitional material phase between fillers and matrices with uniform interphase thickness and regular shape is well-known. In reality, the interphase with irregular shape and non-uniform thickness takes place in real material morphological structures of composites [61, 63, 219]. In order to consider the benefit of real interphase effect in nanocomposite modelling work, interphase volume fraction is one of key interphase material parameters worthwhile to be predetermined. Lewis [63] reported that with the inclusion of mondispersed spherical nanoparticles with

particle diameter being less than 5 nm and interphase thickness of 0.5 nm, the interphase volume fraction could be as high as 50% when compared with that of nanoparticles [63]. However, a full understanding for the effect of interphase volume fraction on the elastic modulus of bulk nanocomposites still remains challenging owing to complex interphase network structures and an overlapping potential for neighbouring interfacial layers [64, 65].

2.6. Applications of Bionanocomposites

2.6.1. Electronic and Sensor Applications

Reinforcing biopolymers with nanofillers improves not only mechanical, thermal and barrier properties of bionanocomposites, but also their electromagnetic shielding, electrical, optical and magnetic properties [25]. These impressive features are related to increasing environmental concerns to replace conventional composites with bionanocomposites, particularly in the manufacture of electric products. For instance, most current polarising films in LCD screens are made of iodine-doped PVA. Furthermore, Du et al. [17] developed a novel electroactive shape memory material with high thermal and electrical performance based on PVA/MWCNT nanocomposites. Transparent and flexible bionanocomposites reinforced with nanocelluloses are used in various applications ranging from displays, organic light emitting diode, solar cells to roll-to-roll technology. The continuous deposition of various functional components is required in order to make electronic deposition devices. Metal wiring and active gas barrier films are good examples of functional components implemented in roll-to-roll technology [220]. Its major drawback is the high coefficient of thermal expansion (CTE) for plastic materials [220], which can be made up for with the inclusion of bacterial cellulose as nanofillers to reduce the CTE.

Such binanocomposites can also be potential substrates used for the roll-to-roll fabrication [221].

2.6.2. Medical Applications

Natural abundance, adaptability and environmental friendliness make bionanocomposites a suitable material candidate for a wide range of medical applications such as the regeneration of natural tissue structures. In this field, fabricated bionanocomposites have the same morphology as extracellular matrix (ECM) including protein, polysaccharides and inorganic matters [222]. In the case of bone regeneration of clinical orthopaedics, it is important to select bionanocomposites such as polymer scaffolds and HAPs with biodegradable and bioresorbable structures to stimulate the bone formation at the implantation sites [223]. More importantly, the structures of selected bionanocomposites must have sufficient porosity in order to facilitate the growth of new tissues such as porous scaffolds of HAP/collagen nanocomposites for the repair of bony defects in animal models [224]. In particular, bionanocomposites reinforced with HNTs have also been used in tissue engineering such as PVA/HNT bionanocomposite films with good compatibility to osteoblast and fibroblast cells [172]. In a similar manner, chitosan/HNT nanocomposite scaffolds exhibit highly porous structures with high compressive strength and modulus for the development of mouse fibroblasts [225]. Electrospun PLGA/HNT bionanocomposites also demonstrate high biocompatibility, and cell proliferation, which are not adversely affected with the incorporation of HNTs [226].

The potential of using bionanocomposites in drug delivery has been widely reported in the previous studies [227, 228]. Nanocomposites reinforced with HNTs become a

promising drug carrier to be loaded in different forms involving powders, suspensions and fibrous scaffolds [45]. A slow release rate occurs when the lumen and outer surfaces of HNTs are loaded with diltiazem hydrochlorire, 5-aminosalicylic acid and propanol hydrochloride [45]. But HNT loading capacity is limited because lumen volume fraction of HNTs cannot exceed 10 vol% [229] . To increase the loading capacity of HNTs, etching alumina from inner surfaces of HNTs is required. Moreover, coating HNTs with biopolymers such as PVA [230], PEI [231] and chitosan [232] was also found to significantly slow down drug release rate as compared to those with uncoated HNTs.

2.6.3. Packaging Applications

Major drawbacks of biopolymers are their narrow processing window, poor gas/water barrier properties and low mechanical properties relative to conventional synthetic polymers, which can be overcome by additional nanofillers into biopolymer matrices. The permeability is one of the most important factors in food packaging industries for the selection of suitable materials [159]. The incorporation of nanofillers, especially nanoclays, into biopolymers leads to a remarkable improvement in barrier properties of bionanocomposites. The fundamental principle lies in a longer path for the transfer of molecules in polymer/clay nanocomposites instead of direct diffusion in neat polymers. As illustrated in Figure 2.21, more tortuous diffusive paths are created in a nanocomposite system with the delay of molecule transfer [159]. As a typical example, PVA and PVA based nanocomposites have been widely used in packaging industries due to their good resistance to most organic compounds and solvents in order to protect packaged products from the secondary contamination by printing links [233]. Moreover, the permeability tends to be reduced when nanofillers content increases. Aloui et al.

[234] reported that the inclusion of 3 wt% HNTs and 5 wt % CNCs within PVA matrices decreased their water and oxygen permeability. Similarly, Strawhecker and Manias [156] found that the water vapour permeability of PVA/Na^+ MMT nanocomposite films decreased by 40% as opposed to that of neat PVA with the inclusion 4–6 wt% nanofillers. Such a finding results from a mix of exfoliated/intercalated clay structures, leading to a tortuous diffusion path through nanocomposite films. Moreover, the incorporation of GO particles within PVA reduced the permeability significantly due to the GO exfoliation within polymer matrices, resulting in a tortuous path again for oxygen molecules [235]. Kim et al. [236] showed that the 20% reduction was determined for the permeability of PVA/GO nanocomposite films with addition of only 0.3 wt% GOs as opposed to that of pure PVA films.

Attractive properties of PHA such as its hydrophobic nature and water vapour barrier properties are similar to those for PE coating applications. However, poor gas barrier properties as well as narrow processing window may limit PHA applications in food package. The inclusion of nanoclays into PHA matrices was used with the relevant results of much lower oxygen and water permeability [237]. On the other hand, the high hydrophilicity of starch also limits its usage in packaging applications. The use of nanofillers into thermoplastic starch has been carried out in various studies with success. Park et al. [238] reported that the water vapour transition rate of TPS/MMT nanocomposites decreased by a half as compared to that of pure TPS thanks to the tortuous pathway. Conversely, Chang et al. [239] investigated the effect of chitosan nanoparticles (CNs) on reduced barrier properties of TPS in that the shape of CNs could not induce a sufficient tortuous path with certain limitations when compared to platelet-like MMTs.

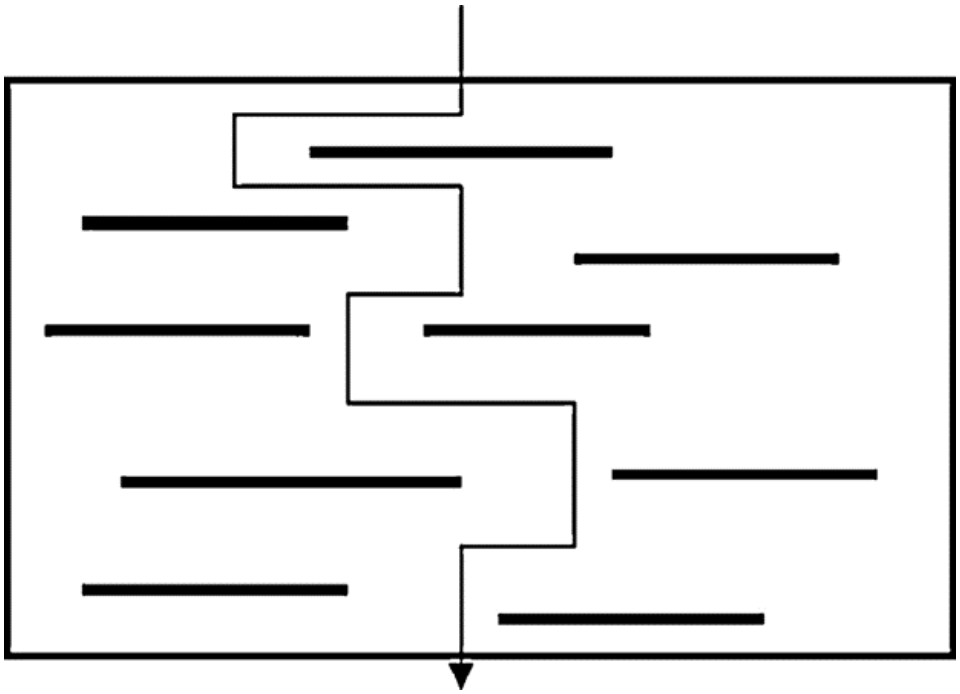

Figure 2.17 A proposed model for the tortuous zigzag path in polymer/clay nanocomposites subjected to gas permeation [143].

2.7. Summary

Increasing environmental concerns due to the use of non-degradable polymers have motivated the researchers and material developers to find alternative polymeric materials. Biodegradable polymers are considered as a suitable material candidate for conventionally synthetic polymers in order to reduce energy consumption and gas emission. A variety of biopolymers, their properties and synthetic methods have been investigated in this chapter. The preparation and properties of corresponding bionanocomposites reinforced with HNTs, OMLS and BCs have also been discussed. Many advantages of bionanocomposites are summarised as follows:

- Improved mechanical properties of bionanocomposites in solid and melt states as opposed to those based on conventional composites.

- Significant enhancement for the thermal stability of bionanocomposites with the addition of nanofillers working as heat barriers in the formation of char after thermal degradation.

- Improved biodegradability of some biopolymers with the inclusion of nanofillers.

The above-mentioned property improvements generally occur at a much lower loading of nanofillers than those of conventional fillers in composite systems. Therefore, bionanocomposites not only offer far lighter products when compared with conventional composites, but also make a superior contribution to widespread applications owing to their excellent material characteristics. Despite numerous studies and research conducted in the past decades, the commercialisation of bionanocomposites is still faced with enormous challenges in material development and innovation in order to meet the applications required by the end users.

Chapter 3.

Materials, Methodology and Characterisation Techniques

3.1. Materials

3.1.1. Polyvinyl Alcohol (PVA)

PVA as a popular water-soluble biopolymer was used in this study, which was supplied by Sigma Aldrich Pty. Ltd, Australia with a material type denoted as MFCD00081922. Such selected PVA has a molecular weight of 89000-98000 g/mol and the degree of hydrolysis of 99.0 - 99.8%, as observed from material specification data sheet [240].

3.1.2. Nanoparticles

Three different structures and shapes of nanofillers were employed in this study, namely Clositie 30B montmorillonite (MMT) clays, hallyosite nanotubes (HNTs) and bamboo charcoals (BCs). All these three nanofillers are naturally abundant, and can be used widely in biomaterial applications; the effects of their different structures and shapes on material performance and properties of PVA nanocomposites are of great interest in this study. 1D platelet-like Cloisite 30B clays comprise –OH groups between their clay interlayer areas, which promotes the insertion of PVA molecules between these layers to form intercalated/exfoliated clay structures. In comparison, HNTs have 2D tubular structures with high aspect ratios and functional groups on their surfaces, and thus make HNTs closely interact with PVA molecules in PVA/HNT nanocomposites. Finally, BCs possess 3D porous structures with the ability to absorb PVA molecules into such internal pores in order to form strong mechanical bonding.

3.1.2.1. Bamboo charcoals (BCs)

Two different types of bioactive BC fillers were used in this study, the first was denoted as microdiameter bamboo charcoals (MBCs) supplied by Jiangshan Luyi

Bamboo Charcoals Co., Ltd, China (molecular weight: 12.01 g/mol and density: 0.2-0.5 g/cm^3) with the particle size being less than 800 nm [240], as illustrated in Figure 3.1(a).The second type was referred to as nanodiameter bamboo charcoals (NBCs) purchased from US Research Nanomaterials, Inc. Co., USA (molecular weight: 12.01 g/mol, density: 0.43 g/cm^3 and particle size less than 100 nm [240]), Figure. 3.1(b).

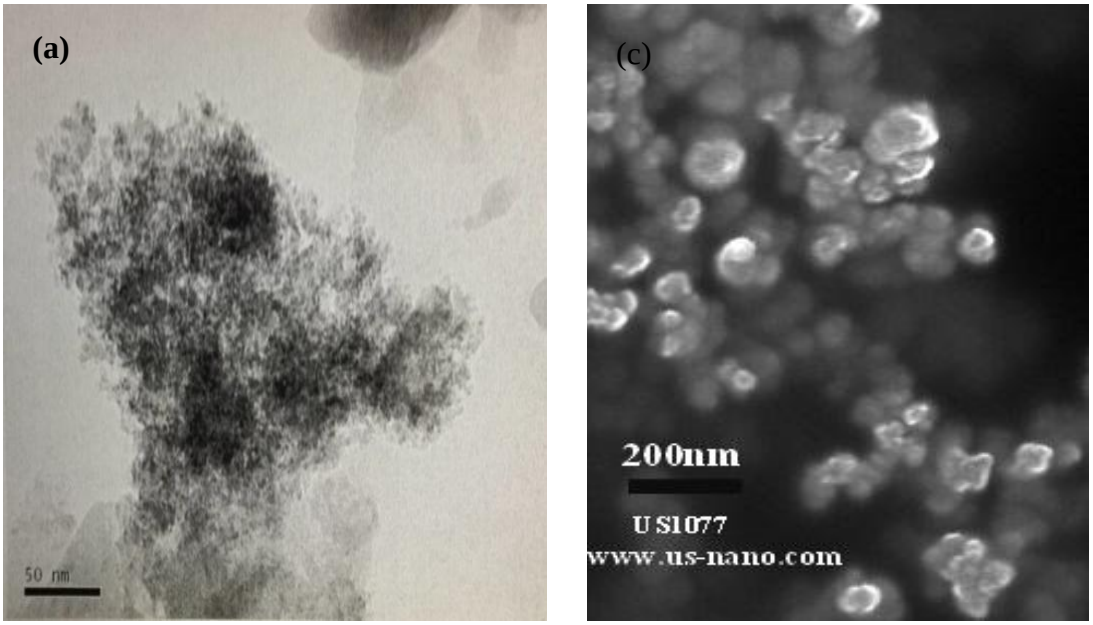

Figure 3.1 (a) TEM micrograph of as-received MBCs [240] and (b) SEM micrograph of as-received NBCs [228].

3.1.2.2. Clay nanofillers

Organomodified Cloisite 30B clays with methyl, tallow, bis-2-hydroxyethyl, quaternary ammonium was used in this study, which were supplied by Southern Clay Products, Gonzales TX. Such clays have an interlayer spacing d_{001}=1.88 nm, density of 1.98 g/cm^3 and cation exchange capacity (CEC) of 90 mequiv/100 g [25]. Their chemical structure is demonstrated in Figure 3. 2.

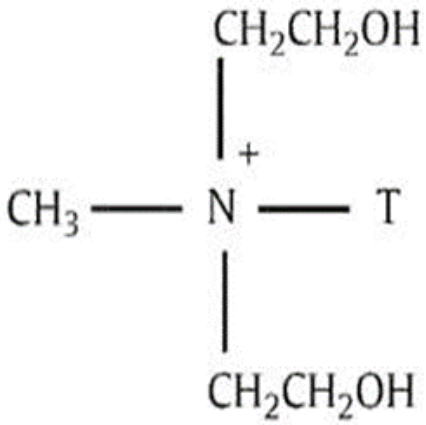

Figure 3.2 Chemical formula for Clositie 30B clays.

3.1.2.3. Halloysite nanotubes (HNTs)

HNTs belong to the kaolin group of clay minerals, with a chemical formula $Al_2Si_2O_5(OH)_4 \cdot nH_2O$ [2]. In this work, HNTs were donated by Imerys Tableware Limited, New Zealand with their material specification listed in Table 3.1.

Table 3.1 Material specification of HNTs [241].

Product	Outer diameter (nm)	Inner diameter (nm)	Length (µm)	SiO_2 (%)	Al_2O_3 (%)	Fe_2O_3 (%)	TiO_2 (%)	Na_2O (%)	MgO (%)
HNTs	40-120	15-100	0.3-1.5	49	34.8	0.35	0.12	0.25	0.15

3.2. Fabrication of PVA Based Nanocomposite Films

PVA/MBC nanocomposite films were prepared by a solution casting method, as shown in Figure 3.3. Initially, 5 wt%/v PVA aqueous solution was prepared by dissolving 10 g PVA into 190 ml deionised water via vigorous magnetic stirring at 400 rpm and 90˚C for 3 h until PVA was completely dissolved to prepare a stock solution. MBC aqueous suspension was obtained by using mechanical mixing in deionised water with a rotor speed of 405 rpm at 40°C for 2 h, which was followed by the ultrasonication (Model ELMA Ti–H–5) at 25 kHz and 40°C with a power intensity of 70% for 1 h. Subsequently, MBC contents of 0, 3, 5 and 10 wt% were

obtained by adding appropriate amounts of PVA. The MBC aqueous suspension was gradually added in a dropwise manner into PVA solutions, simultaneously subjected to mechanical mixing at 405 rpm and 40˚C for 2 h. Then their mixtures were stirred at 400 rpm and 90˚C for 1 h prior to further sonication for 30 min to achieve uniform dispersion of MBCs. Finally, 20 ml prepared solution was cast on a glass petri dish and allowed to dry in an air-circulating oven at 40˚C for 48 h. Afterwards, PVA/MBC nanocomposite films were stored in a silica gel-containing desiccator before material testing and analysis. PVA/NBC nanocomposites, PVA/HNT nanocomposites and PVA/Closite 30B nanocomposites were also subjected to the same fabrication procedure in an identical processing condition.

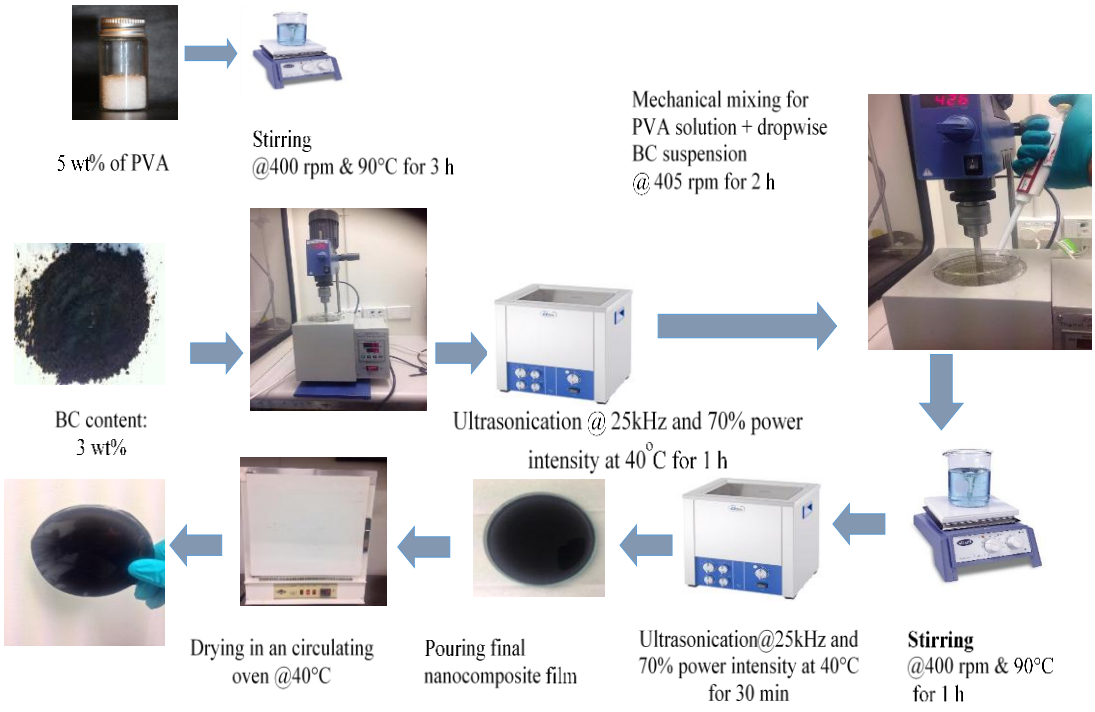

Figure 3.3 Flow chart for the fabrication of PVA/MBC nanocomposite films.

3.3. Characterisation Techniques

The material performance of PVA nanocomposite films and the effect of different nanofiller contents and shapes on final nanocomposite films are often evaluated with

various characterisation techniques. In this study, morphological structures, mechanical and thermal properties, as well as nanomechanical features were holistically investigated, as shown in Figure 3.4 and Table 3.2, which are explained in the following subsections.

Table 3.2 Used charcterisation techniques

Techniques	Set-up parameters	Material characteristics
XRD	• Ni-filtered Cu–Kα radiation • Accelerating voltage=40 kV • Accelerating current =40 mA • 2θ range= 2-50º • Scan rate: 0.015°/s	• Detecting interlayer distance/spacing of intercalated nanoparticles. • Dispersion degree of nanoparticles
FTIR	• Wave-number range of 650-4000 cm^{-1}	• Component identification and analysis • Interfacial interactions
SEM	• accelerating voltage = 5 kV • platinum coating with the layer thickness of 5 nm	• Dispersion degree of nanoparticles • Surface roughness and morphology
DSC	• temperature range of 35 to 300°C • Scan rate= 10°C/min • Flow rate=25 ml/min • Argon atmosphere	• Thermal properties in term of glass transition , melting and crystallisation behaviour
TGA	• Temperature range of 35 to 700°C • Scan rate= 10°C/min • Flow rate=25 ml/min • Argon atmosphere	• Thermal stability in terms of weight loss and thermal decomposition temperatures
Mechanical Testing	• Gauge length =50 mm • crosshead peed=10 mm/min	• Young's modulus • Tensile strength • Elongation at break • Tensile toughness
PFQNM in AFM	• RTESPA 525A probes • Spring constant=200 N/m • Resonant frequency=525 kHz	• Nanomechanical properties. • Nano roughness • Surface morphological structure

3.3.1. X-ray Diffraction (XRD) Analysis

X-ray diffraction analysis is regarded as one of most popular nondestructive technique to reveal the structural status of nanocomposites. Moreover, such a technique is widely used to quantify intercalated/exfoliated clay dispersion in MMT reinforced composites by assessing the characteristic peaks of MMTs in measured XRD patterns. For instance, the XRD peak shift to a lower 2θ diffraction angle indicates the expansion of MMT basal spacing to different extent with a clear sign of MMT intercalation. Additionally, complete disappearance of XRD peaks suggests that full MMT exfoliation may occur, which should be further confirmed with the aid of transmission electron microscopy (TEM). Our XRD analysis was conducted via a Bruker D8 Advance diffractometer, as shown in Figure 3.5. The X-ray source was Ni-filtered Cu–Kα radiation with the wave length of 0.1541 nm at the accelerating voltage and current of 40 kV and 40 mA, respectively, along with the X-ray spectra recorded at small angle 2θ range of 2°-10° and wide angle 2θ range of 10°–50° with the scan rate of 0.015°/s. Small angle range was used to evaluate the intercalation level and dispersion of nanofillers. Whereas wide angle range was employed to investigate the crystalline structure of nanofillers and their PVA based nanocomposites.

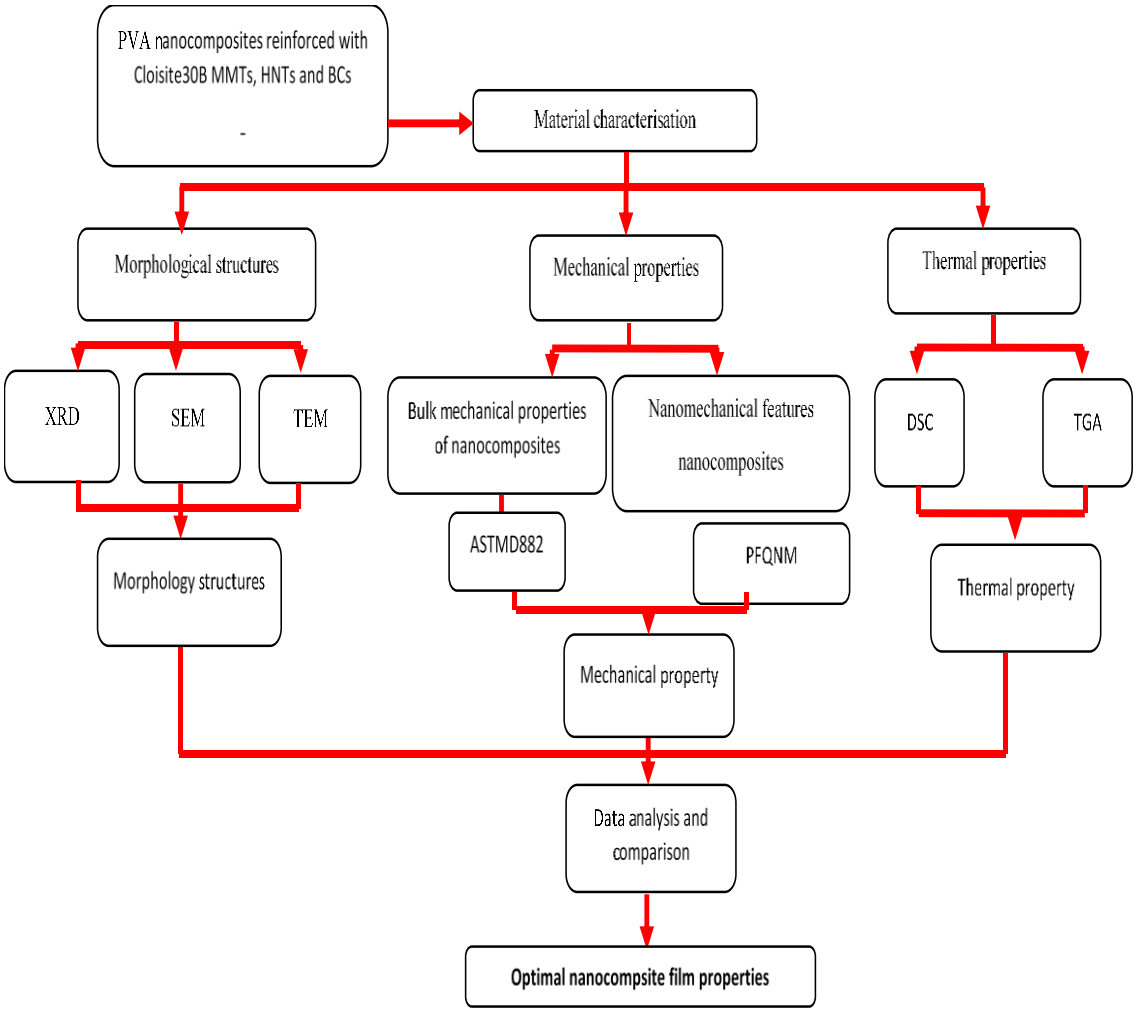

Figure 3.4 Flow chart for material characterisation of PVA based nanocomposite films

Figure 3.5 XRD instrument used in this study.

3.3.2. Fourier Transform Infrared (FTIR) Analysis

FTIR technique is generally utilised to obtain an infrared spectrum of absorption or emission of a solid, liquid or gas sample based on vibration modes of atoms in a molecule. Such a technique is regarded as the footprint for bonds and atoms for material samples by analysing corresponding absorption peaks located at different frequencies. FTIR was carried out to assess the interaction between PVA polymer matrices and nanofillers. It was recorded in a wave-number range from 650-4000 cm^{-1} with a resolution of 4 cm^{-1} according to an attenuated total reflectance (ATR) method [242].

3.3.3. Scanning Electron Microscopy (SEM)

Scanning electron microscopy is one of most commonly used microscopic technique to examine the morphology of material fracture surfaces. In SEM, a focused beam with high energy is applied on the sample surfaces to produce various signals involving 2D visual information about sample surface topography and composition [243]. The signals resulting from electron-sample surface interactions are reformatted to generate topographic images. Fracture surface morphology of PVA nanocomposite films was observed with a field emission scanning electron microscope (FE-SEM, Zeiss NEON 40 EsB Cross Beam, as depicted in Figure 3.6) at an accelerating voltage of 5 kV after being coated with platinum (layer thickness: 5 nm) to reduce electric charging effect.

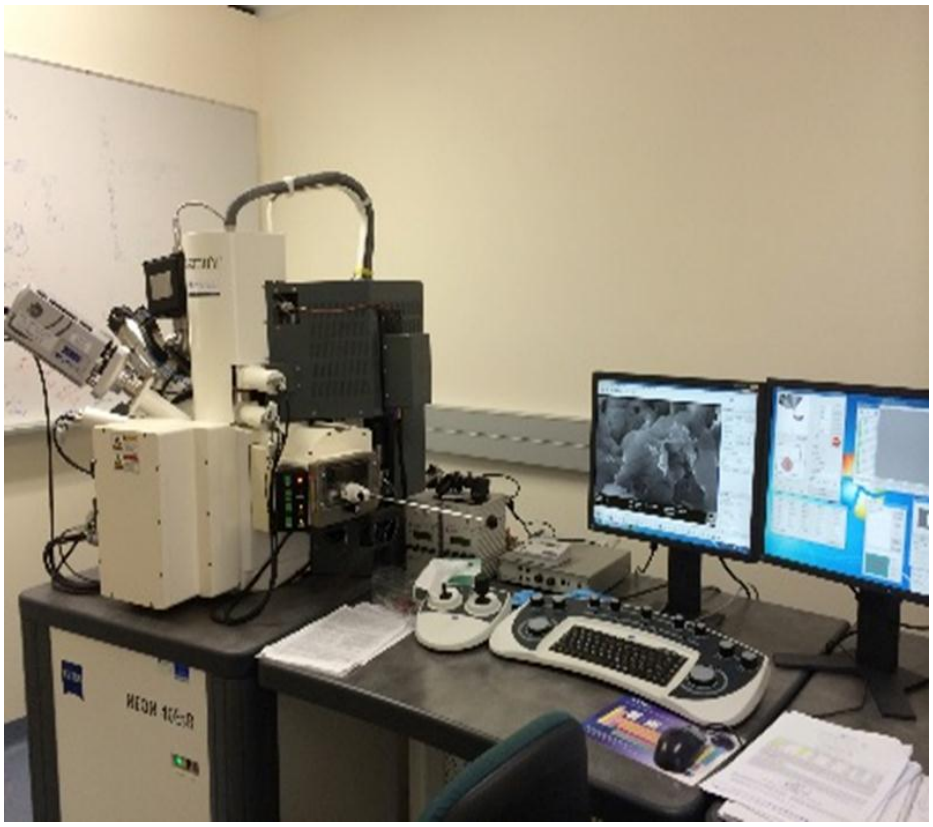

Figure 3.6 SEM instrument

3.3.4. Differential Scanning Calorimetry (DSC)

DSC is a thermal analytical technique used to understand the effects of heating and cooling cycles on polymeric behaviour as well as investigate thermal transitions of polymers and composites [244]. In this study, such a technique was employed to study the impact of different nanofiller contents, sizes, shapes and structures on thermal behaviour of PVA nanocomposite films. DSC was performed on a Mettler Toledo 1 STARe system. Approximately 8-10 mg film samples were sealed in aluminium pans and heated from 35 to 300°C at a scan rate of 10°C/min and flow rate of 25 ml/min under argon atmosphere. The degree of crystallinity χ_c of PVA matrices in PVA nanocomposites was calculated as follows:

$$\chi_C\ (\%) = \frac{\Delta H_m}{w\Delta H_m^O} \times 100\% \qquad 3.1)$$

where ΔH_m is the measured melting enthalpy based on DSC data. ΔH_m^o = 138.6 J/g [245] is the enthalpy of fully crystalline PVA and w is the weight fraction of PVA matrices in corresponding PVA nanocomposites. Moreover, the glass transition temperature (T_g), crystallisation temperature (T_c) and melting temperature (T_m) were determined for PVA nanocomposite films in DSC data analysis.

3.3.5. Thermal Gravimetric Analysis (TGA)

TGA technique is used to measure the mass loss of samples when the temperature increases over time. In this study, TGA was used to investigate effects of different nanofillers on thermal degradation of PVA nanocomposite films. It was also carried out on the same Mettler Toledo 1 STARe system, as shown in Figure 3.7, from 35 to 700°C at a scan rate of 10°C/min and flow rate of 25 ml/min under argon atmosphere.

Figure 3.7 TGA/DSC instrument.

3.3.6. Mechanical Testing

A universal testing machine Lloyd EZ50 shown in Figure 3.8 was implemented to conduct conventional tensile tests at the crosshead speed of 10 mm/min at room temperature with the gauge length of 50 mm. For each material batch, six specimens

were tested with the mean values and standard deviations being calculated accordingly. The tensile toughness was determined based on tensile energy to break (TEB) according to ASTM D882-02.

Figure 3.8 Universal testing machine for conventional tensile tests

3.3.7. Nanomechanical Measurement

Nanomechanical properties of PVA nanocomposites were quantatively assessed via atomic force microscopy (AFM) in a peak force quantitative nanomechanical tapping mode (PFQNM) in this study [246]. In this technique, the vertical motion of cantilever is driven at the frequency below its resonance frequency. At each individual tap, nanomechanical properties as well as peak forces are acquired by collecting the force-distance curve at each pixel [247], Figure 3.9. After that, each force-distance curve is analysed to generate the material property map at the same resolution, which is known as the height image [247]. During the scanning process, the feedback loop of tapping mode can control the maximum force (i.e. peak force) on the tip so that material sample and AFM tip can be protected from any damage. During the data acquisition, cantilever deflection and position are converted into the

force-distance curve. Furthermore, the deflection sensitivity as the representation of deflected distance of the cantilever [246] should be measured accordingly as the requirement for the acquisition of force-distance data. In particular, the determination of deflection sensitivity is based upon the voltage change in the photo detector (nm/V), which can be further converted into the distance (nm) along with the force obtained by multiplying the cantilever deflection with spring constant [246] .

A wide range of material properties, such as adhesion, modulus, deformation, and energy dissipation can be reported by analysing the force-distance data. The elastic modulus was determined by fitting Derjaguin-Muller-Toropov (DMT) model [248] to the initial retrace curve portion, as illustrated in Figure 3.9 (See the green dash line). This model was developed at the low adhesion force between AFM tip with a small tip-end radius and material sample as compared with the compliance counterpart.

The load force on the cantilever F_{Lc} can be given in the following expression [248]

$$F_{\mathrm{Lc}} = \frac{4}{3} E^{*} \sqrt{R\,(z - z_o)^3} + F_{\mathrm{adh}} \tag{3.2}$$

where $E^{*}$is the reduced Young's modulus, R is the tip-end radius, $z - z_o$ is the difference between current piezo position z and orginal position z_0 while F_{adh} is the adhesion force. The sample modulus E_s can be calculated based on $E^{*}$and elastic modulus of AFM tip E_{tip} as well as Poisson's ratios of the sample and AFM tip, respectively (i.e. v_{s} and v_{tip}) using the following equation [248] :

$$E^{*} = \left[\frac{1 - v_s^2}{E_{\ s}} + \frac{1 - v_{tip}^2}{E_{\ tip}}\right]^{-1} \tag{3.3}$$

Adhesion force represents the attraction force between probe tip and sample surface, which can be directly identified as the minimum force illustrated in Figure 3.9. The energy dissipation in a cycle of interaction can be given below [246]

$$W = \int \bar{F}\, d\bar{z} = \int_0^T \bar{F}\, \bar{v}\, dt \tag{3.4}$$

Where $\bar{F}$ is an interaction force vector and $d\bar{z}$ is a displacement vector. Because the velocity vector $\bar{v}$ changes its direction at each half cycle, the integration becomes zero when loading and unloading curves appear to be coincident. Moreover, there is no hysteresis phenomenon above zero loads between repulsive portions of loading-unloading curve, which is associated with very low energy dissipation. In such a case, the work of adhesion represents a dominant contributor to energy dissipation. The associated deformation represents the difference in separation from zero cantilever force to peak forces [246]

In this study, a Bruker Dimension Fastscan AFM system was employed to measure peak force quantitative nanomechanical properties and acquire single force-distance curve under the ambient condition. Moreover, RTESPA 525A probes with a nominal spring constant of 200 N/m, a nominal tip radius of 8 nm and a nominal resonant frequency of 525 kHz were utilised for the direct measurement of correponding nanomechanical properties of PVA nanocomposite films. Before each measurment, it was confirmed that the deflection sensitivity was calibrated by obtaining a force curve based on the stiff sapphire-12 surface. Later on, a thermal tuning method [249] was applied to determine the spring constant, which was considered as one of most accurate methods for detecting the spring constant by measuring cantilever mechanical response to thermal agitation via the Brownian motion of encompassing fluid molecules. AFM imaging analysis was undertaken with the TESPA probe at the nominal spring constant of 40 N/m with a tip radius of 8 nm. The image scan rate was kept at 2 Hz with 256 ×256 digital pixel resolution. AFM topographic images were first-order flattened via Flatten command in Burker Nanoscope 1.5 software,

which was used to remove unwanted features resulting from the vertical (Z) scanner such as noise, bow and tilt.

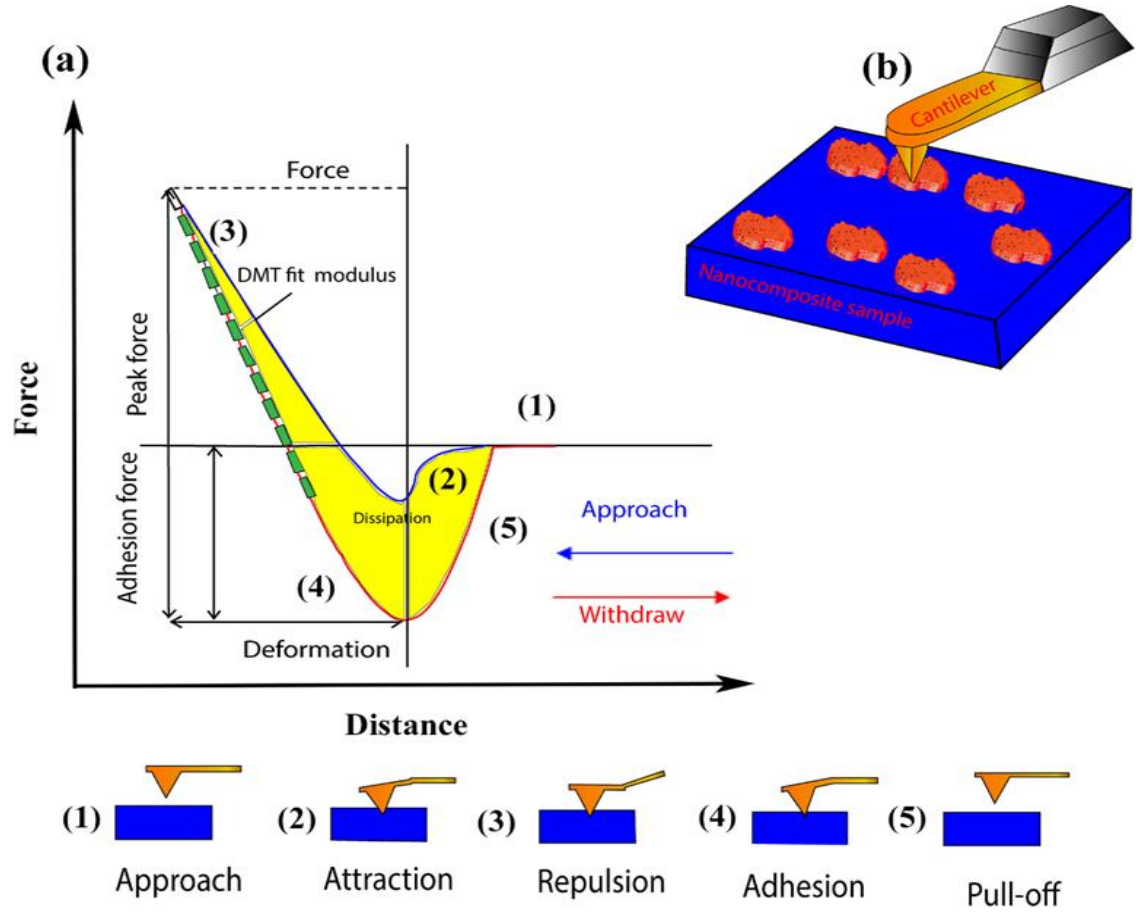

Figure 3.9 Schematic diagram of force vs. tip-sample separation obtained from AFM tapping on the sample surface where the sepration is calculated from *z* peizo poistion and cantilever deflection. Blue and red curves denote loading and unloading portions, respectively and green dash line is obtained by DMT fitting. The minimum force in the withdraw curve is used for mapping adhesion force. Points from (1) to (5) represent tip-sample interactions throughout 0.5 ms [246]. (b) Schematic diagram of nanocomposite sample tapping process.

3.4. Summary

- PVA with the hydrolysis degree of 99.99% was selected as a water soluble biopolymer with three different types of nanofillers. BCs was chosen because their 3D irregular shape and porous structures for the absorption of PVA

molecules. Additionally, Cloisite 30B clays were employed due to their 1D platelet-like shape with a relatively large interlayer spacing as well as functional groups to facilitate the close interaction with PVA molecular chains. HNTs were selected in that such nanofillers possess 2D tubular structures with alumina and silica groups on HNT surfaces, which assist in the good bonding between HNTs and PVA matrices in PVA/HNT nanocomposites.

- Solvent casting method was used in manufacturing PVA nanocomposites. The combination process of magnetic stirring, mechanical mixing and ultrasonication was essential for the fabrication of PVA nanocomposites. The only exception is that no chemical solvent apart from water was used and nanocomposite films were kept in a silica gel-containing desiccator to avoid the moisture effect.
- SEM, XRD and FTIR analyses were carried out to investigate morphological structures of PVA nanocomposites films. Conventional tensile tests were performed to determine their bulk mechanical properties while nanomechanical features were evaluated by PFQNM.
- Thermal stability and thermal properties of all bionanocomposites were determined via TGA and DSC techniques, respectively.

Chapter 4.

PVA/BC Nanocomposite Films with Particle Size Effect

4.1. Particle Characterisation Properties

4.1.1. BC Composition and Surface Area

BCs generally comprise the elements of carbon, oxygen, hydrogen, nitrogen and small quantities of ash [250]. Since the carbon content is a function of many material processing parameters such as pyrolysis temperature, moisture content and composition of biomass [251], it is regarded as a key factor to determine the charcoal quality. As seen from Table 4.1, the carbon content of NBCs is relatively high when compared with that of MBCs (i.e. 84.18 % vs. 80.04%), which was in good accordance with previous results obtained by Li *et al.* [250]. As such, BCs can be considered as good carbon-based fillers for effective reinforcements in nanocomposite systems. Oxygen, hydrogen and nitrogen contents for both NBCs and MBCs become less pronounced (O%: 5-10%, H%: 2.2-2.5% and N%: 0.5-0.7%) accordingly.

Table 4.1 Chemical composition and surface areas of NBCs and MBCs.

Bamboo charcoals	C (%)	H (%)	N (%)	O[a]	*Ash*	S_{BET}[b] ($m^2 g^{-1}$)	S_{mic}[c] ($m^2 g^{-1}$)	S_{ext}[d] ($m^2 g^{-1}$)	V_{mic}[e] ($cm^3 g^{-1}$)	D_p[f] (nm)
NBCs	84.18	2.22	0.66	4.6	8.34	624.81	415.46	209.35	0.17	2.87
MBCs	80.04	2.54	0.52	9.86	6.93	527.41	390.84	136.57	0.16	4.14

[a] *O (%)= 100-(C + H + N + Ash),* [b] S_{BET} *=surface area,* [c] S_{mic} *=micropore area,* [d] S_{ext} *= external surface area,* [e] V_{mic} *= micropore volume and* [f] D_p *= pore diameter.*

Moreover, surface area and pore volume tend to be the other two important controlling factors in effective BC reinforcements. As mentioned previously by Das *et al*. [252], pore volume and number in BCs could promote the absorption capacity of polymer matrices to enable their sufficient interfacial bonding with BCs. All three measured major surface areas including Brunauer–Emmett–Teller (BET) surface

area (S_{BET}), micropore area (S_{micro}) and external surface area (S_{ext}) appear to be consistently higher for NBCs when compared with those of MBCs despite comparable micropore volume (V_{micro}) and relatively low pore diameter (D_p) of NBCs. Such results imply that NBCs have much better adsorption capability towards surrounding media, and can yield more efficient load transfer from polymer matrices to fillers, which is in good agreement with previous work from She *et al.* [253]. The reason for the increase in NBC surface areas may be attributed to high carbonisation temperature (≥ 1300°C) and small particle size [253, 254].

4.1.2. Particle Size and Elastic Modulus Measurement

Topographical analysis in relation to morphological structures of as-received NBCs and MBCs were conducted by means of PFQNM, Figure. 4.1 After the evaluation of 1356 near spherical NBC and 871 MBC particles, it has been statistically determined that average particle diameters are 69.43 and 406.8 nm for NBCs and MBCs, respectively. In addition, the average thickness of NBCs is about 6 nm as compared to 54.4 nm for that of MBCs. Figure. 4.1(a) and (c), as well as Figure 4.1 (b) and (d) display typical cases of NBCs and MBCs deposited on steel substrates from aqueous dispersion at different magnifications, respectively. It is clearly shown that NBCs are more uniformly dispersed with near spherical particle shapes and smaller particle sizes when compared with sharp-edge MBCs. The variations in terms of particle size and thickness visually support different surface areas obtained in Table 4.1.

Young's moduli of NBCs and MBCs are essentially used for the prediction of elastic moduli of corresponding nanocomposites. However, so far, there has been no published literature to report such important parameters in an experimental manner. Nanomechanical properties of NBCs and MBCs were also determined by AFM using

PFQNM to quantitatively measure the stiffness of BCs as nanoreinforcements. Five different zones of interest on NBCs and MBCs were selected in typical QNM maps, illustrated in Figures.4.2 (a)-(e) and Figures 4.3 (a)-(e), respectively.

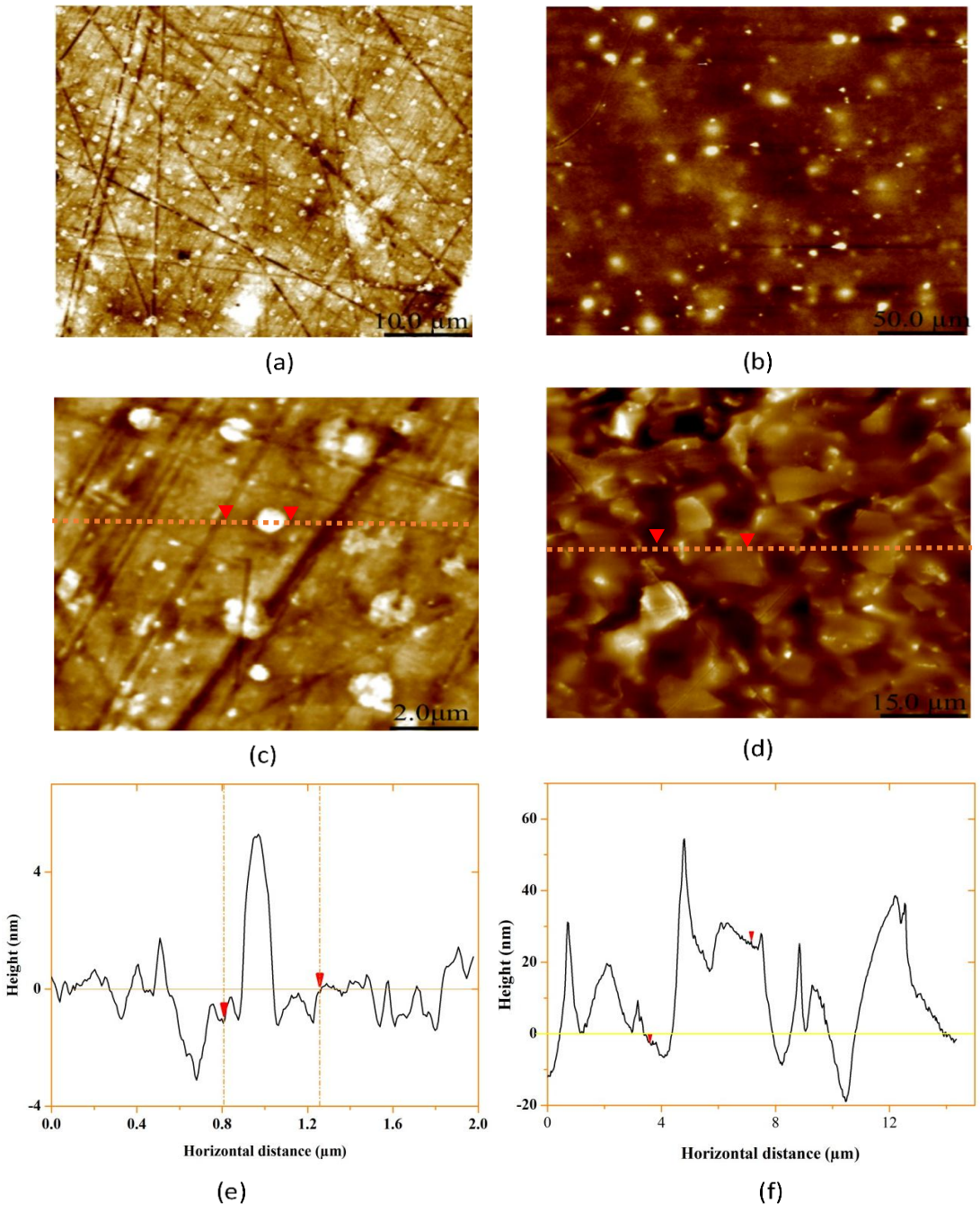

Figure 4.1 Characterisation of individual BC particles: AFM images of NBCs (a) and (c) as well as MBCs (b) and (d) at different magnifications deposited on steel substrates in aqueous solutions. (e) and (f) are height section profiles of NBCs and MBCs, respectively.

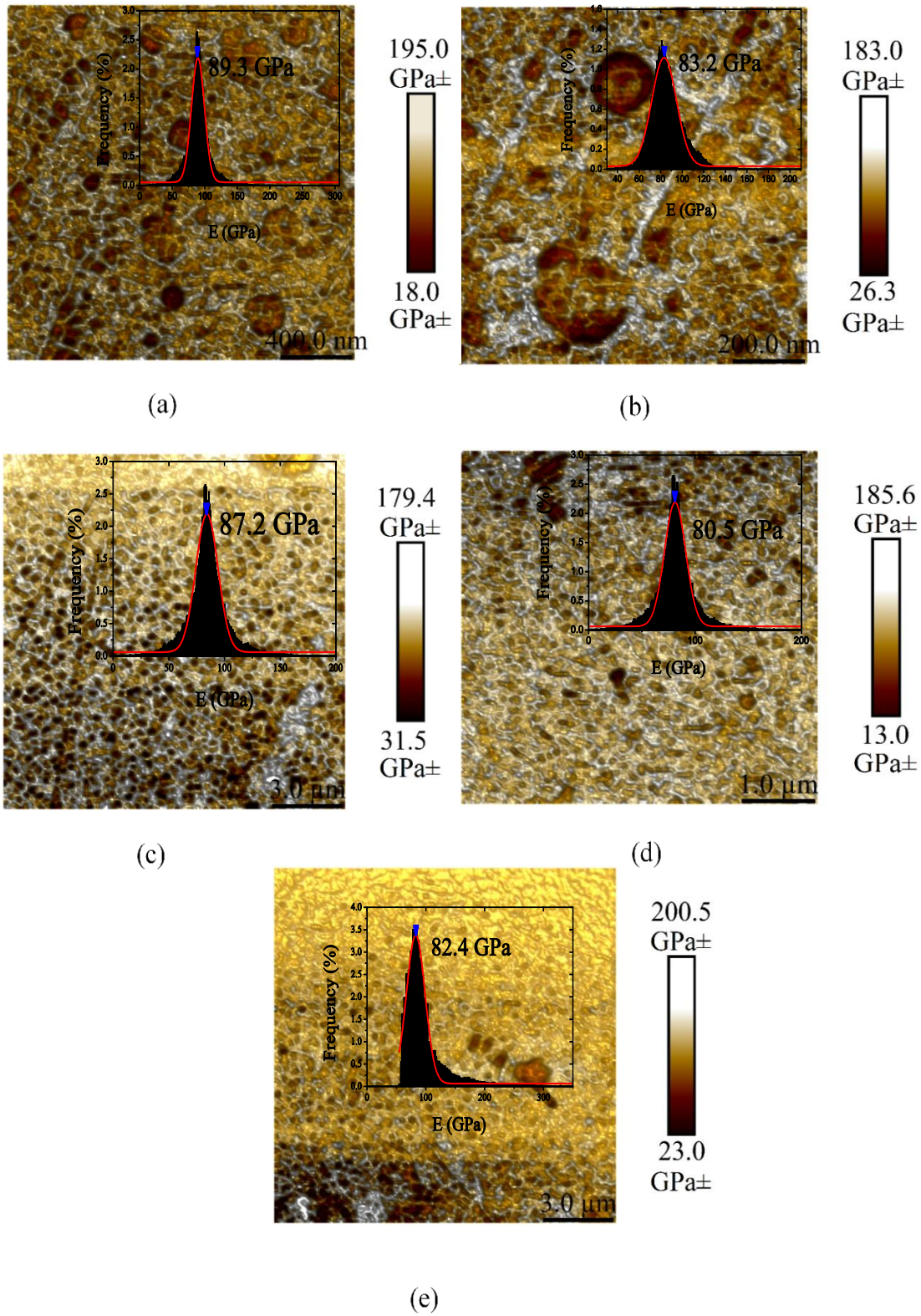

Figure 4.2 Histograms of DMT modulus distribution of whole peak force QNM images: (a)-(e) are five different typical zones of interest for NBCs. Elastic modulus distribution maps are fitted with Gaussian distribution curves for data histograms.

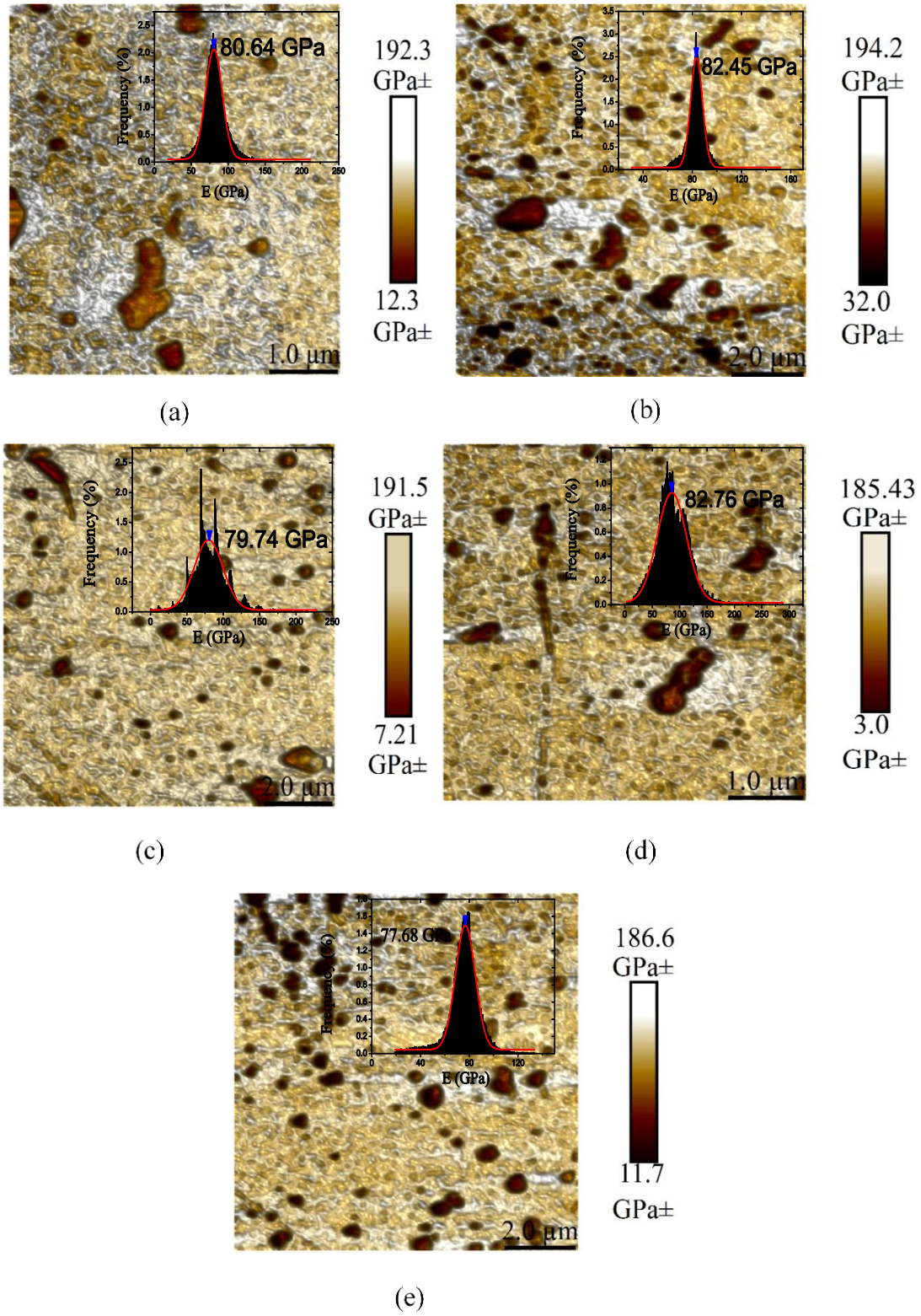

Figure 4.3 Histograms of DMT modulus distribution of whole peak force QNM images: (a)-(e) are five different typical zones of interest for MBCs. Elastic modulus distribution maps are fitted with Gaussian distribution curves for data histograms.

A set of Young's modulus values were estimated according to Derjaguin-Mueller-Toporov (DMT) model [255, 256] for each targeted zone based on corresponding modulus distributions. With the aid of mapping Gaussian distribution curves, Young's moduli of NBCs and MBCs were determined to be 84.5±3.6 GPa and 80.65±2.1GPa, respectively. Such results suggested that particle size effects are minor on Young's moduli of NBCs and MBCs. Compared with other carbon based fillers, elastic moduli of NBCs and MBCs are higher than that of T300 carbon fibres [257], which is in range of 20-40 GPa as well as higher than the modulus of carbon nanoparticles at 43.89 GPa [258]. However, the elastic modulus of BCs determined in this study is still much lower than those of graphene oxides (GOs) in range of 200-250 GPa [259] and multi-walled carbon nanotubes (MWCNTs) at 0.9 TPa [260]. However, graphene oxide sheets can have limited use with a higher tendency to form agglomerates [26] as well as their detrimental effect on human cells , as evidenced by the decrease in A549 cell viability at high GO content levels [150]. Whereas CNTs possess significant drawbacks with high material cost and nanotoxicity since their accumulation in cytoplasm has the ability of destroying human cells under certain inhalational conditions [25]. As such, BCs are regarded as potential carbon-based nanofillers to potentially replace popular GOs and CNTs in the future.

4.1.3. FTIR And XRD Analyses.

FTIR spectra are shown in Figure 4.4 (a) to investigate the surface functionality of as-received MBCs and NBCs. The peaks at about 2439.6 and 2417.5 cm^{-1} are assigned to the C≡H stretching [261]. Whereas the peaks at about 1567.4 and 1566.6 cm^{-1} represent C=C vibration in an aromatic system [253]. The peak spectra at 1696

and 1695.9 cm^{-1} were corresponding to C=O band primarily for ionisable carboxyl groups as an indicator of surface hydrophilicity [262]. The bands existing at 1111.1 and 1075.2 cm^{-1} is ascribed to axial deformation of C-O band. Moreover, the bands at 872.1 and 875 cm^{-1} were referred to as C-H bending (in plane) and C-H bending (out of plane), respectively. The out of plane –OH bending was also designated by the band appearance at 750.2 and 743.6 cm^{-1} for NBCs and MBCs, respectively. Finally, missing –OH peaks at 3350 cm^{-1} in both NBC and MBC spectra infer that both BC types have much lower moisture and alcohol contents [252]. Moreover, XRD patterns of MBCs and NBCs are depicted in Figure. 4.4 (b), revealing the existence of two broad peaks. The board peaks at $2\theta = 22.9°$ were corresponding to those sharp peaks of graphite assigned to the (002) diffraction plane [263]. Besides, the second broad peaks at $2\theta = 43.6°$ characterised 2D in-plane symmetry (101) along with graphene layers. Those board bands confirm that both NBCs and MBCs belong to amorphous carbon. Moreover, NBCs exhibit the highest intensity of (101) diffraction peak as opposed to that of MBCs, which means that NBCs have a relatively high graphitisation degree arising from higher carbonisation temperature of NBCs as opposed to that of MBCs [264].

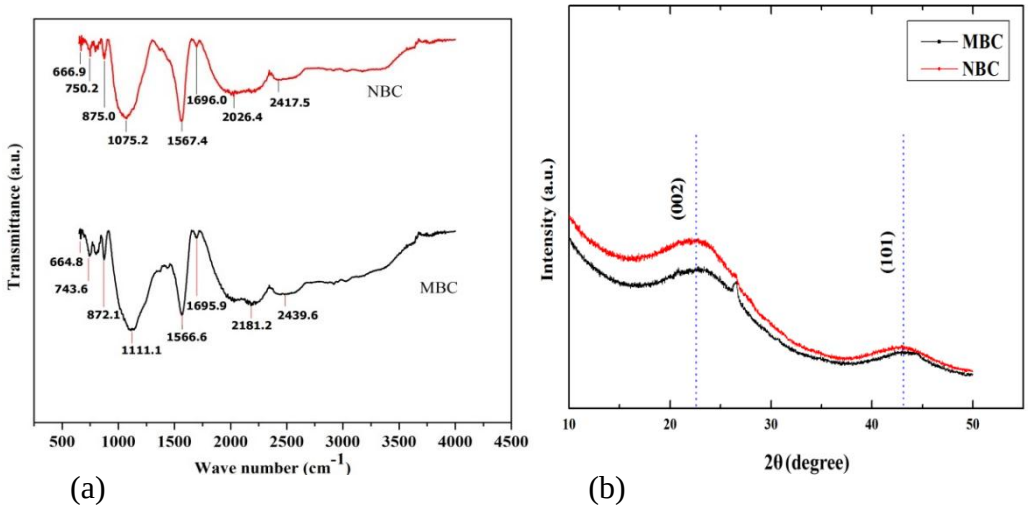

Figure 4.4 FTIR spectra (a) and (b) XRD patterns of as-received NBCs and MBCs.

4.2. PVA/BC Nanocomposite Characterisation and Properties

4.2.1. FTIR and XRD Evaluation

FTIR spectra for NBCs and MBCs with PVA matrices in PVA/BC nanocomposites are illustrated in Figures 4.5 (b) and (c). The change of wave number for –OH and –C–OH stretching bands is well known to be sensitive to hydrogen bonding [265]. Apparently, the originally wide band at approximately 3271.5 cm^{-1} for neat PVA was assigned to the strong hydroxyl band for free and hydrogen bonded alcohols. With increasing NBC and MBC contents from 0 to 10 wt% in PVA/BC nanocomposites, this band peak shifted to lower wave numbers at 3240.6 and 3245.5 cm^{-1}, respectively. This finding could be related to large quantities of hydroxyl groups in PVA molecules [265], as well as strong adhesion of NBC or MBC surfaces to PVA matrices, thus facilitating the generation of hydrogen bonds intertwined at PVA/BC interfaces with a broad O-H band. Such a variation associated with –OH stretching vibration was proven that hydrogen bonds were formed, which was similar to those between PVA matrices and graphene sheets in PVA/graphene nanocomposites [266] and between PVA matrices and BCs in PVA/BC nanocomposites [240]. When compared with the PVA spectrum, new bands at 2853 and 2874 cm^{-1} were detected at the NBC contents of 3 and 5 wt%, respectively, which was assigned to $–CH_2–$ asymmetric and symmetric stretching. The appearance of such new bands and their band increasing tendency demonstrated that NBCs had stronger chemical bonding with PVA molecular chains [267]. At the BC content of 5 wt%, a new band at 2957.8 cm^{-1} assigned to $–CH_2–$ stretching was generated for PVA/NBC nanocomposites along with other significantly increased peaks. However, overall relatively low FTIR peaks were more manifested for PVA/MBC nanocomposites in a wave-number range of 2800-3300 cm^{-1}. This phenomenon may lie in a higher level of NBC interactions with PVA molecular chains when compared with MBCs to form much stronger

interfacial areas owing to relatively high surface areas of NBCs, previously reported in Table 4.1

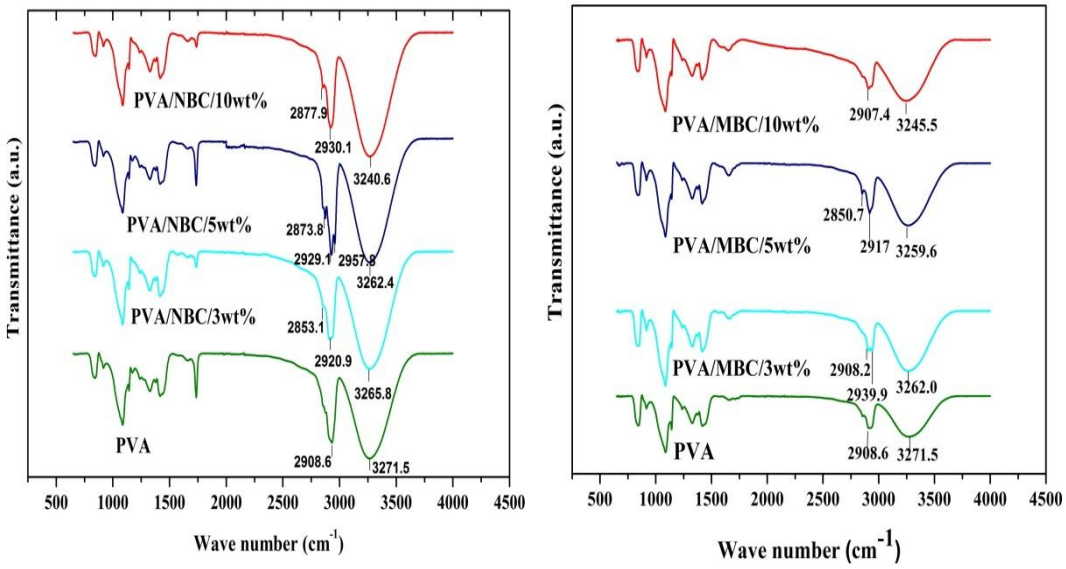

(a) (b)

Figure 4.5 FTIR spectra of (a) PVA/NBC nanocomposites and (b) PVA/MBC nanocomposites

XRD patterns for PVA /NBC nanocomposites and PVA /MBC nanocomposites are shown in Figure. 4.6. Pure PVA films reveal a highest diffraction peak at $2\theta = 19.7°$ corresponding to the (101) total crystalline phase of PVA and the second peak at $2\theta = 40.4°$ in relation to semicrystalline structures of PVA [268]. Moreover, XRD patterns for PVA/NBC nanocomposites in Figure 4.6(a) and PVA/MBC nanocomposites, as seen in Figure. 4.6(b), demonstrate a peak shift to smaller diffraction angles. Moreover, XRD patterns of nanocomposites only display PVA peaks; the diffraction peak of MBCs or NBCs disappeared. Such a finding indicated that PVA had covered nanoparticles and made active bonding inside these pores because BC pores possess 'mechanical anchoring' mechanism [265] when interacting with PVA molecular chains. This phenomenon means that a mechanical interlocking phenomenon takes place due to the existence of PVA molecular chains

inside BC surfaces [265]. Similar results were also detected in PVA/5 wt% GO nanocomposites [269].

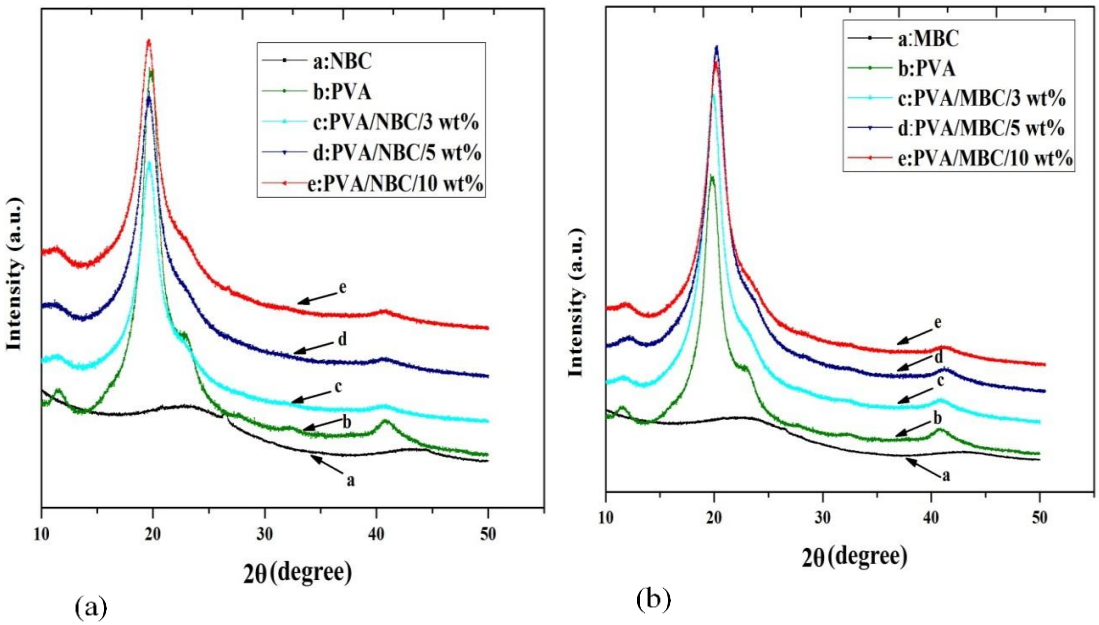

Figure 4.6 XRD patterns of (a) PVA/NBC nanocomposites and (b) PVA/MBC nanocomposites

4.2.2. Mechanical Properties

As illustrated in Figure 4.7(a) and Table 4.2, tensile moduli of PVA nanocomposites reinforced with NBCs and MBCs increased significantly in a monotonic manner with increasing the BC content. The maximum moduli of nanocomposites at 4.63 and 4.16 GPa were achieved with 10 wt% NBC and MBC inclusions, respectively, which indicated the modulus increases by 123 and 100% as opposed to that of neat PVA at 2.08 GPa.

On the other hand, tensile strengths of PVA/NBC nanocomposites and PVA/MBC nanocomposites demonstrated initial enhancements up to 110 and 72% when the BC content was increased from 0 to 3 wt%. Beyond 3 wt% BC inclusions, tensile strengths of both nanocomposites tended to decline until they reached the lowest strength levels of 96.34 and 80.69 MPa, respectively at the BC content of 10 wt%.

However, such lowest strength levels still appeared to be above that of neat PVA. Overall, both tensile moduli and tensile strengths of PVA/NBC nanocomposites were consistently superior to those of PVA/MBC nanocomposites, as illustrated in Figure 4.7 (a). This phenomenon indicated the importance of particle size effect that smaller particles with larger surface areas on nanoscaled levels and good particle dispersion could lead to better mechanical properties of nanocomposites systems. As a matter of fact, when compared with MBCs, NBCs have relatively large surface areas, Table 4.2. Accordingly, more uniform particle dispersion of NBCs could lead to stronger interfacial bonding between NBCs and PVA matrices for effective load transfer from nanofillers to matrices, which might be the major reason for a further strength increase in PVA/NBC nanocomposites.

In addition, both elongation at break and tensile toughness were decreased signficantly by maximum 66 and 58% for PVA/NBC nanocomposites, as well as 66.8 and 66.4% for PVA/MBC nanocomposites, respectively, with increasing the BC content from 0 to 10 wt% as opposed to those of PVA, Figure 4.7 (b). The addition of MBCs gave rise to a more remarkable decreasing trend for elongation at break realtive to that of NBCs. Such a trend was less pronounced as far as tensile toughness of nanocomposites was concerned. Generally, the inclusion of more rigid fillers inevitably improve elastic moduli and enhance the brittleness nature (as reflected from smaller elongation at break) relative to that of neat polymers so that nanocomposites become much stiffer than corresponding unfilled polymers. The other point worth mentioning was that the decreases in tensile strength and tensile toughness of PVA/BC nanocomposites at higher BC contents up to 10 wt% were most likely to do with BC particle agglomeration due to weak particle-particle van

der Waals interactions, which resulted in high stress concentration zones prone to mechanical failure.

Table 4.2 Mechanical properties of PVA/MBC nanocomposites and PVA/NBC nanocomposites

Sample	Tensile modulus (GPa)	Tensile strength (MPa)	Elongation at break (%)	Toughness (MJ/m^3)
PVA	2.08 ± 0.21	70.32 ± 2.9	14.60 ± 0.65	5.84 ± 0.21
PVA/MBC/3 wt%	3.54 ± 0.52	120.64 ± 4.3	6.93 ± 0.72	4.86 ± 0.20
PVA/MBC/5 wt%	4.03 ± 0.39	95.06 ± 3.1	5.98 ± 0.58	3.1 ± 0.25
PVA/MBC/10 wt%	4.16 ± 0.41	80.69 ± 4.4	4.85 ± 0.47	1.96 ± 0.19
PVA/NBC/3 wt%	3.55 ± 0.16	147.94 ± 3.9	10.14 ± 0.29	5.2 ± 0.11
PVA/NBC/5 wt%	4.09 ± 0.25	118.73 ± 4.8	7.22 ± 0.45	3.52 ± 0.11
PVA/NBC/10 wt%	4.63 ± 0.18	96.34 ± 4.1	4.96 ± 0.42	2.45 ± 0.13

Figure 4.7 (c) demonstrates the comparison of tensile strengths of PVA/NBC nanocomposites and PVA/MBC nanocomposites with other PVA based nanocomposites available in previous studies. Xu *et al.* [270] reported that the tensile strength of PVA increased by 70% with the inclusion of 3 wt% GOs due to strong interfacial bonding between PVA and GOs according to their XRD analysis. Arao *et al.* [271] stated that the incorporation of 0.25 wt% of few-layer-graphene (FLG) into PVA matrices enhanced tensile strength of PVA/FLG nanocomposites by 15% because uniform FLG dispersion enabled to form stronger interfaciel bonding with PVA matrices. Furthermore, Liu *et al.* [272] functionalised SWNT surfaces with

multiple hydrogen bonding groups to improve SWNT dispersion in PVA/SWNT nanocomposites. Their tensile strength was found to be improved by 44.6% at the SWNT content of 0.8 wt%, as opposed to that of neat PVA. The use of hybrid nanofillers was also presented by Li *et al.* [273] to achieve increases in tensile strengths of PVA nanocomposites by 57.5 and 75.6% when embedded with 1 wt% multi-walled CNTs (MWNTs) and 2 wt% GOs as well as 2 wt% MWNTs and 4 wt% GOs, respectively. This is becasue hybrid MWNT/ GO reinforements can achieve the strong interfacial interaction with PVA matrices leading to higher tensile strengths of their nanocomposites. On the other hand, Morimune *et al.* [24] mentioned that with the inclusion of 5 wt% nanodiamond (NDs), the tensile strength of PVA nanocomposites was enhanced by 30.5%. In comparison, tensile strengths of PVA/NBC nanocomposites and PVA/MBC nanocomposites at the BC content of 3 wt% were reported in this study to increase by 110% and 72%, which appear to be more desirable than other carbon based nanocomposites reinforced with GOs and SWNTs (despite relatively small SWNT contents used) when both nanofiller cost and enhancement levels of mechanical properties of nanocomposites are concurrently considered.

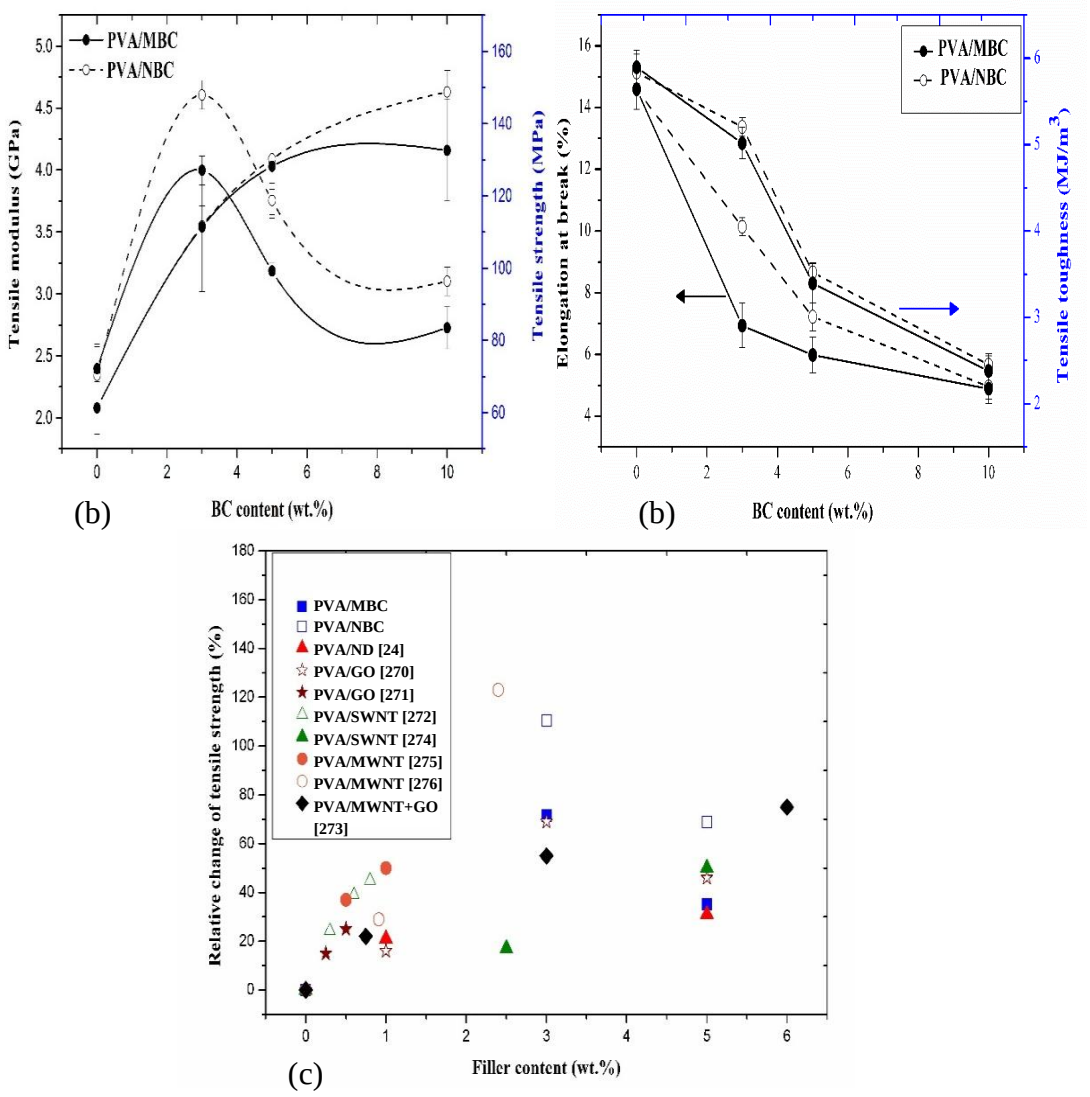

Figure 4.7 Mechanical properties of PVA/NBC nanocomposites and PVA/MBC nanocomposites at different NBC and MBC contents: (a) tensile moduli and tensile strength, (b) elongation at break and tensile toughness and (c) relative change of tensile strength versus filler content.

4.2.3. Fracture Morphology

As observed in Figure. 4.8, all nanocomposites were characterised with rough fracture surfaces due to embedded BC nanoparticles when compared with neat PVA. In particular, uniform multi-layered structures were evident for PVA/NBC nanocomposites with the inclusoin of 3 and 5 wt% NBCs, illustrated in Figures 4.8

(b) and (c), along the parallel direction to tensile loading. Such structures were very similar to nacre structures mentioned elsewhere [48, 240, 267] and in good agreement with those observed in PVA-grafted graphene oxide (PVA-g-GO) nanocomposites [267]. The fibrillation effect of fractured materials also took place particularly in PVA/NBC nanocmposites when nanocomposite films were stretched under the undirectional tension. This phenomenon suggested far higher ductility of PVA/NBC nanocomposites when compared with that of PVA/MBC nanocomposites, which was also confirmed by their consistently higher elongation at break in Figure 4.8 (b).

On the other hand, fracture areas of PVA/MBC nanocomposites demonstrated less layered structures as opposed to PVA/NBC nanocomposites at the BC content of 3 wt%. This phenomenon can be associated with smaller surface areas of MBCs to reduce interfacial interactions between fillers and PVA matrices. As depicted in Figure. 4.8 (g), with increasing the MBC content up to 10 wt%, interparticle distance can be significantly reduced owing to large amounts of particle agglomerates. As a result, the formation of local networks of MBC particles to act as stress concentration sites prone to mechanical failure takes place, thus lowering tensile strengths of nanocomposites, as shown in Figure 4.7 (a).

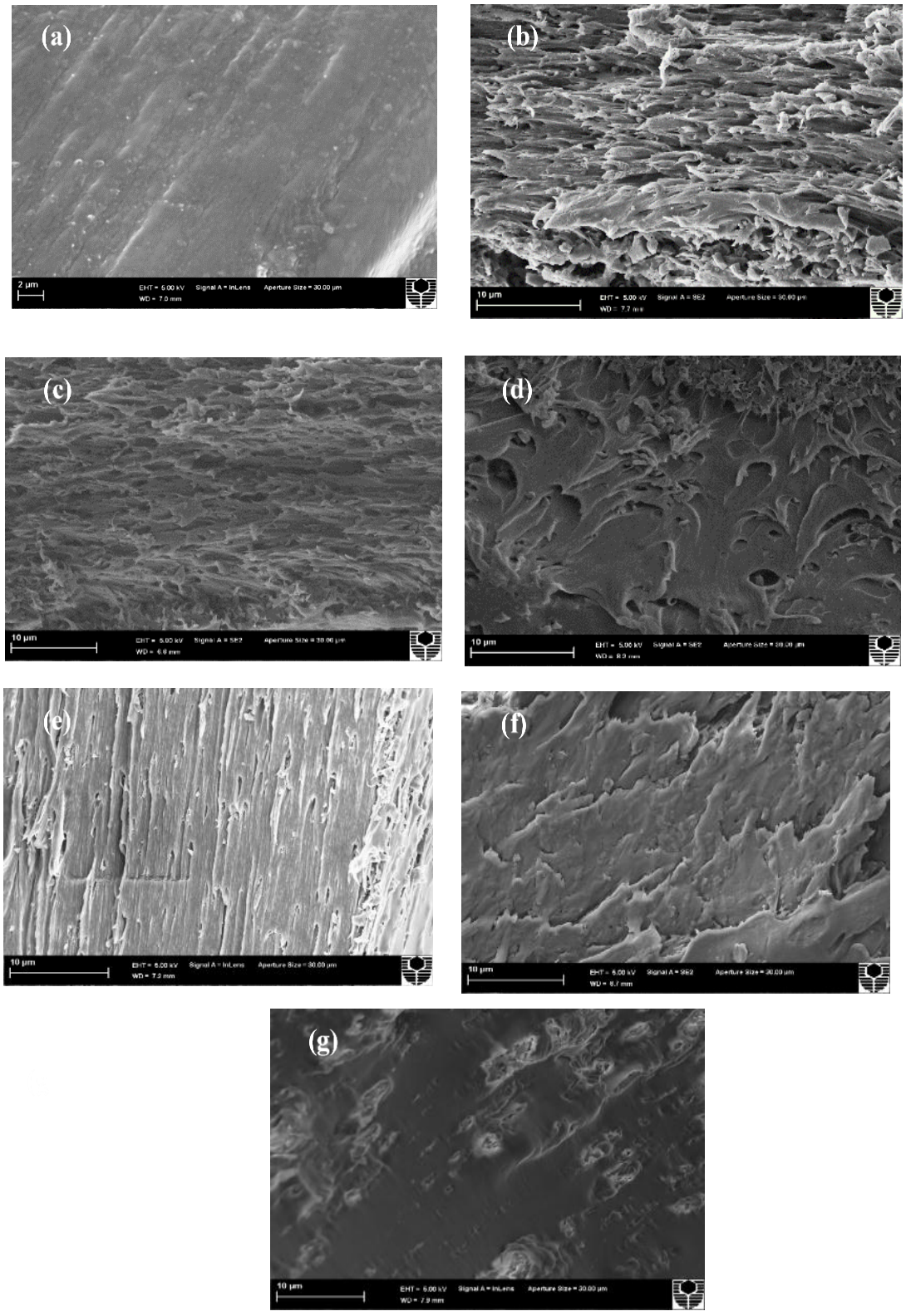

Figure 4.8 SEM micrographs of tensile fracture surfaces of (a) PVA, (b) PVA/3 wt% NBC nanocomposites, (c) PVA/5 wt% NBC nanocomposites, (d) PVA/10 wt% NBC nanocomposites, (e) PVA/3 wt% MBC nanocomposites, (f) PVA/5 wt% MBC nanocomposites and (g) PVA/10 wt% MBC nanocomposites.

4.2.4. Thermal Properties

From our results mentioned earlier, it is believed that effective load transfer from PVA matrices to BCs can be affected by the interaction of strong hydrogen bonding between oxygenated functional groups of BC particles and hydroxyl groups of PVA in terms of mobility of polymeric chains. DSC results, shown in Figure 4.9 (a) and (b) and Table 4.3, indicated that the glass transition temperatures T_g increased monotonically up to 75.06 and 73.66°C for PVA/NBC nanocomposites and PVA/MBC nanocomposites, respectively with increasing the BC content from 0 to 10 wt% when compared with the T_g of PVA at 65.19°C. The incoporation of rigid BC particles could restrict the chain mobility of PVA matrices so that higher T_g values were required for the phase change of nanocomposites from glassy state to rubbery state, This finding is well-known for many types of nanofillers such as nanoclays, GOs, CNTs, HNTs and so on [25]. Manna *et al.* [277] reported a slight increase in the T_g of PVA from 70 to 73°C with the addition of 2 phr selective reduced graphite oxides (SRGOs). Moreover, 10 wt% MWNTs were found to enhance the T_g of PVA by 4.8°C in PVA/MWNT nanocomposites [17]. The strong hydrogen bonding between BC particles and PVA matrices also played an important role in restricting the free movement and arrangement of PVA molecular chains with the required higher T_g, in good accordance with PVA/GO nanocomposites [278]. Relatively high T_g values of PVA/NBC nanocomposites were ascribed to higher surface areas of NBCs (relative to those of MBCs), which yielded the increase in volume fraction of interfacial areas to further constrain the chain mobility of PVA matrices [279]. The melting temperature of nanocomposites (T_m) was nearly unchanged in range of 221-225°C as opposed to 222.91°C for neat PVA irrespective of the inclusion of NBCs or MBCs. The similar trend also existed that the degree of

crystallinity (χ_c) of PVA was only slightly enhnaced from 36.65% for neat PVA to 40 and 38.6% for corresponding nanocomposites with the incorporation of 10 wt% MBCs and NBCs, respectively. This suggested that both MBCs and NBCs had relatively minor effect on crystalline phases of PVA matrices, but highly impacted their amorphous phases instead [22].

TGA and DTG curves in terms of mass loss and their derivatives were presented in Figured. 4.9 c-(f) along with major results listed in Table 4.3. Based on the DTG curve of PVA, there are three major degradation steps according to previous literatures [280]. Initially, the first DTG peak at the temperature 107°C was associated with the evaporation of absorbed water. Then the second peak at the temperature of 274°C was attributed to the decomposition of PVA due to the dehydration reaction on polymeric chains as well as degradation of main backbones. Finally, the third peak in relation to the degradation of polyene residues appeared at the temperature below 429°C. With increasing NBC and MBC contents, the thermal stabilities of PVA/NBC nanocomposites and PVA/MBC nanocomposites were improved significantly with reference to that of PVA, as evidenced by consistently higher $T_{5\%,}$ $T_{80\%}$ and T_d values. Thermal stability level of nanocomposites was even more pronounced when incorporated with NBCs in relation to $T_{5\%,}$ and $T_{80\%}$. The shift of decomposition temperatures T_d and T_d' meant that the dehydration process was hindered, which could result from the interaction between hydroxyl groups of PVA and hydroxyl groups on NBC and MBC surfaces, as confirmed from previous FTIR results. Furthermore, the mass loss process occurring in the third DTG peaks meant that the thermal decomposition of PVA based nanocomposites required more reaction activation energy with the higher reaction order [281]. This finding may be attributed to the existence of NBC and MBC particles acting as barrier materials to

limit the exothermicity of pyrolysis reaction with better thermal resistance of PVA based nanocomposites. On the other hand, DTG peaks of PVA based nanocomposites at the second decomposition step became wider than that of neat PVA, consisting of main and side peaks as opposed to single DTG peak for PVA at the same step. Such a single peak for PVA can be related to the elimination reaction while side and main peaks for PVA/BC nanocomposites correspond to elimination reaction as well as the overlap of continual eliminations and chain-scission reactions that require more energy to accrue at high temperatures [281].

Table 4.3 Thermal properties of PVA/MBC nanocomposites and PVA/NBC nanocomposites

Sample	T_g (°C)	ΔH_m (J/g)	χ_c (%)	T_m (°C)	$T_{5\%}$ (°C)	$T_{80\%}$ (°C)	T_d (°C)	T_d' (°C)
PVA	65.19	50.8	36.65	222.91	200.15	363.5	274.23	
PVA/MBC/3 wt%	68.62	50.6	37.63	223.43	256.22	383.3	281.81	
PVA/MBC/5 wt%	69.89	50.1	38.04	224.37	258.78	410.12	288.93	
PVA/MBC/10 wt%	73.66	49.91	40	224.93	265.9	428.03	305.43	325.03
PVA/NBC/3 wt%	70.53	50.01	37.21	222.12	256.3	390.67	278.48	
PVA/NBC/5 wt%	73.46	49.77	37.83	221.57	262.96	440.28	283.4	303.77
PVA/NBC/10 wt%	75.06	48.16	38.6	222.63	270.73	464.03	294.61	324.12

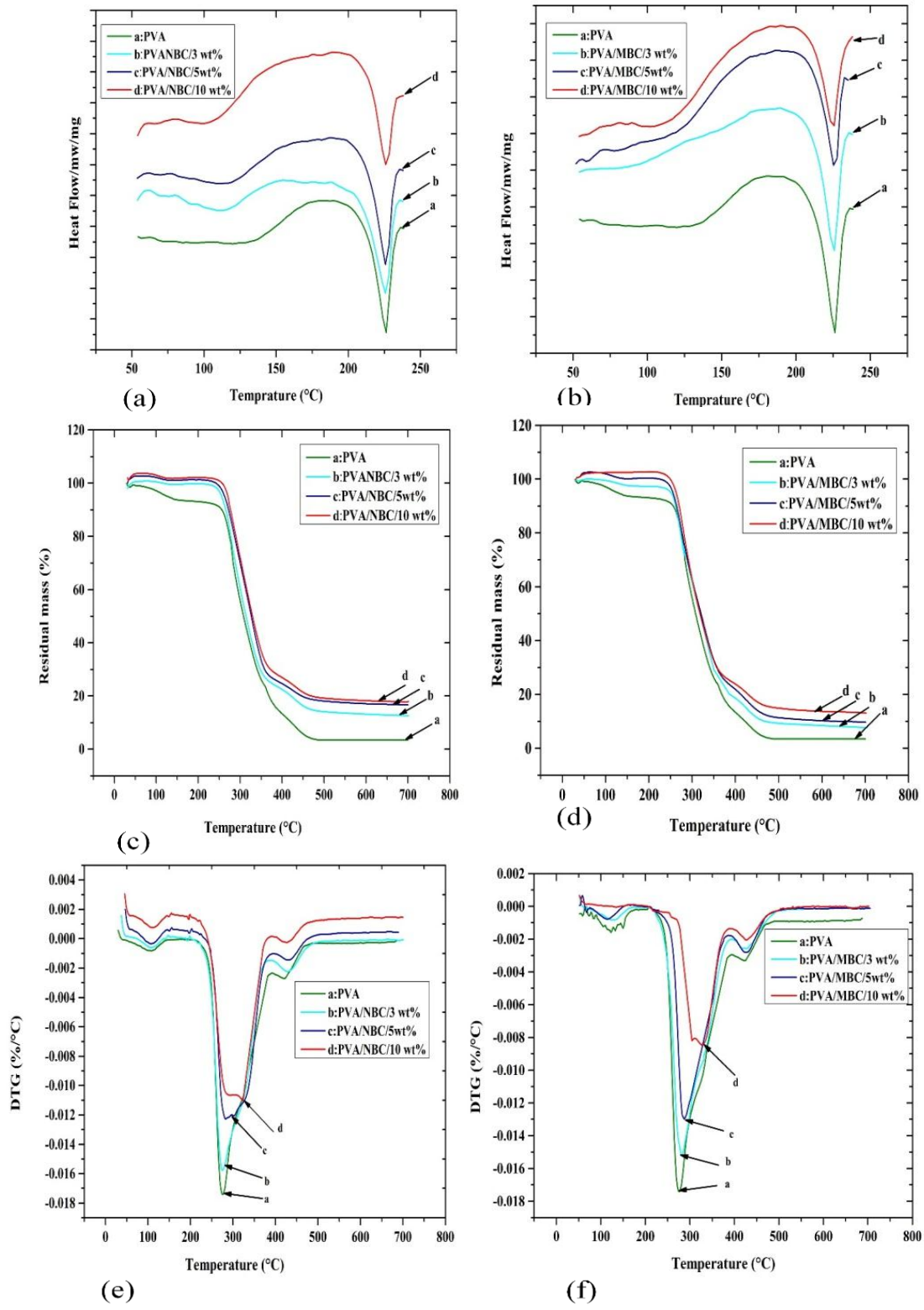

Figure 4.9 DSC diagrams for (a) PVA/NBC nanocomposites and (b) PVA/MBC nanocomposites as well as TGA curves (c) and (e) as well as DTG curves (d) and (f) for PVA/NBC nanocomposites and PVA/MBC nanocomposites, respectively.

4.2.5. Morphological and Nanomechanical Properties

Nanomechanical properties of PVA films are presented in Figure. 4.10. As seen in Figure. 4.10 (a), there are two typical distinct phases known as crystalline phase (in bright white color) and amorphous phase (in dark colour), which are generally detected in semicrystalline polymers [282, 283] like PVA. Derjaguin-Muller-Toropov (DMT) modulus mapping image of PVA, was analysed in its middle section (A_1-B_1) with associated results being depicted in Figure 4.10(c). The regions with a high modulus level of 24±4.2 GPa and phase width of 20-76 nm were related to the bundles of semicrystalline stacks in crystalline phase. This value appeared to be far higher than the elastic modulus of 9.9 GPa for local PVA/poly (acrylic acid) (PAA) nanophase, as previously reported by Pakzad *et* al. [207]. Nonetheless, it was very similar to corresponding elastic modulus of 23.69 GPa obtained from PVA/chitosan composite film coating [284]. In comparison, the regions assigned to amorphous phase had a relatively low modulus of 11.4± 3.1 GPa along with the amorphus phase width of 18-65 nm. The variation of crystalline phase width is attributed to different orientation of semicrystalline buddles for the designated section [282]. Elasti modulus of bulk PVA films was about 2.08 GPa at a macroscopic level, which was less than that of local PVA nanoscaled regions based on AFM. Such a phenomenon is mainfested when nanomechanical properties are compared with those of bulk composites [59, 257]. In epoxy/carbon fibre composites, nanomechanical results showed that the modulus of epoxy was 17 GPa as opposed to 3-4 GPa for bulk composites [59]. In a similar manner, local PVA nanoscaled region yielded a elastic modulus of 11.9 GPa in contrast with 2.08 GPa for bulk PVA films [265]. These differences could be releated to several reasons. Firstly, though the AFM parameters were calibrated prior to each measurement, the shape function for

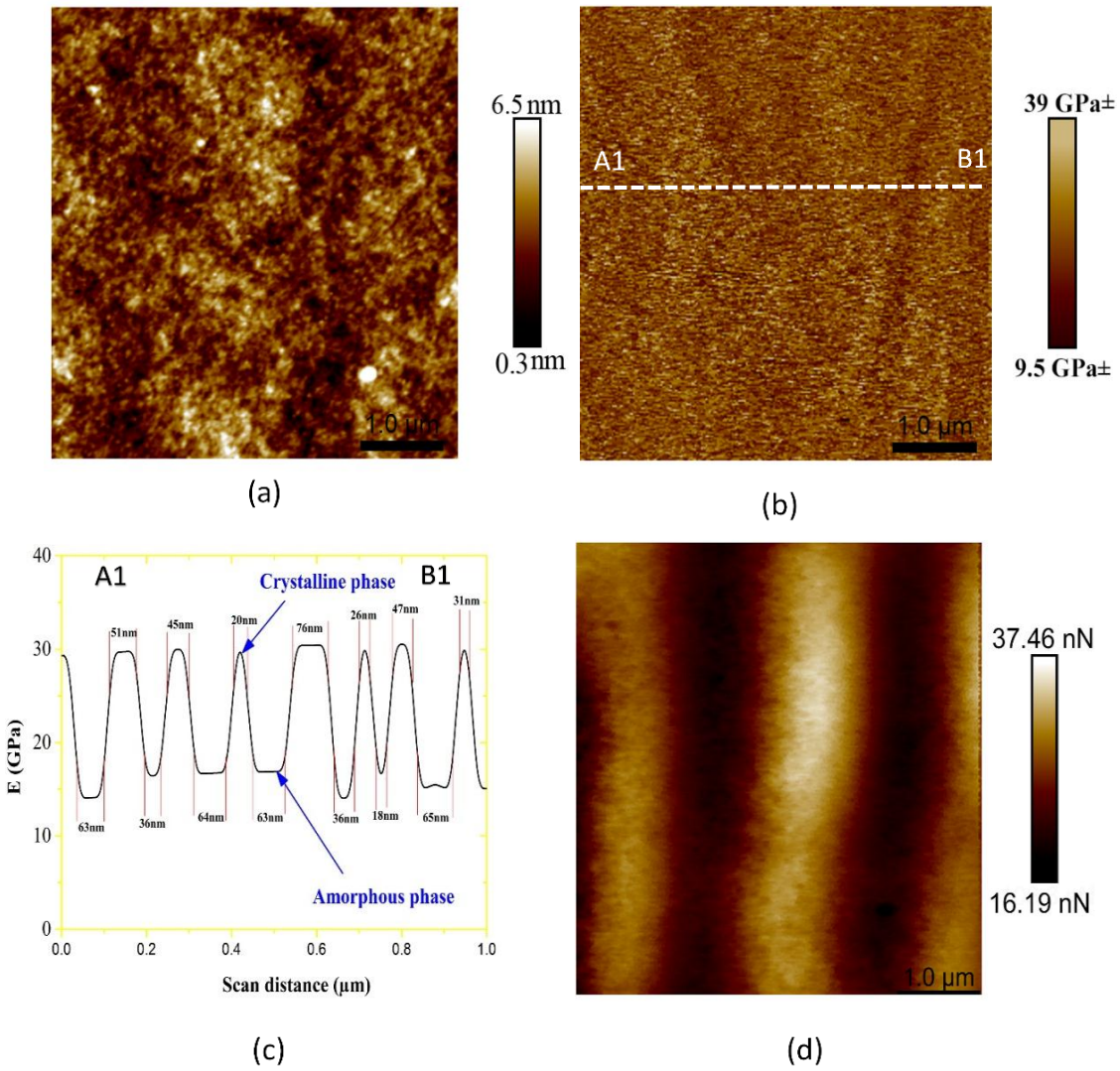

Figure 4.10 2D Height mapping image (a) and DMT modulus (b) mapping images of PVA films, (c) DMT modulus profile of corresponding section area A1-B1 in (b) and (d) 2D adhesion mapping image of PVA films.

the topmost tip of the probe could not be accurate enough at low indentation depth [285]. Low indentation depth comes from low indentation force used to induce residual stress and plastic deformation from next indents, thus leading to the maximisation of lateral resolution capabilities particularly at a nanoscaled level. Secondly, in many cases, local nanosurface properties are different from bulk properties and the penetration depth strongly influences the measurement of elastic

modulus at a nanoscaled level because of the discrepancy taking place in morphological structures between the outer skin on material surfaces and bulk materials [59, 285]. Finaly, Despite the robust data and good repeatability of calculated DMT moduli, PFQNM method is inevitably different from conventional tensile testing to determine the tensile modulus for bulk properties due to distinct measurement mechanisms [286]. The difference in PVA phases could also be characterised by the adhesion force mapping image exhibited in Figure. 4.10 (d), in which adhesion forces for cyrstalline and amorpous phases were measured to be 19.7± 0.6 and 33 ± 2.8 nN, respectively.The higher adhesion of amorphous phase arose from prevalent viscoelastic material behaviour of amorphous polymers in a non-glassy state. This finding indicated that amorphus phase had less density and surface tension as compared to corresponding crystalline phase [283].

The DMT modulus mapping image of PVA/3 wt% NBC bionanocomposites was assessed on the A_2-B_2 section, as depicted in Figure 4.11(b). The circled peaks with high modulus values can be associated with the presence of NBCs within PVA matrices. In addition, the cyclic pattern of low and high modulus domains depicted in Figure 4.11(b) could be correlated with the alternating sequence of amorphous and crystalline phases of PVA accordingly, which is considered as a very common trend in semi-crystalline polymers [282, 283]. Furthermore, the modulus trend of PVA matrices with the addition of 3 wt% NBCs, as shown in Figure 4.11(b), was totally different from that of neat PVA along with the change in the degree of structural orderness, Figure 4.11(c). Such a difference could be attributed to reinforcing effect of NBCs on both crystalline and amorphous phases of PVA matrices. The morphological structure of nanocomposites in term of DMT modulus was further investigated at a high magnifigation in Figure 4.11(c). Furthermore, the data analysis

in the middle of the mapping image (A_3-B_3) is depicted in Figure 4.10 (d). It is worth noting that both crystalline and amorphous phase widths were in range of 5-53 nm and 4-35 nm, respectively, which, however, were lower than that of coresponding PVA (Figure 4.10 (c)). Decreasing the phase width meant that the stack size decreased accodingly from neat polymer to bionanocomposite films. In other words, the number of lamellae stacks per unit volume, on the other hand, increased from neat polymer to nanocomposites, as suggested in Figure 4.11 2(e), thus resulting in the improvement of tensile strengths of nanocomposites. This phenomenon could be interpreted by the Hall–Petch relation [287, 288] where the yield stress and tensile stress depend on the grain size. As a consequence, much higher tensile strength of PVA/NBC nanocomposites at 147.94 MPa could be acheived as opposed to that of PVA at 70.32 MPa. These points offer the insight to esablish a more accurate theoretical modelling framework by combining both nanomechanical properties and bulk properties at the macrosopic level of nanocomposites.

In case of PVA/3 wt% MBC nanocomposites, the DMT modulus mapping image is shown in Figure 4.12 (a) and the data anaylsis in the mapping image (A_4-B_4) is depicted in Figure 4.12 (b). The crystalline phase width was in range of 14-60 nm when compared with the amorphous width of 15-59 nm, which was lower than that of PVA. This finding suggested that the number of lamellae stacks per unit volume increased with the inclusion of MBCs as compared with that of pure PVA. Such a result could also explain higher tensile strength of PVA/3 wt% MBC nanocomposites as opposed to that of pure PVA.

However, In comparesion with PVA/3 wt% NBC nanocomposites, MBC inclusion showed less evident effect on crystalline and amorphuse phases of PVA. In addition,

the widths of amorphouse and crytalline phases were still higher than that of PVA/3 wt% NBC nanocomposites. Such a finding could be related to much higher surface areas of NBCs, which made them cover more contact areas with PVA matrices, and then increased the volume fraction of interphase as compared with that of MBCs. The effect of BC contents on nanomechanical properties as well as interphase features in PVA/BC nanocomposite systems were discussed in the forthcoming chapter 6 in detail.

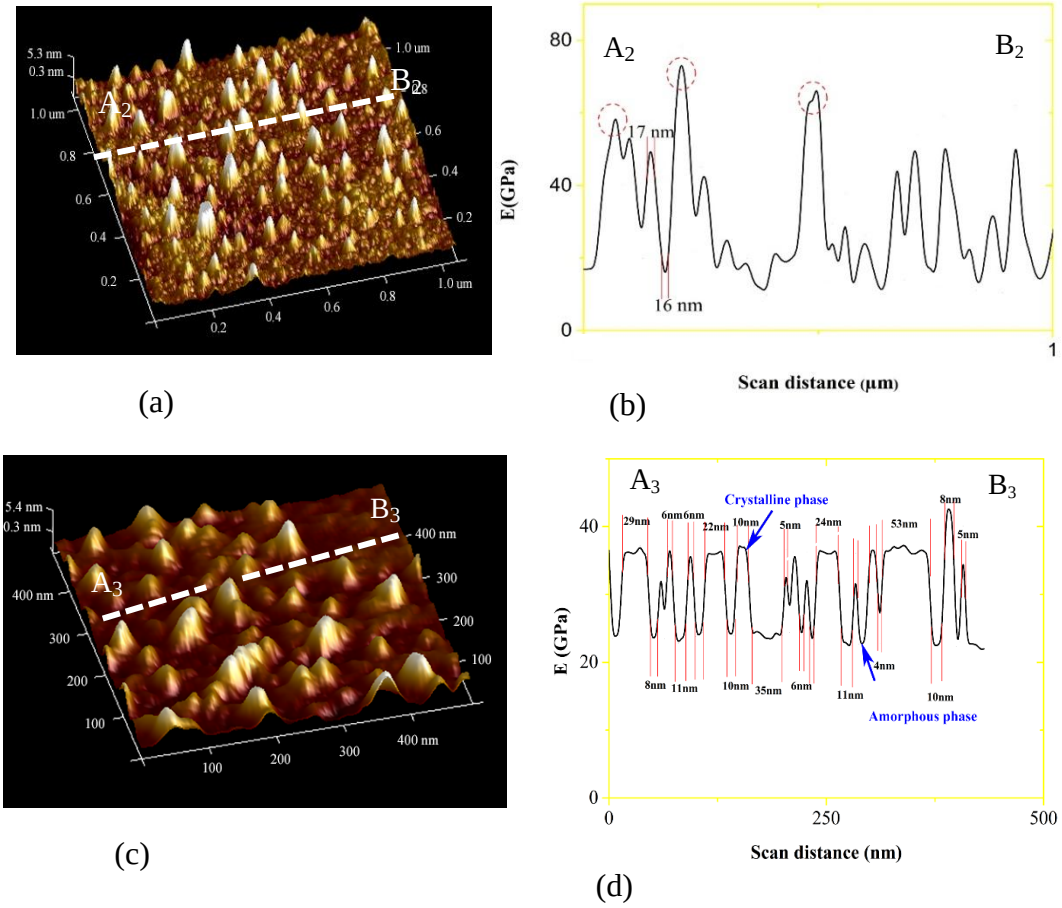

Figure 4.11 (a) 3D height mapping image of PVA/3wt%/NBC nanocomposites and (b) DMT modulus profile curve for corresponding section area A_2-B_2 in (a), (c) 3D Height mappinmg image of PVA/3wt%/NBC nanocomposite at a high magnification, (d) DMT modulus profile for corresponding section area A_3-B_3 in (c), (e) schematic diagram for bundles of lamellar stacks in both neat PVA and PVA/3 wt% NBC nanocomposites

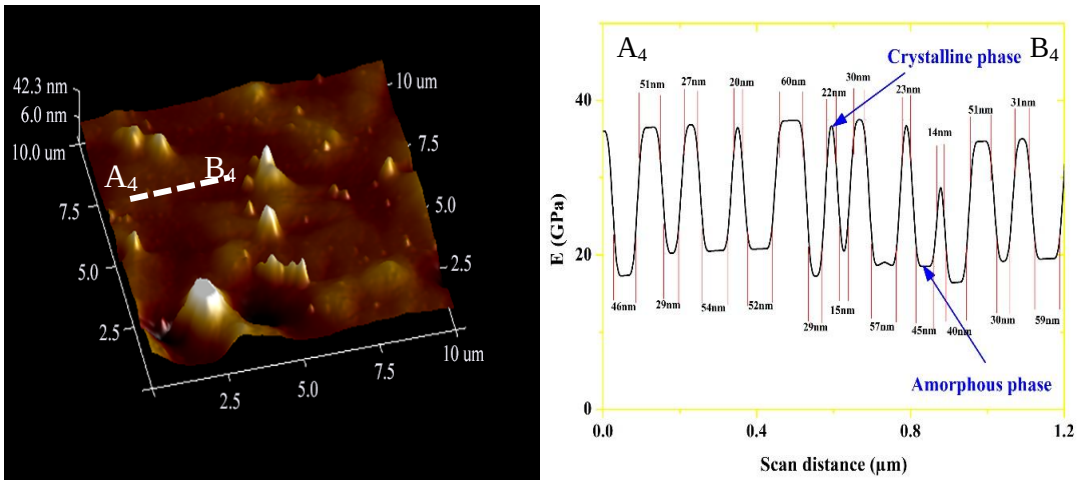

(a) (b)

Figure 4.12 (a) 3D height mapping image of PVA/3 wt%/MBC nanocomposites and (b) DMT modulus profile curve for corresponding section area A_4-B_4 shown in (a).

Figure 4.13 demonstrates 3D height maps and corresponding section profiles of PVA and PVA/NBC bionanocomposites. When the NBC content was below 10 wt%, spiky NBCs appeared to be separated from one another resulting in homogeneous NBC dispersion within PVA matrices, Figures 4.13(b) and (c). Besides, the average root-mean-square (R_q) values for neat PVA and PVA/NBC bionanocomposite films were reported with the focus of 1 μm × 1 μm surface area in Figure 4.13. When the NBC content increased from 3 to 5 wt%, R_q values of PVA/NBC bionanocomposites were enhanced from 2.1±0.11 to 2.5±0.16 nm, which were very close to 1.9±0.17 nm for neat PVA. This finding suggested that smooth PVA/NBC nanocomposite film surfaces were evident at the low NBC contents as expected, which was in good accordance with the experimental result of PVA/nanocelloluse composite films [289]. On the contrary, the inclusion of 10 wt% NBCs in bionanocomposites led to a nearly two-fold *Rq* value of 4.1±0.19 nm as opposed to the counterparts with the inclusion of 3 wt% NBCs, which clearly signified that the presence of aggregated NBCs resulted in much higher surface roughness on PVA surfaces [290]. Nonetheless, this value of 4.1±0.19 nm remained relatively low when compared with

other PVA nanocomposites reinforced with carbon based fillers such as PVA/reduction graphene oxide (rGO) nanocomposites with a R_q value of 4.6±0.55 nm based on deposition layers [291].

In case of PVA/MBC bionanocomposite films, relevant results revealed that MBC particles were dispersed in a unifiorm manner when MBC content increased up to 5 wt%, as depicted in Figures 4.14(a) and (b). However, an excessive amount of MBCs caused an decrease in intra-particle spacing and MBC agglomeration would inevitably take place, as shown in Figure. 4.14 (c). Moreover, the R_q values for PVA/MBC nanocomposites at the MBC contents of 3, 5 and 10 wt% were found to be 5.47 ± 1.23, 8.36 ± 1.98 and 13.7 ± 2.12 nm, respectively, which appeared to be higher than those of pure PVA and PVA/NBC nanocomposites. Such a finding could be associated with the large size and greater thickness of MBCs when compared with that of NBCs.

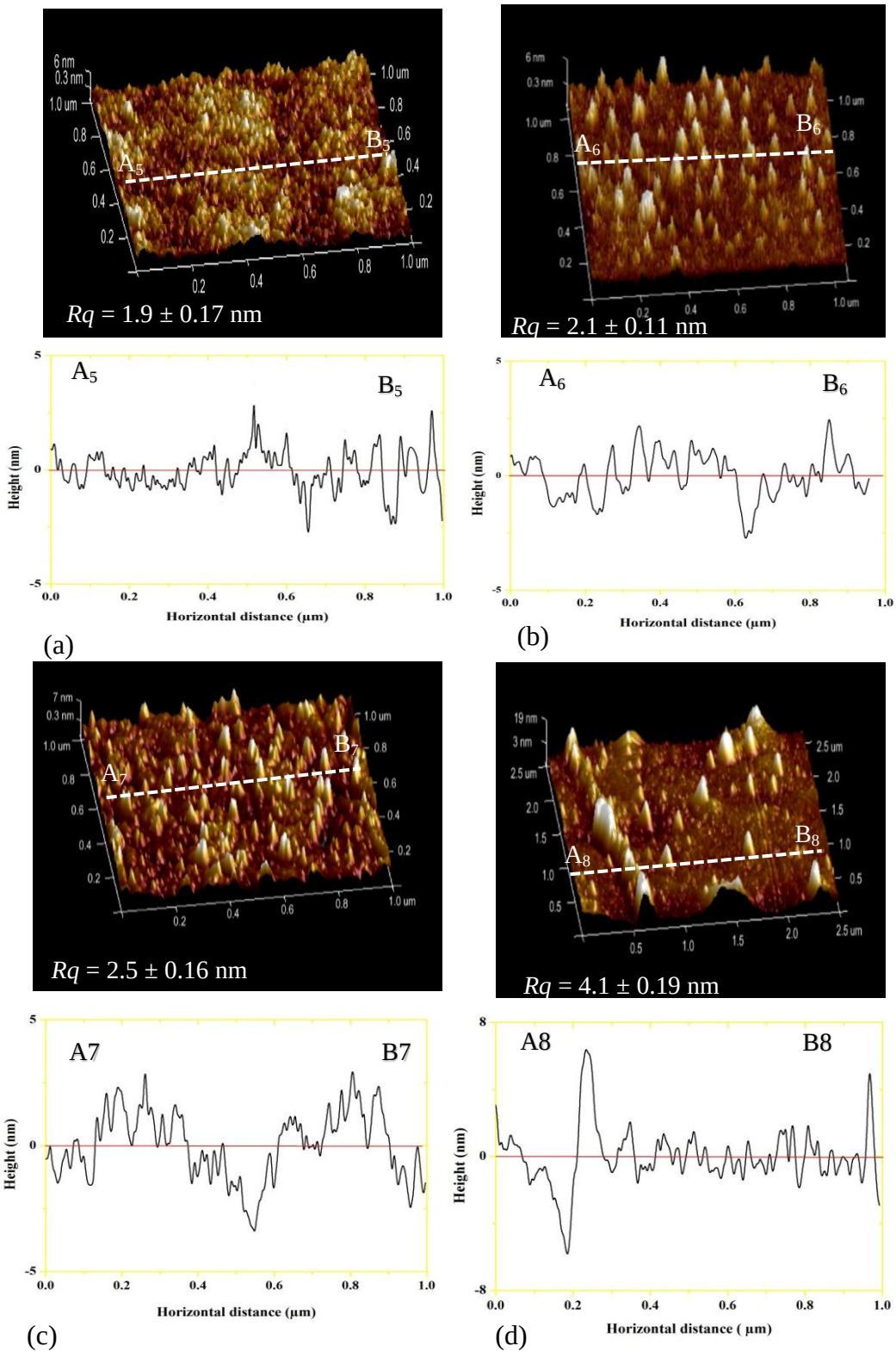

Figure 4.13 3D Height map images and corresponding height profiles for (a) PVA (b) PVA/ 3 wt% NBC nanocomposites (c) PVA/ 5 wt% NBC nanocomposites and (d) PVA/10 wt% NBC nanocomposites.

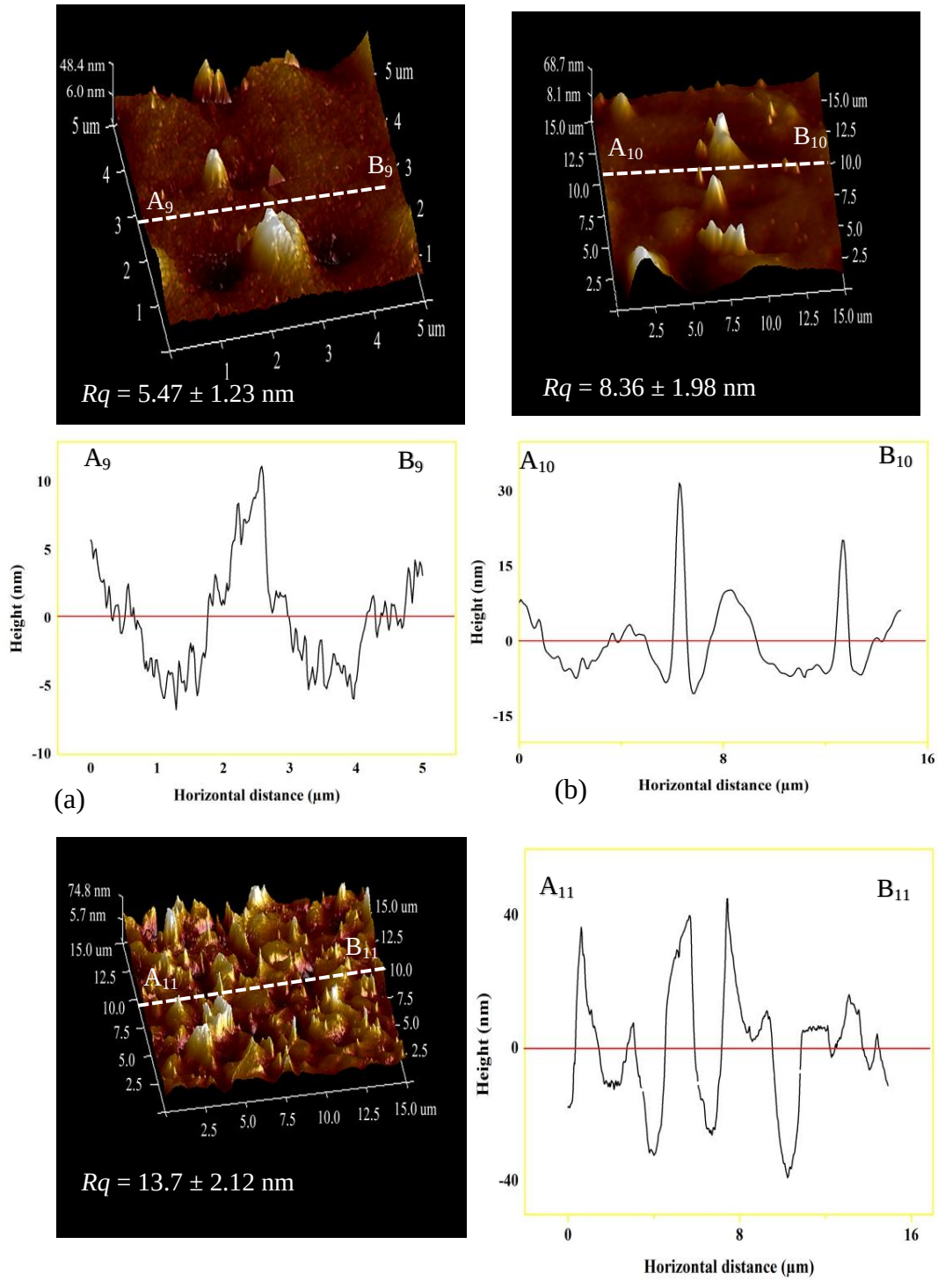

Figure 4.14 3D Height map images and corresponding height profiles for (a) PVA/ 3 wt% MBC nanocomposites; (b) PVA/ 5 wt% MBC nanocomposites and (c) PVA/10 wt% MBC nanocomposites.

4.3. Summary

This chapter covers the manufacture and material characterisation of strong and ecofriendly PVA/NBC nanocomposites and PVA/MBC nanocomposites using a simple solution casting method. Young's moduli of NBCs and MBCs were determined to be 84.5±3.6 GPa and 80.65 ±2.1GPa for the first time via a sophisticated AFM technique. More homogeneous NBC dispersion was shown for PVA/NBC nanocomposites especially at the low BC content up to 3 wt%, as opposed to PVA/MBC nanocomposites, despite a common issue of BC agglomeration at the high BC content level of 10 wt%. Tensile moduli of both nanocomposites were significantly enhanced along with the decreases in both elongation at break and tensile toughness in a monotonic manner when the BC content increased from 0 to 10 wt%. The highest strength improvement of nanocomposites appeared at 3 wt% and the incorporation of NBCs yielded a relatively high strength increasing level to the addition of MBCs, which could be ascribed to smaller particle size and larger surface areas of NBCs in order to achieve more effective load transfer from nanofillers to PVA matrices.

The addition of NBCs and MBCs within PVA matrices also revealed the enhancement of T_g values with higher thermal stability in nanocomposite films. With these determined superior mechanical and thermal properties of PVA/BC nanocomposites, it is anticipated that such fabricated materials can be utilised for more widespread applications with full biodegradability and biocompatibility. Moreover, nanomechanical properties of PVA and PVA/BC nanocomposite films were investigated by PFQNM measurement. The elastic moduli of crystalline and amorphous phases in morphological structures varied from 24±4.2 to 11.4±3.1 GPa, respectively. Moreover, the crystalline and amorphous phase widths were detected to

be 20-76 and 18-65 nm respectively. With the incorporation of BCs, the lamellae size decreased with increasing the number of lamellae stacks per unit volume, which was particularly the case with incorporation of NBCs. It was believed to be the major reason for the significant improvement of mechanical properties of PVA/NBC nanocomposites.

Chapter 5.

PVA Based Nanocomposite Films with Different Particle Shapes and Structures

5.1. Introduction

The effective reinforcing mechanism is based on the fundamental concept that the chain mobility of polymeric molecules is restricted by rigid nanofillers according to matrix-particle interfacial interactions in polymer nanocomposites [2, 8]. The specific areas associated with matrix-filler interactions are known as interfacial regions with distinct properties from those of nanoparticles and polymer matrices. More importantly, the material performance of polymer nanocomposites primarily depends on the volume of interfacial regions and interfacial properties [8] in relation to critical nanofiller factors such as nanoparticle shapes and structures. In addition to the concern on nanoparticle structures, nanoparticle shapes are also equally important when matrix-filler interactions are considered in polymer nanocomposites, which can be classified into three popular shapes, namely 1D platelet-like nanoparticles such as montmorillonite (MMT) clays and nanoplatelet graphene sheets, 2D tubular nanoparticles like HNTs and carbon nanotubes (CNTs), as well as 3D spherical nanoparticles including NBCs, diamond nanoparticles, nanosilica particles, etc. In a nanocomposite system, the alteration of nanoparticle shape means the contact areas inevitably vary between polymer matrices and nanoparticles to effectively control the volume of their interfacial [8]. Most previous studies [9, 10] were based on theoretical or numerical modelling approaches like atomistic and coarse-grained molecular dynamic simulations for evaluating matrix-filler bonding effect. Nonetheless, current computational capability and environment may be mostly restricted to the context of single and two-particle systems by neglecting the effect of actual nanoparticle structures and shapes induced in different material processing techniques [11]. The selection of PVA as based polymer arises from its biodegradability and water solubility to replace conventional petroleum-based

polymers for less marine plastic pollution [12]. Three nanocomposite systems were investigated in this chapter including PVA/HNT nanocomposites, PVA/Cloisite 30B clay nanocomposites and PVA/NBC nanocomposites to assess the influence of different dimensional nanoparticle shapes, structures and contents on the effective reinforcement mechanism.

5.2. FTIR Analysis

FTIR results of PVA, HNTs, Cloisite 30B clays and corresponding PVA nanocomposite films are shown in Figure 5.1. The spectrum of raw HNT powders, as shown in Figure 5.1(a), exhibits two Al_2OH stretching bands at 3691.5 and 3621 cm^{-1} [234], resulting from OH bending to connect two Al atoms, along with other band feature of inorganic aluminosilicate structures of halloysite [234]. Additionally, The peaks at 1004 cm^{-1} was assigned to Si-O-Si stretching while the identified FTIR peak at 906 cm^{-1} was derived from Al-OH stretching [86]. With the inclusion of HNTs, the O-H stretching associated with PVA with the peak located at 3271.5 cm^{-1} shifted to higher wave numbers at 3280 and 3289 cm^{-1} with the addition of 3 and 5 wt% HNTs, respectively. This finding indicates that HNTs interacted with PVA molecular chains, and the hydrogen bonding between PVA chains was partially damaged. Such a similar tendency was also detected when HNTs were incorporated into PVA/ chitosan (CS) composites [292] and PVA/cellulose nanocrystal (CNC) composites [234]. However, with increasing the HNT content up to 10 wt%, two Al_2OH stretching corresponding to HNTs appeared separately within nanocomposite films, which could be ascribed to the HNT agglomeration [86].

On the other hand, the result of as-received Cloisite 30B clays, as showed in Figure 5.1(b), revealed the existing band at 3629.6 cm^{-1} corresponding to Si–OH and Al–

OH stretching. The broad band at 3405 cm^{-1} is attributed to OH groups in relation to interlayer water. Additionally, the bands at 2924.6 and 2853.5 cm^{-1} are associated with $–CH_2$ asymmetric and symmetric stretching [153, 293]. The characteristic peaks at 1647 and 1123.3 cm^{-1} are related to the deformation vibration of interlayer water as well as Si-O bending, respectively. Furthermore, the assigned band at 1470 cm^{-1} arises from the $–CH_2$ bending [293]. With the inclusion of 3 and 5 wt% Cloisite 30B clays, the hydroxyl peak of PVA shifted from 3271.5 to 3279 and 3283 cm^{-1}, respectively. Such a finding results from the strengthening of hydrogen bonds between –OH groups of PVA and –SiOH groups on the surfaces of Cloisite 30B clays, which is in good agreement with previous studies of PVA/OMMT nanocomposites [153] and PCL/Cloisite 30B nanocomposites [294].

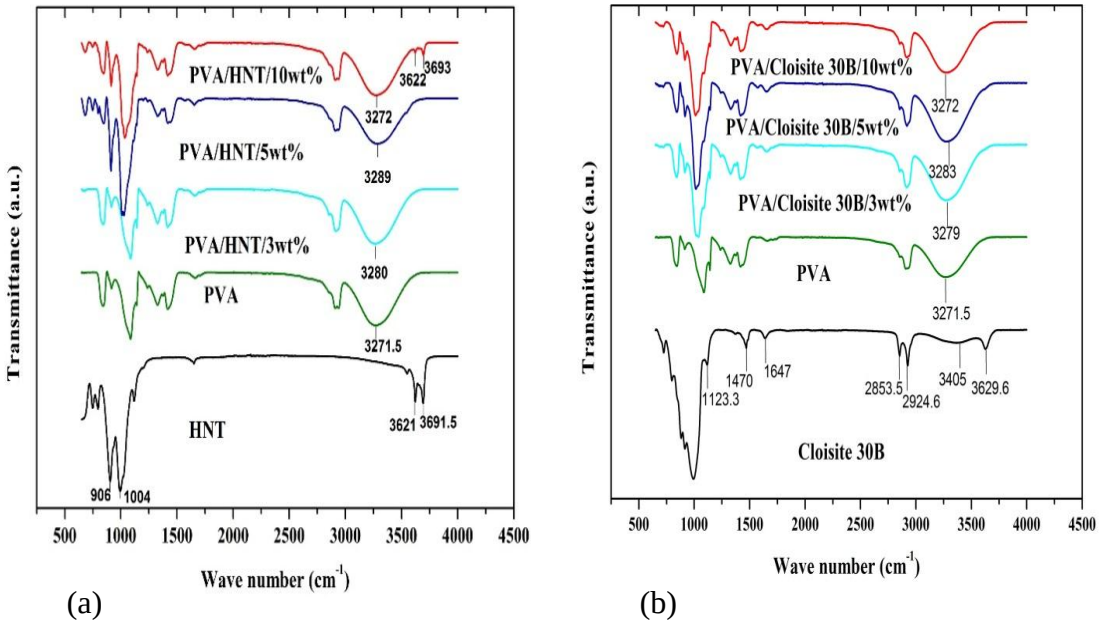

Figure 5.1 FTIR spectra for chemical interactions: (a) PVA/HNT nanocomposite films and (b) PVA/Cloisite 30B clay nanocomposites.

The aforementioned results failed to show the existence of new bands in PVA films after the inclusion of both HNTs and Cloisite 30B clays. On the contrary, the

inclusion of 3 and 5 wt% NBCs within PVA matrices in nanocomposite films gives rise to a new band associated with –CH2– asymmetric and symmetric stretching, as illustrated in Figure 4.5(b). Such a finding could be related to typical porous structures of NBCs, which makes them distinct from nanofillers in that these pores enable to absorb molecular chains of hydrophilic polymers such as PVA with the combination of mechanical and chemical bondings. However, it is clearly shown from above-mentioned results that the inclusion of HNTs and Cloisite 30B clays within PVA matrices could shift the hydroxyl peak of PVA to higher wave numbers. On the contrary, the addition of NBCs within PVA matrices appeared to shift the hydroxyl peak of PVA to lower wave numbers instead, as shown in Figure 4.5(a). These results thus apparently indicate that the numbers of hydrogen bonding formed in PVA/ HNT nanocomposites and PVA/Cloisite 30B clay nanocomposites are higher than those detected in PVA/ NBC nanocomposites, which could be ascribed to different chemical structures of nanofillers. As seen from Figure 4.4(a), since NBCs do not possess –OH peaks, most hydrogen bonding formed in nanocomposites can stem from hydroxyl groups of PVA matrices. Whereas, the existence of additional –OH peaks detected in HNTs and Cloisite 30B clays in PVA nanocomposites can further facilitate generating a higher level of hydrogen bonding within PVA matrices.

5.3. XRD Analysis

XRD is one of most useful material characterisation techniques to evaluate the *d*-spacing between clay interlayers. By monitoring the position and intensity of basal reflections from distributed silicate layers, nanocomposite structures (i.e. intercalated or exfoliated) as well as clay aggregated structures can be identified [159]. XRD patterns of HNTs, Cloisite 30B clays, and corresponding nanocomposites are presented in Figure 5.2, along with the summary of *d*-spacing values listed in Table

5.1. HNT patterns possess three major peaks of (001), ((020)/(110) and (002) located at 2θ=11.9°, 20° and 24.9°, which correspond to *d*-spacing values of 0.74, 0.44 and 0.37 nm, respectively. According to Swapna et al. [213], the relevant peak taking place at 2θ=24.9° is attributed to the presence of silica in form of cristobalite and quartz.

After the incorporation of HNTs into PVA matrices in nanocomposite systems, XRD characteristic peak at 2θ=11.9° appears to be very weak at the low HNT loading of 3 wt%. Similar XRD peaks were detected at 2θ=12.5° and 12.6° with a slight shift at relatively high HNT loadings of 5 and 10 wt%, respectively. Overall, with decreasing the HNT loading, the inclusion of HNTs significantly reduces the intensity of XRD peaks for all PVA/HNT nanocomposites, which could be attributed to uniform HNT dispersion at the low HNT loading as well as relatively high particle agglomeration at high content levels. A similar phenomenon was also reported for PVA/HNT nanocomposites by Swapna et al. [213], which suggested that the disappearance or intensity reduction of XRD peaks at low HNT loadings could arise from uniform HNT dispersion and possible HNT intercalation within PVA matrices. On the other hand, the reappearance of XRD peaks at higher HNT loadings may be indicative of possible HNT agglomeration.

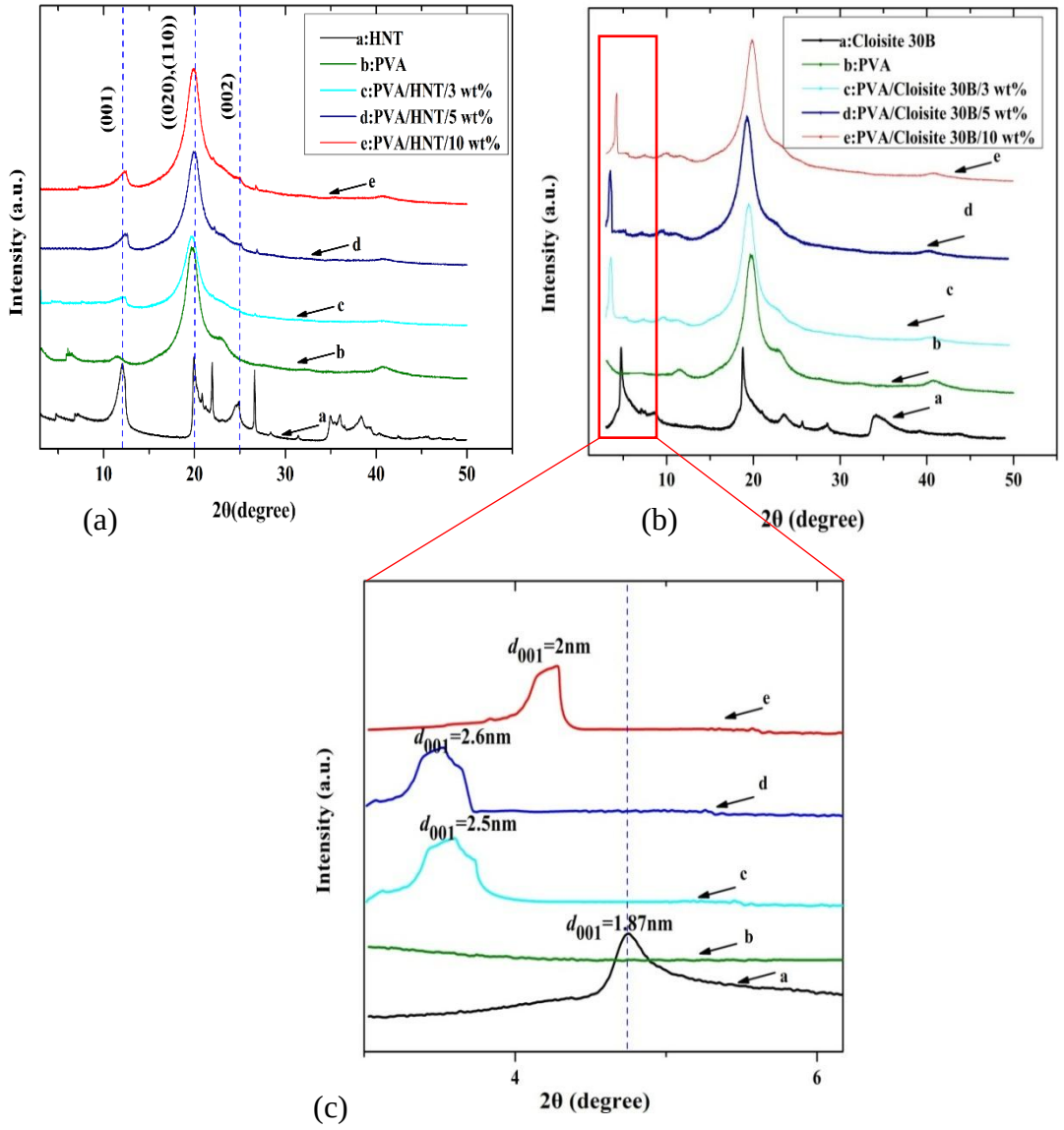

Figure 5.2 Schematic diagrams of XRD patterns: (a) PVA/HNT nanocomposites, (b) and (c) PVA/Cloisite 30B clay nanocomposites with both wide and small diffraction angles, respectively.

Table 5.1 *d*-spacing of as-received HNTs and Cloisite 30B clays and corresponding PVA based nanocomposites.

Sample	2θ (degree)	d_{001} (nm)	2θ (degree)	$d_{020/110}$ (nm)	2θ (degree)	d_{002} (nm)
As- received HNTs	11.9	0.74	20	0.44	24	0.37
PVA	–	–	19.7	0.45	–	–
PVA/HNT/3 wt.%	–	–	19.7	0.45	–	–
PVA/HNT/5 wt.%	12.5	0.71	19.9	0.44	–	–
PVA/HNT/10 wt.%	12.6	0.7	19.8	0.45	–	–
As- received Cloisite30B	4.72	1.87	18.7	0.46	23.5	0.38
PVA/ Cloisite30B /3 wt.%	3.6	2.5	19.3	0.45	–	–
PVA/ Cloisite30B /5 wt.%	3.4	2.6	19.1	0.47	–	–
PVA/ Cloisite30B /10 wt.%	4.3	2	19.8	0.44	–	

The XRD patterns of Cloisite 30B clays reveal the diffraction peak at $2\theta = 4.72°$ corresponding to the *d*-spacing value of 1.87 nm. The (001) diffraction peak shifted to lower angles, as evidenced by d_{001} values of 2.5, 2.6 and 2 nm for PVA/Cloisite 30B clay nanocomposites at the clay contents of 3, 5 and 10 wt%, respectively, which clearly arises from the insertion of polymeric chains inside clay interlayers to induce clay intercalation. In a similar manner, Mallakpour et al. [153] reported that the *d*-spacing value of modified Na^+ MMT increased from 1.17 nm for pristine organoclays to 1.86 nm in PVA nanocomposites. Furthermore, Rhim et al. [51] observed that the interlayer distance of Cloisite 30B and Cloisite 20A clays increased from 1.86 and 2.41 nm to 3.14 and 3.23 nm for corresponding PLA/ Cloisite 30B

clay nanocomposites and PLA/ Cloisite 20A clay nanocomposites, respectively. The XRD peak for PVA alone appears at $2\theta = 19.7°$, which is associated with total (101) crystalline atactic formation of PVA molecular chains [156] to slightly shift to lower diffraction angles, as depicted in Table 5.1 with increasing the Cloisite 30B clay content in PVA nanocomposites. The occurrence of PVA molecular chains at (101) crystalline plane suggests that PVA evolves towards more constrained crystalline structures. A similar behaviour has also been reported by Strawhecker and Manias [156] as well as Gaume et al. [295] in PVA/clay nanocomposites, which is ascribed to strong chemical interactions between nanofillers and polymer matrices.

These results indicate that Cloisite 30B clays were successfully intercalated and/or exfoliated by PVA molecular chains and HNTs at their low contents were homogeneously dispersed within continuous PVA matrices. This finding can be attributed to the strong interaction between PVA matrices and clay nanoparticles due to strong hydrogen bonding between carboxyl groups of PVA matrices and hydroxyl groups in the interlayer gallery of Cloisite 30B clays or at the surface edges of HNTs [296].

In contrast, the XRD patterns of PVA/NBC nanocomposites only showed the PVA diffraction angles, as depicted in Figure 4.6(a). Liang et al [269] demonstrated a similar phenomenon in PVA/5 w% GO nanocomposites, which was ascribed to the disappearance of diffraction peaks from PVA to exfoliated GOs with individual graphene sheets embedded within PVA matrices while regular and periodic structures of graphene disappeared. In PVA/NBC nanocomposites, such a finding could indicate that as mention earlier PVA molecular chains could fill and cover NBC porous structures so that NBC structures tended to be more randomly-oriented.

5.4. Morphological and Nanomechanical Properties

Morphological structures of as-received HNTs and Cloisite 30B clays are illustrated in Figures 5.3 and 5.4, respectively. It is clearly seen from Figure 5.3 (a) that as-received HNT powders show high irregularity in size and morphology. Moreover, Figure 5.3 (b) presents some details of HNT surface morphology, revealed by the combination of TEM and AFM observations. As can be seen, HNT particles have cylindrical shapes and contain a transparent central area that runs longitudinally along the cylindrical structures, indicating that nanotubular particles are in hollow and open-ended shape. It is clearly indicated that HNTs possess outer diameters in range of 20–115 nm and the lumen diameter of 5–30 nm. The lengths of HNTs are quite different in range of 50–1500 nm. On the other hand, morphological structures of Cloisite 30B clays observed by an AFM tapping mode from diluted Cloisite 30B clay suspension deposited onto mica are presented in Figure 5.4. It is clearly seen from the AFM image of Cloisite 30B clays that most clay structures are in non-regular and platelet-like shapes with the average particle length of 100.75±6.5 nm according to the measurements of 925 particles. Moreover, Cloisite 30B clays have a great variation in particle thickness ranging from 1.69-5.9 nm, as shown in typical cross-sectional analysis of a selected area (A_{15}-B_{15}) in Figure 5.4(c). Such a finding indicates that the majority of as-received Cloisite 30B clays demonstrate typical stacks of platelet-like layer structures as the thickness of single platelet was detected to be approximately 1 nm [297].

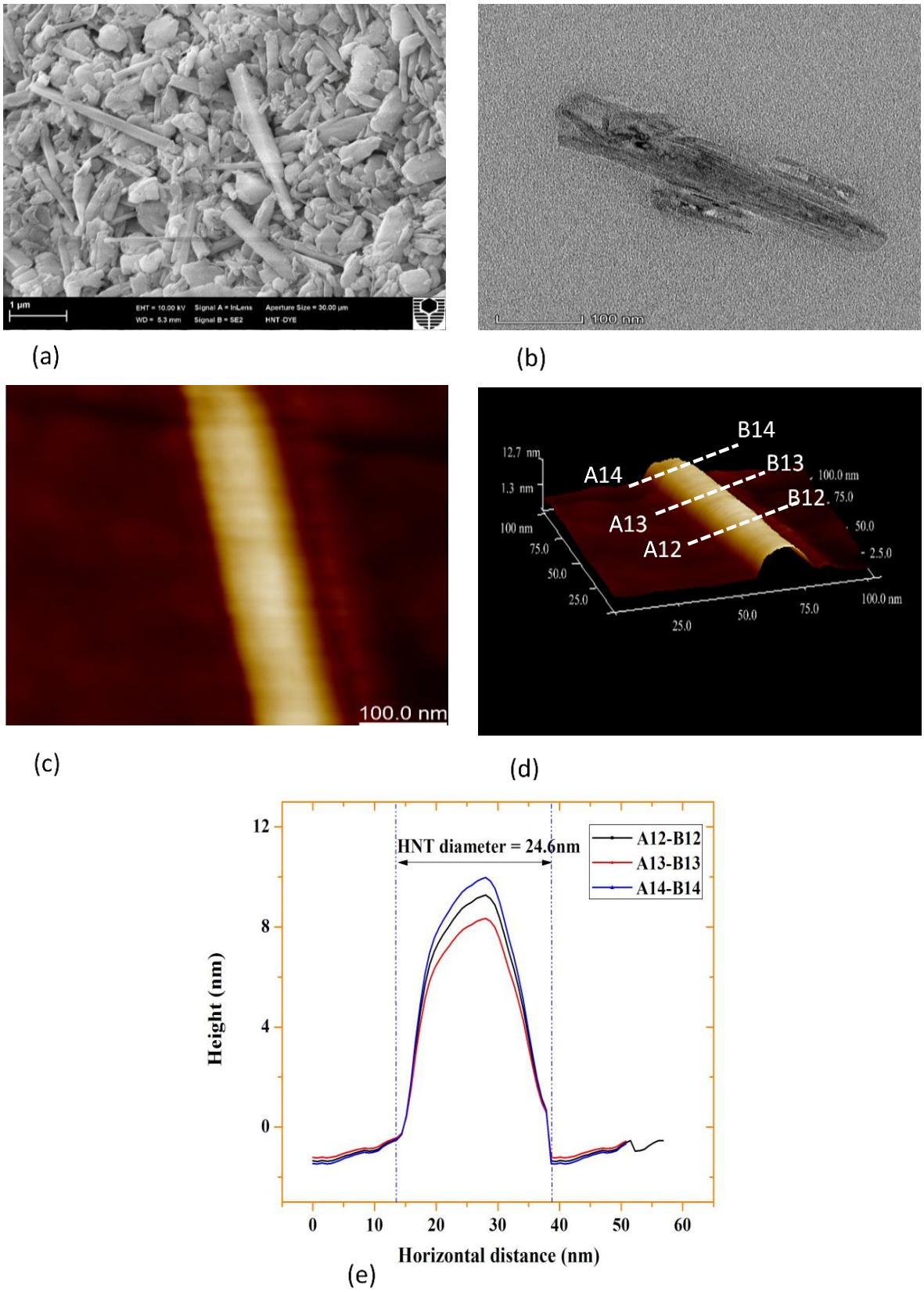

Figure 5.3 Characterisation of HNT particles: (a) SEM image, (b) TEM image, (c) 2D height image, (d) 3D height image and (e) corresponding height section profiles of HNTs.

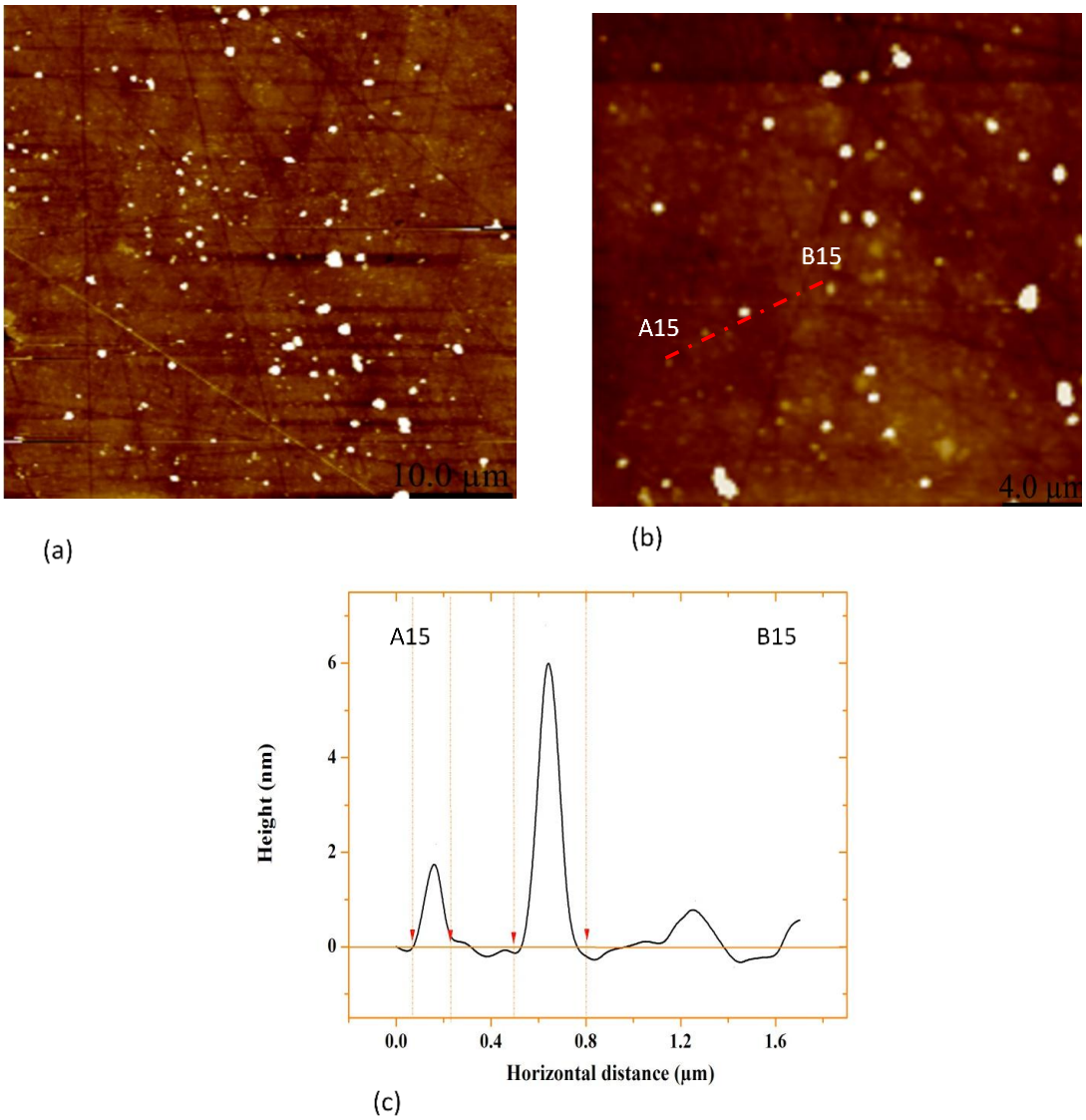

Figure 5.4 Characterisation of Cloisite 30B clays: (a)-(b) AFM images at different magnifications deposited on mica substrates in aqueous solutions and (c) height profile of Cloisite 30B clays.

After the inclusion of both HNTs and Cloisite 30B clays within PVA matrices, clay dispersion plays a key role in determining the material performance of final nanocomposite films. To evaluate the nanofiller distribution within polymer matrices, Figures 5.5 and 5.6 show 3D topographic images and corresponding height profiles for PVA/HNT nanocomposites and PVA/Cloisite 30B nanocomposites, respectively, at different nanoclay loadings of 3, 5 and 10 wt%. In case of PVA/HNT nanocomposites, it can be observed at the HNT loading of 3 wt%, HNT particles are

separated from one another with better particle dispersion while beyond 3 wt%, HNTs appear to be dispersed in a non-uniform manner with typical clay agglomerated and clustering formation. This is because an excessive amount of HNTs results in an decrease in intra-particle spacing and HNTs possess very strong intra-molecular bonding leading to possible particle agglomeration [298]. The roughness value of PVA nanocomposite films reinforced with 3 wt% HNTs is 2.4 ± 0.13 nm, which is higher than that of neat PVA at 1.9 ± 0.17 nm. Such a finding still indicates that surface films remain smooth with the incorporation of HNTs and further confirms HNT uniform dispersion at low nanofiller loadings. Additionally, it is in good accordance with results of PVA/HNT nanocomposite hydrogels reported by Azmi et al [299]. At the low HNT loading of 2 wt%, the smooth surfaces of PVA/HNT nanocomposites are attributed to the combination of good interaction and compatibility between HNTs and PVA molecular chains. Nonetheless, increasing the HNT content up to 5 and 10 wt% leads to roughness improvements at 4.54 ± 0.18 and 13.1 ± 0.23 nm, respectively, which is believed to be caused by the typical presence of HNT aggregates [300]. In case of PVA/Cloisite 30B clay nanocomposites, at a low clay content of 3 wt%, Cloisite 30B clays appear to be separated from one another and dispersed in a homogeneous manner within PVA matrices in nanocomposites, Figures 5.6(a) and (b). More evidently, the average root-mean-square (R_q) value for PVA with the addition of 3 wt% Cloisite 30B clays in nanocomposites is 2.04 ± 0.12 nm, which is close to 1.9±0.17 nm for PVA. Such a finding confirms the smooth surfaces of nanocomposites with a clearer sign of uniform clay dispersion within PVA matrices. When the content of Cloisite 30B clays increases to 5 wt%, R_q values of PVA also increases up to 2.84 ± 0.18 nm, which becomes slightly higher than that of neat PVA. This finding suggests that

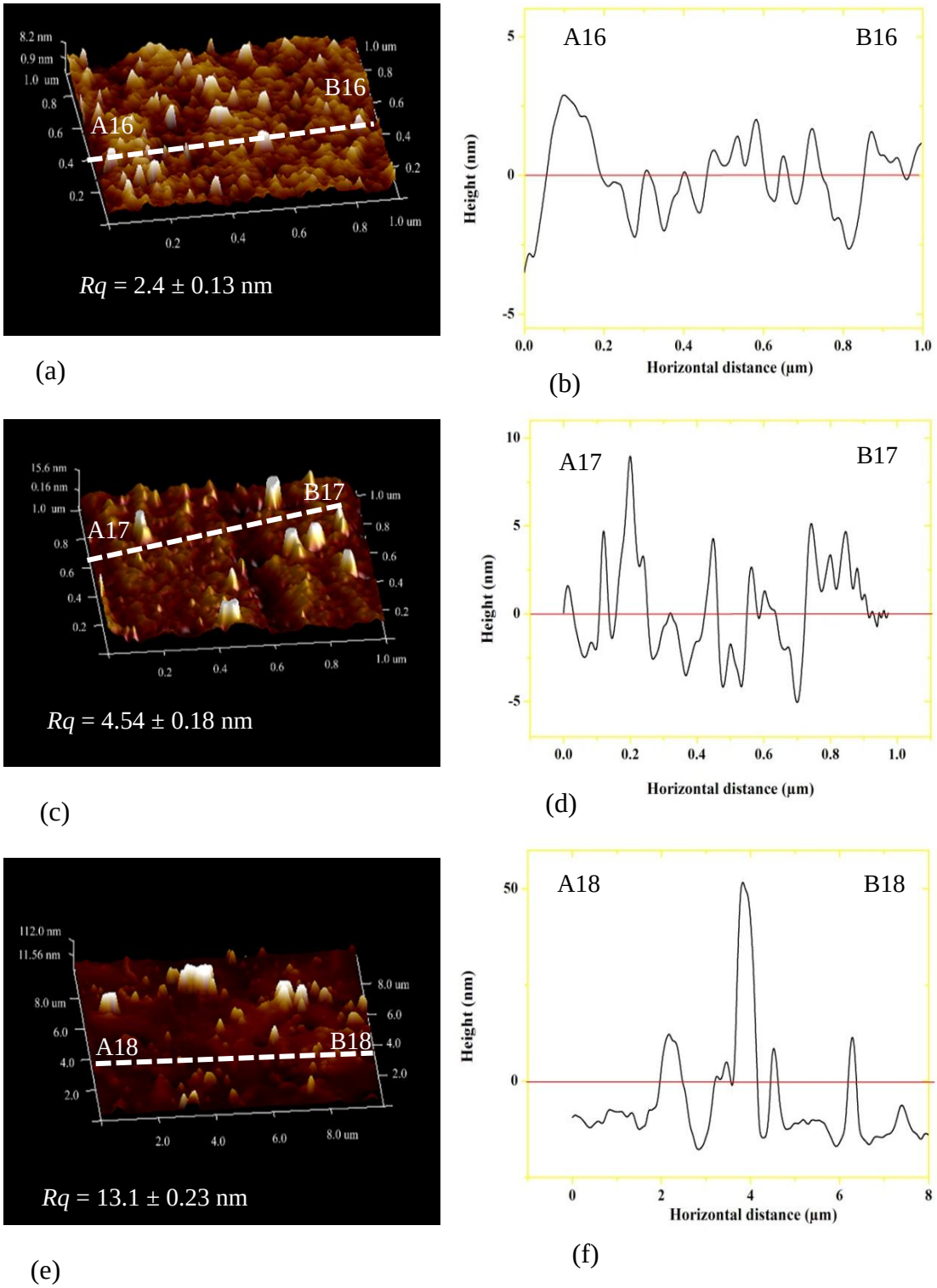

Figure 5.5 3D height map image and corresponding height profiles: (a)-(b) PVA/ 3 wt% HNT nanocomposites, (c)-(d) PVA/ 5 wt% HNT nanocomposites and (e)-(f) PVA/ 10 wt% HNT nanocomposites.

This finding suggests that Cloisite 30B clay content of 5 wt% represents a threshold for achieving uniform dispersion of nanofillers within polymer matrices. On the contrary, the inclusion of 10 wt% Cloisite 30B clays in PVA nanocomposites leads to an increasing *Rq* value up to 6.05 ± 0.23 nm, which is far higher than that of neat PVA with an increase of 218%. This result clearly signifies that the presence of aggregated Cloisite 30B clays results in much higher surface roughness on PVA surfaces. Gaume et al [295] reported that the roughness of PVA increased by ~ 400% with the incorpartion of 10 wt% Na^+ MMTs. In addition, Ataeefard and Moradian [301] has demonstrated similar effect for polypropylene/ Cloisite15A clay nanocomposites. Yeh et al [302] found that the average plane roughness of PVA membrances was increased from 2.175 to 14.703 nm at the Na^+ MMT loading of 10 wt%. The increase in surface roughness with increasing the clay content can be attributed to the presence of typical clay aggregation [301]. It is well known that when nanoclays are uniformly dispersed within polymer matrices, the formation of exfoliated and intercalated structures leads to the improvement of mechanical properties of nanocomposites to different extent. On the contrary, when nanoclays are agglomerated, it generally gives rise to the deterioration of mechanical properties of nanocomposites [25]. To investigate the degree of clay exfoliated structures in details, the height profiles of clay platelets relative to that of PVA matrices have been determined, as shown in Figure 5.7. The thickness of 3 wt% Cloisite 30B clays embedded within PVA matrices in nanocomposites appears to be in range of 0.85-1.43 nm. Such a finding suggests that exfoliated clay structures are most likely to take place within PVA matrices. It has been reported in previous study [297] that MMT clays are considered to be exfoliated when their thickness is close to that of

individual clay platelet (i.e. ~ 1nm). Gaume et al [295] and co-workers [303, 304] also detected intercalated and exfoliated structures of MMT clays in the thickness

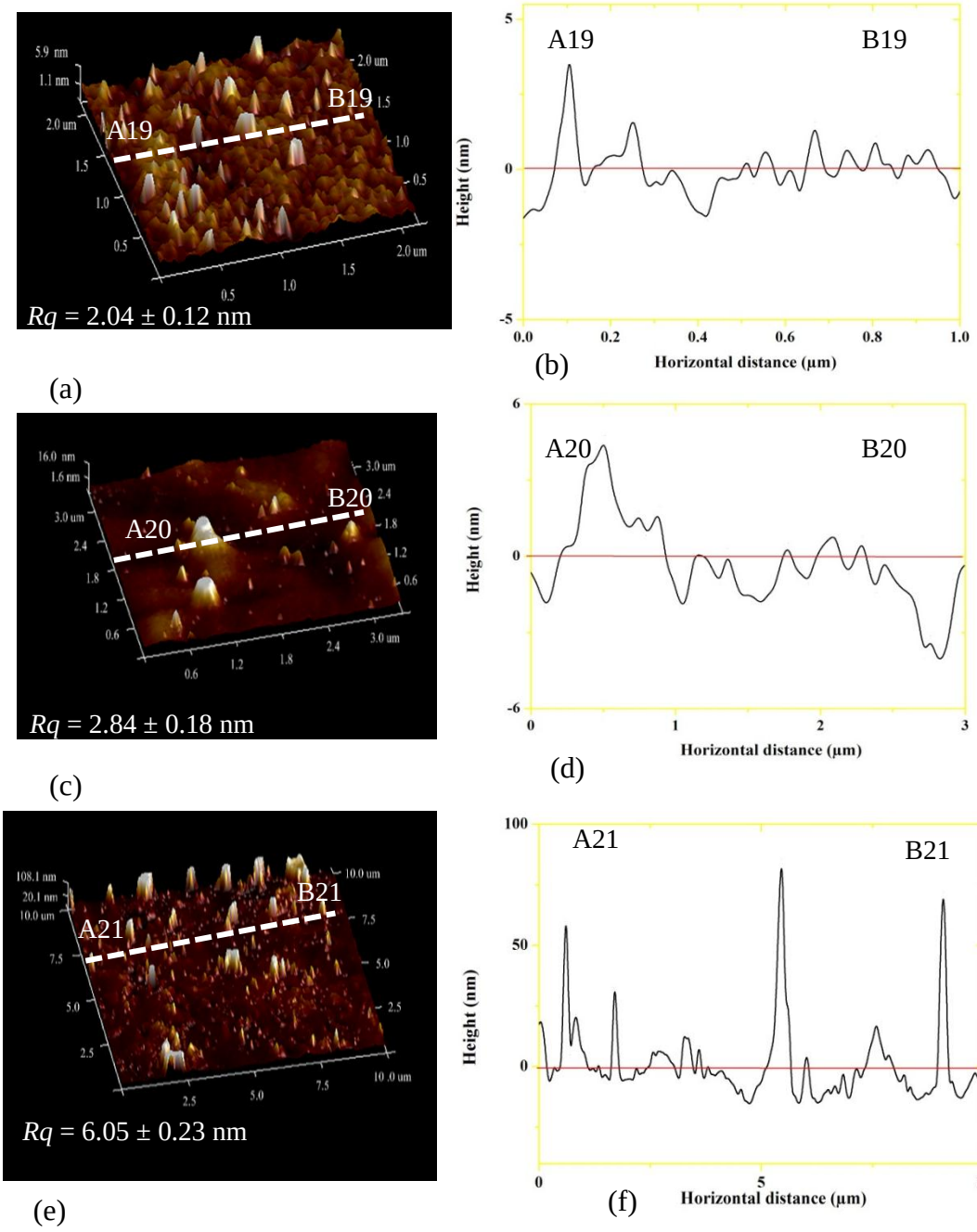

Figure 5.6 3D height mapping images and corresponding height profiles for (a)-(b) PVA/ 3 wt% Cloisite 30B clay nanocomposites, (c)-(d) PVA/ 5 wt% Cloisite 30B clay nanocomposites and (e)-(f) PVA/10 wt% Cloisite 30B clay nanocomposites.

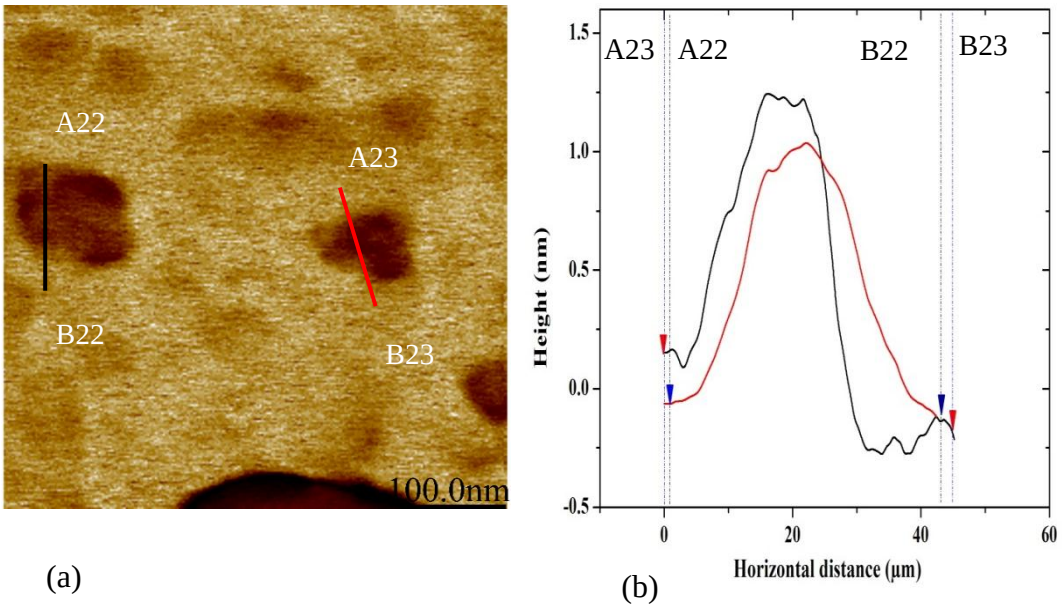

Figure 5.7 Characterisation of PVA/ 3wt% Cloisite 30B clay nanocomposites. (a) height profile and (b) corresponding profiles for the lines A22-B22 and A23-B23.

range of 1.3-5 nm. Notwithstanding that the same manufacturing process condition and nanofiller loadings have been utilised for preparing PVA nanocomposite films, different nanofiller types play an important role in the variation of the roughness level. When incorporated with 5 wt% NBCs, the roughness of PVA nanocomposites increased by 31.58%, which was found to be enhanced at even higher levels of 138.9% and 49.47% at the same loading of HNTs and Cloisite 30B clays. More impressively, the inclusion of 10 wt% NBCs, HNTs and Cloisite 30B clays led to the roughness improvements by 115.78%, 589.47% and 218.42%, respectively. Such a phenomenon suggests that NBCs may have better ability to be dispersed uniformly in PVA matrices as opposed to HNTs and Cloisite 30B clays due to their least increasing roughness level. Surface roughness can be associated with nanofiller shapes and sizes since HNTs and Cloisite 30B clays possess relatively high aspect ratios when compared with that of NBCs with existing ‘nanofiller waviness’ issue. High-aspect-ratio HNTs and Cloisite 30B clays are inevitably subjected to

considerable wavy nanofiller formation, thus undermining their homogeneous dispersion within polymer matrices. In addition, nanofiller dispersion techniques used such as ultrasonication may also potentially damage nanofiller structures if high power intensity or longer sonication time is used [305]. Aspect ratio of nanofillers is regarded as one of key factors in the reinforcement efficiency and mechanical performance of nanocomposites, which is generally defined as the ratio between the largest dimensions over the smallest dimension of nanofillers. According to this fundamental concept, the largest dimension of nanofillers can be represented by lengths of tubular HNTs and platelet-like Cloisite 30B clays or the diameters of NBCs while the smallest dimension denotes the diameter of HNTs or thickness of Cloisite 30B clays and NBCs. Hence, specific dimensions of nanofillers required to calculate their aspect ratios were determined in Table 5.2 for NBCs, HNTs and Cloisite 30B clays, as exemplified in Figures 5.8-5.10, respectively. It is evident that aspect ratios of nanofillers increase from 5.75 to 8.17 for NBCs and 5.9 to 10.5 for HNTs with increasing the nanofiller loading from 3 to 10 wt%. In contrast, aspect ratios of Cloisite 30B clays decrease from 22.7, 12.3 to 13.4 at the clay loadings of 3, 5 and 10 wt%, respectively despite their overall highest aspect ratios among all nanofillers. Such findings implied that the majority of Cloisite 30B clays tended to form exfoliated or intercalated structures with relatively high aspect ratios. However, the decrease in aspect ratios of Cloisite 30B clays could be associated with more severe clay aggregation. It is very convincing that aspect ratios of nanofillers can be greatly influenced by nanofiller shapes and apparently, 3D NBC nanoparticles have lower aspect ratios when compared with 1D platelet-like Cloisite 30B clays [305].

In summary, aspect ratio may play a significant role in mechanical properties of nanocomposites when nanoparticle shapes or structures are only considered within

polymer matrices. However, for different types of nanofillers, several other factors like the number of particles per unit volume, interphase modulus, interphase volume and surface area, as well as ratio of interphase volume per nanoparticle volume should also be taken into account for the material properties, which will be explicitly discussed in the forthcoming Chapter 6.

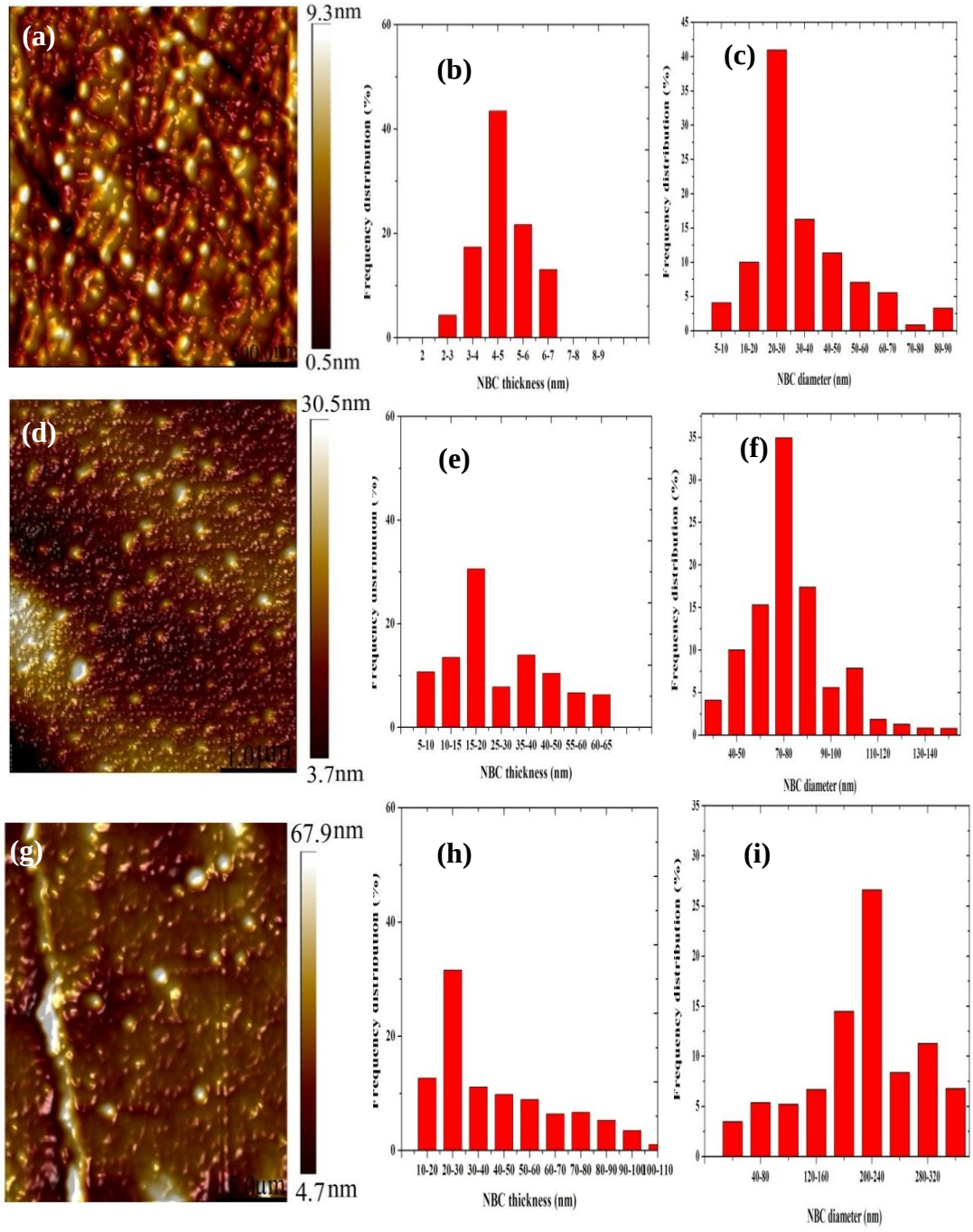

Figure 5.8 AFM imaging characterisation of PVA/NBC nanocomposites: (a)-(c) denote the height mapping image, frequency distributions of NBC thickness and diameter at the NBC loading of 3 wt%, (d)-(f) represent the height mapping image, frequency distributions of NBC thickness and diameter at the NBC loading of 5 wt%, and (g)-(i) display the height mapping image, frequency distribution of NBC thickness and diameter at the NBC loading of 10 wt%.

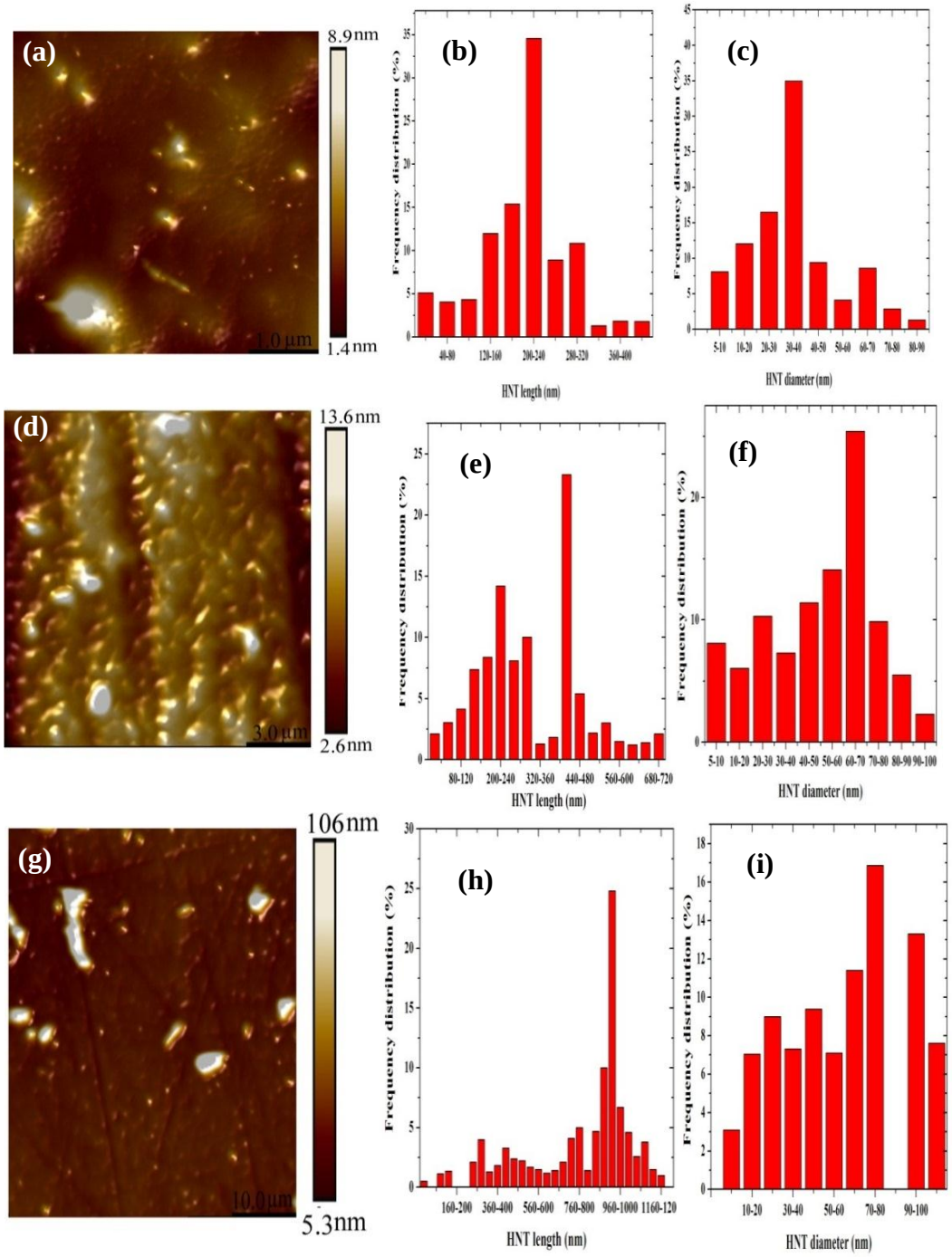

Figure 5.9 AFM imaging characterisation of PVA/HNT nanocomposites: (a)-(c) denote the height mapping image, frequency distributions of HNT length and diameter at the HNT loading of 3 wt%, (d)-(f) represent the height mapping image, frequency distributions of HNT length and diameter at the HNT loading of 5 wt%, and (g)-(i) display the height mapping image, frequency distribution of HNT length and diameter at the HNT loading of 10 wt%

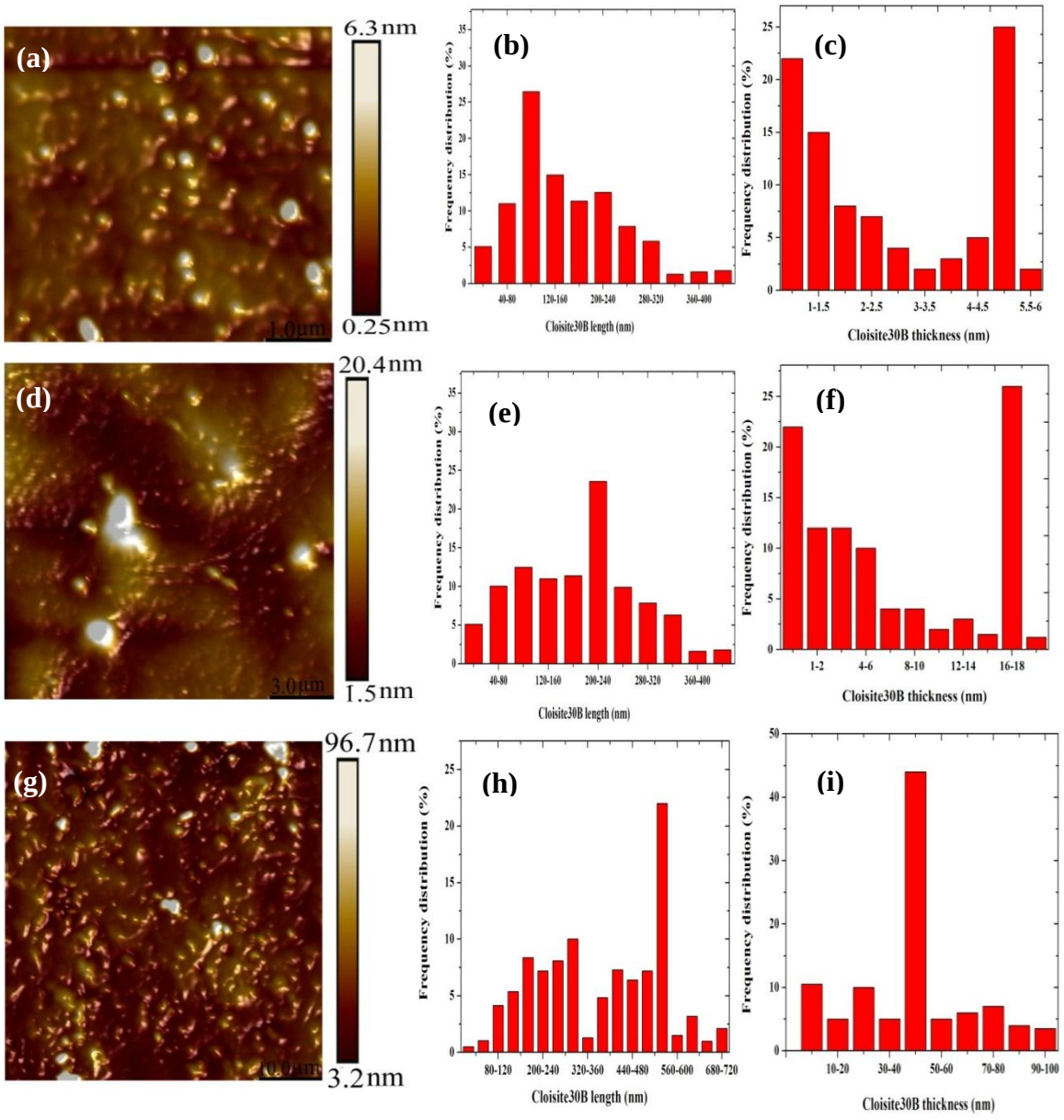

Figure 5.10 AFM imaging characterisation of PVA/Cloisite 30B clay nanocomposites: (a)-(c) denote the height mapping image, frequency distributions of Cloisite 30B clay length and thickness at the clay loading of 3 wt%, (d)-(f) represent the height mapping image, frequency distributions of Cloisite 30B clay length and thickness at the clay loading of 5 wt%, and (g)-(i) display the height mapping image, frequency distributions of Cloisite 30B clay length and thickness at the clay loading of 10 wt%.

Table 5.2 Dimensional parameters of different nanofillers used in this study

Nanofiller content (wt%)	Nanofiller type	Length(L) (nm)	Thickness (t) (nm)	Diameter (D) (nm)	Aspect ratio (L/t) or (D/t)
3	NBCs	-	4.8± 0.52	27.6± 3.32	5.75
5	NBCs	-	11.2± 2.62	78.4±4.25	7
10	NBCs	-	28.4± 4.6	232±7.31	8.17
3	HNTs	208±8.8	-	35.2±3.9	5.9
5	HNTs	410±10.3	-	66.5±4.2	6.16
10	HNTs	900.6±18.7	-	85±5.8	10.5
3	Cloisite 30B clays	109±7.9	4.8±0.25	-	22.7
5	Cloisite 30B clays	208±11.3	16.8±1.2	-	12.3
10	Cloisite 30B clays	560±20.5	41.6±6.3	-	13.4

5.5. Mechanical Properties

Figure 5.11 and Table 5.3 display mechanical properties of PVA nanocomposites reinforced with HNTs and Cloisite 30B clays in terms of nanofiller contents. The addition of only 3 wt% HNTs and Cloisite 30B clays yields the increases in tensile modulus by 40 and 52% as opposed to that of near PVA at 2.08 GPa, which is in good accordance with previous results obtained in PVA/starch/ glycerol/HNT nanocomposites [306] and PVA /chitosan/HNT nanocomposites [15]. Moreover, tensile moduli of nanocomposites increase significantly in a monotonic manner with

increasing the clay content. More remarkably, the maximum increase in tensile modulus is achieved by 61.5% and 84.1% at the clay content of 10 wt% for both HNTs and Cloisite 30B clays, respectively when compared with that of neat PVA. This phenomenon usually takes place for most filled polymers with more rigid inorganic nanoparticles as reinforcements leading to much stiffer nanocomposite materials [16]. In particular, Cloisite 30B clays as nanofillers induces more filler reinforcement efficiency when compared to HNTs, as clearly seen from the overall relatively high tensile moduli of PVA/Cloisite 30B clay nanocomposites, which can arise from much closer interaction between PVA matrices and silicate layers via the formation of hydrogen bonds owing to the strong hydrophilicity of Cloisite 30B clays [12].

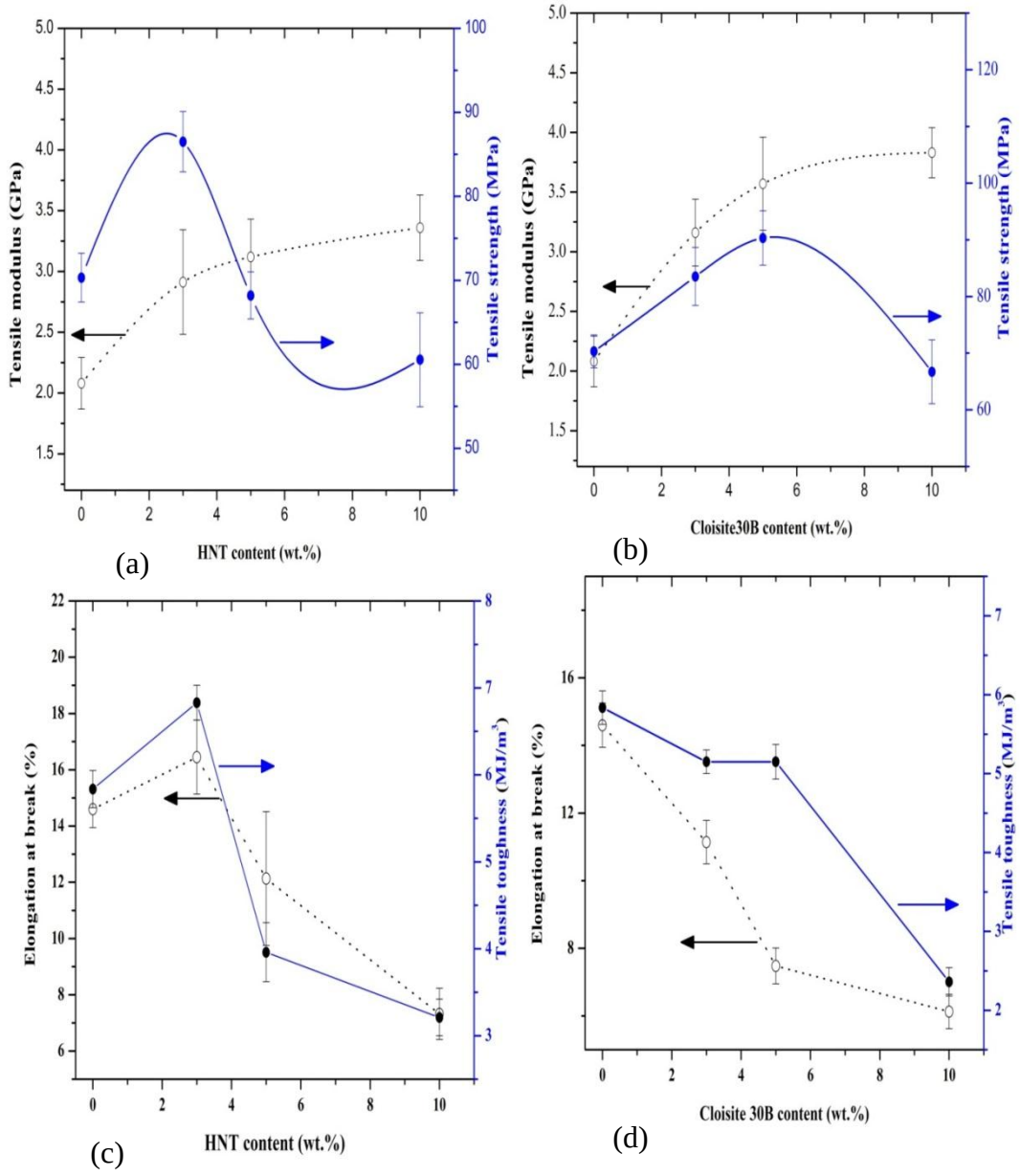

Figure 5.11 Mechanical properties of PVA nanocomposites at different clay contents: tensile modulus and tensile strength curves for (a) PVA/HNT nanocomposites and (b) PVA/Cloisite 30B clay nanocomposites, as well as elongation at break and tensile toughness for (c) PVA/HNT nanocomposites and (d) PVA/Cloisite 30B clay nanocomposites

Table 5.3 Properties and roughness of PVA/HNT nanocomposites and PVA/Cloisite 30 B clay nanocomposites.

Sample	Tensile modulus (GPa)	Tensile strength (MPa)	Elongation at break (%)	Toughness (MJ/m^3)	Roughness (nm)
PVA	2.08 ± 0.21	70.32 ± 2.9	14.60 ± 0.65	5.84 ± 0.21	1.9± 0.17
PVA/HNT/3 wt%	2.912 ± 0.43	86.5 ± 3.6	16.45 ± 1.32	6.83 ± 0.20	2.4 ± 0.13
PVA/HNT/5 wt%	3.12 ± 0.31	68.19 ± 2.81	12.13 ± 2.38	3.96 ± 0.34	4.54 ± 0.18
PVA/HNT/10 wt%	3.36 ± 0.27	60.54± 5.6	7.32 ± 0.91	3.21 ± 0.21	13.1 ± 0.23
PVA/Cloisite30B/3 wt%	3.16 ± 0.28	83.52 ± 5.12	11.14 ± 0.64	5.15 ± 0.15	2.04 ± 0.12
PVA/ Cloisite30B/5 wt%	3.57 ± 0.39	90. 31 ± 4.8	7.48 ± 0.53	3.87 ± 0.22	2.84 ± 0.18
PVA/Cloisite30B/10 wt%	3.83 ± 0.21	66.69 ± 5.63	6.13 ± 0.51	2.36 ± 0.18	6.05 ± 0.23

On the other hand, a different trend for tensile strengths of PVA/Cloisite 30B clay nanocomposites is clearly revealed from those of PVA/HNT nanocomposites. The tensile strengths of PVA/Cloisite 30B clay nanocomposites are increased by 18.8 and 28.4% with the nanofiller incorporation of 3 and 5 wt%, respectively, which is ascribed to more uniform clay dispersion as well as the formation of network structures from polymer matrices to nanofillers resulting from increasing hydrogen bonding between these constituents due to larger clay surface areas [12, 307]. When the clay content increases up to 10 wt%, the tensile strength of PVA/Cloisite 30B clay nanocomposites turns to decrease by 5.16% as opposed to that of near PVA, which suggests that the aggregation of nanofillers at high clay content levels can decline tensile strength. With respect to PVA/HNT nanocomposites, their tensile strength is improved by 23% with the addition of 3 wt% HNTs relative to that of neat

PVA at 70.32 MPa. Nonetheless, a drastic strength-decreasing tendency appears with the strength reduction by 3.2 and 13.9% when embedded with 5 and 10 wt% HNTs, respectively. This result indicates that the enhancement of tensile strengths for PVA/HNT nanocomposites lies in effective stress transfer from PVA matrices to HNTs, resulting from homogeneous HNT dispersion within PVA matrices. On the contrary, increasing the HNT content inevitably gives rise to noticeable particle aggregation with more stress concentration sites around HNT agglomerates as a result of the potential crack initiation to deteriorate mechanical properties of such nanocomposites. Qiu et al. [16] reported an increase in tensile strength for PVA/HNT nanocomposites by 35.2% with the addition of 5 wt% HNTs while the tensile strength declined by 19.2% at the HNT loading of 10 wt% owing to typical particle agglomeration. In a similar manner, Abdullah et al. [306] demonstrated that the tensile strength of PVA/starch blends increased by only 3.4 % when reinforced with 0.5 wt% HNTs along with a strength decrease by approximately 31.11% at the HNT loading of 5 wt%.

The elongation at break and tensile toughness of PVA/Cloisite 30B clay nanocomposites continuously decrease with the clay inclusion (Figure 5.11(d)). Corresponding lowest levels were observed with the decreases by 58 and 59.5%, respectively with the inclusion of 10 wt% Cloisite 30B clays. This finding can be associated with the stiffening effect of clay filler reinforcements to restrict the movement of PVA molecular chains, thus resulting in the overall flexibility reduction of nanocomposite films [308]. In addition, the intercalation of Cloisite 30B clays, as demonstrated by XRD results in Figure 5.2(c), assists in the increase of the number of available reinforcing elements as a result of the improvement of matrix rigidity despite a decrease in fracture toughness of corresponding nanocomposites.

Raheel et al. [308] reported that the elongation at break for PVA was decreased by 70.5%. In a similar manner, it was found that the elongation at break for PVA/ nanocellulose nanocomposites diminished by 42.7% when incorporated with 6 wt% nanocellulose [307]. As for PVA/HNT nanocomposites, elongation at break and tensile toughness increase by 12.7% and 16.9% with the addition of 3 wt% HNTs, beyond which both of them remarkably diminish until maximum reductions by 50 and 45.3% take place at the HNT content of 10 wt%, respectively, as opposed to those of PVA, Figure 5.3(c).The former finding can be explained by good particle-matrix interaction with more uniform particle dispersion at low HNT contents. Whereas, the latter result can be interpreted by typical particle agglomeration at high HNT contents up to 10 wt% with the disapearance of 'nano effect' of HNTs since most HNT aggregates become less favourable microfillers with poor particle dispersion. As such, those HNT aggregates act as typical defects with high stress concentration prone to crack initiation towards mechanical failure, leading to poor material toughness [298].

In this study, the incorporation of three different nanofillers (i.e. NBCs, HNTs and Cloisite 30B clays) has successfully enhanced mechanical and thermal properties of PVA nanocomposite films. According to our results, the highest increasing level among PVA/HNT nanocomposites and PVA/NBC nanocomposites can be achieved at the filler content of 3 wt%, as opposed to the optimum content of 5 wt% for PVA/Cloisite 30B clay nanocomposites. Nonetheless, the increasing rate achieved in PVA nanocomposites using three nanofillers is quite different, which can be associated with a variety of nanofiller features in terms of their structures and geometries, as well as the degree of compatibility between nanofillers and polymer matrices. With respect to nanofiller shape, it is clearly seen that NBCs are regarded

as 3D nanofillers as opposed to 2D nanofillers for HNTs and 1D nanofillers for Cloisite 30B clays. Different nanofiller shapes thereby influence the overall interfacial areas between fillers and polymer matrices, which plays a key role in the improvement of tensile strength of nanocomposites with different filler-matrix interactions. The second aspect is related to the structures, particularly the location of hydroxyl groups for nanofiller structures and amounts of hydroxyl groups within nanofillers. In case of NBCs, hydroxyl groups are located inside their pores, which tend to more closely interact with PVA from a 3D view. As for HNTs, the majority of hydroxyl groups are constrained in inner tubes between layers, which makes matrix-HNT interaction limited to the inner tubes of HNTs only. Moreover, in case of Cloisite 30B clays, hydroxyl groups are located between layered structures, which means that the interaction between polymer matrices and platelet-like clays are limited to small constrained interlayer areas. Tensile moduli of nanocomposite films have been detected to increase consistently when nanofiller content increases. With the incorporation of 3 wt% NBCs, HNTs and Cloisite 30B clays within PVA matrices, the tensile moduli of PVA nanocomposites increase by 70.67%, 40% and 51.6%, respectively. In case of tensile strengths of PVA nanocomposites, the maximum strength improvement is achieved with the inclusion of 3 wt% NBCs, which appears to be increased by 100% as opposed to that of PVA. On the other hand, HNTs and Cloisite 30B clays reach the maximum increasing levels at nanofiller contents of 3 and 5 wt%, respectively, which is evidenced by an increase in tensile strength of corresponding nanocomposites by 23 and 28.4%.

Several reasons can explain the above-mentioned results in relation to mechanical properties of nanocomposites. First, 3D nanofiller shape of NBCs can be generated at low nanofiller loadings and small particle sizes with relatively large interfacial areas

as compared with 2D HNTs and 1D Cloisite 30B clays. Liu and Brinson [309] investigated the effect of nanofiller geometry on the reinforcing efficiency of nanocomposites, which showed that at a low nanofiller loading with the random nanofiller orientation, the transverse modulus of nanoparticle based nanocomposites significantly exceeded those of nanotube based nanocomposites, as well as nanoplatelet based nanocomposites. Schadler et al. [310] reported that in case of a nanocomposite system, with the incorporation of nanoparticles and nanotubes with nanofiller diameter of 10 nm at the volume fraction of 10 vol%, the volume fraction of interfacial polymers was found to be about 30% in case of nanoparticle based nanocomposites as opposed to only 10% for nanotube based nanocomposites.

The second reason in relation to the high mechanical performance of PVA/NBC nanocomposites could be ascribed to chemical structures of nanofillers in terms of the amounts and locations of hydroxyl groups in order to control the dispersion of nanofillers within nanocomposites, and thus reflect upon the bonding between polymer matrices and nanofillers. Pakzad et al [207] reported that the number and nature of hydrogen bonds had substantial effect on mechanical properties of nanocomposites. In case of PVA/ 3 wt% NBC nanocomposites, NBC particles have porous structures with a large amount of hydroxyl groups located inside these pores when NBCs are uniformly dispersed. As confirmed by FTIR and XRD results, polymeric chains enter these pores and form both hydrogen bonding and mechanical bonding. Such two types of bondings can be particularly recognised for NBCs as compared to Cloisite 30B clays and HNTs, thus significantly reflecting upon the enhanced mechanical properties of nanocomposites [240, 265]. In case of PVA/ 5 wt% Cloisite 30B clay nanocomposites as compared to PVA/HNT nanocomposites, the strong adhesion of clays in polymer matrices associated with uniform clay

dispersion leads to the strong interfacial bonding between nanoclays and polymer matrices, which thus significantly contributes to the improvement of mechanical properties of nanocomposites. Carli et al. [296] evaluated the effect of Cloisite 30B clays and HNTs on the mechanical performance of poly(hydroxybutyrate-co-hydroxyvalerate) (PHBV) based nanocomposites. It was found that a high level of reinforcement with the incorporation of Cloisite30B clays was achieved as compared

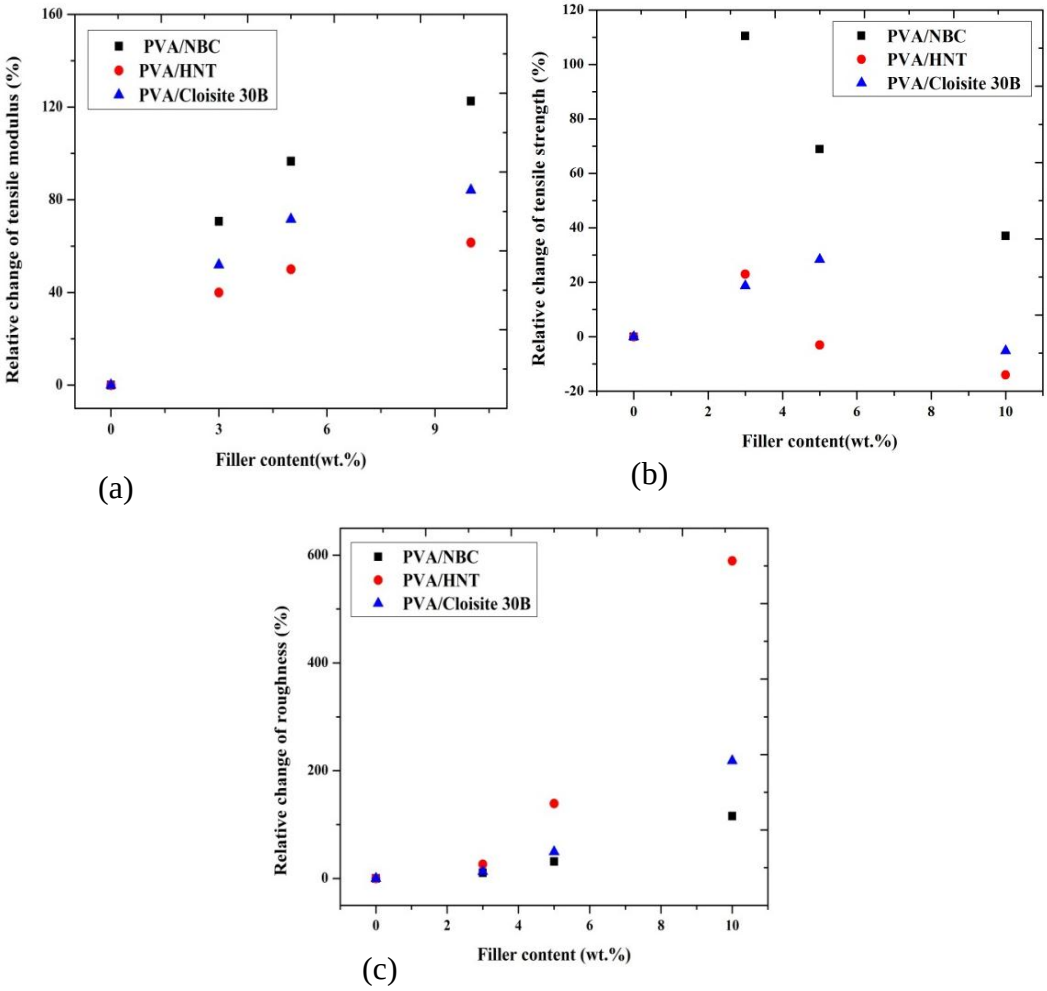

Figure 5.12 Mechanical properties of PVA nanocomposites at different fillers contents: (a) relative changes of (a) tensile modulus, (b) tensile strength and (c) roughness.

with those of HNTs. Such results are correlated to the strong interactions between Cloisite 30B clays and PHBV with apparent reinforcing effect. The dispersion state of nanofillers

also can influence mechanical properties of PVA nanocomposites. As mentioned earlier, NBCs have better dispersion state than Cloisite 30B clays and HNTs. Figure 5.12 demonstrates the comparison of tensile strengths, tensile modulus and roughness of PVA/NBC nanocomposites with those of PVA/HNT nanocomposites and PVA/Cloisite 30B clay nanocomposites. It is clearly seen that the incorporation of NBCs within PVA matrices yields smoother nanocomposite films with higher tensile strength as opposed to those of PVA/HNT nanocomposites and PVA/ Cloisite 30B clay nanocomposites, Figure 5.12(b). The better dispersion state of NBCs improves their intercation with PVA matrices, thus leading to higher tensile strengths of PVA/NBC nanocomposites. On the contrary, increasing nanofiller content appears to induce higher roughness as well as lower tensile strength of nanocomposites, which indicates nanofiller agglomeration apparently has detrimental effect on the improvement of tensile strength. This is particularly the case for PVA/HNT nanocomposites due to poor HNT dispersion state. Figures 5. 12(a) and (c) demonstrate the relationships of tensile modulus and surface roughness in terms of filler content for PVA nanocomposites. As expected, both tensile modulus and roughness of PVA nanocomposites are consistently enhanced with increasing the nanofiller content because of embedded more rigid nanofillers such as NBCs, HNTs and Cloisite 30B clays within soft PVA matrices for their stiffness improvement as well as the tendency of nanofiller agglomeration for higher surface roughness of nanocomposites at high nanofiller content levels.

On the contrary, PVA/ 3 wt% HNT nanocomposites cause much higher elongation at break and fracture toughness as opposed to those of neat PVA, which are opposite to PVA/ 3 wt% NBC nanocomposites and PVA/ 5 wt% Cloisite 30B clay nanocomposites with corresponding lower values. Such results could be explained by two reasons. The first reason is the number of nanoparticles depending on nanoparticle volume and volume fraction in nanocomposites. At the same volume

fraction, the number of near spherical NBCs is significantly larger than those of tubular HNTs or platelet-like Cloisite 30B clays. As such, this results in increasing the number of available reinforcing elements for the improvement of matrix rigidity and the decrease in fracture toughness [305, 311]. The second reason is related to the mechanism of fracture toughness including pre-crack effect for the fracture of nanocomposites. In general, crack deflection and crack pinning are most well-known mechanisms resulting in an increase in fracture energy [312], and consequently in fracture toughness of nanocomposites. In both mechanisms mentioned earlier, crack growth path can increase as long as those cracks reach nanofiller regions and the reinforcement shape highly affects the amount of crack deviation from their initial path. Since HNTs have larger lateral dimensions in comparison with near spherical NBCs, the cracks tend to pass over longer distances in nanocomposites reinforced with HNTs. Moreover, crack bridging is a well-known fracture mechanism in nanocomposites reinforced with high-aspect-ratio nanoparticles [305]. An ideal situation in this mechanism occurs when nanotube fillers are still embedded in matrices while aligned in a perpendicular direction to crack faces. As such, their higher aspect ratios promote the enhancement of fraction toughness when compared with those of near spherical nanoparticles.

5.6. Fracture Morphology

Figure 5.13 shows typical SEM micrographs of fracture cross-section surfaces for PVA/HNT nanocomposites and PVA/Cloisite 30B clay nanocomposites. It can be clearly seen from Figures 5.13(a) and (d) that PVA nanocomposites reinforced with 3 wt% of HNTs and Cloisite 30B clays reveal much rougher fractured surfaces compared with neat PVA films (Figure 4.8(a)). Moreover, 3 wt% HNTs or Cloisite 30B clays are distributed uniformly within PVA matrices. The good dispersion of

both nanoparticles and the strong interaction between clay particles and polymer matrices clearly contributed to the reinforcing effect, as reflected by the increase in both tensile strength and elastic modulus. Nevertheless, in both PVA/HNT nanocomposite and PVA/Cloisite 30B clay nanocomposites, uniform multilayered structures were not achieved similar to those detected in PVA/3 wt% NBC nanocomposites, as illustrated in Figure 4.8(b). Such results could be indicative of high NBC dispersability as compared with those of HNTs and Cloisite 30B clays, resulting in the highest mechanical properties. Meanwhile, at the HNT content of 5 wt%, the particle–particle interactions are more favourable than particle-matrix interactions, as evidenced by more filler agglomeration and presence of debonding and microvoids depicted in Figure 5.13(b). Such defects in nanocomposites could mainly contribute to the decrease in tensile strengths of PVA/HNT nanocomposites. However, as for PVA/ 5wt% Cloisite 30B nanocomposites, the clay dispersion appears to be still relatively uniform with presence of small particle agglomeration shown in Figure 5.13(e).With increasing the HNT and Cloisite 30B clay contents from 5 to 10 wt%, the fracture surfaces of nanocomposite films has changed from ductile to brittle characteristic, as illustrated in Figures 5.13(c) and (f), respectively. A similar phenomenon was also revealed in PVA/NBC nanocomposites, Figure 4.8(d). It is well known that the reduction of surface roughness reveals that the failure mode of PVA composite films can be changed from ductile to brittle fracture [273], which is consistent with the reduction in mechanical properties of nanocomposites in this study.

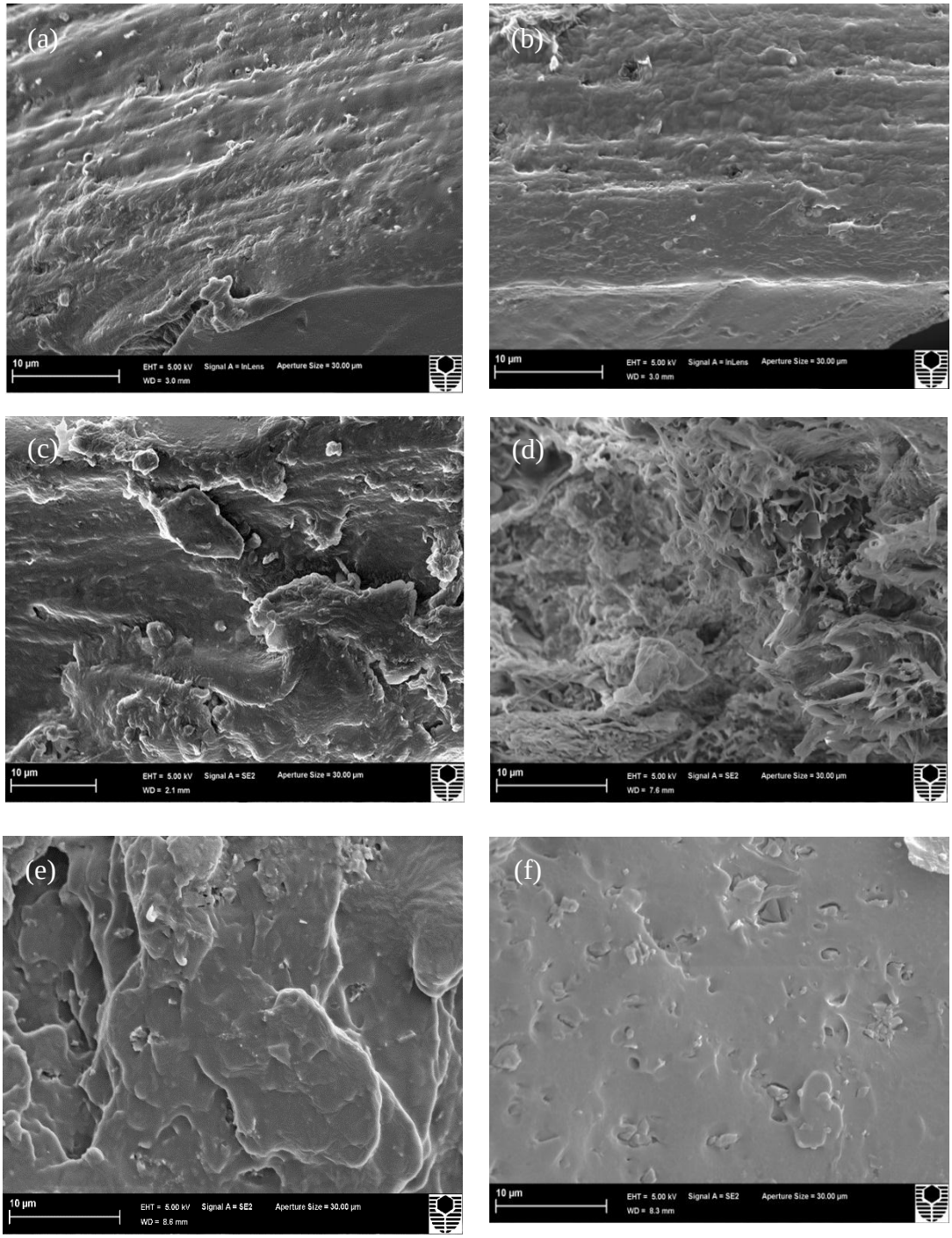

Figure 5.13 SEM micrographs of tensile fracture surfaces of (a) PVA/3 wt% HNT nanocomposites, (b) PVA/5 wt% HNT nanocomposites, (c) PVA/10 wt% HNT nanocomposites, (d) PVA/3 wt% Cloisite 30B clay nanocomposites, (e) PVA/5 wt% Cloisite 30B clay nanocomposites and (f) PVA/10 wt% Cloisite 30B clay nanocomposites.

5.7. Thermal Properties

PVA is a water-soluble semicrystalline polymer, in which high physical interchain and intrachain interactions exist because of hydrogen bonding between hydroxyl groups. The inclusion of nanoclays with hydroxyl groups could alter intramolecular and intermolecular interactions of PVA molecular chains. This may affect both crystallisation behaviour and physical structures of PVA. Similar observations can be found in previous studies dealing with PVA/HNT nanocomposites [16, 157] and PVA/Cloisite 30B clay nanocomposites [296]. Figures 5.14(a) and (b) show the DSC results of PVA/HNT nanocomposites and PVA/Cloisite 30B nanocomposites, respectively. The summary of these characteristics is reported in Table 5.4. As for PVA/HNT nanocomposites, it is clearly seen that the T_g of PVA becomes unchanged with the addition of HNTs in nanocomposite films, indicating that HNTs do not play an important role in inhibiting the chain mobility of PVA molecules. Qiu and Anil [16] also reported a similar result in T_g with the incorporation of HNTs into PVA matrices. Additionally, Dong et al. [313] also revealed that an decreasing T_g tendency of electrospun PLA fibre mats when embedded with 5 wt% HNTs. It was argued that such a finding was related to the reduction for the entanglements and interactions of PLA polymeric chains with the HNT inclusion. The relatively unchanged T_g in PVA/HNT nanocomposites, as compared to that of neat PVA, may arise from nanofiller geometry. The diameters of HNTs are on a nanoscaled level as opposed to microsized tubular lengths that considerably exceed the typical gyration radii of polymeric chains. As a result, HNTs cannot be completely wrapped by PVA molecular chains leading many voids surrounding HNT particles. Nanosized voids offer free volume for chain segments of PVA molecules. As such, this gives rise to lower T_g for PVA with the addition of HNTs. On the contrary, high T_g values for all

PVA/Cloisite 30B clay nanocomposites are evident as opposed to that of neat PVA. With the incorporation of 3, 5 and 10 wt% Cloisite 30B clays, T_g values for PVA nanocomposites are moderately enhanced up to 67.5, 70.2 and 71.8°C, respectively when compared with that of neat PVA at 65.19°C. This phenomenon can be attributed to the confinement of polymeric chains by intercalated clay structures to prevent their segmental motions [25], which has also been reported in PVA/MMT nanocomposites [211, 314], PVA/bentonite nanocomposites [13], as well as PVA/starch/MMT nanocomposites [315]. In particular, Ali *et al* [315] also found a slight increase for the T_g of PVA/starch nanocomposites from 70.28 to 71.75°C with the inclusion of 5 wt% MMTs within PVA matrices. The degree of crystallinity (χ_c) of PVA slightly increases from 36.65% for neat PVA to 38.2% and 37.2% for corresponding nanocomposites with the incorporation of 5 wt% of HNTs and Cloisite 30B clays, respectively. This suggests that both nanofillers have minor effect on crystalline phases of PVA matrices in nanocomposites. On the other hand, the melting temperature T_m of PVA nanocomposites virtually has no change with the addition of Cloisite 30B clays, as evidenced by the given T_m range of 220.44-221.62°C when compared with that of neat PVA at 222.91°C. However, PVA/HNT nanocomposites possess a moderate increase in T_m up to 226.67°C with the inclusion of 10 wt% HNTs. A similar phenomenon was also noticed in PHBV/HNT nanocomposites [24] with their T_m values being increased from 169 to173°C when incoprorated with 5 wt% HNTs. It is believed that based on XRD results in which HNTs were embedded with PHBV matrices, thicker and more oriented HNT structures in such nanocomposites could be formed leading to higher melting temperatures.

Thermal decomposition behaviour of PVA/Cloisite 30B clay nanocomposites and PVA/HNT nanocomposites was evaluated using thermogravimetric analysis (TGA) with associated results being presented in Figures 5.14(c)-(f) and Table 5.4. Relevant findings for both systems reveal the existence of three major degradation steps according to previous study [153]. Initially, the first degradation takes place at 107°C owing to the breakage of hydrogen bonds, impurities, and monomers of vinyl alcohol. Then the second degradation occurring at 274°C involves a dehydration reaction on PVA molecular chains, degradation of main backbones, as well as the decomposition of organic clays. This process is accompanied by a drastic mass change caused by the removal of organic compounds like CO_2 and long molecular chains of alkyl derivatives. Finally, the third degradation step appears at a temperature level below 429°C with more complexity including the further degradation of polyene residues to yield the carbon and hydrocarbon. The incorporation of HNTs and Cloisite 30B clays can increase the thermal stability of PVA by increasing the decomposition temperatures and reducing the weight loss, as presented in Figures 5.14 (c) and (d). For PVA/ HNT nanocomposites, the decomposition temperature at 5% weight loss was increased from 200.2°C for PVA to 265.3, 268.1 and 270.2°C for PVA nanocomposites reinforced with 3, 5 and 10 wt% HNTs, respectively. Such a finding suggests that HNTs work as a barrier material to heat and mass transfer. Moreover, the intrinsic hollow tubular structures of HNTs can produce traps for volatile particles, thus improving thermal stability by delaying the mass transfer during a decomposition process. Abdullah et al [306] reported that the decomposition temperature at 5% weight loss of PVA/starch/ glycerol (GL) blends was increased from 135.3 to 153.3°C with the inclusion of 3 wt% HNTs. Moreover, as clearly seen from DTG curves in Figure 5.14 (e), the T_d of

PVA shifted to a higher temperature level, which means that the dehydration process is hindered, resulting from strong interactions between PVA matrices and HNTs, as well as its role as barrier materials to increase the thermal resistance of PVA based nanocomposites. Furthermore, the second DTG peaks of PVA/HNT nanocomposites reinforced with 5 and 10 wt% HNTs are much wider than that of neat PVA in the presence of main and side peaks, as compared to single DTG peak for PVA at the same step. This signifies that a single peak for PVA can be attributed to the eliminated reaction while side and main peaks of PVA/HNT nanocomposites correspond to the eliminated reaction as well as the overlap of continual elimination and chain-scission reaction with the requirement of more energy to accrue at high temperatures [281].

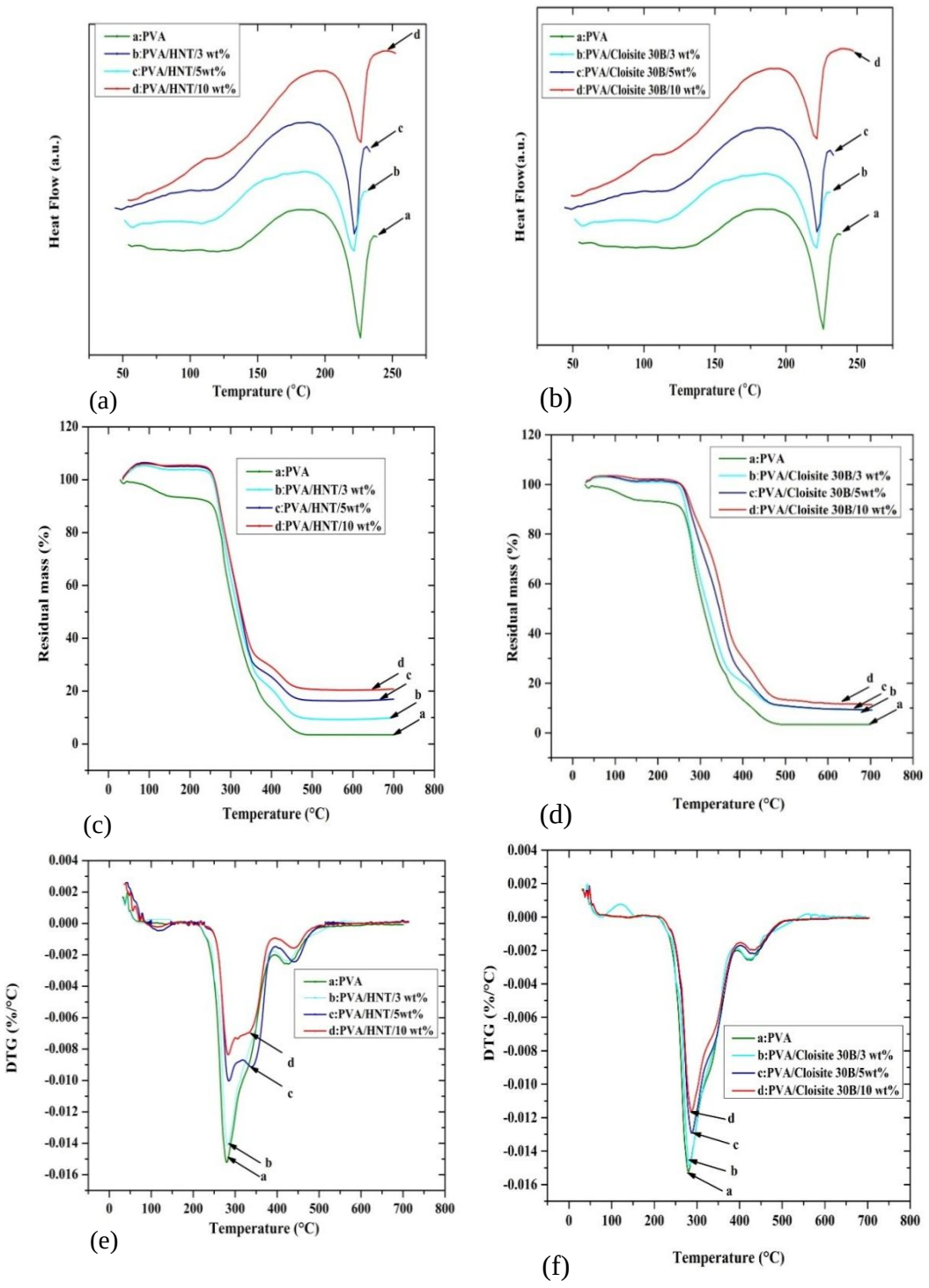

Figure 5.14 DSC diagrams for (a) PVA/HNT nanocomposites and (b) PVA/Cloisite 30B clay nanocomposites as well as TGA curves (c) and (e) and DTG curves (d) and (f) for PVA/HNT nanocomposites and PVA/Cloisite 30B clay nanocomposites, respectively.

Table 5.4 Thermal properties of PVA/HNT nanocomposites and PVA/Cloisite 30B clay nanocomposites.

Sample	T_g (°C)	ΔH_m (J/g)	χ_c (%)	T_m (°C)	$T_{5\%}$ (°C)	$T_{80\%}$ (°C)	T_d (°C)
PVA	65.19	50.8	36.65	222.91	200.15	363.5	274.23
PVA/HNT/3 wt%	65.13	50.5	37.6	224.74	265.29	387	283.2
PVA/ HNT/5 wt%	65.86	50.2	38.2	225.13	268.06	422.87	286.47
PVA/ HNT/10 wt%	64.91	44.15	35.4	226.67	270.21	428.03	287.13
PVA/Cloisite 30B/3 wt%	67.5	49.6	36.9	220.44	253.3	387.9	282.21
PVA/ Cloisite 30B/5 wt%	70.2	49.09	37.2	221.62	261.1	407.12	287.41
PVA/ Cloisite 30B/10 wt%	71.8	45.01	36.1	221.06	265.3	435.3	290.13

On the other hand, In case of PVA/ Cloisite 30B clay nanocomposites, with increasing the clay content, the thermal stability of nanocomposites improves as compared to that of PVA, which is evidently noticeable from consistently high $T_{5\%,}$ $T_{80\%}$ and T_d values. For instance, $T_{80\%}$ of PVA increases from 363.5 to 407°C with the inclusion of 5 wt% Cloisite 30B clays. Such a result is in good agreement with previous literature of PVA/MMT nanocomposites [153, 183]. Mondal et al [183] reported that the decomposition temperature of 50% degradation PVA was increased from 325 to 383.9°C at the Na^+ MMT content of 8 wt%. Moreover, the shift in the decomposition temperatures T_d for PVA/Cloisite 30B nanocomposites suggests the hindrance of dehydration process. Such a finding in thermal stability is associated with the presence of nanolayers acting as barriers to maximise the heat insulation and

minimise the permeability of volatile degradation products in the materials. This increase is also attributed to the decrease in oxygen permeability related to good clay dispersion in PVA matrices.

According to the above-mentioned results, overall the incorporation of HNTs and Cloisite 30B clays has improved thermal properties of PVA nanocomposites, which is also the case for the addition of NBCs, as summaries in Table 4.3. However, the increasing rate for thermal properties has been strongly dependent on nanofiller types. It is clearly seen that the T_g of PVA nanocomposite films with the incorporation of NBCs and Cloisite 30B clays are much higher than that of PVA/ HNT nanocomposites. Such results indicate that NBCs and Cloisite 30B clays can restrict PVA chains more efficiently, as evidently confirmed by improving mechanical properties of corresponding nanocomposite films. According to previous studies [316, 317], the phenomenon of T_g increase is strongly correlated to the reduced mobility of polymeric chains by incorporating inorganics nanofillers. The addition of nanoparticles into polymer matrices could change the distribution of chain segments, which is most likely due to a change in chain packing density in the vicinity of nanofiller surfaces. It should be noted that filler geometry may play a critical role in the effect of T_g. NBCs and Cloisite 30B clays have different nanofiller shapes, which renders the absorption of polymeric chains with entangled structures on their surfaces when nanofiller diameters are comparable to gyration radii of polymeric chains. As such, it leads to an increased packing density for polymeric chains and their chain mobility restriction resulting in higher T_g values. However, the incorporation of HNTs into PVA matrices gives rise to an decrease in T_g , which is consistent with the previous work [157]. Although HNT diameters are on the nanometer scale, their length turns to be microsized, which becomes considerably

higher than typical gyration radii of polymeric chains. As consequence, it is hard for polymeric chains to cover entire HNT structures. Moreover, the presence of microvoids along HNT lengths could offer free sites for polymeric chain segments with a resulting decrease in T_g [157].

The crystallinity of PVA nanocomposite films reinforced with NBCs, HNTs and Cloisite 30B clays are relatively similar. Moreover, the T_m values in case of PVA/ 3 wt% NBC nanocomposites, PVA/ 5 wt% Cloisite 30B clay nanocomposites are nearly the same despite being slightly less than that of neat PVA at 222.91°C. The appearance of lower melting temperature and melting-peak broadening effects could be associated with the recrystallisation phenomenon of PVA matrices in nanocomposites [296]. This is because the decrease in the melting temperatures (T_m) seems to be correlated to the changes in crystal lamellar thickness and its distribution. In PVA/ 3 wt% NBC nanocomposites and PVA/ 5 wt% Cloisite 30B clay nanocomposites, the decrease in T_m appears to be associated with the changes in crystal lamellar thickness and their distribution (i.e. the formation of less perfect crystal structures).

TGA results reveal that the $T_{5\%}$ of PVA/ 3 wt% NBC nanocomposites is determined to be 256.3°C, and increases to 262.95°C with the incorporation of 5 wt% NBCs, which is relatively similar to that of PVA/ 5wt% Cloisite 30B clay nanocomposites at 261.1°C. On the other hand, the $T_{5\%}$ of PVA/ 3 wt% HNT nanocomposites appears to be 265.29°C, which is significantly higher as compared with nanocomposites reinforced with NBCs and Cloisite 30B clays. On the contrary, the $T_{80\%}$ of PVA/ 3 wt% NBC nanocomposites has been found to be 390.67°C, and reaches 440.28°C with the inclusion of 5 wt% NBCs, which is significantly higher than those of PVA

nanocomposites reinforced with HNTs and Cloisite 30B clays. This result suggests that the maximum thermal stability is achieved in the presence of NBCs as compared with HNTs and Cloisite 30B clays. As opposed to other nanofillers, the better NBC dispersion within PVA matrices takes place along with the higher barrier towards the thermal degradation. Therefore, Such barrier effect can counterbalance the degradation effect with the further improvement of thermal stability [240].

5.8. Summary

The following key points are summarised in this chapter:

- When HNTs are embedded within PVA matrices, the properties of PVA nanocomposites are remarkably affected and strongly depend on the HNT content. The morphological structures reveal that nanofiller dispersion can lead to various structures resulting in different enhancement levels of mechanical properties of nanocomposites. The incorporation of 3 wt% HNTs has improved tensile modulus, tensile strength, elongation at break and fracture toughness of PVA/HNT nanocomposites by 40%, 23%, 12.7% and 16.9%, respectively. While increasing HNT content beyond that causes the decreases in tensile strength, elongation at break and tensile toughness of PVA/HNT nanocomposites resulting from debonding effect between nanofillers and polymer matrices. Moreover, thermal properties in term of degree of crystallinity, melting temperature and thermal stability of PVA/HNT nanocomposites were enhanced as compared with those of neat PVA films when the HNT content increases.
- Morphological structures of PVA/Cloisite 30B clay nanocomposites demonstrate uniform clay dispersion within PVA matrices in the formation of combined clay

exfoliated and intercalated structures. These results are in agreement with those obtained from XRD results. The tensile strengths and Young's moduli of PVA/Cloisite 30B clay nanocomposite films were increased by 28.4% and 71.6 % at the clay content of 5 wt%. Nonetheless, the elongation at break and fracture toughness decreased accordingly. Thermal properties of PVA/ Cloisite 30B clay nanocomposites improved compared to those of neat PVA films due to strong hydrogen-bonding interactions between PVA matrices and nanofillers.

- The effect of different nanofiller shapes and structures on the properties of PVA nanocomposite films has been investigated, which reveals that the maximum tensile strength and modulus can be achieved with the incorporation of NBCs. This can be related to the large amount of interphase resulting from a high degree of filler dispersion in case of PVA/NBC nanocomposites as compared to those reinforced with HNTs and Cloisite 30B clays. Moreover, thermal stability of PVA nanocomposites was remarkably enhanced with the inclusion of NBCs as compared to those with the addition of HNTs and Cloisite 30B clays. This could be due to the uniform dispersion of NBCs to generate high interfacial regions as compared with other nanofillers, leading to increasing barrier effect of NBC against the thermal degradation of PVA nanocomposites.

Chapter 6.

3D Interphase of PVA Based Nanocomposite Films with Different Particle Structures and Shapes

6.1. Introduction

Mechanical properties of polymer nanocomposites depend primarily on nanointerphases as transitional zones between nanoparticles and surrounding matrices. Due to the difficulty in the quantitative characterisation of nanointerphases, previous literatures generally deemed such interphases as one-dimensional uniform zones around nanoparticles by assumption for analytical or theoretical modelling. We hereby have demonstrated for the first time direct three-dimensional topography and physical measurement of nanophase mechanical properties between nanoparticles and PVA in polymer nanocomposites. Topographical features, nanomechanical properties and dimensions of nanointerphases were systematically determined via peak force quantitative nanomechanical tapping mode (PFQNM).

6.2. Interphase Characterisation of PVA Based Nanocomposites

6.2.1. Modelling Approach

6.2.1.1. Interphase Modulus

The elastic properties of interphases such as interphase modulus between PVA matrices and dispersed anisotropic NBCs in various shapes and sizes were determined according to a data set of elastic moduli collected based on PVA/NBC interphases surrounding 75 different NBCs at 25 line scan regions (LSRs). The same procedure was employed to detect interphase moduli of PVA/Cloisite 30B clay nanocomposites and PVA/HNT nanocomposites, respectively.

6.2.1.2. Interphase Dimensions

Interphase dimensions in terms of interphase width $W_{\text{iInterphase}}$, interphase length $L_{\text{j Interphase}}$ and interphase height $H_{\text{k Interphase}}$ were detected by scanning individual

PVA/nanoparticle phases using PFQNM with typical features of distinct interphases between nanoparticles and polymer matrices based on the variation of their nanomechanical properties. For instance, $W_{\text{Interphase}}$ was measured by scanning along the *i*th transverse plane (*i*=1, 2, 3…) for PVA/nanoparticle phases. The same procedure reapplied to determine $L_{j\text{Interphase}}$ and $H_{k\text{Interphase}}$ along the *j*th longitudinal plane (*j*=1, 2,3...) and *k*th height plane (*k*=1,2, 3...), respectively (refer to Appendix A for more details).

On the other hand, it was assumed that uniform nanoparticles dispersion took place with two typical categories, namely fully embedded and partially embedded NBCs, HNTs and Cloisite 30B clays within PVA matrices in nanocomposites, as illustrated in Figure 6.1. It is clearly demonstrated that the interphase is surrounded between inner interface area and outer interface area bound by nanofillers and PVA matrices, respectively. By rearranging analytical equations according to Behmer and Hawkins [318] used for calculating the surface areas of anistropic shapes, the following equations (6.1)–(6.4) are derived for determining both surface areas of outer interface ($SA_{\text{outer Interface}}$) and inner interface ($SA_{\text{inner Interface}}$) in a wide range of fully and partially embedded nanoparticles. It is noted that subscripts of 'f' and 'p' mean fully and partially embedded nanoparticles, respectively, depicted in Figure 6.1.

$$\left(SA_{outer\ Interface} \right)_{\text{f}} = a_1 + b_1 L^2_{\text{Interphase}} + c_1 W^2_{\text{Interphase}} + d_1 H^2_{\text{Interphase}} \tag{6.1}$$

$$\left(SA_{outer\ Interface} \right)_{\text{p}} = a_2 + b_2 L'^2_{\text{Interphase-effective}} + c_2 W'^2_{\text{Interphase-effective}} + d_2 H'^2_{\text{Interphase-effective}} \tag{6.2}$$

$$\left(SA_{inner\ Interface} \right)_{\mathrm{f}} = a_3 + b_3\, L_{\mathrm{p}}^2 + c_3 W_{\mathrm{P}}^2 + d_3 H_{\mathrm{P}}^2 \tag{6.3}$$

$$\left(SA_{inner\ Interface} \right)_{\mathrm{p}} = a_4 + b_4\, L'^2_{\mathrm{p-effective}} + c_4 W'^2_{\mathrm{p-effective}} + d_4 H'^2_{\mathrm{p-effective}} \tag{6.4}$$

Where $L'_{\text{Interphase-effective}}$, $W'_{\text{Interphase-effective}}$ and $H'_{\text{Interphase-effective}}$ represent the maximum length, width and thickness for effective interphases. $L'_{\text{p-effective}}$, $W'_{\text{p -effective}}$ and $H'_{\text{p -effective}}$ denote the maximum length, width and thickness for effective nanoparticles. a_1, b_1, c_1, d_1, a_2, b_2, c_2, d_2, a_3, b_3, c_3, d_3 and a_4, b_4, c_4, d_4 are constants determined using curving fitting. For instance, the constants of a_1, b_1, c_1 and d_1 in case of PVA/NBC nanocomposites were determined to be 0.7439, 0.3627, 0.7006, and 0.9979, respectively, by fitting equation (6.1) with experimental data in relation to surface area $(SA'_{outer\ Interface})_{\mathrm{f}}$ obtained from AFM measurements (see more details in Appendix A).

After obtaining surface area data, the associated results were employed in determining interphase / nanoparticle volume $V_{\text{p/Interphase}}$ and nanoparticles volume V_{p} with respect to fully and partially embedded nanoparticles according to modified equations derived from Behmer and Hawkins [318] as follows:

$$\left(SA_{outer\ Interface} \right)_{\mathrm{f}} = e_1 V_{\mathrm{p/Interphase}}^{f_1} \tag{6.5}$$

$$\left(SA_{outer\ Interface} \right)_{\mathrm{p}} = e_2 V_{\mathrm{p/Interphase\ effective}}^{f_2} \tag{6.6}$$

$$\left(SA_{inner\ Interface} \right)_{\mathrm{f}} = e_3 V_{\mathrm{p}}^{f_3} \tag{6.7}$$

$$\left(SA_{inner\ Interface} \right)_{\mathrm{p}} = e_4 V_{\mathrm{p\ effective}}^{f_4} \tag{6.8}$$

e_1, f_1, e_2, f_2, e_3, f_3 *and* e_4, f_4 are constants determined using curving fitting. For example, the constants of e_1 and f_1 in case of PVA/NBC phases were estimated to be 0.3824 and 0.3825, respectively by fitting equation (6.5) with the data value of $V_{\mathrm{p/Interphase}}$ obtained from the AFM measurement (see Appendix A for more details).

Final step is to determine interphase volume $V_{\mathrm{Interphase}}$ for fully or partially embedded nanoparticles in PVA nanocomposites shown in Figures 6.1 as follows:

$$(V_{\mathrm{Interphase}})_{\mathrm{f}} = V_{\mathrm{p/Interphase}} - V_{\mathrm{p}} \tag{6.9}$$

$$(V_{\mathrm{Interphase}})_{\mathrm{p}} = V_{\mathrm{p/Interphase\text{-}effective}} - V_{\mathrm{p\ effective}} \tag{6.10}$$

Note that the aforementioned procedure applied to three PVA nanocomposite systems reinforced with NBCs, HNTs and Cloisite 30B clays used in this study by considering interphase dimensions and properties (see Appendix A for more details).

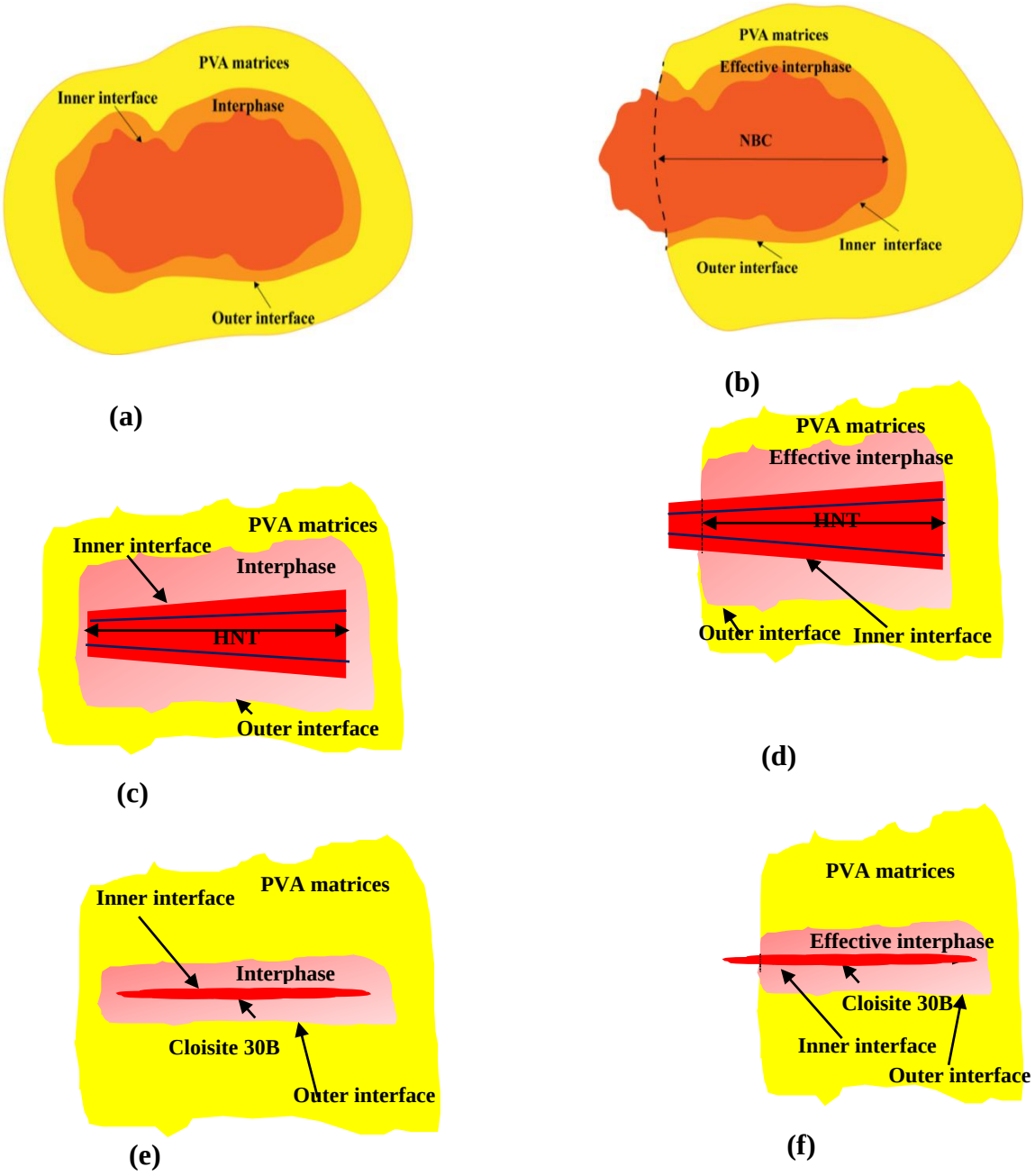

Figure 6.1 Schematic diagrams of fully embedded nanoparticles: (a) NBCs, (c) HNTs and (e) Cloisite 30B clays, as well as partially embedded nanoparticles: (b) NBCs, (d) HNTs and (f) Cloisite 30B clays in PVA nanocomposite systems.

6.2.2. Modulus-Gradient Effect

As illustrated in Figure 6.2(a), strong interactions between NBCs and PVA matrices appear to be not only on NBC surfaces like other nanoparticles such as CNTs, nanosillca, etc., but also into entire NBC particles through the penetration of PVA

molecules. Figures 6.2(b) and (c) demonstrate a typical topographical image of PVA/NBC nanocomposite sample and the variation of elastic moduli from PVA matrices, interphases to NBCs, respectively. According to a typical cut line $A_{24}B_{24}$ shown in Figure 6.2 (c), elastic modulus has significantly increased from the lowest modulus level of 14.8 GPa with respect to PVA matrices to the highest level of 72.86 GPa for NBCs. In particular, the interphase exhibits an almost linearly increasing relationship of its elastic modulus with scan distance except interphase boundary regions around PVA matrices and NBCs alone, which is in range from 17.1 GPa near the PVA region to 64.9 GPa around NBCs with the measured interlayer thickness of 31.8 nm. Final interphase modulus was obtained from the solid black curve by best fitting discrete modulus data sets based on 25 representative LSRs in Figure 6.2 (d), which also applied to determine elastic moduli of NBCs and PVA matrices to be 78.4 ± 4.9 and 24.25± 4.2 GPa, respectively. The same analysis was carried out for PVA/HNT nanocomposites and PVA/Cloisite 30B clay nanocomposites with associated results presented in Figures 6.3 and 6.4. It was found that similar fully and partially embedded Cloisite 30B clays and HNTs were manifested in Figures 6.3(a) and 6.4 (a) , respectively. With respect to PVA/Cloisite 30B clay nanocomposites, their interphase modulus was also increased from 20.6 GPa near PVA matrices to 42.2 GPa surrounding Cloisite 30B clays. Such a modulus-gradient phenomenon was also revealed in PVA/HNT nanocomposites with the interphase modulus varying from 19.3 to 40 GPa accordingly. In particular, PVA modulus appeared to be 21.4± 4.1 and 19.8 ± 3.7 GPa for PVA/Closite 30B clay nanocomposites and PVA/HNT nanocomposites, which was equivalent to 13.4 and 22.5% less than that for PVA/NBC nanocomposites. It was implied that PVA modulus was the highest when incorporated with NBCs as opposed to the other two nanoparticle types, which was

in good agreement with higher tensile strength data of PVA/NBC nanocomposites previously mentioned in Chapter 4. Such a finding could be associated with 3D nanofiller shape of NBCs enabling to possibily restrict more PVA molecular chains as opposed to 2D tubular HNTs and 1D platelet-like Cloisite 30B clays. The interphase could be considered as transitional zones with a typical modulus gradient from polymer matrices to reinforcements in order to achieve effective load transfer for improving the mechanical properties of composite materials. Our result reveals the existence of interphase with excellent elastic properties in PVA/NBC nanocomposites, as shown in Figure 6.2(d) with a modulus gradient ranging from 25.32 ±3.4 GPa for PVA matrices to 66.3±3.2 GPa for NBCs, which appears to be relatively high as opposed to those from 22.2 ± 2.9 to 43.4± 3.1 GPa, as well as from 20.6 ± 3.4 to 41.6± 4.6 GPa in case of PVA/Cloisite 30B clay nanocomposites and PVA/HNT nanocomposites, respectively, as depicted in Figures 6.3 (d) and 6.4 (d). Higher interphase modulus detected in PVA/NBC nanocomposites may directly benefit from highly porous NBC structures that cover all their 3D structures when compared with 1D platelet-like Cloisite 30B clays and 2D tubular HNTs as reinforcements, which can further facilitate the generation of highly positive capilary pressure to drive PVA molecular chains into NBC pores with typical resulting chemical bonding in nanocomposites. These NBC pores also possess ‘mechanical anchoring’ mechanism [319] when interacting with PVA molecular chains, which means that a mechanical interlocking phenomenon takes place due to the existence of PVA molecular chains inside BC surfaces [319]. On the contrary, the interactions of Cloisite 30B clays and HNTs within PVA natrices are limited to the generation of hydrogen bonding between PVA molecular chains and those detected on the surfaces of such nanoparticles. Besides, the formation of mechanocal bonding between

Cloisite 30B clays and HNTs, and PVA matrices is very limited. Moreover, the modulus-gradient effect at the interphase zones from nanofillers to PVA matrices could be associated with the gradient number of hydrogen bonding from nanofillers surfaces to polymer matrices, which plays an important role in controlling mechanical properties of polymer nanocomposites [320, 321]. Nanoelastic behaviour of PVA demonstrates an elastic modulus range of 19.8-24.25 GPa in this study, which is close to the value of 23.69 GPa previously reported via the nanoidentation of PVA/chitsan (CS) copolymer coating [284]. However, the average elastic modulus of bulk PVA films was approximately 2.08 GPa at a macroscopic level, which appeared to be much smaller in contrast with those of individial amorphous phase at 11.4± 3.1 GPa and crystalline phase at 24±4.2 GPa, which were obtained via PFQNM for PVA/NBC nanocomposites shown in Figure 4.10 (c). Such a great difference in measurements can be ascribed to the following reasons: (i) Though instrumental parameters have been calibrated prior to AFM measurements, the shape function of the topmost probe tip may not be accurate enough for the low penetration depth [204, 285]. In this study, the low pentration force has been used, resulting in a low penetration depth in order to minimise the effects of residual stresses as well as plastic deformation from the neighbouring indent, with the provision of the high lateral resolution capability particularly for nanointerphases. (ii) Nanosurface properties often vary from those bulk properties because of the discrepancy in morphological structures between outer skins on material surfaces and bulk films as well as the differences in nanomechanical behaviour and bulk properties [285]. (iii) Despite the data reliability and repeatability of DMT modulus, its determination using the PFQNM is apparently distinct from tensile modulus for bulk properties using conventional tensile testing due to different measurement mechanisms [286].

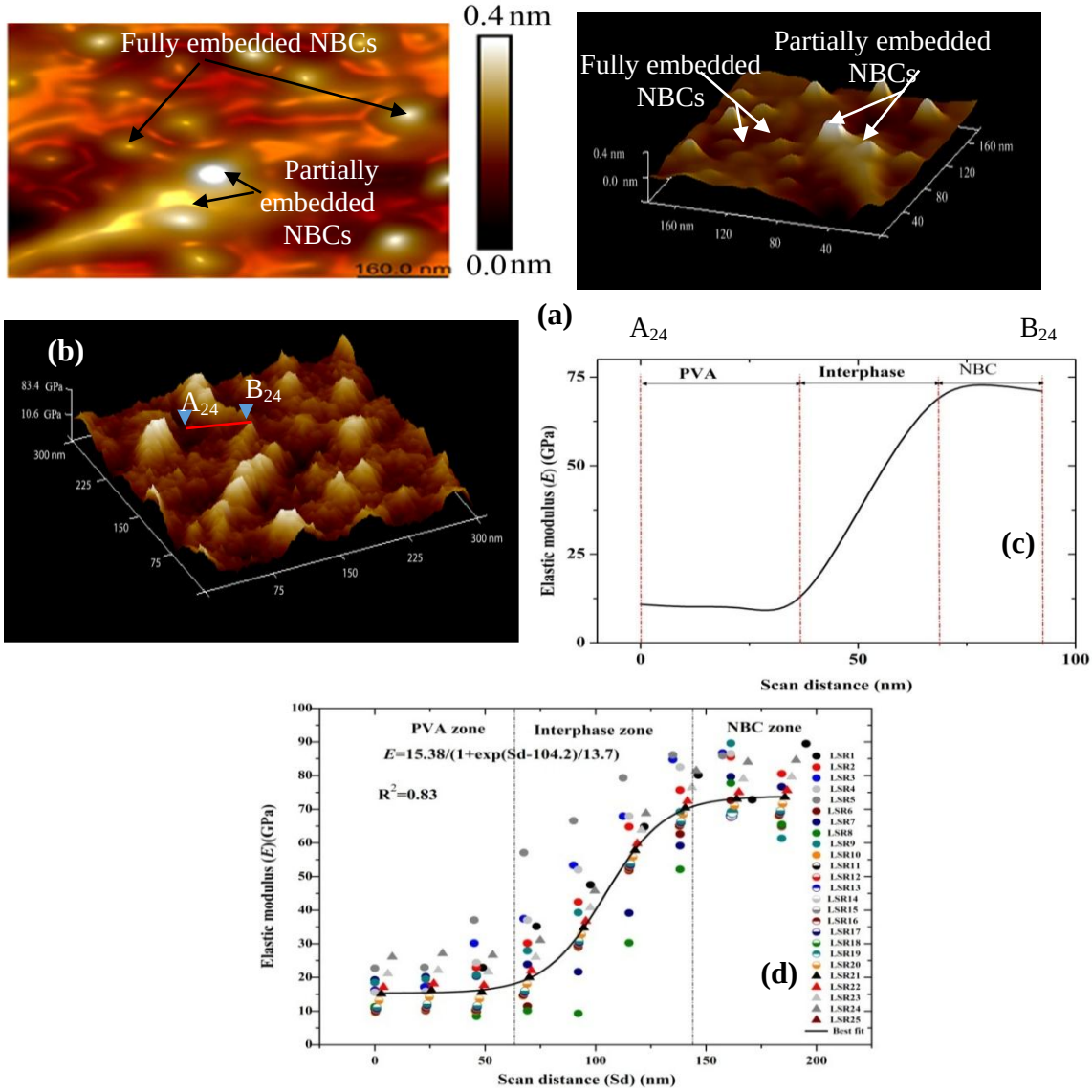

Figure 6.2 proposed scheme for typical PVA/NBC intercation with fully and partially embedded NBCs, (b) 3D AFM modulus mapping image of PVA/ 3 wt% NBC nanocomposites, (c) modulus profile for PVA/3 wt% NBC nanocomposites taken along the line $A_{24}B_{24}$, and(d) typical data sets of modulus profiles along 25 line scan regions (LSRs) of corresponding nanocomposites with the best-fit curve in which S_d represents scan distance.

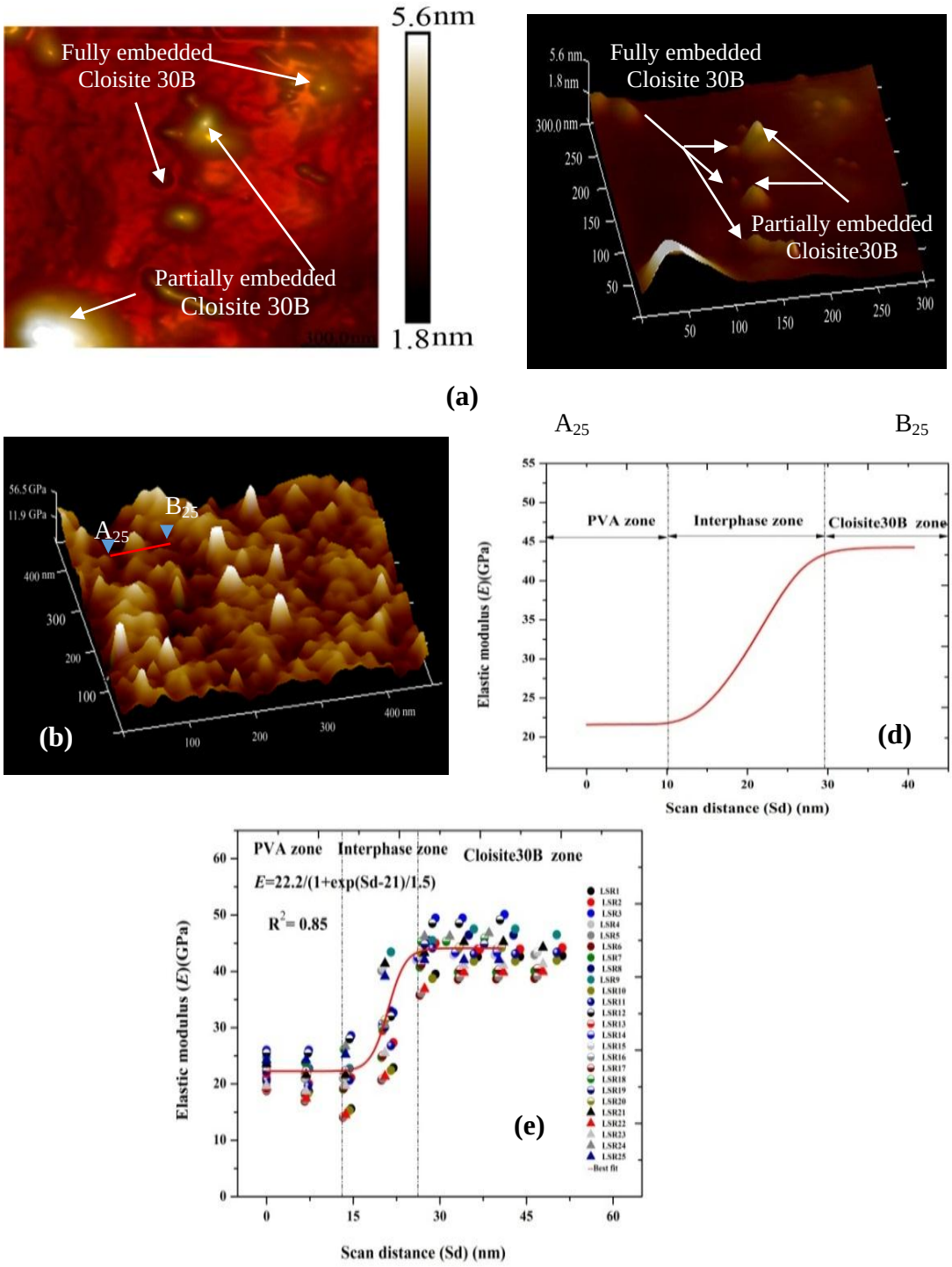

Figure 6.3 (a) proposed scheme for typical PVA/Cloisite 30B clay intercation with fully and partially embedded clays, (b) 3D AFM modulus mapping image of PVA/ 3 wt% Cloisite 30B clay nanocomposites, (c) modulus profile for PVA/3 wt% Cloisite 30B clay nanocomposite with the best-fit curve in which S_d represents scan distance.

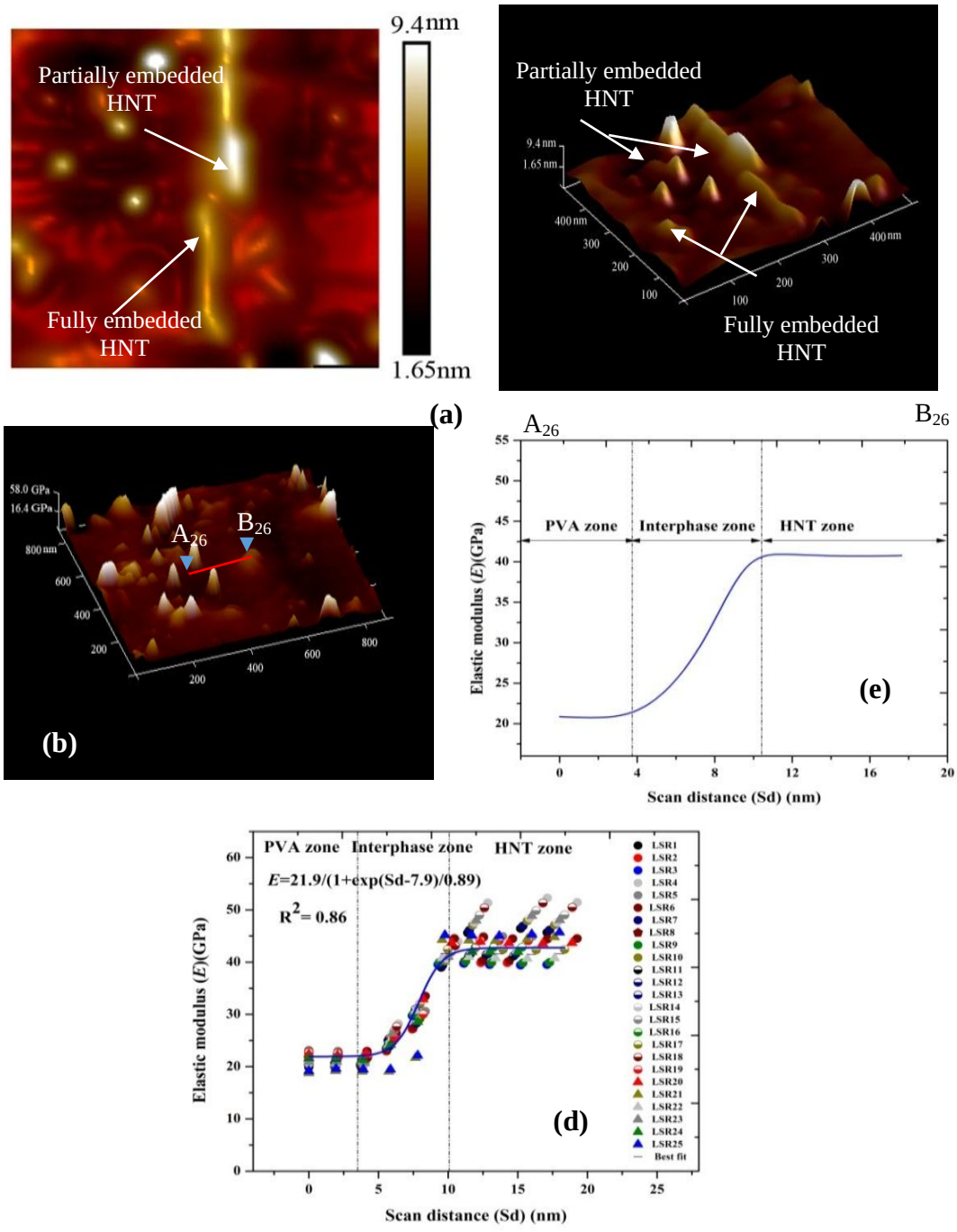

Figure 6.4 (a) proposed scheme for typical PVA/HNT intercation with fully and partially embedded HNTs, (b) 3D AFM modulus mapping image of PVA/ 3 wt% HNT nanocomposites, (c) modulus profile for PVA/3 wt% HNT nanocomposites taken along the line $A_{26}B_{26}$, and(d) typical data sets of modulus profiles along 25 line scan regions (LSRs) of corresponding nanocomposites with the best-fit curve in which S_d represents scan distance.

6.2.3. 3D Interphase Dimensions and Modulus

Elastic properties of interphases generally vary when surrounded by individual particles in different sizes and shapes, thus leading to the change of interphase dimensions. Interphase dimensions can be determined according to AFM height and adhesion images of PVA/NBC composite samples, depicted in Figures 6.5(a) and (b), as well as Figures 6.5 (c) and (d), respectively. As evidently seen in Figures 6.5(a) and (b), the height of NBCs is generally much greater than that of PVA. It is evidently shown that a linearly increasing tendency in height occurs from interphase regions near PVA matrices to those surrounding NBCs. NBCs tend to be easily distinguished from PVA matrices due to their different adhesion properties. The tip adhesion to PVA matrices in PVA/NBC nanocomposites is determined to be 10.76±3.42 nN, which is over five-fold greater than that of NBCs at 2.1±0.87 nN. Such a finding can be associated with the hydrophilic nature of PVA with relatively high adhesion force when compared with hydrophobic NBCs. Accordingly, interphase thickness is represented by the scan distances of 16 and 13 nm with a sharp decreasing adhesion gradient from PVA matrices to NBCs on both sides of selected material regions, as illustrated in Figure 6.5(d). This result is in good accordance with the values of 13 and 12.5 nm, previously determined for epoxy/graphene nanoplatelet (GNP) composites and epoxy/graphene oxide (GO) nanocomposites, respectively [322]. Similar procedure was used to detect interphase thickness in PVA/Cloisite 30B clay nanocomposites and PVA/HNT nanocomposites according to height and adhesion profiles depicted in Figures 6. 6 and 6.7, respectively. In both nanocomposite systems, the tip adhesion to PVA matrices is 14.24±2.31 nN, which appears to be greater than those for HNTs and Cloisite 30B clays at 8.6±1.08 and 8.4±1.1 nN, respectively. It is manifested that the tip adhesion

to HNTs and Cloisite 30B clays are still much higher than that of NBCs at 2.1±0.87 nN, resulting from more hydroxyl groups identified in HNTs and Cloisite 30B clays obtained from previous FTIR results. As illustrated in Figure 6.6(d), interphase thickness is found to be 6.5 and 9.2 nm on both sides of HNTs when compared with 8.4 and 10.2 nm on those of Cloisite 30B clays in Figure 6.7(d). In comparison, high interphase thickness around NBCs is revealed relative to those in the vicinity of HNTs and Cloisite 30B clays, resulting in stronger bonding effect between nanofillers and polymer matrices. Consequently, it is proven from our results that

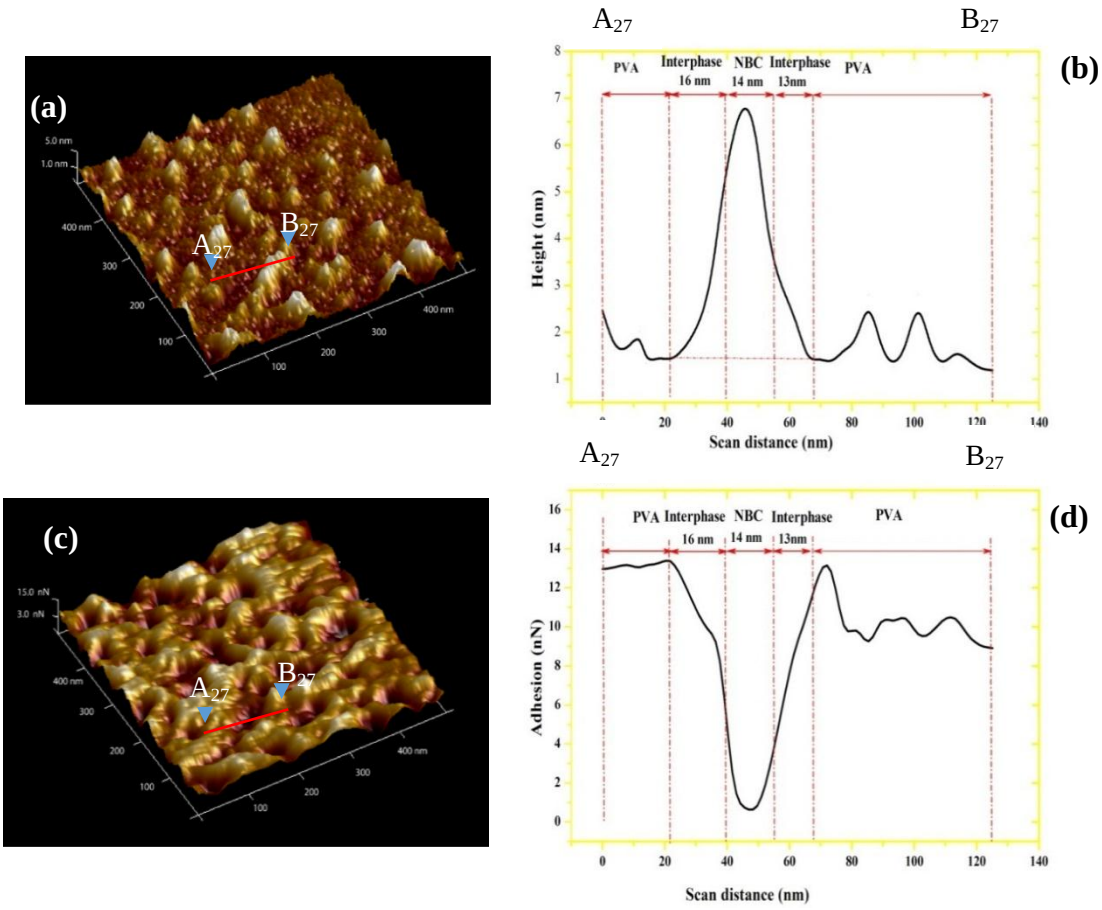

Figure 6.5 (a) 3D AFM height mapping image of PVA/ 3 wt% NBC nanocomposites, (b) height profile of the sample taken along the red line $A_{27}B_{27}$, (c) 3D AFM adhesion mapping image of PVA/3 wt% NBC nanocomposites, and (d) adhesion profile of sample taken along the the line line $A_{27}B_{27}$.

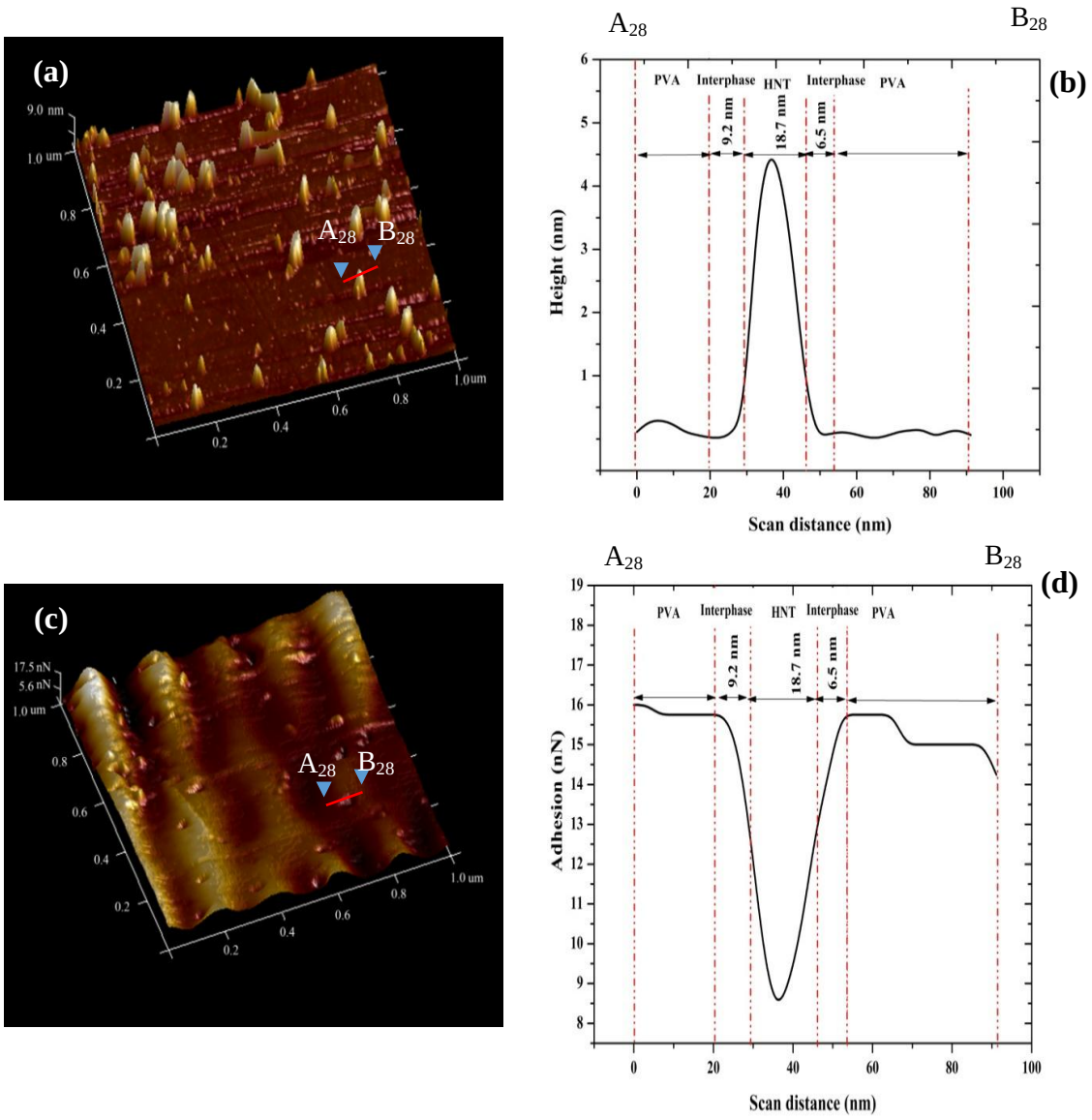

Figure 6.6 (a) 3D AFM height mapping image of PVA/ 3 wt% HNT nanocomposites, (b) height profile of the sample taken along the line $A_{28}B_{28}$, (c) 3D AFM adhesion mapping image of PVA/3 wt% HNT nanocomposites and (d) adhesion profile of sample taken along the line $A_{28}B_{28}$.

interphase thickness $t_{Interphase}$ is a non-uniform and non-constant quantity as far as interphase dimensions are concerned. The uniformity of $t_{Interphase}$ is most likely to be associated with the number of chemical hydrogen bonds and physical roughness

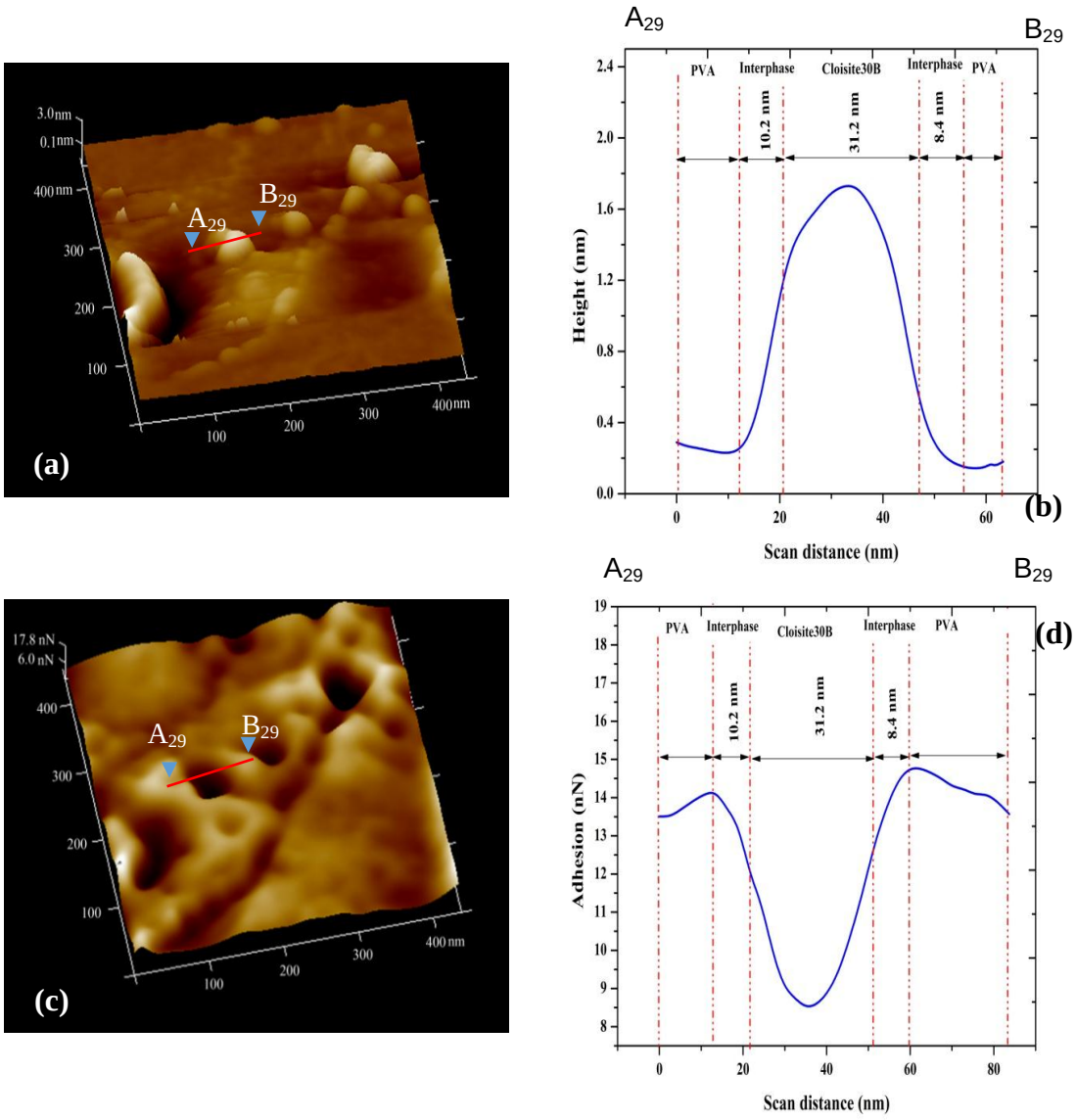

Figure 6.7 (a) 3D AFM height mapping image of PVA/ 3 wt% Cloisite 30B clay nanocomposites, (b) height profile of corresponding nanocomposites taken along the line $A_{29}B_{29}$, (c) 3D adhesion mapping image of PVA/ 3 wt% Cloisite 30B clay nanocomposites, and (d) adhesion profile of corresponding nanocomposites taken along the line $A_{29}B_{29}$.

of NBC surfaces [193, 209, 323]. The major drawback in previous work lies in a simple assumption of one-dimensional interphase layers with contant interphase thickness. However, our study demonstrates that actual nanointerphases should be investigated from a three-dimensional point of view to identify the non-uniformity

and dimensional variations of interphases in terms of $t_{Interphase}$. Here we successfully identified interphase dimensions in term of interphase width ($W_{\text{Interphase}}$), length ($L_{j\ \text{Interphase}}$) and ($H_{k\ \text{Interphase}}$) among individual NBCs, as shown in Figure 6.8(a). It is clearly seen that the parameters of $L_{\text{Interphase}}$, $W_{\ \text{Interphase}}$ and $H_{\ \text{Interphase}}$ were measure to be 97, 40 and 8 nm, respectively Moreover, as shown in Figure 6.8(b), it appears thate there is no direct relationship between interphase thickness and NBC thickness, suggesting that interphase thickness may be independent of particle thickness.

On the other hand, it is evidently seen from Figures 6.8(b)-(e) that $H_{\ \text{Interphase}}$ tends to decrease in a linear manner with an increase in $H_{\ \text{NBC}}$ while $L_{\text{Interphase}}$ and $W_{\ \text{Interphase}}$ linearly increase with an increase in L_{NBC} and $W_{\ \text{NBC,}}$ respectively. This phenomenon is ascribed to more contact surface areas taking place between polymer matrices and nanoparticles in a nanocomposite system [25]. Interphase behaviour for PVA nanocomposites reinforced with HNTs and Cloisite 30B clays is similar to that in PVA/NBC nanocomposites. Besides, $t_{Interphase}$ is irrelevant to HNT diameter (D_{HNT}) and Cloisite 30B clay thickness ($t_{\text{Cloisite30B}}$), as depicted in Figures 6.9 (a) and (b) accordingly.With increasing $D\text{T}_{\text{HNT}}$ and $W_{\ \text{Cloisite 30B}}$ shown in Figures 6.9 (c) and (d), $W_{\ \text{Interphase}}$ is also enhanced in case of PVA/HNT nanocomposites and PVA/Cloisite 30B clay nanocomposites. Furthermore, $L_{\text{Interphase}}$ in both nanocomposite systems are also enlarged while $H_{\text{Interphase}}$ conversely decreases when L_{HNT} and $L_{\text{Cloisite30B}}$ become larger in Figures 6.9(e)-(h) accordingly.

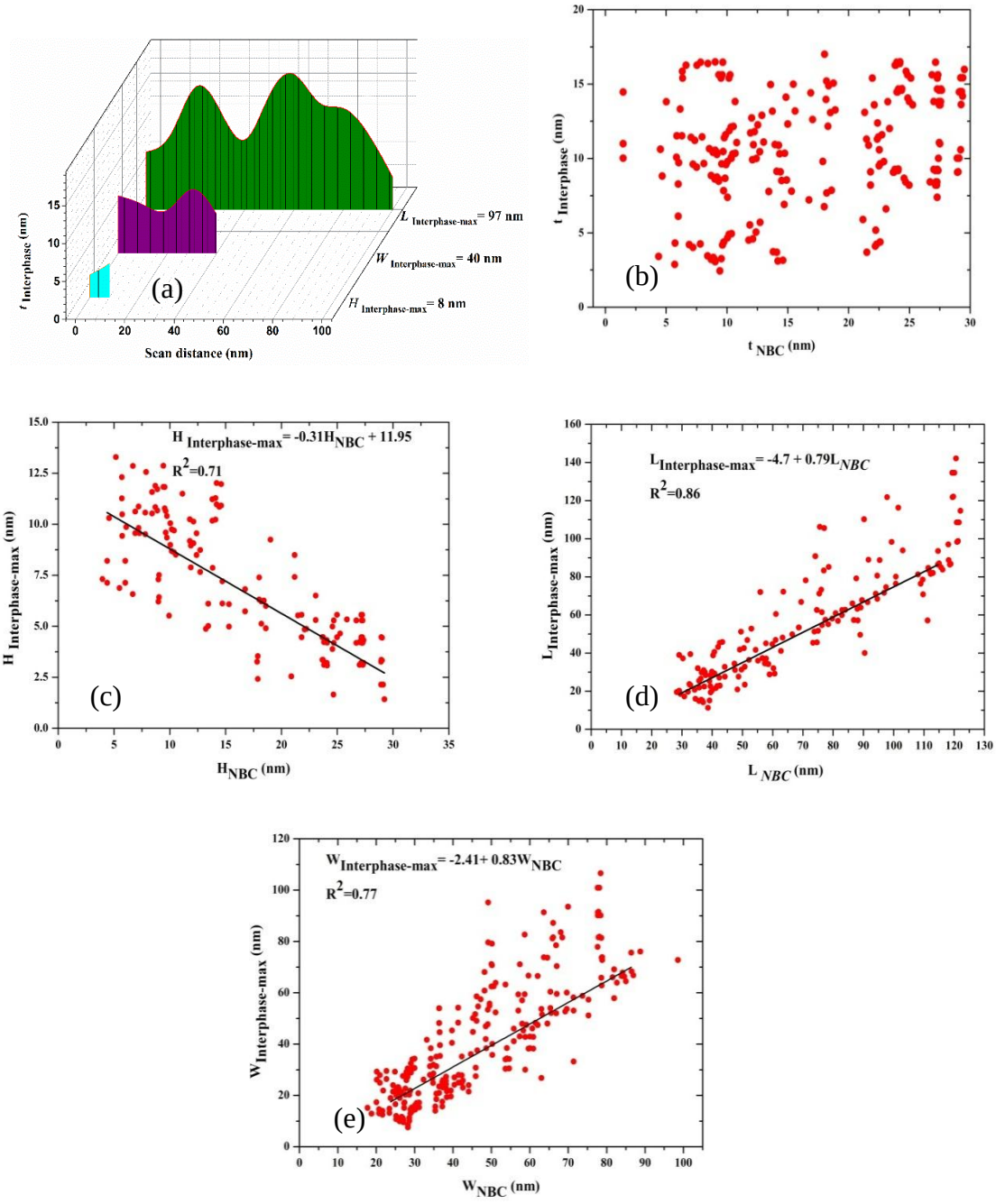

Figure 6.8 (a) Maximum interphase dimensions along typical PVA/NBC interphases and relationships between NBC and interphase dimensionsin PVA/NBC nanocomposites: (b) interphase thickness (tInterphase) and NBC thickness (tNBC), (c maximum interphase height ($H_{\text{Interphase-max}}$) and NBC height ($H_{NBC}$), (d) maximum interphase length ($L_{\text{Interphase-max}}$) and NBC length ($L_{NBC}$) as well as (e) maximum interphase width ($W_{\text{Interphase-max,}}$) and NBC width ($W_{NBC}$).

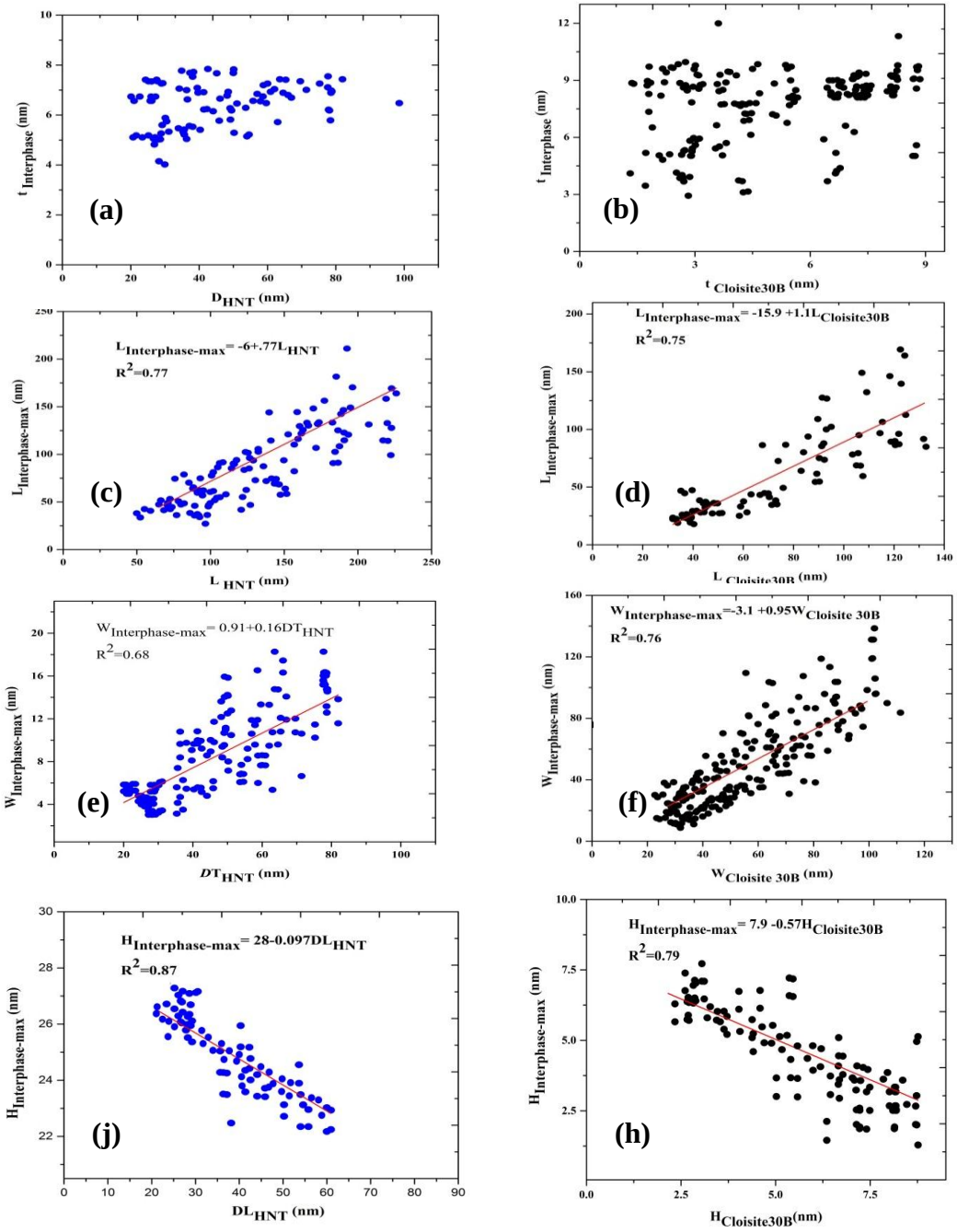

Figure 6.9 Relationship between interphase dimensions and nanofiller dimensions: (a)-(b) interphase thickness ($t_{\text{Interphase}}$) with (a) HNT diameters (D_{HNT}) and (b) Cloisite 30B clay thickness ($t_{Cloisite30B}$), (c)-(d) maximum interphase length ($L_{\text{Interphase-max}}$) with (c) HNT length ($L_{HNT}$)and (d) Cloisite 30B clay length ($L_{Cloisite30B}$), (e)-(f) maximum interphase width ($W_{\text{Interphase-max,}}$) with (e) HNT transverse diameters (DT_{HNT}) and (f) Cloisite 30B clay width ($W_{Cloisite30B}$),and(e)-(f) maximum interphase height ($H_{\text{Interphase-max}}$) with (g) HNT longitudinal diameters (DL_{HNT}) and (h) Cloisite 30B clay height ($H_{\text{Cloisite 30B}}$).

A proposed mechanism model in terms of effects of nanofiller dispersion and particle-matrix interaction is demonstrated in Figures 6.1. It is identified in this study two typical categories for the particle-matrix interaction can be addressed including fully embedded and partially embedded nanoparticles within PVA matrices. The former yields more effective interphases surrounding each side of nanoparticles (i.e. full coverage of nanoparticles by the interphases), which is considered as a good representation for effective load transfer from matrices to nanofillers. The latter offers less pronouced interphase effectiveness since some remarkable portions of nanoparticles are free of contact with PVA matrices, leading to the reduction of more effective interfacial regions. Interphase volume $V_{\text{Interphase}}$ is regarded as an essential characteristic parameter to evaluate the effects of fully or partially embedded nanoparticles in PVA based nanocomposites, which can be specified as $(V_{\text{Interphase}})_f$ and $(V_{\text{Interphase}})_p$, respectively. Figures 6.10(c), Figures 6.11(a) and (b) displays the interphase modulus ($E_{Interphase}$) as a function of $SA_{outer\ interface}$ and $SA_{inner\ interface}$ in case of fully and partially embedded nanoparticles within PVA matrices in, PVA/NBC nanocomposites, PVA/HNT nanocomposites and PVA/Cloisite 30B nanocomposites, respectively. All three nanocomposite types demonstrated the same behaviour with increasing $SA_{outer\ interface}$ and $SA_{inner\ interface}$, $E_{Interphase}$ can be improved remarkably in a non-linear manner accordingly. In particular, fully embedded HNT, Cloisite30B and NBC yield consistently higher interphase modulus as opposed to partially embedded corresponding nanoparticles when either inner or outer interface is considered. Elastic properties of interphases are strongly affected by interphase dimensions since interphase modulus tends to become higher with increasing surface areas of outer and inner interfaces In particular, as for fully embedded HNTs, Cloisite 30B clays and NBCs, a higher modulus increasing trend was evident as opposed to that based

on partially embedded corresponding nanoparticles. This finding suggests that interphases can play a more important role in enhancing mechanical properties of PVA nanocomposites with better bonded matrix-filler interactions. Moreover, it has also been detected that the surface area of inner interface gives rise to relatively high overall interphase modulus in contrast with corresponding surface area of outer interface. As mentioned earlier by Liu *et al.*[322], the interphase zone with modulus gradient effect can be divided into two different regions, namely Region 1 and Region 2 for a typical case in Figure 6.10 (d), in which Region 1 is in contact with nanoparticles zones with relatively high interphase density when compared with Region 2. Additionally, Fan *et al.* [324] reported that increasing the interphase density inevitably led to the modulus enhancement for the same type of materials in good accordance with high interphase modulus results obtained in case of the surface area of inner interface. Apparently, the right boundary of Region 1 where inner interface is located is adjacent to nanoparticles zones with higher density and elastic modulus. The relationship between interphase modulus and interphase volume is demonstrated in Figure 6.10 (e), Figures 6.11 (c) and (d) in case of PVA/NBC nanocomposites, PVA/HNT nanocomposites and PVA/Cloisite 30B clay nanocomposites, respectively, on the basis of fully and partially embedded nanoparticles in PVA based nanocomposites. It is clearly identified that the significant enhancement of interphase modulus takes place with increasing interphase volume, which is similar to the case by increasing $SA_{Interphase.}$ The same applies to fully embedded nanoparticles, resulting in much greater interphase modulus than partially embedded counterparts in terms of interphase volume in PVA based nanocomposites.

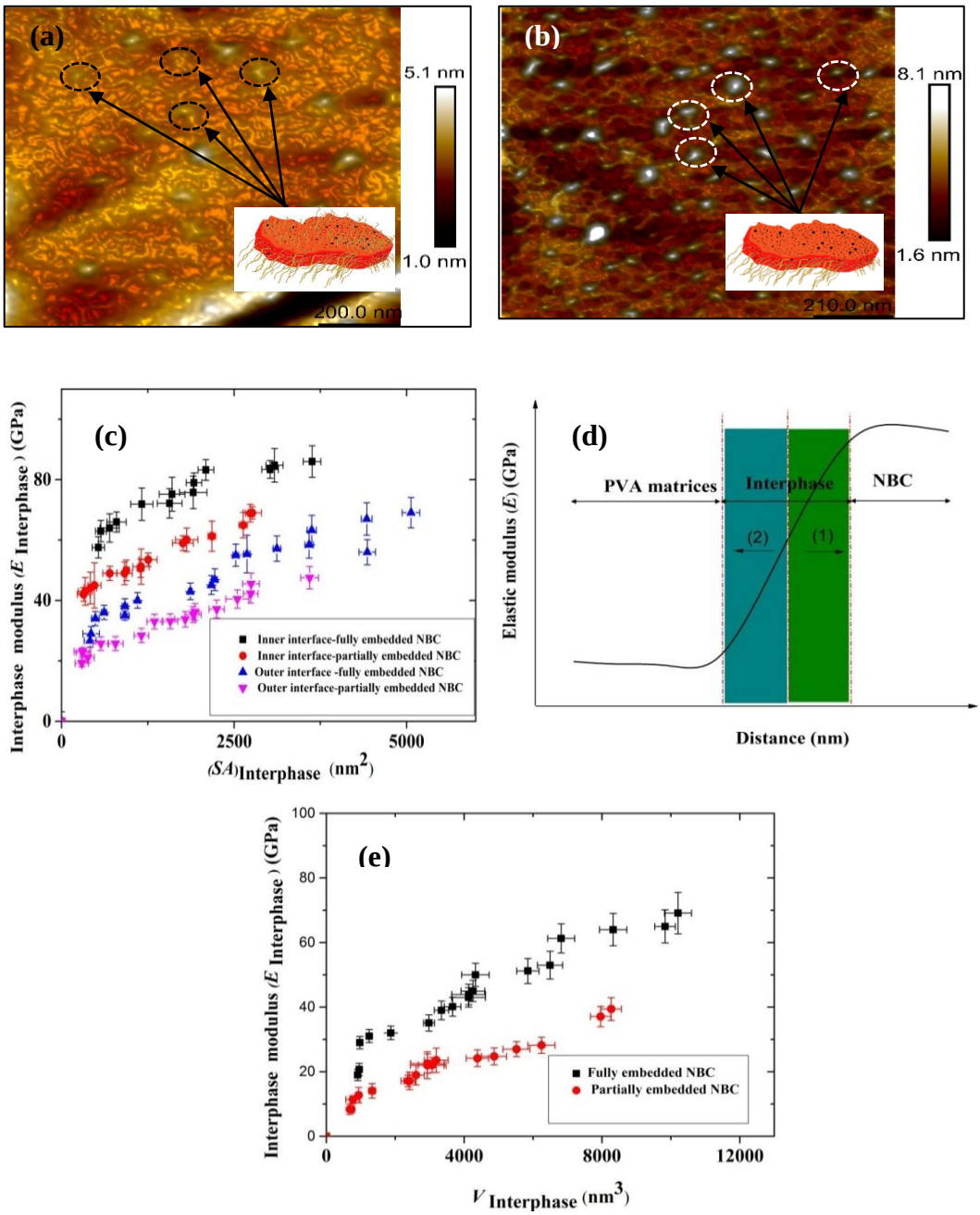

Figure 6.10 2D AFM height mapping images of PVA/NBC nanocomposites: (a) fully embedded NBCs and (b) partially embedded NBCs, (c) relationship between interphase area ($SA_{\text{Interphase}}$) and interphase modulus ($E_{Interphase}$), (d) schematic diagram for two proposed interphase zones and (e) relationship between interphase volume ($V_{Interphase}$) and interphase modulus ($E_{Interphase}$).

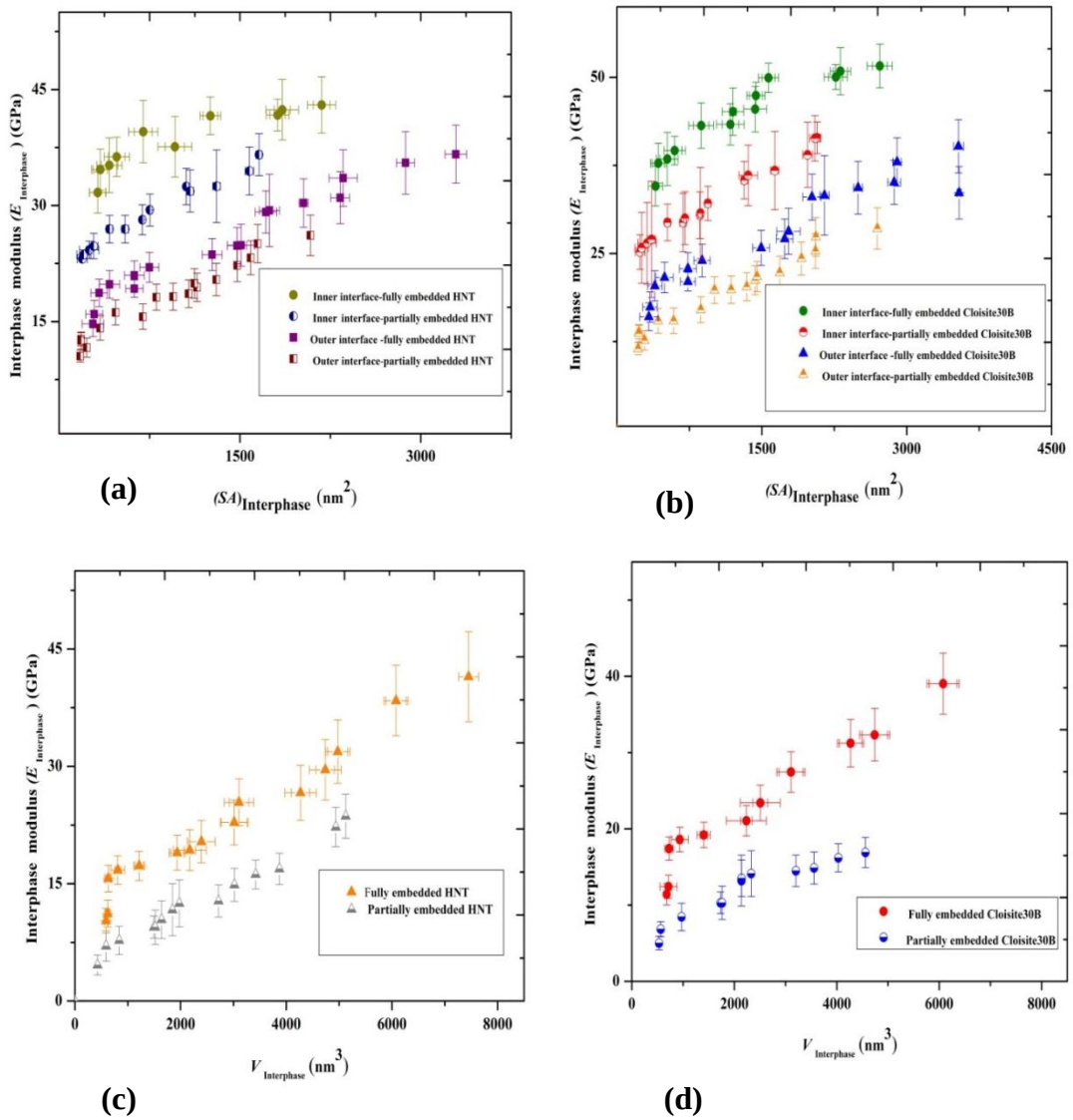

Figure 6.11 Relationships between interphase surface area ($SA_{\text{Interphase}}$) and interphase modulus ($E_{Interphase}$) in (a) PVA/HNT nanocomposites and (b) PVA/Cloisite 30B clay nanocomposites, as well as relationships between interphase volume ($V_{Interphase}$) and interphase modulus ($E_{Interphase}$) in (c) PVA/HNT nanocomposites and (d) PVA/Cloisite 30B clay nanocomposites.

Aspect ratio is used as an important factor to evaluate the reinforcement efficiency of nanofillers within polymer matrices. The determination of aspect ratio can be much easier when dealing with nanofillers in regular size and shape. However, in reality irregular nanofillers in different shapes often occur leading to the complexity of aspect ratios due to the effect of multi-stage dispersion processing techniques used in

manufacturing nanocomposites [309]. In addition to aspect ratios of nanofillers, interphase dimensions and properties can also be affected by the nanofiller dispersion. Liu and Brinson [309] and the other co-worker [305] suggested based on theoretical modelling that an effective parameter in controlling the reinforcement efficiency of nanofillers is the interphase volume per unit nanofiller volume ($V_{interphase}/ V_{nanofillers}$) instead of $V_{interphase}$ alone. In this work, $V_{interphase}/ V_{nanofillers}$ have been implemented in PVA nanocomposites for all three nanofillers used with results being presented in Figure 6.12. It is clearly observed that with increasing $V_{nanofillers}$, $V_{interphase}/ V_{nanofillers}$ significantly decreases for PVA nanocomposites reinforced with NBCs and Cloisite 30B clays though this tendency becomes less pronounced for PVA/HNT nanocomposites. Overall, the inclusion of NBCs in PVA nanocomposites induces the highest $V_{interphase}/ V_{nanofillers}$ when compared with those of HNTs and Cloisite 30B clays. This finding suggests the most effective reinforcement efficiency of NBCs leading to highest mechanical properties of PVA/NBC nanocomposites.

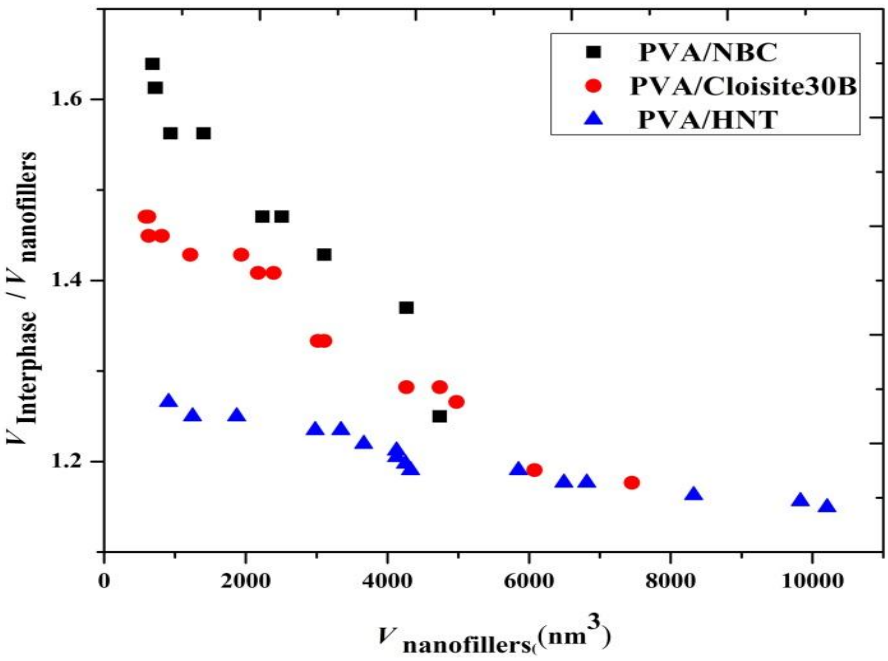

Figure 6.12 $V_{interphase}/ V_{nanofillers}$ as a function of $V_{nanofillers}$ for PVA/NBC nanocomposites, PVA/Closite 30B clay nanocomposites and PVA/HNT nanocomposites.

6.2.4. Particle Debonding

When NBC loading increases up to 5 wt%, interparticle spacing appears to be smaller and NBCs tend to be interconnected with neighbouring particles side by side, illustrated in Figure 6.13 (a), in which contact-free particles are clearly seen on some sides within PVA matrices. Furthermore, a joint particle-to-particle formation may induce the phase separation leading to the scattering of load transfer from PVA matrices to NBCs, as evidenced by the particle overlap of NBCs in Figure 6.13 (b). At the NBC loading of 10 wt%, NBC aggregation appeared to be mainefested with a clear sign of large stacked-up NBC agglomerates, displayed in Figure 6.13 (c). As such, the particle-to-particle separation occurs more evidently with resulting weak interfacial bonding. Figure 6.13 (d) reveals the modulus variation mapping on the surface cross-section of a line scan (i.e. the line between two ovals $A_{30}B_{30}$ in Figure 6.13(c), which highlights two narrow zones with a sharp decline in elastic modulus. In addition to particle dimensions, particle dispersion and distribution patterns in polymer matrices are the other key factors in controlling interfacial bonding between NBCs and PVA matrices in PVA/NBC nanocomposites. When excessive amounts of NBCs are dispersed within PVA matrices, NBCs tend to agglomerate owing to their weak Van der Waals interactions. Additionally, increasing the particle loading inevitably decreases the interparticle spacing, and thus hinders good particle dispersion [192]. Blighe et al. [325] reported that the interparticle spacing was determined to be 6 nm in PVA nanocomposites reinforced with 10 vol% single-walled CNTs (SWCNTs) leading to typical particle aggregation. As a result, the slippage phenomenon of stacked NBCs under mechanical loading gives rise to less effective enhancement level for mechanical properties of nanocomposites. Moreover, Particle agglomeration becomes manifested at high NBC loadings depicted in

Figures 6.13(a)-(d). Such a phenomenon can be explained by Li et al.[193] that in a nanocomposite system, nanoparticles are brushed with modified layers of polymer matrices especially at a high particle volume fraction. Additionally, 'modified polymer shells' surrounding different particles overlap to form continuous phases, which means that such modified polymer shells become the interphases with separated regions from 'parents' matrices', resulting in less desirable properties. Furthermore, some NBCs are unable to actively interact with molecular chains of PVA leading to weaker interfacial bonding and higher possibility of phase separation between NBCs and PVA matrices. This finding is indicative of the existence of particle debonding effect between nanofillers and polymer matrices [59]. It is also worth mentioning that lower interphase modulus can be associated with higher densities of nanoparticles and polymer matrices, as compared to that of interphase zones [318]. The aforementioned NBC dispersion pattern in PVA/NBC nanocomposites suggests that there is a percolation threshold for the NBC loading of 5 wt%, beyond which nanomechanical properties of interphases may diminish in good accordance with PVA/graphene oxide (GO) nanocomposites [324-326].

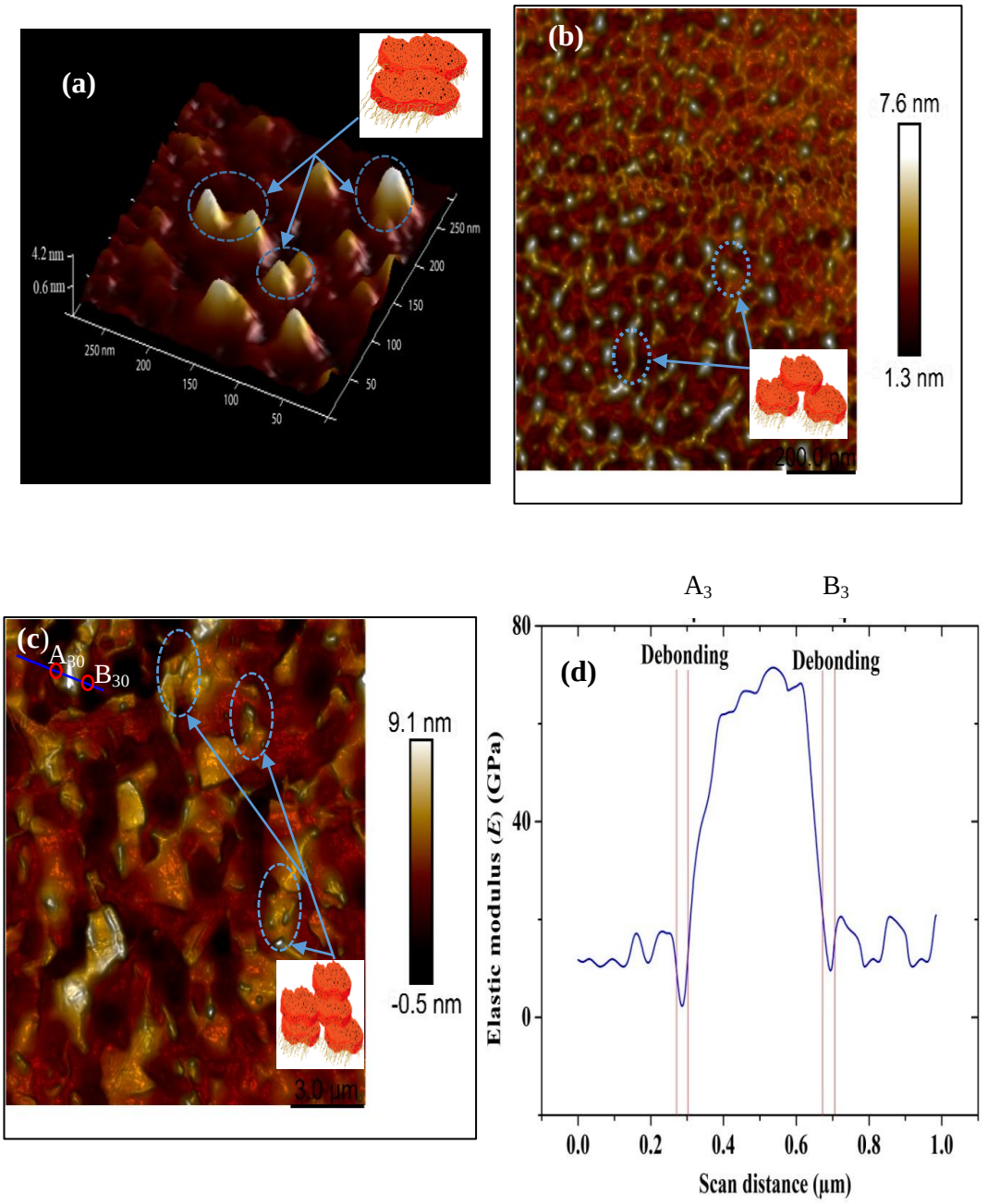

Figure 6.13 (a) Typical 3D AFM height mapping image of PVA/5 wt% NBC nanocomposites with different surface effects: (a) NBC joint edges and (b) NBC overlapping, (c) 2D height mapping image of PVA/10 wt% NBC nanocomposites for phase separation and (d) modulus mapping profile of PVA/10 wt% NBC nanocomposites cut along the red line A_{30} B_{30}.

In case of PVA nanocomposites reinforced with Cloisite 30B clays and HNTs depicted in Figures 6.14(a) and (d), a very similar phenomenon was also noticed that the distance between nanofillers of both Cloisite 30B clays and HNTs decreases to

cause particle overlap and agglomeration when nanofiller loading increases accordingly. It is very clearly shown in Figure 6.14 that Cloisite 30B clay aggregates reveal typical stacks of layered structures. On the other hand, typical debonding effect takes place with the addition of exceesive amounts of Cloisite 30B clays and HNTs, Figures 6.14 (c) and (f), respectively. Nonetheless, as seen from Figures 6.14 (b), (d) and (e), Cloisite 30B clays agglomerated and formed large stacks of layered structures as well as HNTs seem to easily form large particle agglomerates when compared with NBCs. Such results can be associated with their relatively high aspect ratios prone to considerable particle waviness to deteriorate their reinforcement efficiency, thus resulting in less favourable mechanical properties of correponding PVA nanocomposites. In addition, nanofiller dispersion methods such as ultrasonication [305] can also give rise to possible structure damage of nanofillers with high ultrasonic power intensity with resulting declined properties, as evidenced by AFM images of HNTs and Cloisite 30B clays in Figures 5.3(a) and 5.4(a) .

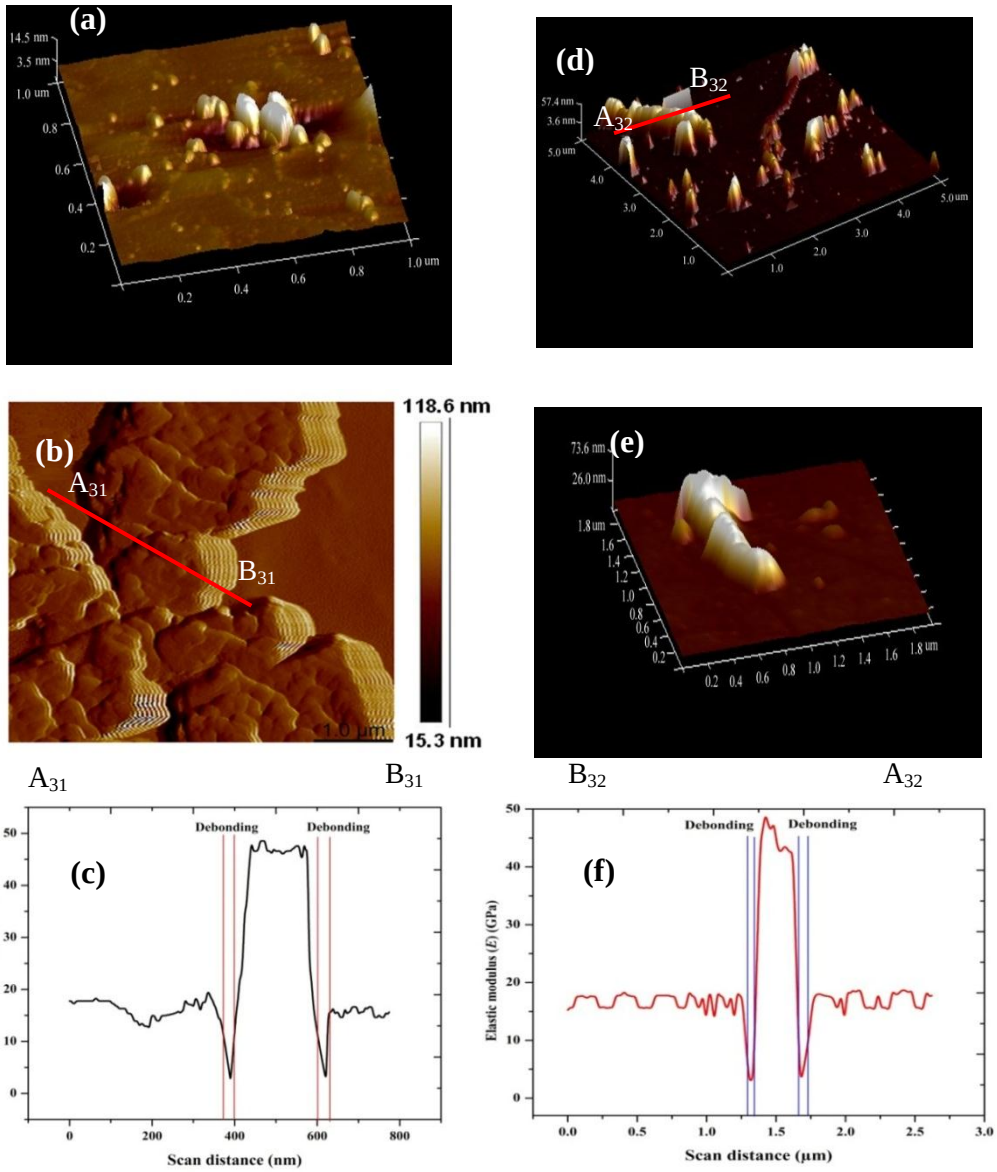

Figure 6.14 (a) Typical 3D height mapping image of PVA/5 wt% Cloisite 30B clay nanocomposite surfaces, (b) 2D height mapping image of PVA/5 wt% Cloisite 30B clay nanocomposite surfaces for phase separation, (c) elastic modulus mapping profile of PVA/10 wt% Cloisite 30B clay nanocomposite sample cut along the red line $A_{31}B_{31}$,(d). 3D height mapping image of PVA/5 wt% HNT nanocomposite surfaces for phase separation, (f) elastic modulus mapping profile of PVA/10 wt% HNT nanocomposite sample cut along the red line $A_{32}B_{32}$, (d) and (e). 3D height mapping image of PVA/10 wt% HNT nanocomposite surfaces for HNT agglomeration.

6.3. Summary

In this chapter, the following key points are summarised:

- A pioneering approach has been developed for determining nanoelastic behaviour of PVA nanocomposites as well as 3D interphase dimensions and interphase moduli in terms of surface area and interphase volume.
- Experimental characterisation results indicate that interphase thickness appears to be non-uniform among individual particles and independent of particle thickness.
- Interphase modulus in PVA based nanocomposite system is enhanced with increasing interphase volume. Moreover, interphase modulus in case of PVA/NBC nanocomposites is higher than those for PVA/Cloisite 30B clay nanocomposites and PVA/HNT nanocomposites based on $V_{\text{interphase}}/ V_{\text{nanofillers}}$.
- Nanomechanical properties and sizes of interphases depend greatly on nanofillers dispersion status. Nevertheless, increasing nanofillers loading was found to result in the decrease in intraparticle spacing leading to particle agglomeration with the interfacial debonding effect between PVA matrices and nanoparticles.
- Two key geometric parameters of interphase surface area and interphase volume are detected to be non-constant variables potentially influenced by nanofiller dimensions and sizes, as well as nanofiller dispersion states. Our approach enlightens an more effective approach to consider actual interphase properties in theoretical and numerical modelling framework instead of using a simple assumption of single interphase layer dimensions and uniform interphase properties in order to achieve more accurate property prediction.

Chapter 7.

Micromechanical Models of PVA Based Nanocomposite Films

7.1. Theory

7.1.1. Micromechanical Model Based on Nominal and Effective Volume Fractions

In general, the prediction of elastic modulus in case of unidirectional or randomly distributed filler reinforced composites can be investigated by means of conventional composite theoretical models such as Halpin-Tsai model. Such a model could also be employed to estimate elastic moduli of PVA based nanocomposites with different nanofiller orientation states, namely well-aligned and randomly oriented nanofillers, which are denoted as E_{random} and $E_{parallel}$, respectively in the following equations:

$$\boldsymbol{E_{random}} = \boldsymbol{E_m}\ \left[\frac{\mathbf{3}}{\mathbf{8}}\frac{\mathbf{1}+\boldsymbol{\eta_L}\boldsymbol{\xi}\,\boldsymbol{\emptyset_p}}{\mathbf{1}-\boldsymbol{\eta_L}\boldsymbol{\emptyset_p}}+\frac{\mathbf{5}}{\mathbf{8}}\frac{\mathbf{1}+\mathbf{2}\boldsymbol{\eta_T}\,\boldsymbol{\emptyset_p}}{\mathbf{1}-\boldsymbol{\eta_T}\boldsymbol{\emptyset_p}}\right] \tag{7.1}$$

$$E_{parallel} = E_m\ \left[\frac{1+\eta_L\xi\,\emptyset_p}{1-\eta_L\emptyset_p}\right] \tag{7.2}$$

$$\eta_L = \frac{\left(E_p/E_m\right)-1}{\left(E_p/E_m\right)+\xi} \tag{7.3}$$

$$\eta_T = \frac{\left(E_p/E_m\right)-1}{\left(E_{fp}/E_m\right)+2} \tag{7.4}$$

$$\xi = \frac{2\alpha}{3} = \frac{2\iota_p}{3t_p} \tag{7.5}$$

$$\emptyset_p = \frac{W_p}{W_p + \left(\rho_p/\rho_m\right)\left(1-W_p\right)} \tag{7.6}$$

Where E_{random} and $E_{parallel}$ represent Young's moduli of PVA based nanocomposites reinforced with randomly oriented nanofillers and well-aligned nanofillers parallel to the material surface under unidirectional loading, respectively. E_m and E_p are Young's moduli of PVA matrices and nanoparticles (i.e. NBCs, HNTs and Cloisite 30B clays) accordingly. α, l_f and t_f refer to the aspect ratio, length and thickness of nanoparticles. ϕ_p and W_p are nominal volume fraction and weight fraction of

nanofillers in PVA based nanocomposites, respectively. ρ_p and ρ_m are densities of PVA and nanoparticles. Furthermore, Mori-Tanaka model is also an effective theoretical model to predict elastic moduli of polymer nanocomposites. It was originally employed by Tandon and Weng [327] using Mori-Tanaka theory [53] and Eshelby's solution [328] to derive a complete analytical solution for calculating elastic moduli of an isotropic matrix containing aligned spheroidal inclusions. Longitudinal and transverse elastic moduli of polymer nanocomposites (E_{11}) and (E_{22}) can be experessed as follows:

$$\frac{\boldsymbol{E_{11}}}{\boldsymbol{E_m}} = \frac{\mathbf{1}}{\mathbf{1} + \emptyset_{\boldsymbol{p}}(\boldsymbol{A_1} + \mathbf{2}\boldsymbol{\nu_m}\boldsymbol{A_2})/\boldsymbol{A}} \tag{7.7}$$

$$\frac{E_{22}}{E_m} = \frac{1}{1 + \emptyset_p(-2\nu_m A_3 + (1-\nu_m)A_4 + (1+\nu_m)A_5 A)/2A} \tag{7.8}$$

where ν_m is the Poisson's ratio of polymer matrices and the A_i (i =1-5) are the functions of Eshelby's tensors and properties of the matrices and fillers such as Young's modulus, Poisson's ratio, aspect ratio and volume fraction of fillers (see Appendix B for more details). When nanofillers are inclined to more random orientation, elastic modulus of nanocomposites can be further predicted by using the combination of laminate theory [329] and Mori-Tanaka model given by:

$$\boldsymbol{E_c \cong 0.375E_{11} + 0.625E_{22}} \tag{7.9}$$

In a nanocomposite system, large specific surface area of nanofillers renders the amounts of polymeric molecular chains to attach to nanofiller surfaces in order to generate interphases in nanocomposites, which means that nominal volume fraction of nanofillers may be altered when reinforced within polymer matrices. As such, effective volume fraction should be used instead for more accurate property prediction in modelling work. Wan and Chen [330] and other co-workers [328, 331]

suugested the following equation to calculate effective volume fraction of nanofillers:

$$\emptyset'_{\boldsymbol{p}} = \emptyset_{\boldsymbol{p}}\left(\mathbf{1} + \boldsymbol{kxRgA_T\rho_p}\right) \quad (7.10)$$

Where A_T and ρ_p are the specific surface area and density of nanofillers, respectively. kx is the layer of absorbed polymeric chains in nanoparticles with a thickness xR_g of the polymer, which means the layer thickness is increased to x times of the radius of gyration of polymer R_g. The value of kx can be changed for different nanocomposite systems due to the variation of interfacial interactions between polymer matrices and nanofillers. Besides, the dynamic behaviour of polymeric chains near attractive interfaces would be different from those bulk polymer phases and the effect of attractive surfaces could be held for the distances larger than the radius of gyration for polymers [332].

The term of kx can be reconsidered based on the equation [328, 330] given below:

$$\boldsymbol{kx} = \frac{\boldsymbol{E_m}}{\boldsymbol{E_p}}\left(\frac{\boldsymbol{t}}{\boldsymbol{Rg}}\right) \quad (7.11)$$

where t is regarded as the thickness of adsorbed layers. In case of organoclay based nanocomposite, the effective volume fraction can depend on whether intercalation or exfoliation of organoclays taking place within polymer matrices in nanocomposites. In case of organoclay intercalated structures $\emptyset'_p$ can be estamiated as follows:

$$\frac{\mathbf{1}}{\emptyset'_{\boldsymbol{p}}} = \mathbf{1} + \frac{\boldsymbol{\rho'_p}(\mathbf{1} - \boldsymbol{W_p W'_p S})[\boldsymbol{d'_1}(\boldsymbol{N} - \mathbf{1}) + \boldsymbol{h}]}{\boldsymbol{W_p \rho_p}[\boldsymbol{d_2}(\boldsymbol{N} - \mathbf{1}) + \boldsymbol{h}]} \quad (7.12)$$

where ρ'_p is referred to as the density of organoclay. W_p is the weight fraction of organoclays in nanocomposites, and W'_p is the weight fraction of clay platelets

within organoclays. S is the polymer uptake in the generic expression $S = (1 - W_p^1)/W_p^1$ to represent the mass of polymers swollen into the unit mass of intercalated clays where W_p^1 is the weight fraction of intercalated clay structures. d'_1 is the basal plane spacing of organoclays. N and h are the average layer number per stack and thickness of platelets, respectively. In case of exfoliated organoclay structures, when clay platelets are dispersed homogeneously in polymer matrices, the effective volume fraction can be calculated according to equation (7.10). The main difference from conventional nanocomposites is the adsorption effect. In equation (7.10), the specific surface area of clay platelets (A_{T}) becomes their total surface area (A_{Tp}), and the density of nanoparticles (ρ_p) is converted into the density of clay platelets (p_p^p). Hence equation (7.10) can be rewritten below:

$$\emptyset_p' = \emptyset_p\left(1 + \boldsymbol{kxRgA_{Tp}p_p^p}\right) \quad (7.13)$$

7.1.2. Micromechanical Model Based on Volume Fraction of Nanofillers and Interphase

The interphase is very critical in nanocomposite systems, which cannot be completely ignored, as mentioned earlier in Chapter 6 since the interphase in PVA based nanocomposites was in possession of non-uniform thickness with their corresponding nanomechanical properties mainly depending on 3D interphase dimensions and features. For instance, when the interphase volume in PVA/NBC nanocomposites increased from 2988 to 4363 nm^3, their interphase modulus was significantly enhanced by 44% from 34.67 to 49.91GPa, as shown in Figure 6.9 (e). Consequently, the implementation of 3D interphase features in terms of interphase size and volume fraction to predict elastic modulus of polymer nanocomposites can induce a more reliable modelling approach for the estimation of bulk nanocomposite

properties according to their nanomechanical behaviour. A simple equation proposed to calculate the volume fraction of nanofillers based on interphase features is given below:

$$\emptyset_{\boldsymbol{p}} = \frac{\emptyset_{\mathbf{Interphase}}\, \boldsymbol{V_p}}{\boldsymbol{V_{interphase}}} \tag{7.14}$$

where $\emptyset_{\mathrm{Interphase}}$ is the volume fraction of interphases surrounding anisotropic nanoparticles, which can be estimated by using the theory of nearest-surface distribution function [333] detailed in the next section. $V_{interphase}$ and V_p are the volumes of interphase and nanoparticles, respectively, which can be estimated according to corresponding equations (6.5) and (6.7).

7.1.3. Interphase Volume Fraction ($\emptyset_{\mathbf{Interphase}}$)

Theoretical interfacial volume fraction can be derived from the nearest-surface distribution theory [333], in which composite media are composed of 3D rigid particles and voids. Lu and Torquato [333] employed statistical geometries of composites and geometric probability to determine a void exclusion probability $e_{\mathrm{v}}(r)$, which is defined as the probability of a designated empty region of composite media with the radius of particle cavities *r* at an arbitrary point. Accordingly, $e_{\mathrm{v}}(r)$ can be given by

$$\boldsymbol{e_{\mathrm{v}}(r) = (1-\eta)\exp[-\pi\rho(er + dr^3 + gr^3)]} \tag{7.15}$$

$$e = \frac{4\langle R^2\rangle}{1-\eta} \tag{7.16}$$

$$d = \frac{4\langle R\rangle}{1-\eta} + \frac{8\pi\rho\langle R^2\rangle^2}{(1-\eta)^2} \tag{7.17}$$

$$\mathrm{g} = \frac{4}{3(1-\eta)} + \frac{16\pi\rho\langle R\rangle\langle R^2\rangle}{3(1-\eta)^2} + \frac{64m\pi^2\rho^2\langle R^2\rangle^3}{27(1-\eta)^3} \tag{7.18}$$

In practice, $e_{\mathrm{v}}(r)$ represents the expected void fraction in such a two-phase composite system [334]. m is a parameter associated with the theoretical estimation of the radial distribution function in a spherical particle system. In particular, m=2 has been used in this study based on Carnahan-Starling approximation [335]. ρ is the number density of isotropic particles with a radius R. η can be further calculated according to equation (7.19) as follows:

$$\boldsymbol{\eta = \rho\langle V\rangle = \rho\frac{\pi^{3/2}\langle R^3\rangle}{\Gamma(1+3/2)} = \frac{4\pi}{3}\,\rho\,\langle R^3\rangle} \qquad (7.19)$$

where $\langle V\rangle$ is the average volume of hard particles, $\Gamma(x)$ is the gamma function. According to quantitative stereology [336], η denotes the volume fraction of 3D rigid particles.

Composite materials are supposed to consist of a packing of rigid particles and matrices, $e_{\mathrm{v}}(r)$, as mentioned earlier, can thus be considered as the matrices in a two-phase composite material. When a three-phase composite material, consisting of rigid nanoparticles, matrices and soft-shell interphases (layer thickness $r = t$) surrounding particles, is taken into consideration, the combination of each of isotropic particles and associated soft-shell interphase can be regarded as a composite particle. Therefore, a three-phase composite system can be simplified as a two-phase equivalent system including rigid composite particles (i.e. original particles and corresponding interphases), as well as matrices. Nonetheless, for such a three-phase composite system, $e_{\mathrm{v}}(t)$ is not applicable for equations (7.15)-(7.18), but can be subjected to the geometric configuration of anisotropic particles instead. The incorporation of geometric details of particles yields the modified equations given by:

$$\boldsymbol{e_v(t) = (1-\eta)\exp[-\pi\rho(et + dt^3 + gt^3)]} \quad (7.20)$$

$$e = \frac{\langle S\rangle}{\pi(1-\eta)} \quad (7.21)$$

$$d = \frac{4\langle R\rangle}{1-\eta} + \frac{\rho\langle R^2\rangle}{2\pi(1-\eta)^2} \quad (7.22)$$

$$g = \frac{4}{3(1-\eta)} + \frac{4\rho\langle R\rangle\langle S\rangle}{3(1-\eta)^2} + \frac{m\rho^2\langle S\rangle^3}{27\pi(1-\eta)^3} \quad (7.23)$$

Where $\langle S\rangle$ is the average area of rigid particles. According to equations (7.20)-(7.23), it can be clearly shown that $e_v(t)$ depends primarily on R, ρ, and surface area of isotropic particles S. Similarly, in an anisotropic particle system $e_v(t)$ should be calculated based on the geometric details of such particles. Hence, the key step is how to determine these characteristic parameters of anisotropic particles. According to the previous studies [337, 338], an equivalent diameter (D_{eq}) is widely used as an alternative dimension of anisotropic irregular particles with complex geometries. The number density of anisotropic particles can be estimated by a quantitative stereological theory [336], which is equal to the ratio of the volume fraction of solid phase to the average volume of rigid particles, or the ratio of specific surface area of solid phase to the average surface area of rigid particles. In terms of $D_{eq,}$ average volume$\langle V\rangle$ and average surface area $\langle S\rangle$ of anisotropic particles can be calculated as

$$\boldsymbol{\langle V\rangle = \frac{\pi}{6}\ \langle D_{eq}^3\rangle, \langle S\rangle\ = \frac{\pi}{s}\ \langle D_{eq}^2\rangle} \quad (7.24)$$

The volume fraction of solid phase with various geometries has been found to be relatively similar to the volume fraction of rigid particles [339]. As a result, the number density (N_V) of anisotropic particles is given by the stereological theory shown below

$$\boldsymbol{N_V = \frac{V_p}{\langle V\rangle}\ = \frac{S_V}{\langle S\rangle}\ = \frac{6V_p}{\pi\langle D_{eq}^3\rangle}} \quad (7.25)$$

where S_{V} is the specific surface area of rigid anisotropic particles. By substituting equations (7.24) and (7.24) into equations (7.20)-(7.23), $e_{\mathrm{v}}(t)$ for composite materials reinforced with anisotropic particles can be expressed as

$$\boldsymbol{e_{\mathrm{v}}(t) = (1 - \mathrm{V}_p)\exp\left[-\frac{6\mathrm{V}_p}{\langle D_{eq}^3\rangle}(e't + d't^3 + \mathrm{g}'t^3)\right]} \tag{7.26}$$

$$\emptyset_{\mathrm{interphase}} = 1 - \mathrm{V}_p - e_{\mathrm{v}}(t) = (1 - \mathrm{V}_p)\left\{1 - \exp\left[-\frac{6\mathrm{V}_p}{\langle D_{eq}^3\rangle}(e't + d't^3 + \mathrm{g}'t^3)\right]\right\} \tag{7.27}$$

In a PVA based bionanocomposite system, V_p represents the nominal volume fraction of nanofillers ($\emptyset_{p-\mathrm{nominal}}$). As such, the equation (7.27) can be rewritten as:

$$\emptyset_{\mathbf{Interphase}} = \left(1 - \emptyset_{p-\mathbf{nominal}}\right)\left\{1 - \exp\left[-\frac{6\emptyset_{p-\mathbf{nominal}}}{\langle D_{eq}^3\rangle}(e't + d't^3 + \mathrm{g}'t^3)\right]\right\} \tag{7.28}$$

$$e' = \frac{\langle D_{eq}^2\rangle}{S(1 - \emptyset_{p-\mathrm{nominal}})} \tag{7.29}$$

$$d' = \frac{2\langle D_{eq}\rangle}{1 - \emptyset_{p-\mathrm{nominal}}} + \frac{3\emptyset_{p-\mathrm{nominal}}\langle D_{eq}^2\rangle^2}{S^2(1 - \emptyset_{p-\mathrm{nominal}})^2\langle D_{eq}^3\rangle} \tag{7.30}$$

$$\mathrm{g}' = \frac{4}{3(1 - \emptyset_{p-\mathrm{nominal}})} + \frac{4\emptyset_{p-\mathrm{nominal}}\langle D_{eq}\rangle\langle D_{eq}^2\rangle}{S(1 - \emptyset_{p-\mathrm{nominal}})^2\langle D_{eq}^3\rangle} + \frac{4m\emptyset_{p-\mathrm{nominal}}\langle D_{eq}^2\rangle^3}{3S^3(1 - \emptyset_{p-\mathrm{nominal}})^3\langle D_{eq}^3\rangle^2} \tag{7.31}$$

$$S = \frac{(1 + 1.5\alpha)^{2/3}}{1 + \alpha} \tag{7.32}$$

In a typical nanocomposite system, nanoparticles can be dispersed uniformly with relatively similar sizes, which are known as monodispersed nanoparticles [340]. On the contrary, when nanoparticles with different sizes and diameters are dispersed randomly, they are called polydispersed nanoparticles [340].

In the case of a monodispersed particle system, the parameters e', $d'$and g' are expressed as:

$$\boldsymbol{e'} = \frac{\boldsymbol{D_{eq}^2}}{\boldsymbol{S(1-\emptyset_{p-nominal})}} \tag{7.33}$$

$$d' = \frac{2D_{eq}}{1-\emptyset_{p-\mathrm{nominal}}} + \left[2 + \frac{3\emptyset_{p-\mathrm{nominal}}}{S^2(1-\emptyset_{p-\mathrm{nominal}})}\right] \tag{7.34}$$

$$\mathrm{g}' = \frac{4}{3(1-\emptyset_{p-\mathrm{nominal})}} + \left[\frac{1}{3} + \frac{\emptyset_{p-\mathrm{nominal}}}{S\,(1-\emptyset_{p-\mathrm{nominal}})} \quad + \quad \frac{m\,\emptyset_{p-\mathrm{nominal}}^2}{3S^3\,(1-\emptyset_{p-\mathrm{nominal}})^2}\right] \tag{7.35}$$

By substituting equations (25)-(27) into equation (20), and then letting $\lambda = \frac{t}{D_{eq}}$, $\emptyset_{\mathrm{Interphase}}$, one can obtain

$$\emptyset_{\mathbf{Interphase}} = \left(\mathbf{1}-\emptyset_{\boldsymbol{p-nominal}}\right)\left\{\mathbf{1}-\mathbf{exp}\left[-\frac{6\emptyset_{\boldsymbol{p-nominal}_p}\boldsymbol{\lambda^3}}{\mathbf{1}-\emptyset_{\boldsymbol{p-nominal}}}\left[\frac{\mathbf{1}}{\boldsymbol{S\lambda^2}}+\frac{\mathbf{1}}{\boldsymbol{\lambda}}\left[\mathbf{2}+\frac{\mathbf{3}\emptyset_{\boldsymbol{p-nominal}_p}}{\boldsymbol{S^2(1-\emptyset_{p-nominal})}}\right]+\right.\right.\right. \tag{7.36}$$
$$\left.\left.\left.\frac{\mathbf{4}}{\mathbf{3}}+\frac{\mathbf{4}\emptyset_{\boldsymbol{p-nominal}_p}}{\boldsymbol{S(1-\emptyset_{p-nominal})}}+\frac{\mathbf{4}\boldsymbol{m}\emptyset_{\boldsymbol{p-nominal}}^{\mathbf{2}}}{\mathbf{3}\boldsymbol{S^3(1-\emptyset_{p-nominal})^2}}\right]\right]\right\}$$

where λ represents the geometric size factor of anisotropic particles.

On the contrary, with respect to a polydispersed particle system, it is necessary to evaluate the effect of particle size distribution (PSD) on both volume fraction of interphases and reinforcement efficiency of nanocomposites. The gradation of irregular aggregates can be experimentally investigated using a sieve analyser or laser particle analyser where the size of each irregular aggregate is evaluated relative to the corresponding size of spherical particles [65]. The PSD of spherical particles can be transformed into that of anisotropic particles when the equivalent diameter is defined according to previous research work [337]. In this study, two particulate gradations, namely Fuller [339] gradation and equal volume fraction (EVF) [337, 339] gradation, were employed with their specific equations given below:

$$\boldsymbol{F_V(D) = \frac{\sqrt{D} - \sqrt{D_{min}}}{\sqrt{D_{max}} - \sqrt{D_{min}}}} \quad (7.37)$$

$$F_V(D) = \frac{\mathrm{In}D - \mathrm{In}D_{\min}}{\mathrm{In}D_{\max} - \mathrm{In}D_{\min}} \quad (7.38)$$

where $F_V(D)$ is the cumulative volume percentage of isotopic particles with their corresponding diameter of D, in which $D_{\max}$ and D_{min} are the maximum and minimum diameters of isotopic particles, respectively. PSD of anisotropic particles can be connected to that of isotopic particles by substituting D_{eq} into D, as mentioned in equation (7.38). The optimised Fuller and EVF gradations for anisotropic particles are presented in the following equations

$$\boldsymbol{F_V(D_{eq}) = \frac{\sqrt{D_{eq}} - \sqrt{D_{min\,eq}}}{\sqrt{D_{max\,eq}} - \sqrt{D_{min\,eq}}}} \quad (7.39)$$

$$F_V(D_{eq}) = \frac{InD_{eq} - InD_{\min eq}}{InD_{\max eq} - InD_{\min eq}} \quad (7.40)$$

where $F_V(D_{eq})$ should be derived to generate the number of polydispersed particles. The volume-based probability density function $f_V(D_{eq})$ is determined in terms of D_{eq} based upon the first-order derivative of $F_V(D_{eq})$.

$$\boldsymbol{f_V(D_{eq}) = \frac{1}{(\sqrt{D_{max\,eq}} - \sqrt{D_{min\,eq}})\sqrt{D_{eq}}}} \quad (7.41)$$

$$f_V(D_{eq}) = \frac{1}{(InD_{\max eq} - InD_{\min eq})D_{eq}} \quad (7.42)$$

The number dN of particles with various sizes in range of $[D_{eq}, D_{eq} + dD_{eq}]$ is then calculated as:

$$\boldsymbol{dN = \frac{f_V(D_{eq})dD_{eq}}{V(D_{eq})}} \quad (7.43)$$

where V(D_{eq}) is the volume of anisotropic particles. Consequently, the number-based probability density function $f_N(D_{eq})$ for anisotropic particles is expressed as:

$$\boldsymbol{f_N(D_{eq}) = \frac{f_V(D_{eq})}{V(D_{eq})N}} \tag{7.44}$$

and N is define by

$$\boldsymbol{N = \int_{D_{\min eq}}^{D_{\max eq}} \frac{f_V(D_{eq})}{V(D_{eq})}\, dD_{eq}} \tag{7.45}$$

By substituting equations (7.39), (7.40) and (7.45) into equation (7.45), $f_N(D_{eq})$ is given by:

$$\boldsymbol{f_N(D_{eq}) = \frac{-q}{(D_{\max eq}^{-q} - D_{\min eq}^{-q}) D_{eq}^{q+1}}} \qquad \begin{cases} \boldsymbol{q = 2.5 \rightarrow \text{Fuller gradation}} \\ \boldsymbol{q = 3.0 \rightarrow \text{EVF gradation}} \end{cases} \tag{7.46}$$

Moreover, the *k*th moment $\langle D_{eq}^{\,k} \rangle$ of area of $f_N(D_{eq})$ is given by

$$\boldsymbol{\langle D_{eq}^{k} \rangle = \int_{D_{\min eq}}^{D_{\max eq}} D_{eq}^{k} fn(D_{eq}) dD_{eq}} \tag{7.47}$$

By substituting equation (7.46) into equation (4.47), $\langle D_{eq} \rangle$, $\langle D_{eq}^{\,2} \rangle$, and $\langle D_{eq}^{\,3} \rangle$ are obtained to determine the volume fraction of interphases for an anisotropic polydispersed particle system. In addition, the parameters required to calculate $\emptyset_{\text{Interphase}}$ in term of $D_{eq\text{-min}}$, $D_{eq\text{-max}}$, $D_{eq\text{-mean}}$, H and $t_{\text{ interphase}}$, can be then measured for each nanofiller.

7.2. Prediction of Elastic Moduli of PVA Based Nanocomposites

Elastic moduli of PVA/NBC nanocomposites using Halpin-Tsai model based on two different orientation states were compared with experimental data, as depected in

Figure 7.1 (a). In between, modelling parameters in Table 7.1 were utlised to substitute into equations (7.1) - (7.6). Clearly, experimental data for nanocomposite systems are in better agreement with Halpin-Tsai model (parallel) at low NBC nominal volume fractions ranging from 0.085 to 0.137 vol%. However, such data coincide more closely with Halpin-Tsai model (random) at the high NBC norminal volume fraction of 0.251 vol%. This phenomenon suggests that well-aligned NBC uniform dispersion may be prevalent at the low NBC contents while heterogenous and randomly oriented NBCs become quite mainifested due to large NBC agglomeration at the high NBC content levels. The general trend of experimental data in this study falls within the theoretical curves of Halpin-Tsai model (parallel) and Halpin-Tsai model (random) as upper and lower bounds, respectively, in good accordance with previous work on PVA/PVA-g-GO nanocomposites [341].

Moreover, Mori-Tanaka model and the combination of laminate theory [329] and Mori-Tanaka model are also used to predict elastic moduli of PVA/NBC nanocomposite by subsituting the parameters in Table 7.1 into equations (7.7) to (7.9), with associated results being presented in Figure.7.1(b). It is clearly seen that a similar trend was identified when compared with prediction results based on Halpin-Tsai model. It is indicated that experimental data of PVA/NBC nanocomposites appeared to be close to the estimated results by using Mori-Tanaka model (parrallel) at the low NBC norminal volume fractions as opposed to better agreement with the predictions obtained from the combinatioin of laminate theory and Mori-Tanaka model. In case of PVA/HNT nanocomposites and PVA/Cloisite 30B clay nanocomposites, modelling parameters in Table 7.1 were also employed in equations (7.1) - (7.9) for the modulus predictions of nanocomposites according to Halpin-Tsai model, Mori-Tanaka model as well as the combination of laminate theory [329] and

Mori-Tanaka model, as illustrated in Figure 7.2. In both nanocomposite systems, experimental data did not have good accordance with predicted results, respectively at low nominal volume fractions of HNTs and Cloisite 30B clays. The deviation between experimental data and predicating values in Figure 7.2 is related to the concept that Halpin-Tsai model and Mori-Tanaka model are micromechanical models more suitable for conventional composites rather than nanocomposites. Furthermore, the major drawback in using Halpin-Tsai model and Mori-Tanaka model lies in their common assumption that both fillers and polymer matrices in nanocomposites are linearly elastic and isotropic materials in uniform filler distribution with the neglect of partcile-particle interaction [341]. In a nanocomposite system, isotropic nanoparticles generally have large surface areas, on which substantial amounts of polymeric molecular chains can be absorbed by the hydrogen bonding or electrostatic forces, resulting in the formation of interphase layers in nanocomposites. Thus these interphase layers behave like solid transitional material phases to restrict the mobility of other molecular chains of matrices with the positive contribution to the total volume of reinforcements [328, 331]. As a result, actual volume fractions of fillers in composite theoretical models should be reconsidered by using effective volume fraction instead. Wan and Chen [330] and other co-workers [328, 331] have reported that when nanoparticles are fully embedded within polymer matrices, the layers of absorbed polymeric chains in nanoparticles have a thickness xR_g of the polymer, in which the layer thickness is increased to x times of the radius of gyration of polymer R_g . The total volume fraction of nanoparticle is increased with the additional term of $kxR_gA_T\rho_p$, which is defined by the effective volume fraction according to equations (7.10)- (7.13)

The parameters of PVA based nanocomposite films in Table 7.1 were used to estimate effective volume fraction, and subsequently prediction results obtained from Halpin-Tsai model and Mori-Tanaka model were determined in terms of effective volume fraction of nanofillers, which are demonstrated in Figures 7.1 and 7.2. The predictions on the basis of effective volume fraction of nanofillers appear to be in better agreement with experimental data as opposed to those in terms of nominal volume fraction, which have also been proven by previous findings [330, 331]. With respect to PVA/Cloisite 30B clay nanocomposite films at the low volume fraction of 0.085 vol%, experimental data coincide more closely with predicted results based on effective volume fraction and exfoliated clay structures while better agreement is manifested for those predicted in terms of effective volume fraction and intercalated clay structures at high volume fraction levels. Such a phenomenon suggests that a majority of Cloisite 30B clays tend to be exfoliated at low volume fractions, as confirmed by the AFM evaluation in Chapter 5. Whereas, intercalated clay structures are manifested with increasing the volume fraction of Cloisite 30B clays. Consequently, predicted results cannot unanimously fit well with experimental data based on effective volume fraction and intercalated clay structures.

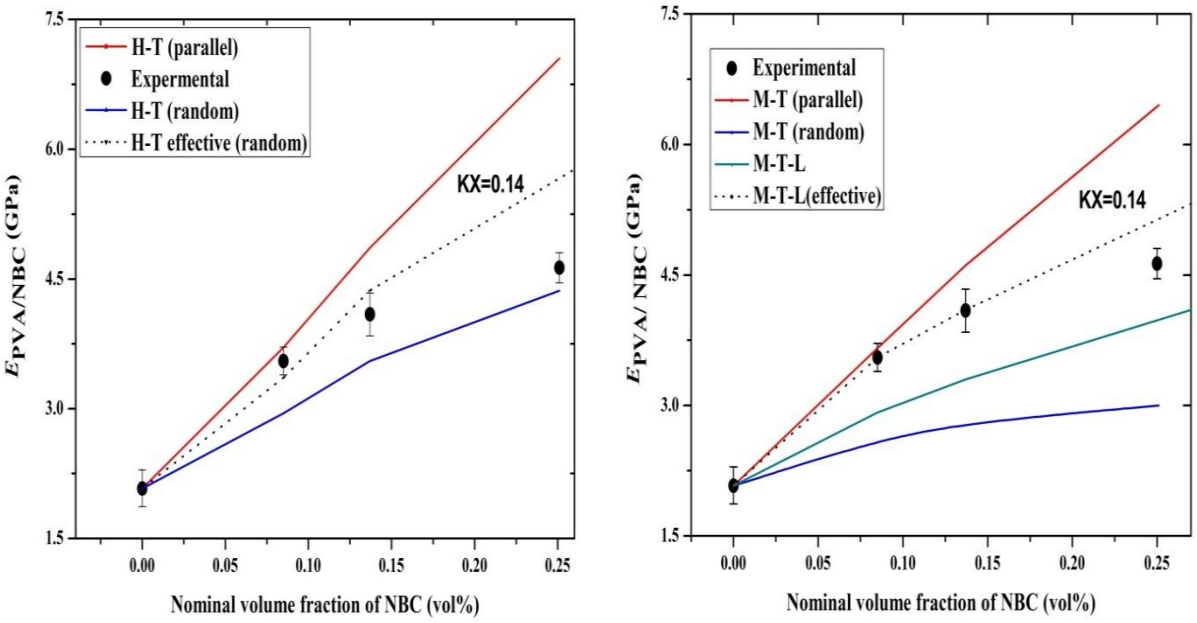

(a) (b)

Figure 7.1 Prediction of Young's moduli of PVA/NBC nanocomposites in well-aligned and randomly oriented NBCs represented by (a) Halpin-Tsai model (H-T) as well as (b) Mori-Tanaka model (M-T) and the combination of Mori-Tanaka model and laminate theory (M-T-L) based on nominal and effective volume fractions of NBCs, respectively.

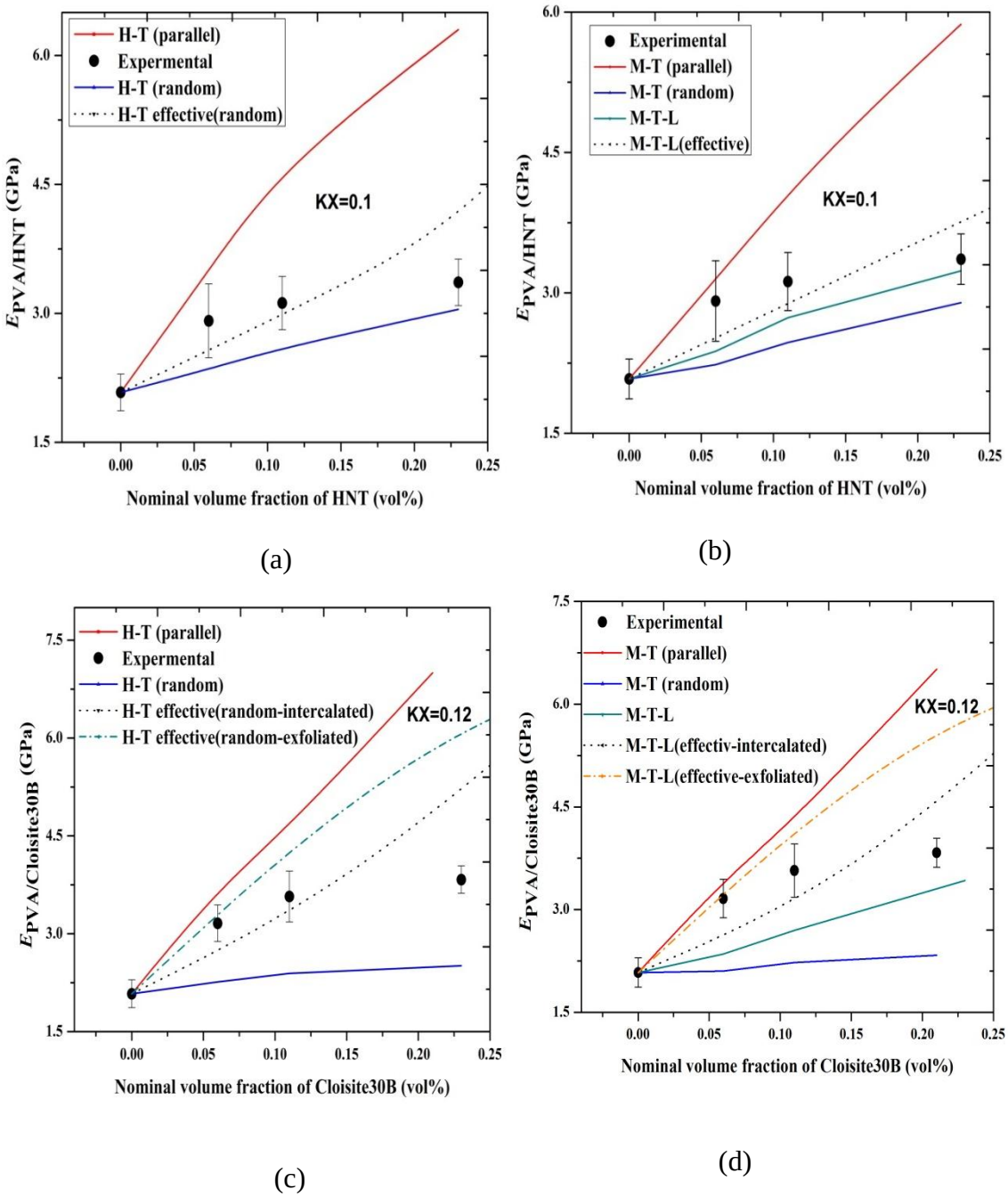

Figure 7.2 Prediction of Young's moduli of PVA/HNT nanocomposites and PVA/Cloisite 30B clay nanocomposites in well-aligned and randomly oriented nanofillers represented by (a) and (c) Halpin-Tsai model (H-T) as well as (b) and (d) Mori-Tanaka model (M-T) and the combination of Mori-Tanaka model and laminate theory (M-T-L) based on nominal and effective volume fractions of nanoparticles, respectively.

Table 7.1 Modelling parameters used for PVA nanocomposite films.

Modeling parameter	Reference values			Reference
	PVA/NBC	PVA/HNT	PVA/Cloisite 30B	
E_m (GPa)	2.08	2.08	2.08	Our experimental data
E_p (GPa)	84.5[a]	140[b)]	178[c]	[a] Our experimental data [b] [328] [c] [117]
l_f (nm)	-	208 (at 3 wt%) 410 (at 5 wt%) 900.6 (at 10 wt%)	109 (at 3 wt%) 206 (at 5 wt%) 560 (at 10 wt%	Our experimental data
t_f (nm)	4.8 (at 3 wt%) 11.2 (at 5 wt%) 28.4 (at 10 wt%)	-	4.6 (at 3 wt%) 15.8 (at 5 wt%) 41.6 (at 10 wt%)	Our experimental data
d (nm)	27.6 (at 3 wt%) 78.4 (at 5 wt%) 232 (at 10 wt%)	35.2 (at 3 wt%) 66.5 (at 5 wt%) 85 (at 10 wt%)	-	Our experimental data
ρ_m (gcm^{-3})	0.39	0.39	0.39	Our experimental data
ρ_p (gcm^{-3})	1.3	1.8	1.98	Material data sheet
t (nm)	~58	~7.3	~10.4	Our experimental data
Rg (nm)	10	10	10	[342]
ν_m	0.4	0.4	0.4	[342]
W'_p	-	-	0.66	[328]
d'_1 (nm)	-	-	1.87	Our experimental data
d_2 (nm)	-	-	3.6	Our experimental data
N (nm)	-	-	5.6	Our experimental data
h (nm)			0.98	[328]
p_p^p (gcm^{-3})			3.1	[328]
A_T (m^{2}g^{-1})	624.81[d]	40.3[e]	658[f]	[d] Our experimental data [e] [343] [f] [328]

According to above-mentioned results, the use of effective volume fraction can lead to more accurate prediction to experimental data in comparison with nominal volume

fraction in PVA based nanocomposites. However, the layer thickness of polymeric molecules absorbed on nanofiller surfaces (kx) even in the same grades of polymers with different molecular structures and polarities. As noted earlier in Chapter 6, interphase features do not possess uniform layer thickness and their dimensions and properties vary greatly when embedded with heterogeneous nanoparticles with the alteration of particle sizes/dimensions as well as nanomechanical properties depending on particle/filler interactions. As a result, it is suggested that a new and simple formula in equation (7.14) should be utilised to calculate nanofiller volume fraction from both interphase volume and volume fraction, in which interphase volume fraction $\emptyset_{\text{Interphase}}$ is estimated in two different system, namely uniform particle mono-dispersion and particle poly-dispersion. Modelling parameters in Table 7.2 is substituted into equations (7.36) and (7.28), respectively to estimate associated $\emptyset_{\text{Interphase}}$ values in PVA nanocomposite systems in this study. Besides, interphase volume can be calculated according to equation (6.5) with the relevant results being used for the calculation of volume fractions of nanofillers. Such recalculated volume fractions of nanoparticles in relation to interphase effect were introduced into Halpin-Tsai model and Mori-Tanaka model accordingly along with the predicted results presented for elastic modfuli of PVA based nanocomposites in Figures 7.3 and 7.4. In a consistent manner, all E_c values in our modelling work with the consideration of interphase effect demonstrate a much closer relationship with experimental data as opposed to corresponding theoretical models using both nominal and effective volume fractions without interphase. More evidently, our proposed models in a monodispersed particle system appear to maintain relatively good agreement with experimental data at a low volume fraction up to 0.085 vol% in contrast with those in a polydispersed particle system with both Fuller and EVF particulate gradations. A

completely opposite trend has been detected beyond 0.085 vol% where polydispersed particle system tends to be more pronounced. It is easily understood since NBCs, HNTs and Cloisite 30B clays are expected to be more uniformly dispersed in PVA nanocomposites in relatively similar sizes, as validated in our morphological structure results. Whereas, typical nanoparticle agglomeration is evidently observed to have a better correlation with a polydispersed particle system. In terms of particulate gradation effect, those predictions based on the Fuller gradation appear to be slight in better agreement with experimental data, possibly resulting from the theoretical assumption of finer particle dispersion taking place in the EVF counterpart at the same nominal volume fraction. As a result, larger specific surface areas of particles take place in case of EVF gradation, further leading to the increases in $\emptyset_{\text{Interphase}}$ and volume fraction of nanoparticles.

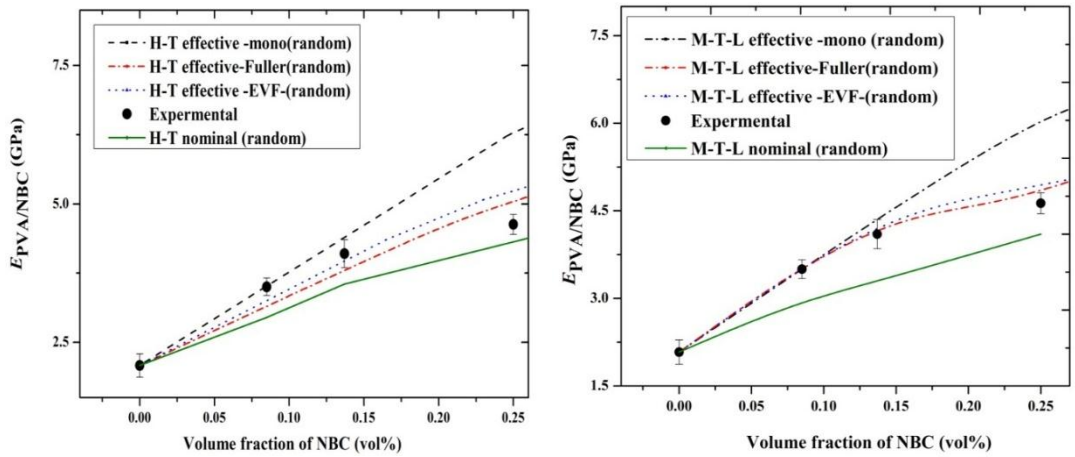

Figure 7.3 Elastic moduli of PVA/NBC nanocomposite films predicted by (a) Halpin-Tsai model and (b) Mori-Tanka model. Four categories are considered based on nominal volume fraction of NBCs, effective volume fraction of NBCs in a monodispersed particle system, effective volume fraction of NBCs in a polydispersed particle system with Fuller particular gradation, as well as effective volume fraction of NBCs in a polydispersed particle system with EVF particulate gradation.

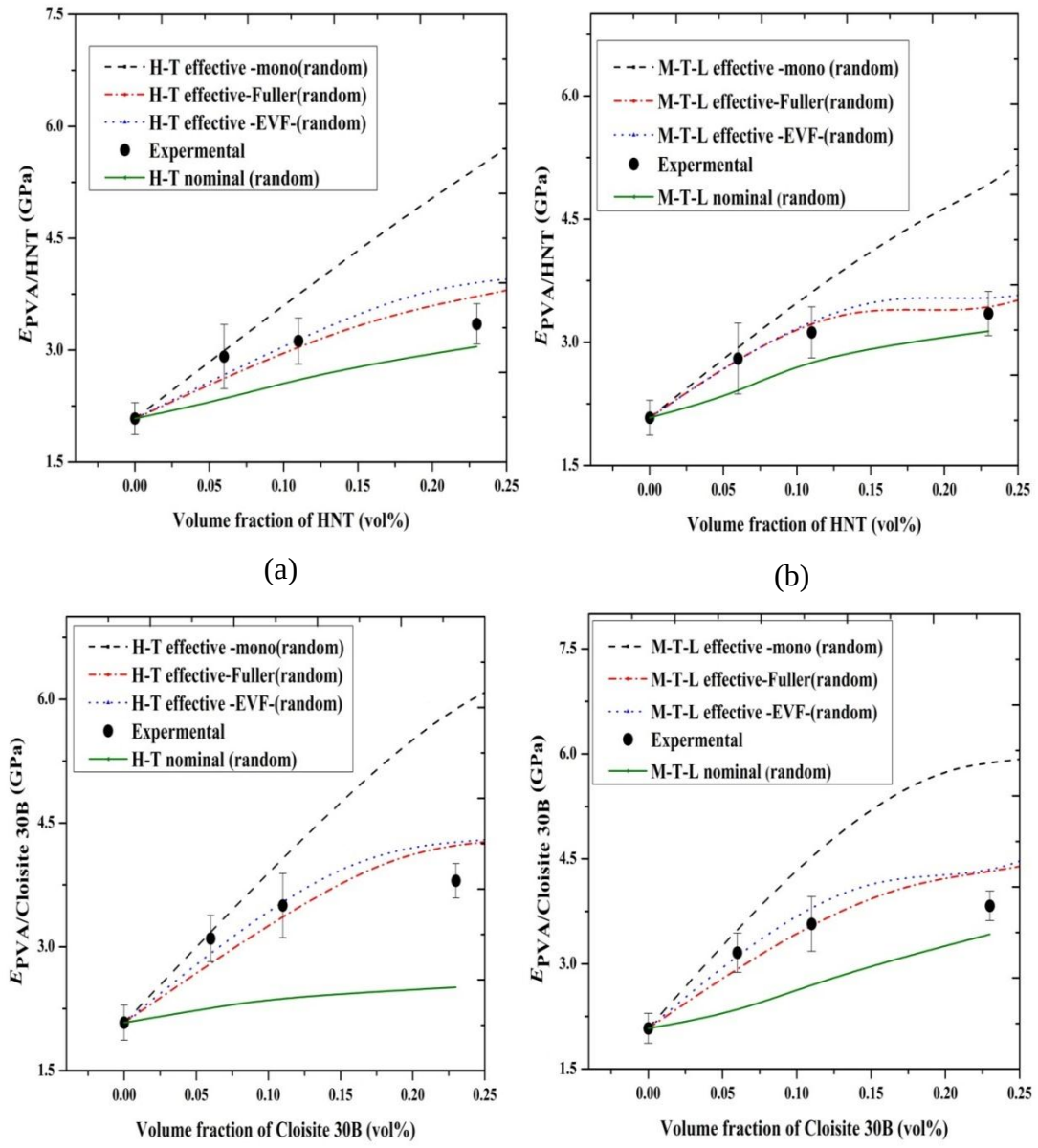

Figure 7.4 Elastic moduli of PVA/HNT nanocomposites and PVA/Cloisite 30B clay nanocomposites predicted by (a) Halpin-Tsai model and (b) Mori-Tanka model. Four categories are considered based on nominal volume fraction of nanoparticles, effective volume fraction of nanoparticles in a monodispersed particle system, effective volume fraction of nanoparticles in a polydispersed particle system with Fuller particular gradation, as well as effective volume fraction of nanoparticles in a polydispersed particle system with EVF particulate gradation.

Table 7.2 Modelling parameters measured to calculate $\emptyset_{\text{Interphase}}$ in PVA based nanomposites

Modeling parameter (nm)	Nanofiller content (wt%)	PVA/NBC	PVA/HNT[(a)]	PVA/Cloisite 30B
$D_{eq\text{-min}}$	3	14	64.5	34.1
$D_{eq\text{-min}}$	5	32.5	168.5	54.3
$D_{eq\text{-min}}$	10	66	245.7	141.6
$D_{eq\text{-max}}$	3	74.3	836	436
$D_{eq\text{-max}}$	5	1017	2460	1836.2
$D_{eq\text{-max}}$	10	2013	4645	3141
$D_{eq\text{-mean}}$	3	27	208	109
$D_{eq\text{-mean}}$	5	75.5	410	206
$D_{eq\text{-mean}}$	10	232	900.6	560
$t_{interphase}$	5	15.3 (at 5 wt %)	8.6 (at 5 wt %)	10.7(at 5 wt %)

Note: [(a)] means in case of PVA/HNT nanocomposites, $D_{eq\text{-}min}$, $D_{eq\text{-}max}$ and $D_{eq\text{-}mean}$ are equivalent to $L_{eq\text{-}min}$, $L_{eq\text{-}max}$ and $L_{eq\text{-}mean}$, respectively for HNTs. In case of HNTs, the $D_{eq\text{-}min}$ in equations (7.37)-(7.47) represent length of HNTs.

7.3. Summary

In this chapter, the following key points are summarised:

- Halpin-Tsai model and the combination of Mori-Tanaka model and laminate theory were successfully employed to predict elastic moduli of PVA based nanocomposites.
- Effective volume fraction of reinforcing phases was introduced in conventional composite theory with the consideration of interphases for the reinforcement effect, resulting in better agreement with experimental data as opposed to those based on nominal volume fraction.

- For the first time, we have also developed a theoretical approach to calculate effective volume fraction of nanoparticles based on 3D interphase dimensions and volume fraction, which is allowed to be used for studying the effect of experimentally measured interphases on the elastic moduli of PVA bionanocomposite films. Besides, the implementation of effective volume fraction of reinforcing phases in Halpin-Tsai model and the combination of Mori-Tanaka model and laminate theory in a polydispersed particle system with Fuller and EVF particulate gradations demonstrates much better agreement with experimental data as compared with those using nominal volume fraction of nanoparticles.

Chapter 8.

Conclusions and Future work

8.1. Conclusions

This study has created novel PVA bionanocomposite systems reinforced with MBCs, NBCs, HNTs and Cloisite 30B clays as nanofillers with the aim of achieving much stronger binanocomposite films potentially used as the alternative to synthetic polymer based nanocomposite films. The effects of nanofiller size, shape and content on the material performance of bionanocomposite films were holistically investigated. Furthermore, the work employed PFQNM measurements to quantitatively characterise 3D interphase dimensions and properties as well as evaluate nanomechanical properties of bionanocomposite films in terms of their elastic modulus, interphase modulus, interphase volume and surface area.Micromechanical modelling was carried out by considering effective volume fraction of nanoparticles, 3D interphase dimensions and volume fraction for the first time. The following important conclusions were drawn from this study:

- PVA was reinforced by using NBCs and MBCs in corresponding strong PVA/NBC nanocomposites and PVA/MBC nanocomposites. With increasing the BC content, a noticeable increase was found in tensile moduli of both nanocomposites along with the decrease in elongation at break and tensile toughness. The maximum tensile strength of nanocomposites achieved with incorporation of 3 wt% BCs, and NBC inclusion demonstrates relatively high strength increasing level as compared to those based on MBCs. These findings were related to smaller nanoparticles size and larger surface areas of NBCs due to more effective load transfer from NBCs to PVA matrices in nanocomposites. Moreover, thermal properties of PVA nanocomposites in term of T_g revealed the enhancement with incorporation of BCs, particularly with the inclusion of

NBCs. Thermal stability of nanocomposites in term of $T_{5\%}$, $T_{80\%}$ and T_d greatly improved with increasing the BC content.

- The incorporation of low HNT content has been shown to significantly improve mechanical properties of PVA nanocomposite films. However, further increasing the HNT content up to 10 wt% causes poor dispersion and high agglomeration of HNTs, as confirmed from the results of morphological and fracture structures for PVA/HNT nanocomposites, leading to decreasing mechanical properties in term of their tensile strength, elongation at break and tensile toughness. Thermal stability and thermal properties were enhanced after the incorporation of HNTs and the enhancing level increased with increasing the HNT content. Moreover, the inclusion of Cloisite 30B clays within PVA matrices also induced the improvements of mechanical, thermal properties and thermal stability of nanocomposite films. Nevertheless, an excessive Cloisite 30B content caused a typical drop in mechanical properties of PVA/Cloisite 30B clay nanocomposites in terms of their tensile strength, elongation at break and tensile toughness. This phenomenon could be associated with Cloisite 30B clay agglomeration at high clay contents, thus causing the interfacial debonding issue between Cloisite 30B clays and PVA matrices.
- Thermal and mechanical properties highlighted the great potential of using NBCs as 3D nanoparticles compared to HNTs as 2D tubular nanofillers and Cloisite 30B clays as 1D platelet-like nanoparticles for the best reinforcement efficiency in PVA nanocomposites. NBCs demonstrate a high degree of nanofiller dispersion within PVA matrices when compared with those based on HNTs and Cloisite 30B clays, which is ascribed to the relatively small particle sizes of NBCs among all three different nanofillers in this study. Moreover,

porous structures of NBCs enable them to have much larger contact surface areas with PVA molecular chains with strong mechanical and hydrogen bondings in order to achieve remarkable improvements of mechanical properties.

- Interphase dimensions and properties between nanofillers and PVA matrices were determined experimentally, suggesting a consistent sign of non-uniform thickness for all nanofillers. Nanomechanical properties of interphase appeared to be quite different from those of PVA matrices and nanoparticles as expected. Moreover, elastic modulus of interphase was significantly enhanced with increasing the interphase volume.
- The discussions for interphase dimensions and properties indicated that PVA/NBC phases possessed the higher interphase modulus when compared with those for PVA/HNT and PVA/Cloisite 30B clay phases in PVA nanocomposite systems.
- The prediction of elastic moduli of PVA nanocomposites using Halpin-Tsai model and the combination of Mori-Tanaka model and laminate theory did not offer good agreement with experimental data based on the nominal volume fractions of nanofillers and neglect of the interphase properties. Conversely, better agreement was achieved for predicting the elastic modulus of nanocomposites when effective volume fraction of nanofillers employed in this modelling work.
- 3D interphase properties and volume fraction were successfully implemented in this study for the first time in the best accordance with experimental data as opposed to those according to nominal volume fraction and effective volume

faction of nanofillers alone when predicting elastic moduli of PVA nanocomposites.

8.2. Future work

Based on the outcomes of this study, several plans concerning the improvement of the material performance of bionanocomposite films can be recommended as follows:

- Our results indicate that BCs are effective nanofillers for the property enhancement of PVA nanocomposites due to their existing mechanical bonding with PVA matrices based on typically highly porous BC structures. The reinforcement efficiency of BCs could be further enhanced by their surface modification to use with different hydrophilic and hydrophobic polymers in the development of advanced nanocomposites, which can directly benefit from enlarging pore diameters and the supply of more surface functional groups. As such, their interaction and miscibility can be promoted with different types of polymers as matrices in nanocomposite systems.
- BCs in possession of excellent absorption capacity could be reused for retaining food and inhibiting the bacteria growth particularly for the fabrication of PVA bionanocomposite films with the potential use in packaging applications.
- On the other hand, BCs have large surface area, absorbance efficiency and biocompatibility, and can be considered as suitable carrier candidate for drug delivery with their ability to improve the human microcirculation system. The similar case can also apply to PVA/HNT nanocomposites as HNTs are well known to be effective carriers for drug delivery l.

- Although micromechanical models used in this study are developed to evaluate the impact of 3D interphase dimension, interphase volume, aspect ratio and content of nanofillers, nanofiller dispersion states with much better and more reasonable predictions for tensile moduli of PVA based nanocomposites, interphase modulus should also be considered for better understanding the overall macroscopic material behaviour of nanocomposites.
- PVA based nanocomposites successfully manufactured by a solution casting method, leading to strong PVA/NBC nanocomposites, and good PVA/HNT nanocomposites and PVA/Cloisite 30B clay nanocomposites. A layer-by-layer method is also suggested in order to obtain more desirable properties of nanocomposite thin films. In such a process, deposition layers of polymer and nanfillers suspension can be placed on the substrate and then using different technologies such as dipping, dewetting, roll-to-roll process and centrifugation for the assemblies to generate films on the substrate.

References

1. Geyer, R., J.R. Jambeck, and K.L. Law, *Production, use, and fate of all plastics ever made.* Science advances, 2017. **3**(7): p. e1700782.
2. Reddy, M.M., M. Misra, and A.K. Mohanty, *Bio-based materials in the new bio-economy.* Chemical Engineering Progress, 2012. **108**(5): p. 37-42.
3. Averous, L. and N. Boquillon, *Biocomposites based on plasticized starch: thermal and mechanical behaviours.* Carbohydrate Polymers, 2004. **56**(2): p. 111-122.
4. Ray, S.S. and M. Bousmina, *Biodegradable polymers and their layered silicate nanocomposites: in greening the 21st century materials world.* Progress in materials science, 2005. **50**(8): p. 962-1079.
5. Robyt, J.F., *Starch: Structure, properties, chemistry, and enzymology*, in *Glycoscience*. 2008, Springer. p. 1437-1472.
6. Eagan, J.M., Xu J, Di Girolamo R, Thurber CM, Macosko CW, LaPointe AM, Bates FS, Coates GW, *Combining polyethylene and polypropylene: Enhanced performance with PE/iPP multiblock polymers.* Science, 2017. **355**(6327): p. 814-816.
7. Xanthos, D. and T.R. Walker, *International policies to reduce plastic marine pollution from single-use plastics (plastic bags and microbeads): a review.* Marine pollution bulletin, 2017. **118**(1-2): p. 17-26.
8. Avérous, L., *Biodegradable multiphase systems based on plasticized starch: a review.* Journal of Macromolecular Science, Part C: Polymer Reviews, 2004. **44**(3): p. 231-274.
9. Huang, D. and A. Wang, *Non-covalently functionalized multiwalled carbon nanotubes by chitosan and their synergistic reinforcing effects in PVA films.* RSC Advances, 2013. **3**(4): p. 1210-1216.
10. Pan, Y.-S., D.-S. Xiong, and R.-Y. Ma, *A study on the friction properties of poly (vinyl alcohol) hydrogel as articular cartilage against titanium alloy.* Wear, 2007. **262**(7-8): p. 1021-1025.
11. Espinosa, H.D., Rim JE, Barthelat F, Buehler MJ, *Merger of structure and material in nacre and bone–Perspectives on de novo biomimetic materials.* Progress in Materials Science, 2009. **54**(8): p. 1059-1100.
12. Sapalidis, A.A., F.K. Katsaros, and N.K. Kanellopoulos, *PVA/montmorillonite nanocomposites: development and properties*, in *Nanocomposites and polymers with analytical methods*. 2011, InTech.
13. Jose, T., George SC, Maria HJ, Wilson R, Thomas S, *Effect of bentonite clay on the mechanical, thermal, and pervaporation performance of the poly (vinyl alcohol) nanocomposite membranes.* Industrial & Engineering Chemistry Research, 2014. **53**(43): p. 16820-16831.
14. Fujii, K., Nakagaito AN, Takagi H, Yonekura D, *Sulfuric acid treatment of halloysite nanoclay to improve the mechanical properties of PVA/halloysite transparent composite films.* Composite Interfaces, 2014. **21**(4): p. 319-327.
15. Khoo, W., H. Ismail, and A. Ariffin, *Tensile, swelling, and oxidative degradation properties of crosslinked polyvinyl alcohol/chitosan/halloysite nanotube composites.* International Journal of Polymeric Materials and Polymeric Biomaterials, 2013. **62**(7): p. 390-396.
16. Qiu, K. and A.N. Netravali, *Halloysite nanotube reinforced biodegradable nanocomposites using noncrosslinked and malonic acid crosslinked polyvinyl alcohol.* Polymer Composites, 2013. **34**(5): p. 799-809.
17. Du, F.-P., Ye EZ, Yang W, Shen TH, Tang CY, Xie XL, Zhou XP, Law WC, *Electroactive shape memory polymer based on optimized multi-walled carbon*

nanotubes/polyvinyl alcohol nanocomposites. Composites Part B: Engineering, 2015. **68**: p. 170-175.
18. Minus, M.L., H.G. Chae, and S. Kumar, *Interfacial crystallization in gel-spun poly (vinyl alcohol)/single-wall carbon nanotube composite fibers.* Macromolecular Chemistry and Physics, 2009. **210**(21): p. 1799-1808.
19. Thayumanavan, N., P. Tambe, and G. Joshi, *Effect of surfactant and sodium alginate modification of graphene on the mechanical and thermal properties of polyvinyl alcohol (PVA) nanocomposites.* Cellul. Chem. Technol, 2015. **49**: p. 69-80.
20. Li, Y.Q., Yu T, Yang TY, Zheng LX, Liao K., *Bio-inspired nacre-like composite films based on graphene with superior mechanical, electrical, and biocompatible properties.* Advanced Materials, 2012. **24**(25): p. 3426-3431.
21. Cheng, Q., S. Wang, and Z. Tong, *Poly (vinyl alcohol) cellulose nanocomposites*, in *Handbook of polymer nanocomposites. Processing, Performance and Application*. 2015, Springer. p. 433-447.
22. Leitão, A.F., Silva J, Dourado F, Gama M, *Production and characterization of a new bacterial cellulose/poly (vinyl alcohol) nanocomposite.* Materials, 2013. **6**(5): p. 1956-1966.
23. Ren, W., Wu R, Guo P, Zhu J, Li H, Xu S, Wang J, *Preparation and characterization of covalently bonded PVA/Laponite/HAPI nanocomposite multilayer freestanding films by layer-by-layer assembly.* Journal of Polymer Science Part B: Polymer Physics, 2015. **53**(8): p. 545-551.
24. Morimune, S., Kotera M, Nishino T, Goto K, Hata K, *Poly (vinyl alcohol) nanocomposites with nanodiamond.* Macromolecules, 2011. **44**(11): p. 4415-4421.
25. Mousa, M.H., Y. Dong, and I.J. Davies, *Recent advances in bionanocomposites: Preparation, properties, and applications.* International Journal of Polymeric Materials and Polymeric Biomaterials, 2016. **65**(5): p. 225-254.
26. Putz, K.W., Compton OC, Palmeri MJ, Nguyen ST, Brinson LC, *High-nanofiller-content graphene oxide–polymer nanocomposites via vacuum-assisted self-assembly.* Advanced Functional Materials, 2010. **20**(19): p. 3322-3329.
27. Liao, P., Ismael ZM, Zhang W, Yuan S, Tong M, Wang K, Bao J, *Adsorption of dyes from aqueous solutions by microwave modified bamboo charcoal.* Chemical engineering journal, 2012. **195**: p. 339-346.
28. Singh, K., Singh RS, Rai BN, Upadhyay SN, B*iofiltration of toluene using wood charcoal as the biofilter media.* Bioresource technology, 2010. **101**(11): p. 3947-3951.
29. Asada, T., Ohkubo T, Kawata K, Oikawa K. Ammonia , *Ammonia adsorption on bamboo charcoal with acid treatment.* Journal of Health Science, 2006. **52**(5): p. 585-589.
30. Lou, C.-W., Lin CW, Lei CH, Su KH, Hsu CH, Liu ZH, Lin JH. , *PET/PP blend with bamboo charcoal to produce functional composites.* Journal of Materials Processing Technology, 2007. **192**: p. 428-433.
31. Ho, M.-p., Lau KT, Wang H, Hui D, *Improvement on the properties of polylactic acid (PLA) using bamboo charcoal particles.* Composites Part B: Engineering, 2015. **81**: p. 14-25.
32. Yeh, J.T., Hsiung HH, Wei W, Zhu P, Chen KN, Jiang T, *Negative air ion releasing properties of tourmaline/bamboo charcoal compounds containing ethylene propylene diene terpolymer/polypropylene composites.* Journal of applied polymer science, 2009. **113**(2): p. 1097-1110.
33. Zhao, R.-S., Wang X, Yuan JP, Lin JM, *Investigation of feasibility of bamboo charcoal as solid-phase extraction adsorbent for the enrichment and determination of four phthalate esters in environmental water samples.* Journal of Chromatography A, 2008. **1183**(1-2): p. 15-20.
34. Li, X., Lin Z, Huang L, Tan S, Cai X, *The utilization of bamboo charcoal enhances wood plastic composites with excellent mechanical and thermal properties.* Materials & Design, 2014. **53**: p. 419-424.

35. Nitayaphat, W., Jiratumnukul N, Charuchinda S, Kittinaovarat S, *Mechanical properties of chitosan/bamboo charcoal composite films made with normal and surface oxidized charcoal.* Carbohydrate Polymers, 2009. **78**(3): p. 444-448.
36. Yang, F.-C., Wu KH, Lin WP, Hu MK, *Preparation and antibacterial efficacy of bamboo charcoal/polyoxometalate biological protective material.* Microporous and Mesoporous Materials, 2009. **118**(1-3): p. 467-472.
37. Kamada, K., *Study on Healthy Housing Using Recycled Organic Industrial Waste First Report: Overview of Trends in the Development of the LatestTechnology and New Materials in Japan.* 2008.
38. Wu, J., Wei Y, Lin J, Lin S., *Preparation of a starch-graft-acrylamide/kaolinite superabsorbent composite and the influence of the hydrophilic group on its water absorbency.* Polymer International, 2003. **52**(12): p. 1909-1912.
39. Lin, J., Wu J, Yang Z, Pu M, *Synthesis and properties of poly (acrylic acid)/mica superabsorbent nanocomposite.* Macromolecular Rapid Communications, 2001. **22**(6): p. 422-424.
40. Zhang, F., Guo Z, Gao H, Li Y, Ren L, Shi L, Wang L, *Synthesis and properties of sepiolite/poly (acrylic acid-co-acrylamide) nanocomposites.* Polymer Bulletin, 2005. **55**(6): p. 419-428.
41. Ferfera-Harrar, H., Aiouaz N, Dairi N, Hadj- Hamou AS, *Preparation of chitosan-g-poly (acrylamide)/montmorillonite superabsorbent polymer composites: Studies on swelling, thermal, and antibacterial properties.* Journal of Applied Polymer Science, 2014. **131**(1).
42. Filippi, S., Paci M, Polacco G, Dintcheva NT, Magagnini P, *On the interlayer spacing collapse of Cloisite® 30B organoclay.* Polymer degradation and stability, 2011. **96**(5): p. 823-832.
43. Tavares, L.L., Almeida CB, Caruso ÍP, Cornélio ML, Lopes Filho JF, *Effect of modified clays on the structure and functional properties of biofilms produced with zein.* Food Science and Technology, 2012. **32**(2): p. 314-322.
44. Rhim, J.-W. and P.K. Ng, *Natural biopolymer-based nanocomposite films for packaging applications.* Critical reviews in food science and nutrition, 2007. **47**(4): p. 411-433.
45. Liu, M., Jia Z, Jia D, Zhou C., *Recent advance in research on halloysite nanotubes-polymer nanocomposite.* Progress in polymer science, 2014. **39**(8): p. 1498-1525.
46. Zhu, J., J. Jia, and S.C. Tjong, *Preparation, structure, and application of carbon nanotubes/bamboo charcoal composite*, in *Nanocrystalline Materials (Second Edition)*. 2014, Elsevier. p. 1-25.
47. Gray, M., Johnson MG, Dragila MI, Kleber M, *Water uptake in biochars: the roles of porosity and hydrophobicity.* biomass and bioenergy, 2014. **61**: p. 196-205.
48. Brockhoff, S.R., Christians NE, Killorn RJ, Horton R, Davis DD, *Physical and mineral-nutrition properties of sand-based turfgrass root zones amended with biochar.* Agronomy Journal, 2010. **102**(6): p. 1627-1631.
49. You, Z. and D. Li, *Highly filled bamboo charcoal powder reinforced ultra-high molecular weight polyethylene.* Materials Letters, 2014. **122**: p. 121-124.
50. Wu, K., et al., *Synthesis and microwave electromagnetic characteristics of bamboo charcoal/polyaniline composites in 2–40 GHz.* Synthetic Metals, 2008. **158**(17-18): p. 688-694.
51. Rhim, J.-W., S.-I. Hong, and C.-S. Ha, *Tensile, water vapor barrier and antimicrobial properties of PLA/nanoclay composite films.* LWT-Food Science and Technology, 2009. **42**(2): p. 612-617.
52. Kulkarni, D.D., Choi I, Singamaneni SS, Tsukruk VV, *Graphene oxide− polyelectrolyte nanomembranes.* ACS nano, 2010. **4**(8): p. 4667-4676.
53. Mori, T. and K. Tanaka, *Average stress in matrix and average elastic energy of materials with misfitting inclusions.* Acta metallurgica, 1973. **21**(5): p. 571-574.

54. Zare, Y. and H. Garmabi, *Attempts to simulate the modulus of polymer/carbon nanotube nanocomposites and future trends.* Polymer Reviews, 2014. **54**(3): p. 377-400.
55. Hu, K., Gupta MK, Kulkarni DD, Tsukruk VV, *Ultra-Robust Graphene Oxide-Silk Fibroin Nanocomposite Membranes.* Advanced Materials, 2013. **25**(16): p. 2301-2307.
56. Sisakht Mohsen, R., Saied NK, Ali Z, Hosein EM, Hasan P. , *Theoretical and experimental determination of tensile properties of nanosized and micron-sized CaCO3/PA66 composites.* Polymer Composites, 2009. **30**(3): p. 274-280.
57. Zare, Y., *Development of simplified Tandon-Weng solutions of Mori-Tanaka theory for Young's modulus of polymer nanocomposites considering the interphase.* Journal of Applied Polymer Science, 2016. **133**(33).
58. Zare, Y., *The roles of nanoparticles accumulation and interphase properties in properties of polymer particulate nanocomposites by a multi-step methodology.* Composites Part A: Applied Science and Manufacturing, 2016. **91**: p. 127-132.
59. Gu, Y., Li M, Wang J, Zhang Z *Characterization of the interphase in carbon fiber/polymer composites using a nanoscale dynamic mechanical imaging technique.* Carbon, 2010. **48**(11): p. 3229-3235.
60. Qiao, R. and L.C. Brinson, *Simulation of interphase percolation and gradients in polymer nanocomposites.* Composites Science and Technology, 2009. **69**(3-4): p. 491-499.
61. Appiah, K., Z. Wang, and W. Lackey, *Characterization of interfaces in C fiber-reinforced laminated C–SiC matrix composites.* Carbon, 2000. **38**(6): p. 831-838.
62. Dwivedi, H., et al., *Evidence for the benefit of adding a carbon interphase in an all-carbon composite.* Carbon, 2006. **44**(4): p. 699-709.
63. Lewis, T., *Interfaces: nanometric dielectrics.* Journal of Physics D: Applied Physics, 2005. **38**(2): p. 202.
64. Shen, Y. Lin Y, Li M, Nan CW Advanced Materials, 2007. **19**(10): p. 1418-1422.
65. Gao, Y., G. De Schutter, and G. Ye, *Micro-and meso-scale pore structure in mortar in relation to aggregate content.* Cement and Concrete Research, 2013. **52**: p. 149-160.
66. Jem, K.J., J.F. van der Pol, and S. de Vos, *Microbial lactic acid, its polymer poly (lactic acid), and their industrial applications*, in *Plastics from bacteria*. 2010, Springer. p. 323-346.
67. Martin, O. and L. Averous, *Poly (lactic acid): plasticization and properties of biodegradable multiphase systems.* Polymer, 2001. **42**(14): p. 6209-6219.
68. Ho, K.-L.G., Pometto AL, Gadea-Rivas A, Briceño JA, Rojas A, *Degradation of polylactic acid (PLA) plastic in Costa Rican soil and Iowa state university compost rows.* Journal of environmental polymer degradation, 1999. **7**(4): p. 173-177.
69. Hakkarainen, M., *Aliphatic polyesters: abiotic and biotic degradation and degradation products*, in *Degradable aliphatic polyesters*. 2002, Springer. p. 113-138.
70. Kawaguchi, Y. and Y. Doi, *Kinetics and mechanism of synthesis and degradation of poly (3-hydroxybutyrate) in Alcaligenes eutrophus.* Macromolecules, 1992. **25**(9): p. 2324-2329.
71. Lenz, R.W. and R.H. Marchessault, *Bacterial polyesters: biosynthesis, biodegradable plastics and biotechnology.* Biomacromolecules, 2005. **6**(1): p. 1-8.
72. Bastioli, C., et al., *Physical state and biodegradation behavior of starch-polycaprolactone systems.* Journal of environmental polymer degradation, 1995. **3**(2): p. 81-95.
73. Averous, L., Moro L, Dole P, Fringant C, *Properties of thermoplastic blends: starch–polycaprolactone*. Polymer, 2000. **41**(11): p. 4157-4167.
74. Koenig, M. and S. Huang, *Evaluation of crosslinked poly (caprolactone) as a biodegradable, hydrophobic coating.* Polymer degradation and stability, 1994. **45**(1): p. 139-144.

75. Goldberg, D., *A review of the biodegradability and utility of poly (caprolactone).* Journal of environmental polymer degradation, 1995. **3**(2): p. 61-67.
76. Bastioli, C. *Biodegradable materials—present situation and future perspectives*. in *Macromolecular Symposia*. 1998. Wiley Online Library.
77. Okada, M., *Chemical syntheses of biodegradable polymers.* Progress in polymer science, 2002. **27**(1): p. 87-133.
78. Gross, R.A. and B. Kalra, *Biodegradable polymers for the environment.* Science, 2002. **297**(5582): p. 803-807.
79. Gross RA, Kalra B. Biodegradable polymers for the environment. Science. 2002 Aug 2;297(5582):803-7.
80. Wolk, S.K., Swift G, Paik YH, Yocom KM, Smith RL, Simon ES. , *One-and two-dimensional nuclear magnetic resonance characterization of poly (aspartic acid) prepared by thermal polymerization of L-aspartic acid.* Macromolecules, 1994. **27**(26): p. 7613-7620.
81. Hallensleben, M.L., R. Fuss, and F. Mummy, *Polyvinyl compounds, others.* Ullmann's Encyclopedia of Industrial Chemistry, 2000.
82. Baker, M.I., Walsh SP, Schwartz Z, Boyan BD, *A review of polyvinyl alcohol and its uses in cartilage and orthopedic applications.* Journal of Biomedical Materials Research Part B: Applied Biomaterials, 2012. **100**(5): p. 1451-1457.
83. Finch, C.A., *Polyvinyl alcohol; properties and applications*. 1973: John Wiley & Sons.
84. Oviedo, I.R., Méndez NN, Gómez MG, Rodríguez HC, Martínez AR, *Design of a physical and nontoxic crosslinked poly (vinyl alcohol) hydrogel.* International Journal of Polymeric Materials, 2008. **57**(12): p. 1095-1103.
85. Briscoe, B., P. Luckham, and S. Zhu, *The effects of hydrogen bonding upon the viscosity of aqueous poly (vinyl alcohol) solutions.* Polymer, 2000. **41**(10): p. 3851-3860.
86. Abdullah, Z.W., Dong Y, Davies IJ, Barbhuiya S, *PVA, PVA blends, and their nanocomposites for biodegradable packaging application.* Polymer-Plastics Technology and Engineering, 2017. **56**(12): p. 1307-1344.
87. Chang, I.-S., C.-I. Kim, and B.-U. Nam, *The influence of poly-vinyl-alcohol (PVA) characteristics on the physical stability of encapsulated immobilization media for advanced wastewater treatment.* Process Biochemistry, 2005. **40**(9): p. 3050-3054.
88. Hara, C. and M. Matsuo, *Phase separation in aqueous poly (vinyl alcohol) solution.* Polymer, 1995. **36**(3): p. 603-609.
89. Liu, M., R. Cheng, and R. Qian, *Effect of solution concentration on the gelation of aqueous polyvinyl alcohol solution.* Journal of Polymer Science Part B: Polymer Physics, 1995. **33**(12): p. 1731-1735.
90. Nozakura, S.I. and S. Kida, *Polymerization of vinyloxyaluminum and formation of syndiotactic poly (vinyl alcohol).* Journal of Polymer Science Part A: Polymer Chemistry, 1974. **12**(10): p. 2337-2348.
91. Napper, D., *Flocculation studies of sterically stabilized dispersions.* Journal of Colloid and Interface Science, 1970. **32**(1): p. 106-114.
92. Maeda, H., T. Kawai, and S. Sekii, *Intra-and intermolecular hydrogen bonds in polyvinyl alcohol solutions.* Journal of Polymer Science Part A: Polymer Chemistry, 1959. **35**(128): p. 288-292.
93. Miranda-Trevino, J.C. and C.A. Coles, *Kaolinite properties, structure and influence of metal retention on pH.* Applied Clay Science, 2003. **23**(1-4): p. 133-139.
94. Chiu, C.-W., Huang TK, Wang YC, Alamani BG, Lin JJ, *Intercalation strategies in clay/polymer hybrids.* Progress in Polymer Science, 2014. **39**(3): p. 443-485.
95. Beyer, G., *Nanocomposites: a new class of flame retardants for polymers.* Plastics, Additives and Compounding, 2002. **4**(10): p. 22-28.
96. Solomon, M.J., Almusallam AS, Seefeldt KF, Somwangthanaroj A, Varadan P., *Rheology of polypropylene/clay hybrid materials.* Macromolecules, 2001. **34**(6): p. 1864-1872.

97. Alexandre, M. and P. Dubois, *Polymer-layered silicate nanocomposites: preparation, properties and uses of a new class of materials.* Materials Science and Engineering: R: Reports, 2000. **28**(1-2): p. 1-63.
98. Francis, C., *ADSORPTION OF POLYVINYLPYRROLIDONE ON REFERENCE CLAY MINERALS.* Soil Science, 1973. **115**(1): p. 40-54.
99. Aranda, P. and E. Ruiz-Hitzky, *Poly (ethylene oxide)-silicate intercalation materials.* Chemistry of Materials, 1992. **4**(6): p. 1395-1403.
100. Zanetti, M., S. Lomakin, and G. Camino, *Polymer layered silicate nanocomposites.* Macromolecular Materials and Engineering, 2000. **279**(1): p. 1-9.
101. Nuruzzaman, M., Rahman MM, Liu Y, Naidu R. , *Nanoencapsulation, nano-guard for pesticides: a new window for safe application.* Journal of agricultural and food chemistry, 2016. **64**(7): p. 1447-1483.
102. Chin, I.-J., Thurn-Albrecht T, Kim HC, Russell TP, Wang J, *On exfoliation of montmorillonite in epoxy.* Polymer, 2001. **42**(13): p. 5947-5952.
103. Fischer, H., *Polymer nanocomposites: from fundamental research to specific applications.* Materials Science and Engineering: C, 2003. **23**(6-8): p. 763-772.
104. Xu, L., Reeder S, Thopasridharan M, Ren J, Shipp DA, Krishnamoorti R, *Structure and melt rheology of polystyrene-based layered silicate nanocomposites.* Nanotechnology, 2005. **16**(7): p. S514.
105. Wang, K.H., Choi MH, Koo CM, Choi YS, Chung IJ, *Synthesis and characterization of maleated polyethylene/clay nanocomposites.* Polymer, 2001. **42**(24): p. 9819-9826.
106. Kerr, P.F., *Formation and occurrence of clay minerals.* Clays and clay minerals, 1952. **1**(1): p. 19-32.
107. Rawtani, D. and Y. Agrawal, *Multifarious applications of halloysite nanotubes: a review.* Rev. Adv. Mater. Sci, 2012. **30**(3): p. 282-295.
108. Guo, B., Zou Q, Lei Y, Jia D., *Structure and performance of polyamide 6/halloysite nanotubes nanocomposites.* Polymer journal, 2009. **41**(10): p. 835.
109. Du, M., B. Guo, and D. Jia, *Newly emerging applications of halloysite nanotubes: a review.* Polymer International, 2010. **59**(5): p. 574-582.
110. Du, M., Guo B, Wan J, Zou Q, Jia D., *Effects of halloysite nanotubes on kinetics and activation energy of non-isothermal crystallization of polypropylene.* Journal of polymer research, 2010. **17**(1): p. 109.
111. Ismail, H., S. Salleh, and Z. Ahmad, *Properties of halloysite nanotubes-filled natural rubber prepared using different mixing methods.* Materials & Design, 2013. **50**: p. 790-797.
112. Wei, W., Minullina R, Abdullayev E, Fakhrullin R, Mills D, Lvov Y., *Enhanced efficiency of antiseptics with sustained release from clay nanotubes.* RSC Advances, 2014. **4**(1): p. 488-494.
113. Yuan, P., Tan D, Annabi-Bergaya F, Yan W, Fan M, Liu D, He H, *Changes in structure, morphology, porosity, and surface activity of mesoporous halloysite nanotubes under heating.* Clays and Clay Minerals, 2012. **60**(6): p. 561-573.
114. Hassan-Nejad, M., Ganster J, Bohn A, Pinnow M, Volkert B *Bio-Based Nanocomposites of Cellulose Acetate and Nano-Clay with Superior Mechanical Properties*. in *Macromolecular symposia*. 2009. Wiley Online Library.
115. Joo, Y., Jeon Y, Lee SU, Sim JH, Ryu J, Lee S, Lee H, Sohn D, *Aggregation and stabilization of carboxylic acid functionalized halloysite nanotubes (HNT-COOH).* The Journal of Physical Chemistry C, 2012. **116**(34): p. 18230-18235.
116. Liu, M., Guo B, Zou Q, Du M, Jia D, *Interactions between halloysite nanotubes and 2, 5-bis (2-benzoxazolyl) thiophene and their effects on reinforcement of polypropylene/halloysite nanocomposites.* Nanotechnology, 2008. **19**(20): p. 205709.
117. Lecouvet, B., Horion J, D'haese C, Bailly C, Nysten B, *Elastic modulus of halloysite nanotubes.* Nanotechnology, 2013. **24**(10): p. 105704.

118. Guimaraes, L., Enyashin AN, Seifert G, Duarte HA, *Structural, electronic, and mechanical properties of single-walled halloysite nanotube models.* The Journal of Physical Chemistry C, 2010. **114**(26): p. 11358-11363.
119. Liu, M., Guo B, Du M, Cai X, Jia D, *Properties of halloysite nanotube–epoxy resin hybrids and the interfacial reactions in the systems.* Nanotechnology, 2007. **18**(45): p. 455703.
120. Pasbakhsh, P., G.J. Churchman, and J.L. Keeling, *Characterisation of properties of various halloysites relevant to their use as nanotubes and microfibre fillers.* Applied Clay Science, 2013. **74**: p. 47-57.
121. Liu, M., Guo B, Du M, Lei Y, Jia D, *Natural inorganic nanotubes reinforced epoxy resin nanocomposites.* Journal of Polymer Research, 2008. **15**(3): p. 205-212.
122. Li, C., Liu J, Qu X, Guo B, Yang Z, *Polymer-modified halloysite composite nanotubes.* Journal of Applied Polymer Science, 2008. **110**(6): p. 3638-3646.
123. Haroosh, H.J., Dong Y, Chaudhary DS, Ingram GD, Yusa SI, *Electrospun PLA: PCL composites embedded with unmodified and 3-aminopropyltriethoxysilane (ASP) modified halloysite nanotubes (HNT).* Applied Physics A, 2013. **110**(2): p. 433-442.
124. Riza Erdogan, A., I. Kaygusuz, and C. Kaynak, *Influences of aminosilanization of halloysite nanotubes on the mechanical properties of polyamide-6 nanocomposites.* Polymer Composites, 2014. **35**(7): p. 1350-1361.
125. Liu, C., Luo YF, Jia ZX, Zhong BC, Li SQ, Guo BC, Jia DM, *Enhancement of mechanical properties of poly (vinyl chloride) with polymethyl methacrylate-grafted halloysite nanotube.* Express Polymer Letters, 2011. **5**(7).
126. Zhang, J., Zhang D, Zhang A, Jia Z, Jia D., *Poly (methyl methacrylate) grafted halloysite nanotubes and its epoxy acrylate composites by ultraviolet curing method.* Journal of Reinforced Plastics and Composites, 2013. **32**(10): p. 713-725.
127. Yah, W.O., A. Takahara, and Y.M. Lvov, *Selective modification of halloysite lumen with octadecylphosphonic acid: new inorganic tubular micelle.* Journal of the American Chemical Society, 2012. **134**(3): p. 1853-1859.
128. Solomon, D., *Clay minerals as electron acceptors and/or electron donors in organic reactions.* Clays and Clay Minerals, 1968. **16**(31).
129. Liu, M., Guo B, Du M, Jia D, *The role of interactions between halloysite nanotubes and 2, 2'-(1, 2-ethenediyldi-4, 1-phenylene) bisbenzoxazole in halloysite reinforced polypropylene composites.* Polymer journal, 2008. **40**(11): p. 1087.
130. Du, M., Guo B, Liu M, Jia D, *Formation of reinforcing inorganic network in polymer via hydrogen bonding self-assembly process.* Polymer journal, 2007. **39**(3): p. 208.
131. Du, M., Guo B, Liu M, Cai X, Jia D, Reinforcing thermoplastics with hydrogen bonding bridged inorganics. Physica B: Condensed Matter, 2010. **405**(2): p. 655-662.
132. Song-lin, Z., Shang-yu G, Xi-gen Y, Bo-sen X, *Carbonization mechanism of bamboo (phyllostachys) by means of Fourier Transform Infrared and elemental analysis.* Journal of forestry research, 2003. **14**(1): p. 75-79.
133. Jiang, Z.-H., Zhang DS, Fei BH, Yue YD, Chen XH, *Effects of carbonization temperature on the microstructure and electrical conductivity of bamboo charcoal.* New Carbon Mater, 2004. **19**(4): p. 249-253.
134. Zhu, J., Jia J, Kwong FL, Ng DH, Tjong SC, *Synthesis of multiwalled carbon nanotubes from bamboo charcoal and the roles of minerals on their growth.* biomass and bioenergy, 2012. **36**: p. 12-19.
135. Cheng, H.-M., Endo H, Okabe T, Saito K, Zheng GB, *Graphitization behavior of wood ceramics and bamboo ceramics as determined by X-ray diffraction.* Journal of Porous Materials, 1999. **6**(3): p. 233-237.
136. Ye, Y.J. and Z.F. Zhang. *Research Progress of the Properties and Application of Bamboo Charcoal*. in *Applied Mechanics and Materials*. 2013. Trans Tech Publ.

137. Asada, T., et al., *Science of bamboo charcoal: study on carbonizing temperature of bamboo charcoal and removal capability of harmful gases.* Journal of health science, 2002. **48**(6): p. 473-479.
138. Baughman, R.H., A.A. Zakhidov, and W.A. De Heer, *Carbon nanotubes--the route toward applications.* science, 2002. **297**(5582): p. 787-792.
139. Coleman, J.N., Khan U, Blau WJ, Gun'ko YK, *Small but strong: a review of the mechanical properties of carbon nanotube–polymer composites.* Carbon, 2006. **44**(9): p. 1624-1652.
140. An, K.H., WS, Park YS, Moon JM, Bae DJ, Lim SC, Lee YS, Lee YH, *Electrochemical properties of high-power supercapacitors using single-walled carbon nanotube electrodes.* Advanced functional materials, 2001. **11**(5): p. 387-392.
141. Niu, C., Sichel EK, Hoch R, Moy D, Tennent H, *High power electrochemical capacitors based on carbon nanotube electrodes.* Applied Physics Letters, 1997. **70**(11): p. 1480-1482.
142. Zandonella, C., *Is it all just a pipe dream?* 2001, Nature Publishing Group.
143. Reddy, M.M., Vivekanandhan, S., Misra, M., Bhatia, S.K. and Mohanty, A.K., *Biobased plastics and bionanocomposites: Current status and future opportunities.* Progress in Polymer Science, 2013. **38**(10-11): p. 1653-1689.
144. Ma, P.-C., Siddiqui NA, Marom G, Kim JK, *Dispersion and functionalization of carbon nanotubes for polymer-based nanocomposites: a review.* Composites Part A: Applied Science and Manufacturing, 2010. **41**(10): p. 1345-1367.
145. Baur, J. and E. Silverman, *Challenges and opportunities in multifunctional nanocomposite structures for aerospace applications.* MRS bulletin, 2007. **32**(4): p. 328-334.
146. Postek, M.T., Vladár A, Dagata J, Farkas N, Ming B, Wagner R, Raman A, Moon RJ, Sabo R, Wegner TH, Beecher J, *Development of the metrology and imaging of cellulose nanocrystals.* Measurement Science and Technology, 2010. **22**(2): p. 024005.
147. Freire, C.S., Silvestre AJ, Neto CP, Gandini A, Martin L, Mondragon I, *Composites based on acylated cellulose fibers and low-density polyethylene: Effect of the fiber content, degree of substitution and fatty acid chain length on final properties.* Composites Science and Technology, 2008. **68**(15-16): p. 3358-3364.
148. Li, C., J. Adamcik, and R. Mezzenga, *Biodegradable nanocomposites of amyloid fibrils and graphene with shape-memory and enzyme-sensing properties.* Nature Nanotechnology, 2012. **7**(7): p. 421.
149. Lawrence, B.D., Wharram S, Kluge JA, Leisk GG, Omenetto FG, Rosenblatt MI, Kaplan DL., *Effect of hydration on silk film material properties.* Macromolecular bioscience, 2010. **10**(4): p. 393-403.
150. Chang, Y., Yang ST, Liu JH, Dong E, Wang Y, Cao A, Liu Y, Wang H, *In vitro toxicity evaluation of graphene oxide on A549 cells.* Toxicology letters, 2011. **200**(3): p. 201-210.
151. Ghebaur, A., S.A. Garea, and H. Iovu, *New polymer–halloysite hybrid materials—potential controlled drug release system.* International journal of pharmaceutics, 2012. **436**(1-2): p. 568-573.
152. Mallakpour, S. and A. Barati, *Application of modified cloisite Na+ with L-phenylalanine for the preparation of new poly (vinyl alcohol)/organoclay bionanocomposite films.* Polymer-Plastics Technology and Engineering, 2012. **51**(3): p. 321-327.
153. Mallakpour, S. and V. Shahangi, *Bio-modification of cloisite Na+ with chiral L-leucine and preparation of new poly (vinyl alcohol)/organo-nanoclay bionanocomposite films.* Synthesis and Reactivity in Inorganic, Metal-Organic, and Nano-Metal Chemistry, 2013. **43**(8): p. 966-971.
154. Kaboorani, A., B. Riedl, and P. Blanchet, *Ultrasonication technique: a method for dispersing nanoclay in wood adhesives.* Journal of Nanomaterials, 2013. **2013**: p. 3.

155. Mallakpour, S. and S. Moslemi, *Dispersion of chiral amino acid organomodified Cloisite Na+ in poly (vinyl alcohol) matrix for designing of novel bionanocomposite films.* Progress in Organic Coatings, 2012. **74**(1): p. 8-13.
156. Strawhecker, K. and E. Manias, *Structure and properties of poly (vinyl alcohol)/Na+ montmorillonite nanocomposites.* Chemistry of materials, 2000. **12**(10): p. 2943-2949.
157. Liu, M., Guo B, Du M, Jia D, *Drying induced aggregation of halloysite nanotubes in polyvinyl alcohol/halloysite nanotubes solution and its effect on properties of composite film.* Applied Physics A, 2007. **88**(2): p. 391-395.
158. Pavlidou, S. and C. Papaspyrides, *A review on polymer–layered silicate nanocomposites.* Progress in polymer science, 2008. **33**(12): p. 1119-1198.
159. Ray, S.S. and M. Okamoto, *Polymer/layered silicate nanocomposites: a review from preparation to processing.* Progress in polymer science, 2003. **28**(11): p. 1539-1641.
160. Kojima, Y., Usuki A, Kawasumi M, Okada A, Fukushima Y, Kurauchi T, Kamigaito O, *Mechanical properties of nylon 6-clay hybrid.* Journal of Materials Research, 1993. **8**(5): p. 1185-1189.
161. Okamoto, M., S. Morita, and T. Kotaka, *Dispersed structure and ionic conductivity of smectic clay/polymer nanocomposites.* Polymer, 2001. **42**(6): p. 2685-2688.
162. Akelah, A. and A. Moet, *Polymer-clay nanocomposites: free-radical grafting of polystyrene on to organophilic montmorillonite interlayers.* Journal of Materials Science, 1996. **31**(13): p. 3589-3596.
163. Hsu, S.L.-C. and K.-C. Chang, *Synthesis and properties of polybenzoxazole–clay nanocomposites.* Polymer, 2002. **43**(15): p. 4097-4101.
164. Tudor, J., Willington L, O'Hare D, Royan B, *Intercalation of catalytically active metal complexes in phyllosilicates and their application as propene polymerisation catalysts.* Chemical Communications, 1996(17): p. 2031-2032.
165. Sepehr, M., Utracki LA, Zheng X, Wilkie CA, *Polystyrenes with macro-intercalated organoclay. Part I. Compounding and characterization.* Polymer, 2005. **46**(25): p. 11557-11568.
166. Lin, Y., Ng KM, Chan CM, Sun G, Wu J., *High-impact polystyrene/halloysite nanocomposites prepared by emulsion polymerization using sodium dodecyl sulfate as surfactant.* Journal of colloid and interface science, 2011. **358**(2): p. 423-429.
167. Andrews, R., Jacques D, Minot M, Rantell T, *Fabrication of carbon multiwall nanotube/polymer composites by shear mixing.* Macromolecular Materials and Engineering, 2002. **287**(6): p. 395-403.
168. Breuer, O. and U. Sundararaj, *Big returns from small fibers: a review of polymer/carbon nanotube composites.* Polymer composites, 2004. **25**(6): p. 630-645.
169. Gorrasi, G., Tortora M, Vittoria V, Pollet E, Lepoittevin B, Alexandre M, Dubois P, *Vapor barrier properties of polycaprolactone montmorillonite nanocomposites: effect of clay dispersion.* polymer, 2003. **44**(8): p. 2271-2279.
170. Pluta, M., *Morphology and properties of polylactide modified by thermal treatment, filling with layered silicates and plasticization.* Polymer, 2004. **45**(24): p. 8239-8251.
171. Garcıa-López, D., Picazo O, Merino JC, Pastor JM, *Polypropylene–clay nanocomposites: effect of compatibilizing agents on clay dispersion.* European polymer journal, 2003. **39**(5): p. 945-950.
172. Zhou, W.Y., Guo B, Liu M, Liao R, Rabie AB, Jia D, *Poly (vinyl alcohol)/halloysite nanotubes bionanocomposite films: Properties and in vitro osteoblasts and fibroblasts response.* Journal of Biomedical Materials Research Part A, 2010. **93**(4): p. 1574-1587.
173. Lin, C.-A., T.-C. An, and Y.-H. Hsu, *Study on the far infrared ray emission property and adsorption performance of bamboo charcoal/polyvinyl alcohol fiber.* Polymer-Plastics Technology and Engineering, 2007. **46**(11): p. 1073-1078.

174. Li, J. and I. Zhitomirsky, *Cathodic electrophoretic deposition of manganese dioxide films.* Colloids and Surfaces A: Physicochemical and Engineering Aspects, 2009. **348**(1-3): p. 248-253.
175. Deen, I., X. Pang, and I. Zhitomirsky, *Electrophoretic deposition of composite chitosan–halloysite nanotube–hydroxyapatite films.* Colloids and Surfaces A: Physicochemical and Engineering Aspects, 2012. **410**: p. 38-44.
176. Deen, I. and I. Zhitomirsky, *Electrophoretic deposition of composite halloysite nanotube–hydroxyapatite–hyaluronic acid films.* Journal of Alloys and Compounds, 2014. **586**: p. S531-S534.
177. Fornes, T., Yoon PJ, Hunter DL, Keskkula H, Paul DR, *Effect of organoclay structure on nylon 6 nanocomposite morphology and properties.* Polymer, 2002. **43**(22): p. 5915-5933.
178. Krishnamoorti, R. and E.P. Giannelis, *Rheology of end-tethered polymer layered silicate nanocomposites.* Macromolecules, 1997. **30**(14): p. 4097-4102.
179. Vaia, R.A. and E.P. Giannelis, *Polymer melt intercalation in organically-modified layered silicates: model predictions and experiment.* Macromolecules, 1997. **30**(25): p. 8000-8009.
180. Raquez, J.-M., Habibi Y, Murariu M, Dubois P*Polylactide (PLA)-based nanocomposites.* Progress in Polymer Science, 2013. **38**(10-11): p. 1504-1542.
181. Krishnamoorti, R., R.A. Vaia, and E.P. Giannelis, *Structure and dynamics of polymer-layered silicate nanocomposites.* Chemistry of Materials, 1996. **8**(8): p. 1728-1734.
182. Wang, B., Q. Wang, and L. Li, *Morphology and properties of poly (vinyl alcohol)/MMT nanocomposite prepared by solid-state shear milling (S3M).* Journal of Macromolecular Science, Part B, 2014. **53**(1): p. 78-92.
183. Mondal, D., Mollick MM, Bhowmick B, Maity D, Bain MK, Rana D, Mukhopadhyay A, Dana K, Chattopadhyay D, *Effect of poly (vinyl pyrrolidone) on the morphology and physical properties of poly (vinyl alcohol)/sodium montmorillonite nanocomposite films.* Progress in Natural Science: Materials International, 2013. **23**(6): p. 579-587.
184. Tian, H., Wang K, Liu D, Yan J, Xiang A, Rajulu AV., *Enhanced mechanical and thermal properties of poly (vinyl alcohol)/corn starch blends by nanoclay intercalation.* International journal of biological macromolecules, 2017. **101**: p. 314-320.
185. Zhang, L., Wang H, Jin C, Zhang R, Li L, Li X, Jiang S, *Sodium lactate loaded chitosan-polyvinyl alcohol/montmorillonite composite film towards active food packaging.* Innovative Food Science & Emerging Technologies, 2017. **42**: p. 101-108.
186. Allison, P.G., Moser RD, Chandler MQ, Caminero-Rodriguez JA, Torres-Cancel K, Rivera OG, Goodwin JR, Gore ER., *Mechanical, thermal, and microstructural analysis of polyvinyl alcohol/montmorillonite nanocomposites.* Journal of Nanomaterials, 2015. **16**(1): p. 135.
187. Hotta, S. and D. Paul, *Nanocomposites formed from linear low density polyethylene and organoclays.* Polymer, 2004. **45**(22): p. 7639-7654.
188. Rooj, S., A. Das, and G. Heinrich, *Tube-like natural halloysite/fluoroelastomer nanocomposites with simultaneous enhanced mechanical, dynamic mechanical and thermal properties.* European Polymer Journal, 2011. **47**(9): p. 1746-1755.
189. Albdiry, M. and B. Yousif, *Morphological structures and tribological performance of unsaturated polyester based untreated/silane-treated halloysite nanotubes.* Materials & Design, 2013. **48**: p. 68-76.
190. Abu Taqa, A.G., Abu Al-Rub RK, Senouci A, Popelka A, Al-Nuaimi N, Bani-Hani KA, *Experimental Prediction of the Elastic Properties of Nanocomposite Cementitious Materials Based on Nanoindentation Measurements.* Science of Advanced Materials, 2017. **9**(5): p. 830-846.

191. Virgilio, N., Favis BD, Pépin MF, Desjardins P, L'Espérance G, *High contrast imaging of interphases in ternary polymer blends using focused ion beam preparation and atomic force microscopy.* Macromolecules, 2005. **38**(6): p. 2368-2375.
192. Jesson, D.A. and J.F. Watts, *The interface and interphase in polymer matrix composites: Effect on mechanical properties and methods for identification.* Polymer Reviews, 2012. **52**(3): p. 321-354.
193. Li, Y., Huang Y, Krentz T, Natarajan B, Neely T, Schadler LS, *Polymer Nanocomposite Interfaces: The Hidden Lever for Optimizing Performance in Spherical Nanofilled Polymers*, in *Interface/Interphase in Polymer Nanocomposites*. 2016, Scrivener Publishing LLC Beverly, MA.
194. Qu, M., Deng F, Kalkhoran SM, Gouldstone A, *Nanoscale visualization and multiscale mechanical implications of bound rubber interphases in rubber–carbon black nanocomposites.* Soft Matter, 2011. **7**(3): p. 1066-1077.
195. Litvinov, V. and P. Steeman, *EPDM− Carbon black interactions and the reinforcement mechanisms, as studied by low-resolution 1H NMR.* Macromolecules, 1999. **32**(25): p. 8476-8490.
196. Pompe, G. and E. Mäder, *Experimental detection of a transcrystalline interphase in glass-fibre/polypropylene composites.* Composites Science and Technology, 2000. **60**(11): p. 2159-2167.
197. Brown, D., Marcadon V, Mele P, Alberola ND, *Effect of filler particle size on the properties of model nanocomposites.* Macromolecules, 2008. **41**(4): p. 1499-1511.
198. Li, Y., A.M. Waas, and E.M. Arruda, *A closed-form, hierarchical, multi-interphase model for composites—Derivation, verification and application to nanocomposites.* Journal of the Mechanics and Physics of Solids, 2011. **59**(1): p. 43-63.
199. VanLandingham, M., Dagastine RR, Eduljee RF, McCullough RL, Gillespie Jr JW, *Characterization of nanoscale property variations in polymer composite systems: 1. Experimental results.* Composites Part A: applied science and manufacturing, 1999. **30**(1): p. 75-83.
200. Hodzic, A., Kim JK, Lowe AE, Stachurski ZH, *The effects of water aging on the interphase region and interlaminar fracture toughness in polymer–glass composites.* Composites science and technology, 2004. **64**(13-14): p. 2185-2195.
201. Wright-Charlesworth, D.D., Peers WJ, Miskioglu I, Loo LL, *Nanomechanical properties of self-reinforced composite poly (methyl methacrylate) as a function of processing temperature.* Journal of Biomedical Materials Research Part A, 2005. **74**(3): p. 306-314.
202. Gao, S.-L. and E. Mäder, *Characterisation of interphase nanoscale property variations in glass fibre reinforced polypropylene and epoxy resin composites.* Composites Part A: applied science and manufacturing, 2002. **33**(4): p. 559-576.
203. Gao, S.-L., E. Mäder, and S.F. Zhandarov, *Carbon fibers and composites with epoxy resins: topography, fractography and interphases.* Carbon, 2004. **42**(3): p. 515-529.
204. Yedla, S., Kalukanimuttam M, Winter RM, Khanna SK, *Effect of shape of the tip in determining interphase properties in fiber reinforced plastic composites using nanoindentation.* Journal of Engineering Materials and Technology, 2008. **130**(4): p. 041010.
205. Jafarzadeh, S., Claesson PM, Sundell PE, Pan J, Thormann E., *Nanoscale electrical and mechanical characteristics of conductive polyaniline network in polymer composite films.* ACS applied materials & interfaces, 2014. **6**(21): p. 19168-19175.
206. Sababi, M., Kettle J, Rautkoski H, Claesson PM, Thormann E , *Structural and nanomechanical properties of paperboard coatings studied by peak force tapping atomic force microscopy.* ACS applied materials & interfaces, 2012. **4**(10): p. 5534-5541.
207. Pakzad, A., J. Simonsen, and R.S. Yassar, *Gradient of nanomechanical properties in the interphase of cellulose nanocrystal composites.* Composites Science and Technology, 2012. **72**(2): p. 314-319.

208. Fortunati, E., Puglia D, Monti M, Santulli C, Maniruzzaman M, Kenny JM, *Cellulose nanocrystals extracted from okra fibers in PVA nanocomposites.* Journal of Applied Polymer Science, 2013. **128**(5): p. 3220-3230.
209. Widjojo, N., Chung TS, Weber M, Maletzko C, Warzelhan V. , *The role of sulphonated polymer and macrovoid-free structure in the support layer for thin-film composite (TFC) forward osmosis (FO) membranes.* Journal of Membrane Science, 2011. **383**(1-2): p. 214-223.
210. Knauer, K.M., Jennings AR, Bristol AN, Iacono ST, Morgan SE, *Enhanced Surface Properties of Branched Poly (ether sulfone) from Semifluorinated Polyhedral Oligomeric Silsequioxanes.* ACS applied materials & interfaces, 2016. **8**(19): p. 12434-12444.
211. Yu, Y.-H., Lin CY, Yeh JM, Lin WH, *Preparation and properties of poly (vinyl alcohol)–clay nanocomposite materials.* Polymer, 2003. **44**(12): p. 3553-3560.
212. Katti, K.S., D.R. Katti, and R. Dash, *Synthesis and characterization of a novel chitosan/montmorillonite/hydroxyapatite nanocomposite for bone tissue engineering.* Biomedical Materials, 2008. **3**(3): p. 034122.
213. Swapna, V., Suresh KI, Saranya V, Rahana MP, Stephen R, *Thermal properties of poly (vinyl alcohol)(PVA)/halloysite nanotubes reinforced nanocomposites.* International Journal of Plastics Technology, 2015. **19**(1): p. 124-136.
214. Cavallaro, G., De Lisi R, Lazzara G, Milioto S, *Polyethylene glycol/clay nanotubes composites.* Journal of thermal analysis and calorimetry, 2013. **112**(1): p. 383-389.
215. Schmitt, H., Prashantha K, Soulestin J, Lacrampe MF, Krawczak P, *Preparation and properties of novel melt-blended halloysite nanotubes/wheat starch nanocomposites.* Carbohydrate polymers, 2012. **89**(3): p. 920-927.
216. Affdl, J. and J. Kardos, *The Halpin-Tsai equations: a review.* Polymer Engineering & Science, 1976. **16**(5): p. 344-352.
217. De Villoria, R.G. and A. Miravete, *Mechanical model to evaluate the effect of the dispersion in nanocomposites.* Acta Materialia, 2007. **55**(9): p. 3025-3031.
218. Kovalev, A., Shulha H, Lemieux M, Myshkin N, Tsukruk VV, *Nanomechanical probing of layered nanoscale polymer films with atomic force microscopy.* Journal of materials research, 2004. **19**(3): p. 716-728.
219. Mousa, M. and Y. Dong, *Novel Three-Dimensional Interphase Characterisation of Polymer Nanocomposites Using Nanoscaled Topography.* Nanotechnology, 2018.
220. Forrest, S.R., *The path to ubiquitous and low-cost organic electronic appliances on plastic.* Nature, 2004. **428**(6986): p. 911.
221. Nogi, M. and H. Yano, *Transparent nanocomposites based on cellulose produced by bacteria offer potential innovation in the electronics device industry.* Advanced materials, 2008. **20**(10): p. 1849-1852.
222. McCullen, S.D., Ramaswamy S, Clarke LI, Gorga RE, *Nanofibrous composites for tissue engineering applications.* Wiley Interdisciplinary Reviews: Nanomedicine and Nanobiotechnology, 2009. **1**(4): p. 369-390.
223. Hule, R.A. and D.J. Pochan, *Polymer nanocomposites for biomedical applications.* Mrs Bulletin, 2007. **32**(4): p. 354-358.
224. Yunoki, S., Ikoma T, Monkawa A, Ohta K, Kikuchi M, Sotome S, Shinomiya K, Tanaka J., *Control of pore structure and mechanical property in hydroxyapatite/collagen composite using unidirectional ice growth.* Materials letters, 2006. **60**(8): p. 999-1002.
225. Liu, M., Wu C, Jiao Y, Xiong S, Zhou C, *Chitosan–halloysite nanotubes nanocomposite scaffolds for tissue engineering.* Journal of Materials Chemistry B, 2013. **1**(15): p. 2078-2089.
226. Qi, R., Guo R, Shen M, Cao X, Zhang L, Xu J, Yu J, Shi X, *Electrospun poly (lactic-co-glycolic acid)/halloysite nanotube composite nanofibers for drug encapsulation and sustained release.* Journal of materials chemistry, 2010. **20**(47): p. 10622-10629.

227. Levis, S. and P. Deasy, *Characterisation of halloysite for use as a microtubular drug delivery system.* International Journal of Pharmaceutics, 2002. **243**(1-2): p. 125-134.
228. Aguzzi, C., Viseras C, Cerezo P, Salcedo I, Sánchez-Espejo R, Valenzuela C, *Release kinetics of 5-aminosalicylic acid from halloysite.* Colloids and Surfaces B: Biointerfaces, 2013. **105**: p. 75-80.
229. Hasook, A., Muramatsu H, Tanoue S, Iemoto Y, Unryu T, Preparation of nanocomposites by melt compounding polylactic acid/polyamide 12/organoclay a*t different screw rotating speeds using a twin screw extruder.* Polymer Composites, 2008. **29**(1): p. 1-8.
230. Hoidy, W.H., Ahmad MB, Al-Mulla EA, Ibrahim NA, Preparation and characterization of polylactic acid/polycaprolactone clay nanocomposites. Journal of Applied sciences, 2010. **10**(2): p. 97-106.
231. Lepoittevin, B., Pantoustier N, Devalckenaere M, Alexandre M, Calberg C, Jérôme R, Henrist C, Rulmont A, Dubois P, *Polymer/layered silicate nanocomposites by combined intercalative polymerization and melt intercalation: a masterbatch process.* Polymer, 2003. **44**(7): p. 2033-2040.
232. Cyras, V.P., Manfredi LB, Ton-That MT, Vázquez A, *Physical and mechanical properties of thermoplastic starch/montmorillonite nanocomposite films.* Carbohydrate Polymers, 2008. **73**(1): p. 55-63.
233. Tang, X. and S. Alavi, *Recent advances in starch, polyvinyl alcohol based polymer blends, nanocomposites and their biodegradability.* Carbohydrate Polymers, 2011. **85**(1): p. 7-16.
234. Aloui, H., Khwaldia K, Hamdi M, Fortunati E, Kenny JM, Buonocore GG, Lavorgna M, *Synergistic effect of halloysite and cellulose nanocrystals on the functional properties of PVA based nanocomposites.* ACS Sustainable Chemistry & Engineering, 2016. **4**(3): p. 794-800.
235. Loryuenyong, V., Saewong C, Aranchaiya C, Buasri A, *The improvement in mechanical and barrier properties of poly (vinyl alcohol)/graphene oxide packaging films.* Packaging Technology and Science, 2015. **28**(11): p. 939-947.
236. Kim, H.M., J.K. Lee, and H.S. Lee, *Transparent and high gas barrier films based on poly (vinyl alcohol)/graphene oxide composites.* Thin Solid Films, 2011. **519**(22): p. 7766-7771.
237. Sanchez-Garcia, M. and J. Lagaron, *Novel clay-based nanobiocomposites of biopolyesters with synergistic barrier to UV light, gas, and vapour.* Journal of applied polymer science, 2010. **118**(1): p. 188-199.
238. Park, H.-M., Lee WK, Park CY, Cho WJ, Ha CS, *Environmentally friendly polymer hybrids Part I Mechanical, thermal, and barrier properties of thermoplastic starch/clay nanocomposites.* Journal of Materials Science, 2003. **38**(5): p. 909-915.
239. Chang, P.R., Jian R, Yu J, Ma X, *Fabrication and characterisation of chitosan nanoparticles/plasticised-starch composites.* Food Chemistry, 2010. **120**(3): p. 736-740.
240. Mousa, M., Y. Dong, and I.J. Davies, *Eco-friendly polyvinyl alcohol (PVA)/bamboo charcoal (BC) nanocomposites with superior mechanical and thermal properties.* Advanced Composite Materials, 2017: p. 1-11.
241. Haroosh, H.J. and Y. Dong, *Systematic development of electrospun PLA/PCL fibre hybrid mats: Preparation, material characterisation and application in drug delivery*, in *Biodegradable Polyesters*. 2015, Wiley-VCH Verlag GmbH & Co. KGaA. p. 191-213.
242. Chittur, K.K., *FTIR/ATR for protein adsorption to biomaterial surfaces.* Biomaterials, 1998. **19**(4-5): p. 357-369.
243. Bozzola, J.J., *Electron microscopy*. 1992: Wiley Online Library.
244. Menczel, J.D., Judovits L, Prime RB, Bair HE, Reading M, Swier S, *Differential scanning calorimetry (DSC).* Thermal analysis of polymers: Fundamentals and applications, 2009: p. 7-239.

245. Ma, H.-L., Zhang L, Zhang Y, Wang S, Sun C, Yu H, Zeng X, Zhai M, *Radiation preparation of graphene/carbon nanotubes hybrid fillers for mechanical reinforcement of poly (vinyl alcohol) films.* Radiation Physics and Chemistry, 2016. **118**: p. 21-26.
246. Pittenger, B., N. Erina, and C. Su, *Quantitative mechanical property mapping at the nanoscale with PeakForce QNM.* Application Note Veeco Instruments Inc, 2010: p. 1-12.
247. Van Der Werf, K.O., Putman CA, de Grooth BG, Greve J. , *Adhesion force imaging in air and liquid by adhesion mode atomic force microscopy.* Applied physics letters, 1994. **65**(9): p. 1195-1197.
248. Derjaguin, B.V., V.M. Muller, and Y.P. Toporov, *Effect of contact deformations on the adhesion of particles.* Journal of Colloid and interface science, 1975. **53**(2): p. 314-326.
249. Ohler, B., *Practical advice on the determination of cantilever spring constants.* Bruker Application Note# AN94, 2007. **1**.
250. Li, S., Li X, Chen C, Wang H, Deng Q, Gong M, Li D, *Development of electrically conductive nano bamboo charcoal/ultra-high molecular weight polyethylene composites with a segregated network.* Composites Science and Technology, 2016. **132**: p. 31-37.
251. Srinivasan, P., Sarmah AK, Smernik R, Das O, Farid M, Gao W, *A feasibility study of agricultural and sewage biomass as biochar, bioenergy and biocomposite feedstock: production, characterization and potential applications.* Science of the Total Environment, 2015. **512**: p. 495-505.
252. Das, O., A.K. Sarmah, and D. Bhattacharyya, *A novel approach in organic waste utilization through biochar addition in wood/polypropylene composites.* Waste management, 2015. **38**: p. 132-140.
253. She, B., Tao X, Huang T, Lu G, Zhou Z, Guo C, Dang Z, *Effects of nano bamboo charcoal on PAHs-degrading strain Sphingomonas sp. GY2B.* Ecotoxicology and environmental safety, 2016. **125**: p. 35-42.
254. Wang, X., Wang Y, Wang X, Liu M, Xia SQ, Yin DQ, Zhang YL, Zhao JF, *Microwave-assisted preparation of bamboo charcoal-based iron-containing adsorbents for Cr (VI) removal.* Chemical Engineering Journal, 2011. **174**(1): p. 326-332.
255. Pirzada, T., Arvidson SA, Saquing CD, Shah SS, Khan SA, *Hybrid silica–PVA nanofibers via sol–gel electrospinning.* Langmuir, 2012. **28**(13): p. 5834-5844.
256. Yang, X., Li L, Shang S, Tao XM, *Synthesis and characterization of layer-aligned poly (vinyl alcohol)/graphene nanocomposites.* Polymer, 2010. **51**(15): p. 3431-3435.
257. Niu, Y.-F., Yang Y, Gao S, Yao JW, *Mechanical mapping of the interphase in carbon fiber reinforced poly (ether-ether-ketone) composites using peak force atomic force microscopy: Interphase shrinkage under coupled ultraviolet and hydro-thermal exposure.* Polymer Testing, 2016. **55**: p. 257-260.
258. Hossain, M.A., Islam S, Chowdhury FA, Mohiuddin TG, Uchida K, Tamura T, Sugawa K, Mochida T, Otsuki J, Alam MS, *Structural, mechanical, and electrical properties of carbon nanoparticles synthesized from diesel.* Fullerenes, Nanotubes and Carbon Nanostructures, 2016. **24**(1): p. 43-51.
259. Suk, J.W., Piner RD, An J, Ruoff RS, *Mechanical properties of monolayer graphene oxide.* ACS nano, 2010. **4**(11): p. 6557-6564.
260. Demczyk, B., Wang YM, Cumings J, Hetman M, Han W, Zettl A, Ritchie RO, *Direct mechanical measurement of the tensile strength and elastic modulus of multiwalled carbon nanotubes.* Materials Science and Engineering: A, 2002. **334**(1-2): p. 173-178.
261. Fu, D., Zhang Y, Lv F, Chu PK, Shang J, *Removal of organic materials from TNT red water by Bamboo Charcoal adsorption.* Chemical engineering journal, 2012. **193**: p. 39-49.

262. Lorenzoni, M., Evangelio L, Verhaeghe S, Nicolet C, Navarro C, Pérez-Murano F, *Assessing the local nanomechanical properties of self-assembled block copolymer thin films by peak force tapping.* Langmuir, 2015. **31**(42): p. 11630-11638.
263. Li, S., Li X, Deng Q, Li D., *Three kinds of charcoal powder reinforced ultra-high molecular weight polyethylene composites with excellent mechanical and electrical properties.* Materials & Design, 2015. **85**: p. 54-59.
264. Yang, E., Yao C, Liu Y, Zhang C, Jia L, Li D, Fu Z, Sun D, Kirk SR, Yin D, *Bamboo-derived porous biochar for efficient adsorption removal of dibenzothiophene from model fuel.* Fuel, 2018. **211**: p. 121-129.
265. Mousa, M. and Y. Dong, *Strong Poly (Vinyl Alcohol)(PVA)/Bamboo Charcoal (BC) Nanocomposite Films with Particle Size Effect.* ACS Sustainable Chemistry & Engineering, 2017. **6**(1): p. 467-479.
266. Lu, L., Sun H, Peng F, Jiang Z, *Novel graphite-filled PVA/CS hybrid membrane for pervaporation of benzene/cyclohexane mixtures.* Journal of membrane science, 2006. **281**(1-2): p. 245-252.
267. Cheng, H.K.F., Sahoo NG, Tan YP, Pan Y, Bao H, Li L, Chan SH, Zhao J, *Poly (vinyl alcohol) nanocomposites filled with poly (vinyl alcohol)-grafted graphene oxide.* ACS applied materials & interfaces, 2012. **4**(5): p. 2387-2394.
268. Zhang, J., Lei W, Liu D, Wang X, *Synergistic influence from the hybridization of boron nitride and graphene oxide nanosheets on the thermal conductivity and mechanical properties of polymer nanocomposites.* Composites Science and Technology, 2017. **151**: p. 252-257.
269. Liang, J., Huang Y, Zhang L, Wang Y, Ma Y, Guo T, Chen Y, *Molecular-level dispersion of graphene into poly (vinyl alcohol) and effective reinforcement of their nanocomposites.* Advanced Functional Materials, 2009. **19**(14): p. 2297-2302.
270. Xu, Y., Hong W, Bai H, Li C, Shi G, *Strong and ductile poly (vinyl alcohol)/graphene oxide composite films with a layered structure.* Carbon, 2009. **47**(15): p. 3538-3543.
271. Arao, Y., Mizuno Y, Araki K, Kubouchi M, *Mass production of high-aspect-ratio few-layer-graphene by high-speed laminar flow.* Carbon, 2016. **102**: p. 330-338.
272. Liu, L., Barber AH, Nuriel S, Wagner HD. *Mechanical properties of functionalized single-walled carbon-nanotube/poly (vinyl alcohol) nanocomposites.* Advanced Functional Materials, 2005. **15**(6): p. 975-980.
273. Li, Y., Yang T, Yu T, Zheng L, Liao K, *Synergistic effect of hybrid carbon nantube–graphene oxide as a nanofiller in enhancing the mechanical properties of PVA composites.* Journal of Materials Chemistry, 2011. **21**(29): p. 10844-10851.
274. Paiva, M., Zhou B, Fernando KA, Lin Y, Kennedy JM, Sun YP, *Mechanical and morphological characterization of polymer–carbon nanocomposites from functionalized carbon nanotubes.* Carbon, 2004. **42**(14): p. 2849-2854.
275. Wang, Y., Z. Shi, and J. Yin, *Unzipped multiwalled carbon nanotubes for mechanical reinforcement of polymer composites.* The Journal of Physical Chemistry C, 2010. **114**(46): p. 19621-19628.
276. Chen, W., Tao X, Xue P, Cheng X, *Enhanced mechanical properties and morphological characterizations of poly (vinyl alcohol)–carbon nanotube composite films.* Applied Surface Science, 2005. **252**(5): p. 1404-1409.
277. Manna, K., S.K. Srivastava, and V. Mittal, *Role of enhanced hydrogen bonding of selectively reduced graphite oxide in fabrication of poly (vinyl alcohol) nanocomposites in water as EMI shielding material.* The Journal of Physical Chemistry C, 2016. **120**(30): p. 17011-17023.
278. Salavagione, H.J., M.A. Gomez, and G. Martinez, *Polymeric modification of graphene through esterification of graphite oxide and poly (vinyl alcohol).* Macromolecules, 2009. **42**(17): p. 6331-6334.
279. Miaudet, P., Derré A, Maugey M, Zakri C, Piccione PM, Inoubli R, Poulin P, *Shape and temperature memory of nanocomposites with broadened glass transition.* Science, 2007. **318**(5854): p. 1294-1296.

280. Qiao, R., Deng H, Putz KW, Brinson LC, *Effect of particle agglomeration and interphase on the glass transition temperature of polymer nanocomposites.* Journal of Polymer Science Part B: Polymer Physics, 2011. **49**(10): p. 740-748.
281. Peng, Z. and L.X. Kong, *A thermal degradation mechanism of polyvinyl alcohol/silica nanocomposites.* Polymer Degradation and Stability, 2007. **92**(6): p. 1061-1071.
282. Panaitescu, D.M., A.N. Frone, and C. Nicolae, *Micro-and nano-mechanical characterization of polyamide 11 and its composites containing cellulose nanofibers.* European Polymer Journal, 2013. **49**(12): p. 3857-3866.
283. Voss, A., R.W. Stark, and C. Dietz, *Surface versus volume properties on the nanoscale: Elastomeric polypropylene.* Macromolecules, 2014. **47**(15): p. 5236-5245.
284. Mishra, S.K. and S. Kannan, *Development, mechanical evaluation and surface characteristics of chitosan/polyvinyl alcohol based polymer composite coatings on titanium metal.* Journal of the mechanical behavior of biomedical materials, 2014. **40**: p. 314-324.
285. Clifford, C.A. and M.P. Seah, *Quantification issues in the identification of nanoscale regions of homopolymers using modulus measurement via AFM nanoindentation.* Applied surface science, 2005. **252**(5): p. 1915-1933.
286. Syed Asif, S., Wahl KJ, Colton RJ, Warren OL, Quantitative imaging of nanoscale mechanical properties using hybrid nanoindentation and f*orce modulation.* Journal of Applied Physics, 2001. **90**(3): p. 1192-1200.
287. Hall, E., *The deformation and ageing of mild steel: III discussion of results.* Proceedings of the Physical Society. Section B, 1951. **64**(9): p. 747.
288. Song, K., Y. Zhang, and M.L. Minus, *Polymer Interphase Self-Reinforcement and Strengthening Mechanisms in Low-Loaded Nanocomposite Fibers.* Macromolecular Chemistry and Physics, 2015. **216**(12): p. 1313-1320.
289. Hakalahti, M., Mautner A, Johansson LS, Hänninen T, Setälä H, Kontturi E, Bismarck A, Tammelin T, *Direct interfacial modification of nanocellulose films for thermoresponsive membrane templates.* ACS applied materials & interfaces, 2016. **8**(5): p. 2923-2927.
290. Liu, M., Zhou C, Dong B, Wu Z, Wang L, Yu S, Gao C, *Enhancing the permselectivity of thin-film composite poly (vinyl alcohol)(PVA) nanofiltration membrane by incorporating poly (sodium-p-styrene-sulfonate)(PSSNa).* Journal of Membrane Science, 2014. **463**: p. 173-182.
291. Humood, M., Qin S, Song Y, Polychronopoulou K, Zhang Y, Grunlan JC, Polycarpou AA, *Influence of Graphene Reduction and Polymer Cross-Linking on Improving the Interfacial Properties of Multilayer Thin Films.* ACS applied materials & interfaces, 2016. **9**(1): p. 1107-1118.
292. Huang, D., Wang W, Kang Y, Wang A, *A chitosan/poly (vinyl alcohol) nanocomposite film reinforced with natural halloysite nanotubes.* Polymer Composites, 2012. **33**(10): p. 1693-1699.
293. Ramadan, A.R., A.M. Esawi, and A.A. Gawad, *Effect of ball milling on the structure of Na+-montmorillonite and organo-montmorillonite (Cloisite 30B).* Applied Clay Science, 2010. **47**(3-4): p. 196-202.
294. Babu, S.S., Mathew S, Kalarikkal N, Thomas S, *Antimicrobial, antibiofilm, and microbial barrier properties of poly (ε-caprolactone)/cloisite 30B thin films.* 3 Biotech, 2016. **6**(2): p. 249.
295. Gaume, J., Taviot-Gueho C, Cros S, Rivaton A, Therias S, Gardette JL, *Optimization of PVA clay nanocomposite for ultra-barrier multilayer encapsulation of organic solar cells.* Solar energy materials and solar cells, 2012. **99**: p. 240-249.
296. Carli, L.N., J.S. Crespo, and R.S. Mauler, *PHBV nanocomposites based on organomodified montmorillonite and halloysite: the effect of clay type on the morphology and thermal and mechanical properties.* Composites Part A: Applied Science and Manufacturing, 2011. **42**(11): p. 1601-1608.

297. Ploehn, H.J. and C. Liu, *Quantitative analysis of montmorillonite platelet size by atomic force microscopy.* Industrial & Engineering Chemistry Research, 2006. **45**(21): p. 7025-7034.
298. Cheng, Z.L., Qin XX, Liu Z, Qin DZ, *Electrospinning preparation and mechanical properties of PVA/HNTs composite nanofibers.* Polymers for Advanced Technologies, 2017. **28**(6): p. 768-774.
299. Azmi, S., Razak SI, Abdul Kadir MR, Iqbal N, Hassan R, Nayan NH, Abdul Wahab AH, Shaharuddin S, *Reinforcement of poly (vinyl alcohol) hydrogel with halloysite nanotubes as potential biomedical materials.* Soft Materials, 2017. **15**(1): p. 45-54.
300. Ormanci-Acar, T., Celebi F, Keskin B, Mutlu-Salmanlı O, Agtas M, Turken T, Tufani A, Imer DY, Ince GO, Demir TU, Menceloglu YZ, *Fabrication and characterization of temperature and pH resistant thin film nanocomposite membranes embedded with halloysite nanotubes for dye rejection.* Desalination, 2018. **429**: p. 20-32.
301. Ataeefard, M. and S. Moradian, *Surface properties of polypropylene/organoclay nanocomposites.* Applied Surface Science, 2011. **257**(6): p. 2320-2326.
302. Yeh, J.M., M.Y. Yu, and S.J. Liou, *Dehydration of water–alcohol mixtures by vapor permeation through PVA/clay nanocomposite membrane.* Journal of applied polymer science, 2003. **89**(13): p. 3632-3638.
303. Carrado, K.A., P. Thiyagarajan, and D.L. Elder, *Polyvinyl alcohol-clay complexes formed by direct synthesis.* Clays and Clay Minerals, 1996. **44**(4): p. 506-514.
304. Theng, B. *Clay–polymer interactions: summary and perspectives*. in *Clays and Clay Minerals*. 1982. Citeseer.
305. Alishahi, E., Shadlou S, Doagou- R S, Ayatollahi MR, *Effects of Carbon Nanoreinforcements of Different Shapes on the Mechanical Properties of Epoxy-Based Nanocomposites.* macromolecular Materials and Engineering, 2013. **298**(6): p. 670-678.
306. Abdullah, Z.W. and Y. Dong, *Preparation and characterisation of poly (vinyl) alcohol (PVA)/starch (ST)/halloysite nanotube (HNT) nanocomposite films as renewable materials.* Journal of Materials Science, 2018. **53**(5): p. 3455-3469.
307. Asad, M., Saba N, Asiri AM, Jawaid M, Indarti E, Wanrosli WD, *Preparation and characterization of nanocomposite films from oil palm pulp nanocellulose/poly (Vinyl alcohol) by casting method.* Carbohydrate polymers, 2018. **191**: p. 103-111.
308. Raheel, M., Yao K, Gong J, Chen XC, Liu DT, Lin YC, Cui DM, Siddiq M, Tang T, *Poly (vinyl alcohol)/GO-MMT nanocomposites: Preparation, structure and properties.* Chinese Journal of Polymer Science, 2015. **33**(2): p. 329-338.
309. Liu, H. and L.C. Brinson, *Reinforcing efficiency of nanoparticles: A simple comparison for polymer nanocomposites.* Composites Science and Technology, 2008. **68**(6): p. 1502-1512.
310. Schadler, L., L. Brinson, and W. Sawyer, *Polymer nanocomposites: a small part of the story.* Jom, 2007. **59**(3): p. 53-60.
311. Santos, K., Castel CD, Liberman SA, Oviedo MA, Mauler RS, *Polyolefin-based nanocomposite: The effects of processing aids.* Journal of Applied Polymer Science, 2011. **119**(3): p. 1567-1575.
312. Wetzel, B., Rosso P, Haupert F, Friedrich K., *Epoxy nanocomposites–fracture and toughening mechanisms. Engineering fracture mechanics*, 2006. **73**(16): p. 2375-2398.
313. Dong, Y., Marshall J, Haroosh HJ, Mohammadzadehmoghadam S, Liu D, Qi X, Lau KT, *Polylactic acid (PLA)/halloysite nanotube (HNT) composite mats: Influence of HNT content and modification.* Composites Part A: Applied Science and Manufacturing, 2015. **76**: p. 28-36.
314. Sirousazar, M., Kokabi M, Hassan ZM, Bahramian AR, *Polyvinyl alcohol/Na-montmorillonite nanocomposite hydrogels prepared by freezing–thawing method: Structural, mechanical, thermal, and swelling properties.* Journal of Macromolecular Science, Part B, 2012. **51**(7): p. 1335-1350.

315. Ali, S.S., Tang X, Alavi S, Faubion J, *Structure and physical properties of starch/poly vinyl alcohol/sodium montmorillonite nanocomposite films.* Journal of agricultural and food chemistry, 2011. **59**(23): p. 12384-12395.
316. Nakane, K., Yamashita T, Iwakura K, Suzuki F, *Properties and structure of poly (vinyl alcohol)/silica composites.* Journal of Applied Polymer Science, 1999. **74**(1): p. 133-138.
317. Mbhele, Z., Salemane MG, Van Sittert CG, Nedeljković JM, Djoković V, Luyt AS, *Fabrication and characterization of silver− polyvinyl alcohol nanocomposites.* Chemistry of Materials, 2003. **15**(26): p. 5019-5024.
318. Behmer, D.J. and C.P. Hawkins, *Effects of overhead canopy on macroinvertebrate production in a Utah stream.* Freshwater biology, 1986. **16**(3): p. 287-300.
319. Kim, J.-K. and Y.-W. Mai, *Engineered interfaces in fiber reinforced composites*. 1998: Elsevier.
320. Tashiro, K. and H. Tadokoro, *Calculation of three-dimensional elastic constants of polymer crystals. 3. α and γ forms of nylon 6.* Macromolecules, 1981. **14**(3): p. 781-785.
321. Tashiro, K. and M. Kobayashi, *Theoretical evaluation of three-dimensional elastic constants of native and regenerated celluloses: role of hydrogen bonds.* Polymer, 1991. **32**(8): p. 1516-1526.
322. Liu, Y., Hamon AL, Haghi-Ashtiani P, Reiss T, Fan B, He D, Bai J., *Quantitative Study of Interface/Interphase in Epoxy/Graphene-Based Nanocomposites by Combining STEM and EELS.* ACS applied materials & interfaces, 2016. **8**(49): p. 34151-34158.
323. D'Souza, N., Pendse S, Sahu L, Ranade A, Vidhate S, *Impact of Crystallization on the Interface in Polymer Nanocomposites.* Interface/Interphase in Polymer Nanocomposites, 2016: p. 139-170.
324. Fan, H., Hartshorn C, Buchheit T, Tallant D, Assink R, Simpson R, Kissel DJ, Lacks DJ, Torquato S, Brinker CJ, *Modulus–density scaling behaviour and framework architecture of nanoporous self-assembled silicas.* Nature materials, 2007. **6**(6): p. 418.
325. Blighe, F.M., Young K, Vilatela JJ, Windle AH, Kinloch IA, Deng L, Young RJ, Coleman JN, *The effect of nanotube content and orientation on the mechanical properties of polymer–nanotube composite fibers: separating intrinsic reinforcement from orientational effects.* Advanced Functional Materials, 2011. **21**(2): p. 364-371.
326. Zhao, X., Zhang Q, Chen D, Lu P, *Enhanced mechanical properties of graphene-based poly (vinyl alcohol) composites.* Macromolecules, 2010. **43**(5): p. 2357-2363.
327. Tandon, G. and G. Weng, *The effect of aspect ratio of inclusions on the elastic properties of unidirectionally aligned composites.* Polymer composites, 1984. **5**(4): p. 327-333.
328. Chen, B. and J.R. Evans, *Nominal and effective volume fractions in polymer− clay nanocomposites.* Macromolecules, 2006. **39**(5): p. 1790-1796.
329. Van Es, M., *Polymer-clay nanocomposites.* Delft: PhD Thesis, 2001.
330. Wan, C. and B. Chen, *Reinforcement and interphase of polymer/graphene oxide nanocomposites.* Journal of Materials Chemistry, 2012. **22**(8): p. 3637-3646.
331. Wan, C., M. Frydrych, and B. Chen, *Strong and bioactive gelatin–graphene oxide nanocomposites.* Soft Matter, 2011. **7**(13): p. 6159-6166.
332. Buenviaje, C., Ge S, Rafailovich M, Sokolov J, Drake JM, Overney RM, *Confined flow in polymer films at interfaces.* Langmuir, 1999. **15**(19): p. 6446-6450.
333. Lu, B. and S. Torquato, *Nearest-surface distribution functions for polydispersed particle systems.* Physical Review A, 1992. **45**(8): p. 5530.
334. Torquato, S., *Random heterogeneous materials: Microstructure and macroscopic properties. Springer-Verlag, New York.* Google Scholar, 2002: p. 701.
335. Mansoori, G., Carnahan NF, Starling KE, Leland Jr TW, *Equilibrium thermodynamic properties of the mixture of hard spheres.* The Journal of Chemical Physics, 1971. **54**(4): p. 1523-1525.

336. Underwood, E., *Stereology, or the quantitative evaluation of microstructures.* Journal of microscopy, 1969. **89**(2): p. 161-180.
337. Xu, W. and H. Chen, *Analytical and modeling investigations of volume fraction of interfacial layers around ellipsoidal aggregate particles in multiphase materials.* Modelling and Simulation in Materials Science and Engineering, 2012. **21**(1): p. 015005.
338. Xu, W., W. Chen, and H. Chen, *Modeling of soft interfacial volume fraction in composite materials with complex convex particles.* The Journal of chemical physics, 2014. **140**(3): p. 034704.
339. Xu, W. and H. Chen, *Numerical investigation of effect of particle shape and particle size distribution on fresh cement paste microstructure via random sequential packing of dodecahedral cement particles.* Computers & Structures, 2013. **114**: p. 35-45.
340. Xu, W., Duan Q, Ma H, Chen W, Chen H, *Interfacial effect on physical properties of composite media: Interfacial volume fraction with non-spherical hard-core-soft-shell-structured particles.* Scientific reports, 2015. **5**: p. 16003.
341. Fornes, T. and D. Paul, *Modeling properties of nylon 6/clay nanocomposites using composite theories.* polymer, 2003. **44**(17): p. 4993-5013.
342. Zhmayev, Y., Pinge S, Shoorideh G, Shebert GL, Kaur P, Liu H, Joo YL, *Controlling the Placement of Spherical Nanoparticles in Electrically Driven Polymer Jets and its Application to Li-Ion Battery Anodes.* Small, 2016. **12**(40): p. 5543-5553.
343. Yuan, P., Southon PD, Liu Z, Green ME, Hook JM, Antill SJ, Kepert CJ, *Functionalization of halloysite clay nanotubes by grafting with γ-aminopropyltriethoxysilane.* The Journal of Physical Chemistry C, 2008. **112**(40): p. 15742-15751.
344. Erdoğan, S., *Simple Estimation of the Surface Area of Irregular 3D Particles.* Journal of Materials in Civil Engineering, 2016. **28**(8): p. 04016062.

APPENDICES

Appendix A: Interphase Dimension Measurement

A.1 PVA/NBC Nanocomposite Films

According to our previous work [265], NBCs are regarded as anisotropic particles resulting in the interaction with polymer matrices to generate interphase. Interphase could also be anisotropic between NBC/PVA phases. The variation of interphase dimension leads to different nanomechanical properties to influence overall material performance of nanocomposites. A simple approach to measure 3D interphase dimensions to determine interphase surface area and interphase volume based on nanomechanical properties was developed as follows:

- At the first step, interphase dimensions in term of interphase width $W_{\text{Interphase}}$, interphase length $L_{\text{Interphase}}$ and interphase height $H_{\text{Interphase}}$ within PVA/NBC phases were detected. Such dimensions could be determined expermintally by using PFQNM with typical features of distinguishing the interphase between nanoparticles and polymer matrices based on different nanomechanical properties. Therofore, PVA/NBC phases were first scanned transversely by PFQNM at a scanning interval of 10 nm, in which the interphase width $W_{\text{iInterphase}}$ along the ith transverse plane (i =1, 2, 3….) is equal to the summation of individual NBC width W_{iNBC} and its corresponding transverse interphase thickness t_{wi1} and t_{wi2}, as illustrated in Figure A1, namely.

$$W_{\text{i Interphase}} = W_{\text{iNBC}} + t_{\text{Wi1}} + t_{\text{Wi2}} \quad \text{(A1)}$$

The same applies to further AFM measurements of interphase length ($L_{j\ \text{Interphase}}$) and interphase height ($H_{k\ \text{Interphase}}$) with similar equations being used as follows:

$$L_{\text{j Interphase}} = L_{\text{jNBC}} + t_{\text{Lj1}} + t_{\text{Lj2}} \quad \text{(A2)}$$

$$H_{\text{k Interphase}} = H_{\text{kNBC}} + t_{\text{Hk1}} + t_{\text{Hk2}} \quad \text{(A3)}$$

Where the interphase length $L_{\text{j Interphase}}$ along the jth longitudinal plane (j =1, 2, 3….) is equal to the summation of individual NBC length L_{jNBC} and its corresponding longitudinal interphase thickness t_{Lj1} and t_{Lj2}, Figure A2 (a). Furthermore, as shown in Figure A2 (b), the interphase height $H_{\text{k Interphase}}$ along the kth height plane (k =1, 2, 3….) can be given by adding up individual NBC height H_{kNBC}, height interphase thickness t_{Hk1} and t_{Hk2}

.

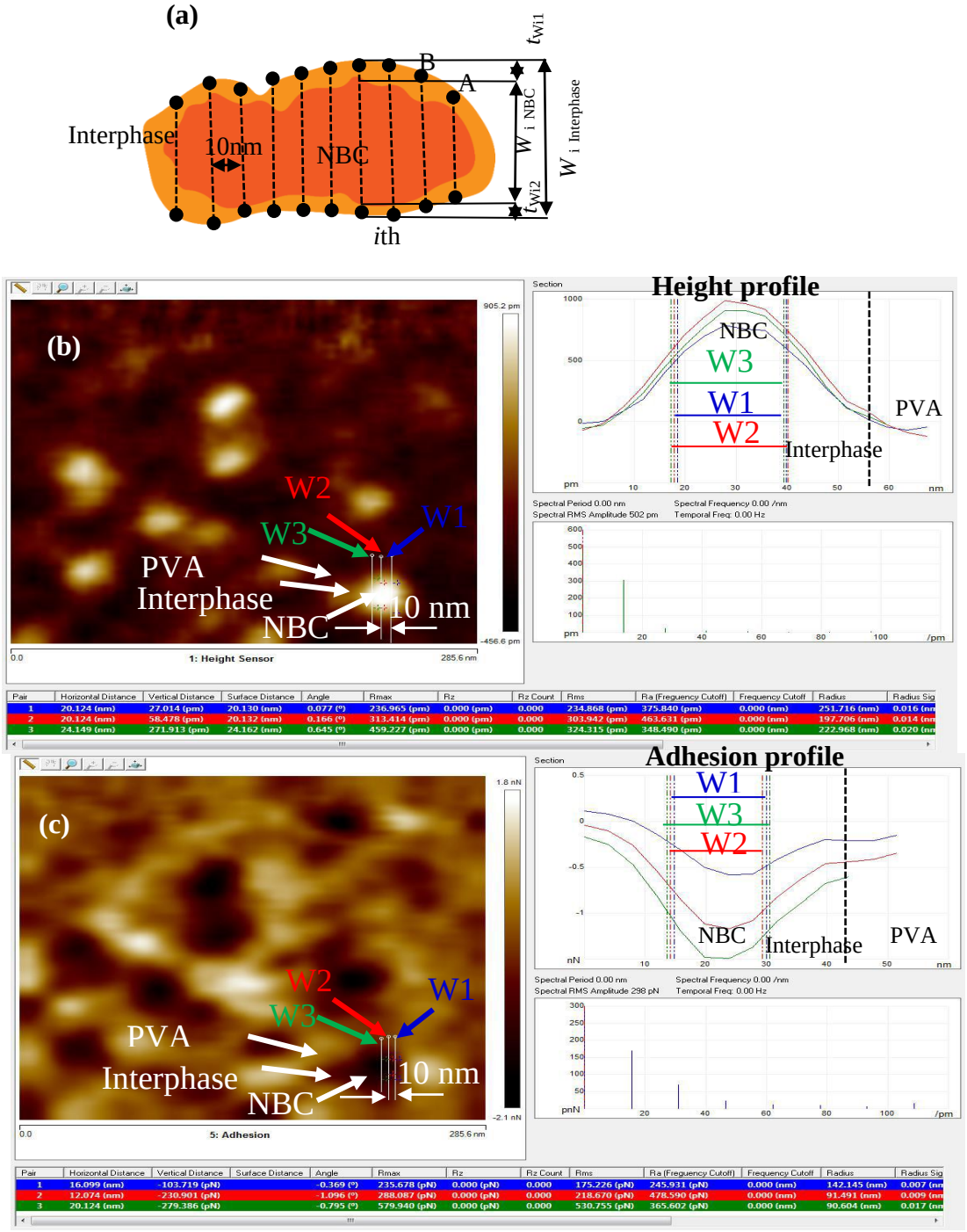

Figure A.1 (a) Schematic diagrams of cross-sectional scanning of PVA/NBC interphases in PVA/NBC nanocomposites along transverse plane with (b) height profile and (c) adhesion profile.

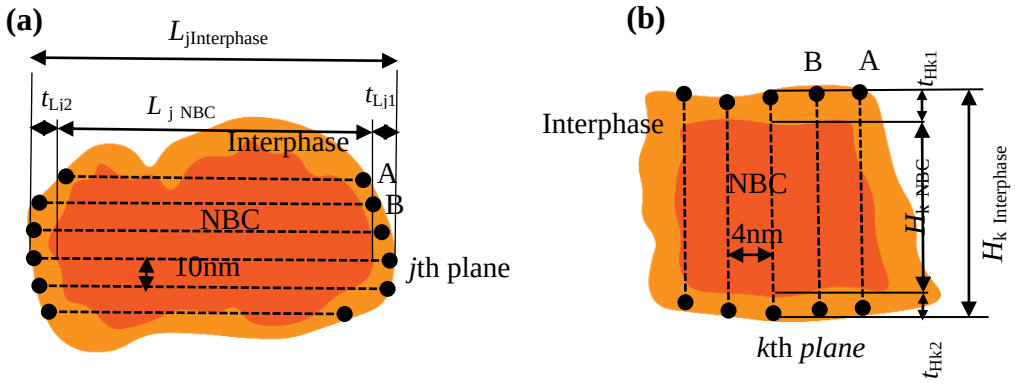

Figure A.2 Schematic diagrams of cross-sectional scanning of PVA/NBC interphases in PVA/NBC nanocomposites along (a) longitudinal plane in a top view, and (c) height plane in a side view.

- The next step is to employ these dimensions in calculating interphase surface areas. In PVA/NBC nanocomposites, Surface area calculations of NBCs and interphases should take into consideration the fundamental concept of particle shapes of anisotropic NBCs. According to Behmer and Hawkins [318]. surface area (SA_p) of anisotropic particles could be calculated in the following equation:

$$\boldsymbol{SA_p = a + b\,L^2 + cW^2 + dH^2} \qquad \text{(A4)}$$

Where L, W and H denote the maximum length, width and thickness of anisotropic particles, respectively and a, b, c and d, are constants that can be determine by fitting experimentally derived SA_p with equation (A4) [344]. In PVA/NBC nanocomposites, it is assumed that NBCs are uniformed dispersed within PVA matrices, resulting in two typical categories for the particle-matrix interaction including fully embedded and partially embedded NBCs within PVA matrices. Equation (A4) can be rewritten for calculating surface areas of outer interface ($SA_{outer\ Interface}$) and inner interface ($SA_{inner\ Interface}$) for a wide range of fully and partially embedded NBCs (subscripts of 'f' and 'p' mean fully and partially embedded NBCs) given by:

$$\left(SA_{outer\ Interface}\right)_{f} = a_1 + b_1 L^2_{\text{Interphase}} + c_1 W^2_{\text{Interphase}} + d_1 H^2_{\text{Interphase}} \quad \text{(A5)}$$

$$\left(SA_{outer\ Interface}\right)_{p} = a_2 + b_2 L'^2_{\text{Interphase-effective}} + c_2 W'^2_{\text{Interphase-effective}} + d_2 H'^2_{\text{Interphase-effective}} \quad \text{(A6)}$$

$$\left(SA_{inner\ Interface}\right)_{f} = a_3 + b_3 L^2_{\text{NBC}} + c_3 W^2_{\text{NBC}} + d_3 H^2_{\text{NBC}} \quad \text{(A7)}$$

$$\left(SA_{inner\ Interface}\right)_{p} = a_4 + b_4 L'^2_{\text{NBC-effective}} + c_4 W'^2_{\text{NBC-effective}} + d_4 H'^2_{\text{NBC-effective}} \quad \text{(A8)}$$

where $L'_{\text{Interphase-effective}}$, $W'_{\text{Interphase-effective}}$ and $H'_{\text{Interphase-effective}}$ represent the maximum length, width and thickness for effective interphases. $L'_{\text{NBC-effective}}$, $W'_{\text{NBC-effective}}$ and $H'_{\text{NBC-effective}}$ denote the maximum length, width and thickness for effective NBCs. a_1, b_1, c_1, d_1, a_2, b_2, c_2, d_2, a_3, b_3, c_3, d_3 and a_4, b_4, c_4, d_4 are constants determined using curving fitting. For instance, the constants of a_1, b_1, c_1 and d_1 were determined to be 0.7439, 0.3627, 0.7006, and 0.9979, respectively, by fitting equation (A5) with measured surface area $(SA_{outer\ Interface})_f$ obtained from the AFM, as depicted in Figure A3. Using such coefficients on the training set, the average error was about 8.7% while the maximum error is 26.7%, which were similar to those obtained from the validation sets.

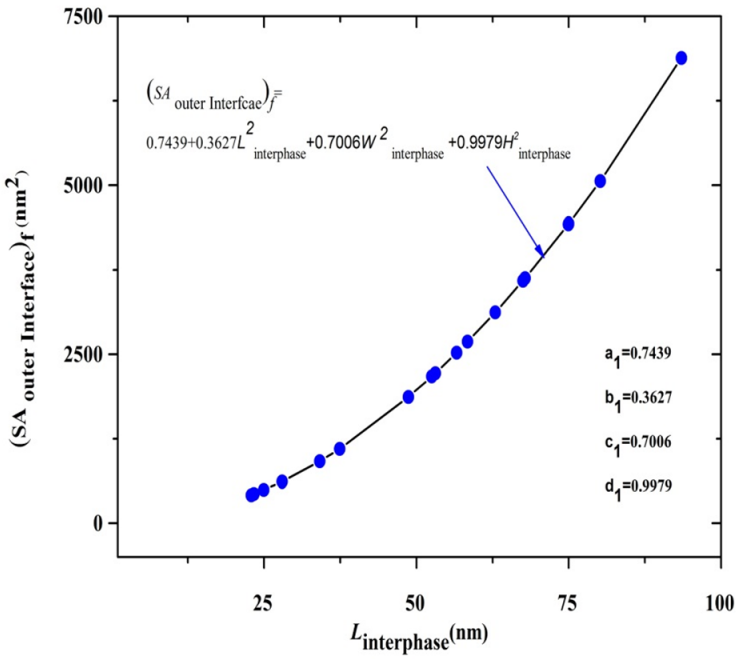

Figure A.3 Relationship between surface area of outer interface ($SA_{\text{outer interface}}$) and interphase length ($L_{\text{Interphase}}$) in PVA/NBC phases.

- At the third step, the interphase volume was calculated based on the following equation suggested by Erdoğan [344]:

$$\boldsymbol{SA_p = eV_p^f} \tag{A9}$$

Where V represents the volume of anisotropic particles and e and f are also constants to be determine by fitting experimentally acquired SA_p with equation (A5). In case of PVA/NBC nanocomposite system, equation (A9) can be rewritten to calculate interphase and NBC volume $V_{\text{NBC/Interphase}}$ as well as NBC volume V_{NBC} in case of fully and partially embedded NBCs by rearranging the following equations:

$$\left(\boldsymbol{SA_{outer\ Interface}}\right)_{\mathbf{f}} = \boldsymbol{e_1 V^{f_1}_{\text{NBC/Interphase}}} \tag{A10}$$

$$\left(SA_{outer\ Interface}\right)_{\text{p}} = e_2 V^{f_2}_{\text{NBC/Interphase-effective}} \tag{A11}$$

$$\left(SA_{inner\ Interface}\right)_{\text{f}} = e_3 V^{f_3}_{\text{NBC}} \tag{A12}$$

$$\left(SA_{inner\ Interface}\right)_{p} = e_4 V_{NBC-effective}^{f_4} \quad \text{(A13)}$$

e_1, f_1, e_2, f_2, e_3, f_3 and e_4, f_4 are constants determined using curving fitting. For example, the constants of e_1 and f_1 were estimated to be 0.3824 and 0.3825, respectively with R^2= ~0.995, as depicted in Figure A4. Such estimation was achieved by fitting equation (A10) with the data of $V_{NBC/Interphase}$ being obtained from the AFM measurement.

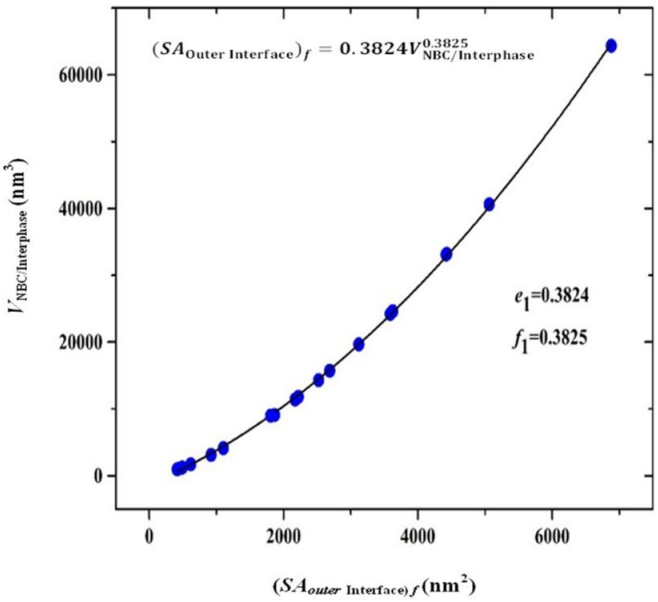

Figure 0.4 Relationship between surface area of outer interface ($SA_{outer\ interface}$) and NBC/interphase volume ($V_{NBC/Interphase}$).

- Final step represents the calculation of interphase volume $V_{Interphase}$ for fully or partially embedded NBCs in PVA/NBC nanocomposites based on Figures 6.1(a) and (b) given by:

$$(V_{Interphase})_f = V_{NBC/Interphase} - V_{NBC} \quad \text{(A14)}$$

$$(V_{Interphase})_p = V_{NBC/Interphase\text{-}effective} - V_{NBC\ effective} \quad \text{(A15)}$$

A.2 PVA/Cloisite30B Clay Nanocomposite Films

Despite a general concept of platelet-like shapes for Cloisite 30B clays, morphological structures of Cloisite 30B clays within PVA matrices reveal that their shapes can be more complex and irregular, as shown in Figure (5.8). Moreover, PVA/Cloisite 30B clay interphase has non-uniform thickness presented in Figure 6.6 with a similar behaviour to PVA/NBC interphase in PVA nanocomposites. Hence, an identical approach to detect 3D interphase dimensions in PVA/NBC nanocomposites was also employed for PVA/Cloisite 30B clay nanocomposites as follows:

- First of all, PVA/ Cloisite 30B clay phases were scanned transversely in Figure A5 in order to detect $W_{\text{iInterphase}}$. The scanning process was carried out within a size interval of 10 nm. Interphase width $W_{\text{iInterphase}}$ along the *i*th transverse plane (i =1, 2, 3….) can be rewritten according to equation A1 as below:

$$W_{\text{i Interphase}} = W_{\text{iCloisite30B}} + t_{\text{Wi1}} + t_{\text{Wi2}} \quad \text{(A16)}$$

The $L_{\text{j Interphase}}$ and $H_{\text{k Interphase}}$ in case of PVA/Cloisite 30B clay nanocomposites were determined by scanned PVA/Cloisite 30B clay phases via PFQNM along the *j*th longitudinal plane (j =1, 2, 3….) and along the *k*th height plane (k =1, 2, 3….), as presented in Figures A6 (a) and (b), respectively. Accordingly, equations (A5) and (A6) can be rewritten as follows

$$L_{\text{j Interphase}} = L_{\text{jCloisite30B}} + t_{\text{Lj1}} + t_{\text{Lj2}} \quad \text{(A17)}$$

$$H_{\text{k Interphase}} = H_{\text{kCloisite30B}} + t_{\text{Hk1}} + t_{\text{Hk2}} \quad \text{(A18)}$$

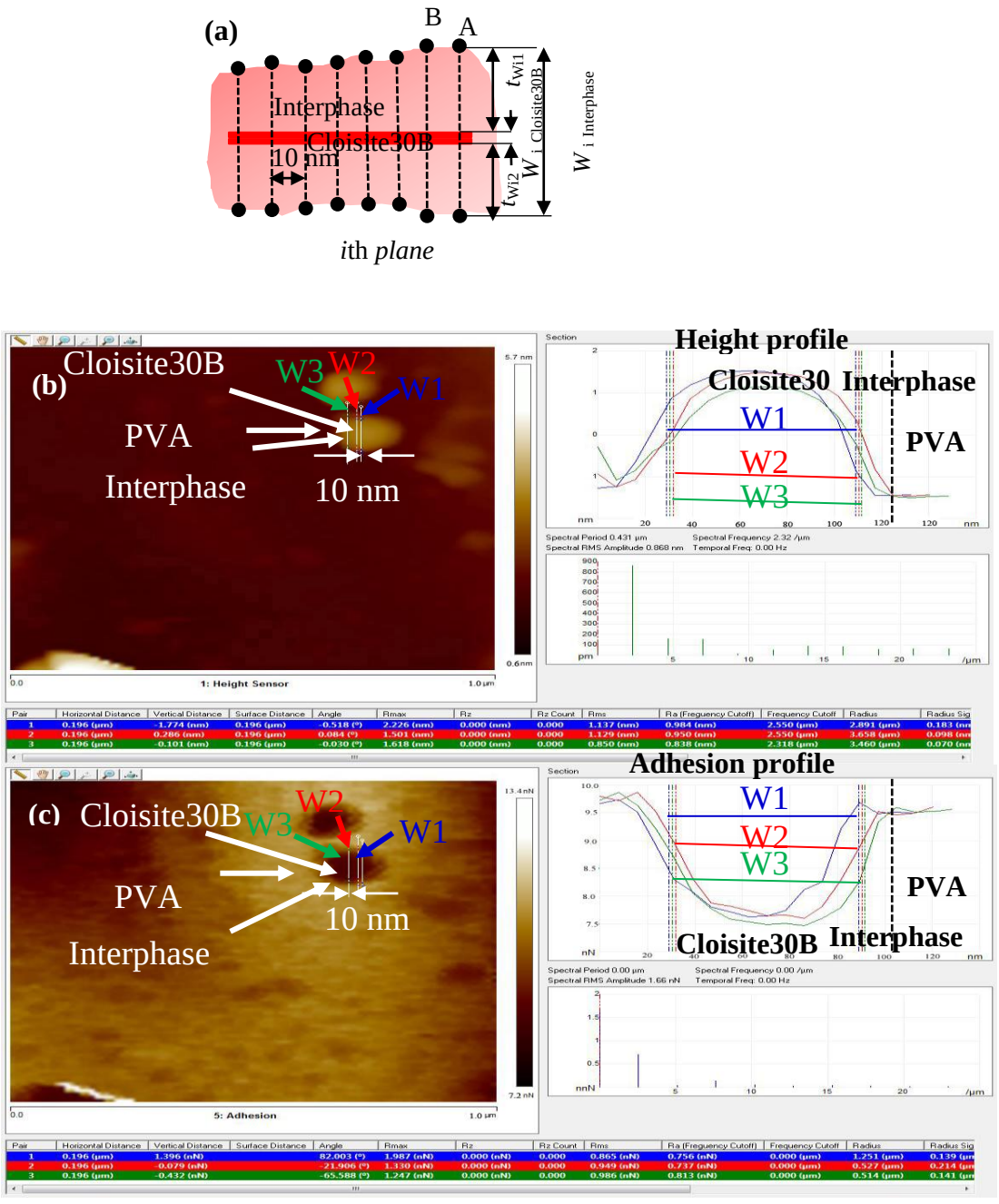

Figure 0.5 (a) Schematic diagrams of cross-sectional scanning of PVA/Cloisite30B clay interphases in PVA/ Cloisite30B clay nanocomposites along transverse plane with (b) height profile and (c) adhesion profile.

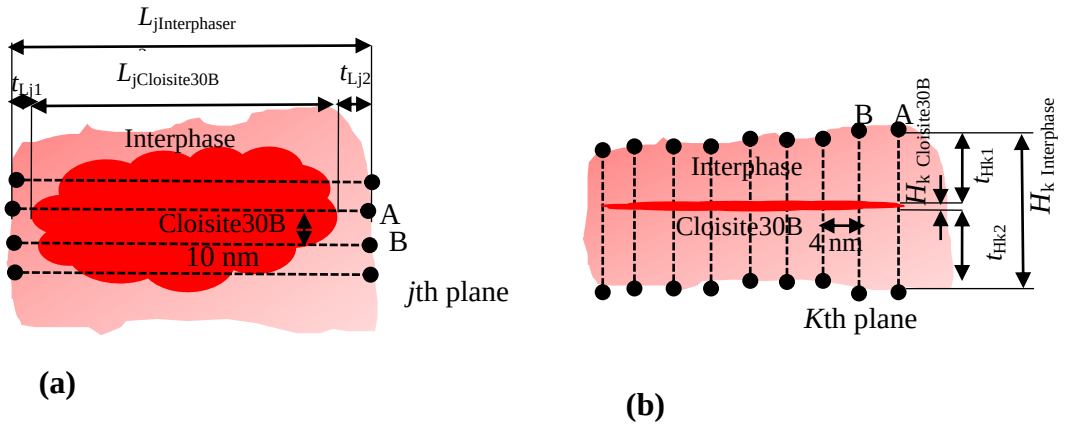

Figure A.6 Schematic diagrams of cross-sectional scanning of PVA/ Cloisite 30B clay interphases in PVA/ Cloisite 30B clay nanocomposites along (a) longitudinal plane both in a top view, and (b) height plane in a side view.

- Next step is to calculate $(SA_{outer\ Interface})_f$, $(SA_{outer\ Interface})_p$, $(SA_{inner\ Interface})_f$ and $(SA_{inner\ Interface})_p$ in PVA/Cloisite 30B phases by using equation (6.1)-(6.4) with the consideration of interphase dimensions as given by:

$$(\boldsymbol{SA_{outer\ Interface}})_f = \boldsymbol{a'_1} + \boldsymbol{b'_1}\,\boldsymbol{L^2_{Interphase}} + \boldsymbol{c'_1}\boldsymbol{W^2_{Interphase}} + \boldsymbol{d'_1}\boldsymbol{H^2_{Interphase}} \quad \text{(A19)}$$

$$(SA_{outer\ Interface})_p \quad \text{(A20)}$$

$$= a'_2 + b'_2\,L'^2_{Interphase-effective} + c'_2 W'^2_{Interphase-effective} + d'_2 H'^2_{Interphase-effective}$$

$$(SA_{inner\ Interface})_f = a'_3 + b'_3\,L^2_{Cloisite30B} + c'_3 W^2_{Cloisite30B} + d'_3 H^2_{Cloisite30B} \quad \text{(A21)}$$

$$(SA_{inner\ Interface})_p \quad \text{(A22)}$$

$$= a'_4 + b'_4\,L'^2_{Cloisite30B-effective} + c'_4 W'^2_{Cloisite30B-effective} + d'_4 H'^2_{Cloisite30B-effective}$$

a'_1, b'_1, c'_1, d'_1, a'_2, b'_2, c'_2, d'_2, a'_3, b'_3, c'_3, d'_3 and a'_4, b'_4, c'_4, d'_4 are constants determined via curving fitting. For instance, the constants of a'_1, b'_1, c'_1 and d'_1 were determined to be 0.6695, 0.3264, 0.7431, and 0.8981, respectively, as shown in

Figure A7 by fitting equation (A19) with measured surface area ($SA_{outer\ Interface}$)$_f$ obtained from the AFM.

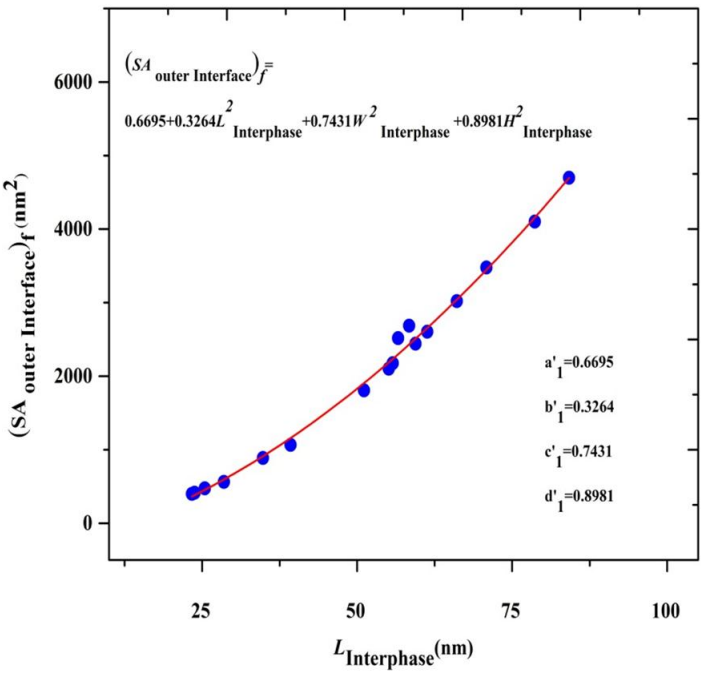

Figure A.7 Relationship between surface area of outer interface ($SA_{outer\ interface}$) and interphase length ($L_{Interphase}$) in PVA/Cloisite 30B clay phases.

- At this step, the interphase volume in PVA/Cloisite 30B clay phases was calculated in case of fully and partially embedded Cloisite 30B clays by rearranging equations (6.5)-(6.8) to yield:

$$\left(\boldsymbol{SA_{outer\ Interface}}\right)_{\mathbf{f}} = \boldsymbol{e'_1 V^{f'_1}_{Cloisite30B/Interphase}} \quad \text{(A23)}$$

$$\left(SA_{outer\ Interface}\right)_{\mathrm{p}} = e'_2 V^{f'_2}_{\mathrm{Cloisite30B/Interphase-effective}} \quad \text{(A24)}$$

$$\left(SA_{inner\ Interface}\right)_{\mathrm{f}} = e'_3 V^{f'_3}_{\mathrm{Cloisite30B}} \quad \text{(A25)}$$

$$\left(SA_{inner\ Interface}\right)_{\mathrm{p}} = e'_4 V^{f'_4}_{\mathrm{Cloisite30B-effective}} \quad \text{(A26)}$$

e'_1, f'_1, e'_2, f'_2, e'_3, f'_3 and e'_4, f'_4 are constants determined using curving fitting. For instance, the constants of e'_1 and f'_1 were calculated to be 0.4015 and 0.4116, respectively with R^2= ~0.96, as shown in Figure A8.

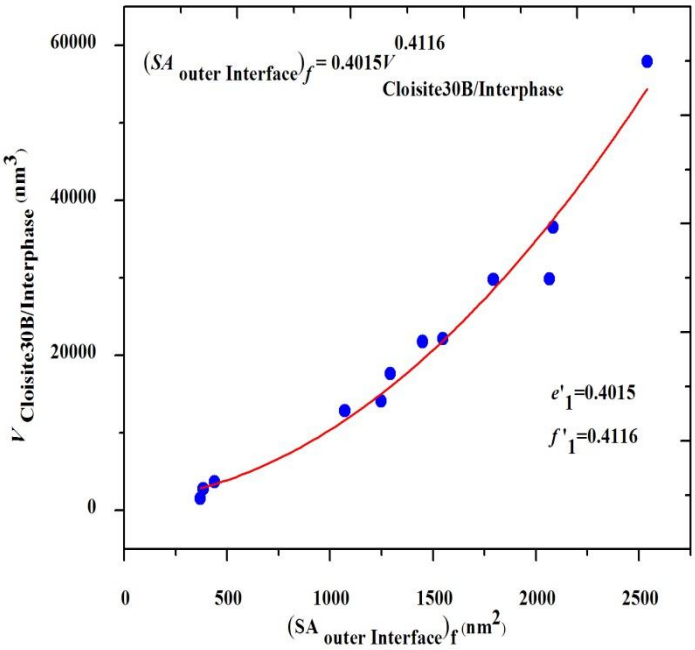

Figure 0.8 Relationship between surface area of outer interface ($SA_{\text{outer interface}}$) and Cloisite 30B clay /interphase volume ($V_{\text{Cloisite30B}}/_{\text{Interphase}}$).

- At the last step, $V_{\text{Interphase}}$ was calculated for fully or partially embedded Cloisite 30B clays in PVA/ Cloisite 30B clay nanocomposites based on Figures 6.1(c) and (d), which is given by:

$$(V_{\text{Interphase}})_f = V_{\text{Cloisite30B/Interphase}} - V_{\text{Cloisite30B}} \quad \text{(A27)}$$

$$(V_{\text{Interphase}})_p = V_{\text{Cloisite30B/Interphase-effective}} - V_{\text{Cloisite30B effective}} \quad \text{(A28)}$$

A.3 PVA/HNT Nanocomposite Films

In a similar manner, real HNTs can show irregular shapes as well though they tend to mainly possess hollow tubular structures, as evidenced in Figure 5.3.Non-uniform interphase thickness is once more proven for PVA/HNT interaction in corresponding nanocomposites, as presented in Figure 6.5. Thus the determination of 3D interphase dimensions of PVA/HNT nanocomposites also follows the same procedure mentioned earlier in PVA nanocomposites reinforced with NBCs and Cloisite 30B clays as follows:

- Two typical diameters were assumed for PVA/ HNT phases, as shown in Figure A9 (a), consisting of the diameter along transverse section (DT_{iHNT}) and the diameter along longitudinal plane section (DL_{jHNT}). Thus, to determine $W_{i\ Interphase}$ in PVA/ HNT phases, they were scanned transversely, as depicted in Figure A9 to yield the following equation:

$$W_{i\ Interphase} = DT_{iHNT} + t_{Wi1} + t_{Wi2} \quad \text{(A29)}$$

The $L_{j\ Interphase}$ and $H_{k\ Interphase}$ of PVA/ HNT phases were measured by scanning along the *j*th longitudinal plane (*j* =1, 2, 3….) and along the *k*th height plane (*k* =1, 2, 3….), as shown in Figures A10 (a) and (b), respectively. Hence, equations (A2) and (A3) can be rewritten as follows:

$$L_{j\ Interphase} = L_{jHNT} + t_{Lj1} + t_{Lj2} \quad \text{(A30)}$$

$$H_{k\ Interphase} = DL_{iHNT} + t_{Hk1} + t_{Hk2} \quad \text{(A31)}$$

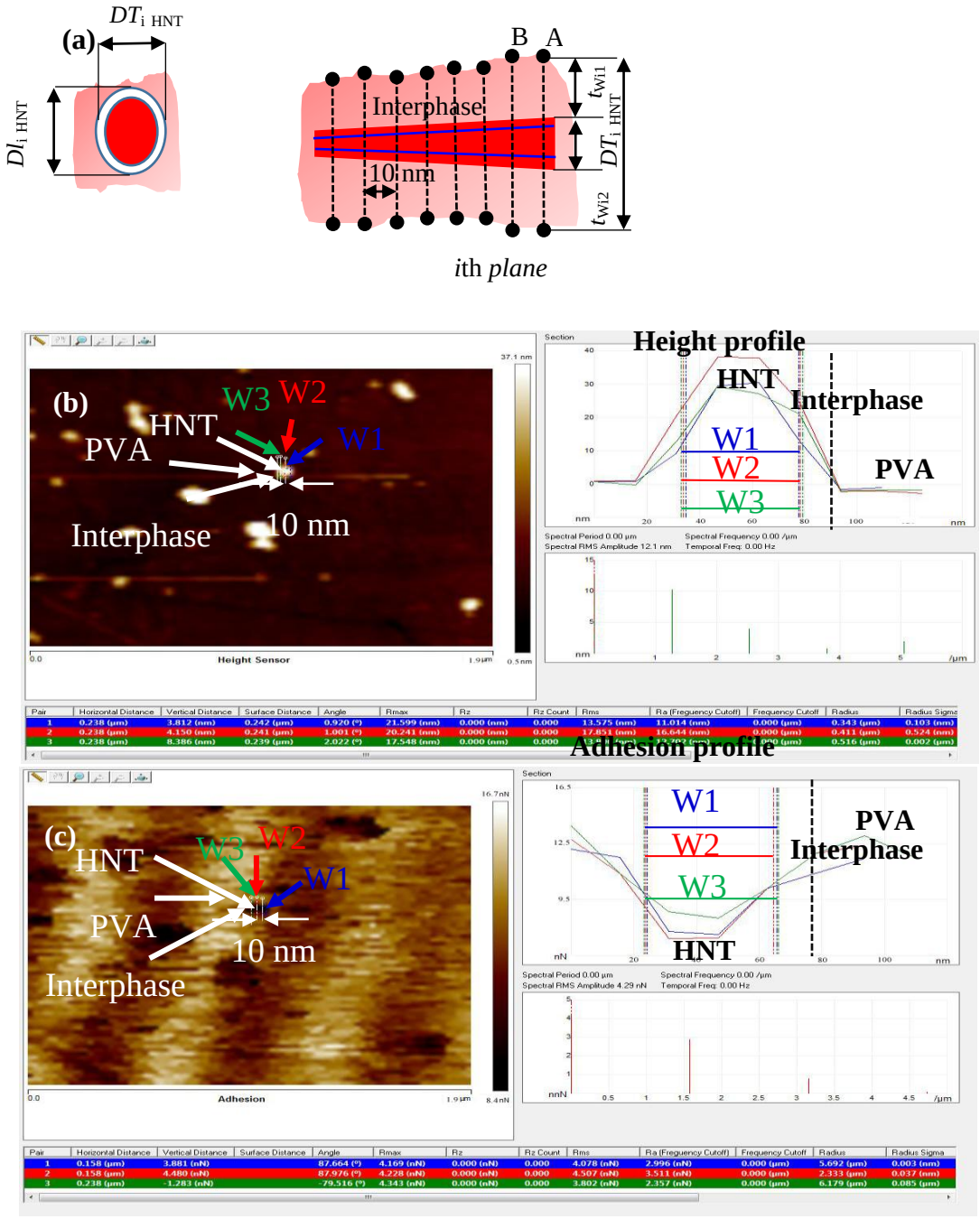

Figure 0.9 (a) Schematic diagrams of cross-sectional scanning of PVA/HNT interphases in PVA/HNT nanocomposites along transverse plane with (b) height profile and (c) adhesion profile.

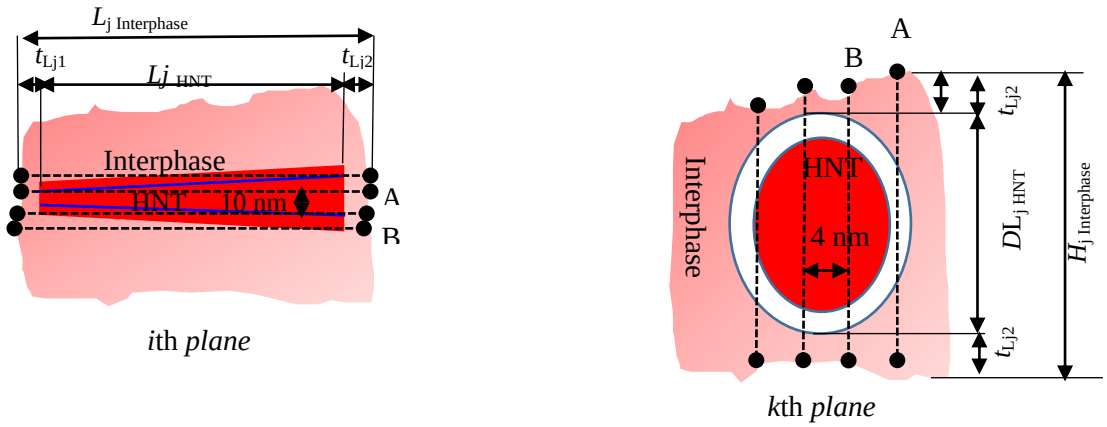

Figure A.10 Schematic diagrams of cross-sectional scanning of PVA/HNT interphases in PVA/HNT nanocomposites along (a) longitudinal plane in a top view, and (b) height plane in a side view.

- Next step is to determine interphase dimensions of PVA/HNT phases to calculate $(\ SA_{outer\ Interface}\ )_{\ f}$, $(\ SA_{outer\ Interface}\ )_{\ p}$, $(\ SA_{inner\ Interface}\ )_{\ f}$ and $(\ SA_{inner\ Interface}\ )_{\ p}$ as given by:

$$(\ \boldsymbol{SA_{outer\ Interface}}\ )_{\ \mathbf{f}} = \boldsymbol{a''_1} + \boldsymbol{b''_1}\,\boldsymbol{L^2_{Interphase}} + \boldsymbol{c''_1}\boldsymbol{W^2_{Interphase}} + \boldsymbol{d''_1}\boldsymbol{H^2_{Interphase}} \quad \text{(A32)}$$

$$(\ SA_{outer\ Interface}\ )_{\ p} = a''_2 + b''_2\,L'^2_{\text{Interphase}-\text{effective}} + c''_2 W'^2_{\text{Interphase}-\text{effective}} + d''_2 H'^2_{\text{Interphase}-\text{effective}} \quad \text{(A33)}$$

$$(\ SA_{inner\ Interface}\ )_{\ f} = a''_3 + b''_3\,L^2_{HNT} + c''_3 W^2_{HNT} + d''_3 H^2_{HNT} \quad \text{(A34)}$$

$$(\ SA_{inner\ Interface}\ )_{\ p} = a''_4 + b''_4\,L'^2_{\text{HNT}-\text{effective}} + c''_4 W'^2_{\text{HNT}-\text{effective}} + d''_4 H'^2_{\text{HNT}-\text{effective}} \quad \text{(A35)}$$

a''_1, b''_1, c''_1, d''_1, a''_2, b''_2, c''_2, d''_2, a''_3, b''_3, c''_3, d''_3 and a''_4, b''_4, c''_4, d''_4 are constants determined by curving fitting. For example, the constants of a''_1, b''_1, c''_1 and d''_1 were detected to be 0.4932, 0.4135, 0.6613, and 0.7621, respectively, as depicted in Figure A11 by fitting equation (A32) with measured surface area ($SA_{outer\ Interface}$)$_f$ obtained from the AFM.

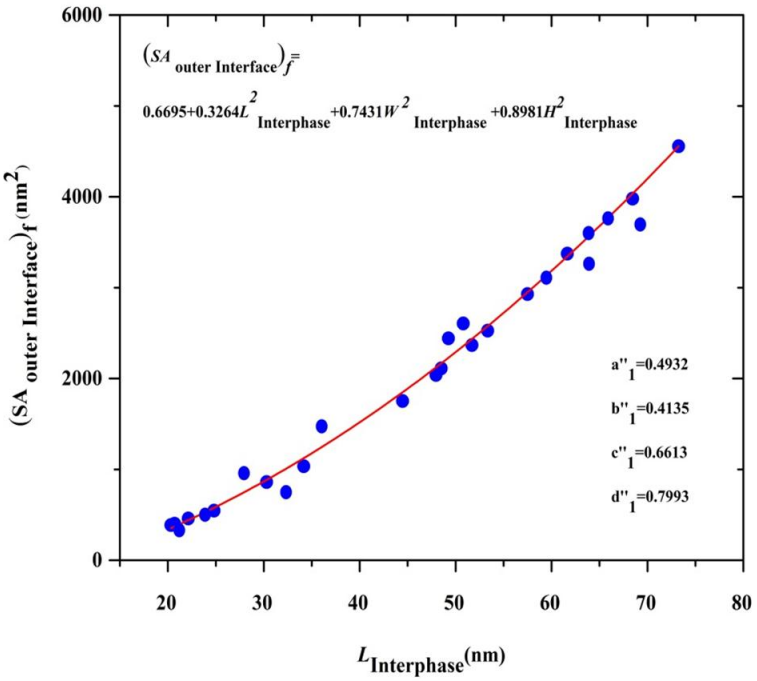

Figure 0.11 Relationship between surface area of outer interface ($SA_{\text{outer interface}}$) and interphase length ($L_{\text{Interphase}}$) in the PVA/HNT phases.

- At the third step, interphase volume in PVA/HNT phases was calculated in case of fully and partially embedded HNT by rewriting the equations(6.5)-(6.7) in the following:

$$\left(\boldsymbol{SA_{outer\ Interface}}\right)_{\mathbf{f}} = \boldsymbol{e''_1 V^{f''_1}_{HNT/Interphase}} \qquad \text{(A36)}$$

$$\left(SA_{outer\ Interface} \right)_{p} = e''_2 V_{\mathrm{HNT/Interphase-effective}}^{f''_2} \quad \text{(A37)}$$

$$\left(SA_{inner\ Interface} \right)_{f} = e''_3 V_{\mathrm{HNT}}^{f''_3} \quad \text{(A38)}$$

$$\left(SA_{inner\ Interface} \right)_{p} = e''_4 V_{\mathrm{HNT-effective}}^{f''_4} \quad \text{(A39)}$$

e''_1, f''_1, e''_2, f''_2, e''_3, f''_3 and e''_4, f''_4 are constants determined by curving fitting. For instance, the constants of e''_1 , and f''_1 were calculated to be 0.4432 and 0.4726, respectively with R^2= ~0.95, as shown in Figure A12.

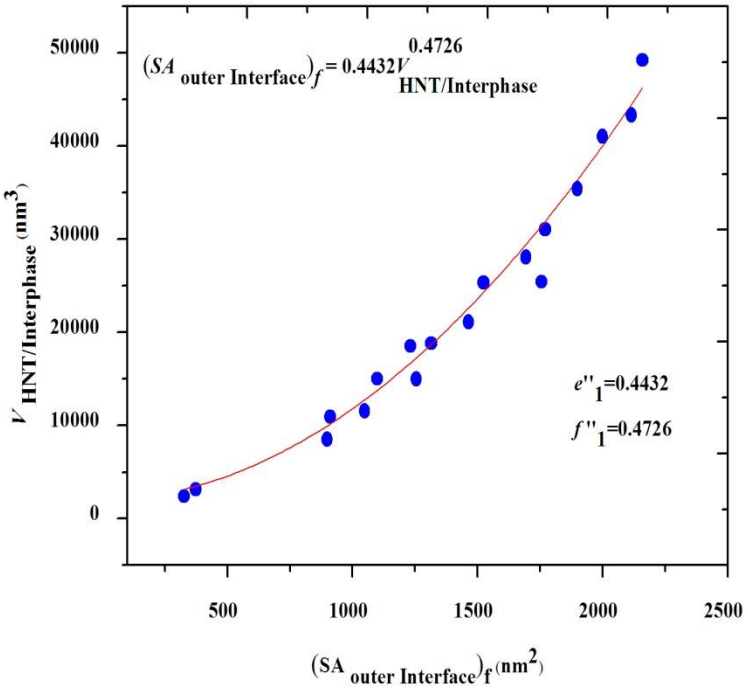

Figure 0.12 Relationship between surface area of outer interface ($SA_{\text{outer interface}}$) and HNT/interphase volume ($V_{\text{HNT/Interphase}}$).

- According to Figures 6.1(e) and (f) ,the $V_{\text{Interphase}}$ was estimated in case of fully or partially embedded HNT in PVA/ HNT nanocomposites as below:

$$(V_{\text{Interphase}})_f = V_{\text{HNT/Interphase}} - V_{\text{HNT}} \quad \text{(A40)}$$

$$(V_{\text{Interphase}})_p = V_{\text{HNT/Interphase-effective}} - V_{\text{HNT effective}} \quad \text{(A41)}$$

Appendix B: Mori-Tanaka Eshelby's Solution

Mori-Tanaka theory [53] and Eshelby's solution [328] were employed to derive a complete analytical solution for calculating elastic moduli of an isotropic matrix containing aligned sperodial inclusions. Longitudinal and transverse elastic moduli of polymer nanocomposites (E_{11}) and (E_{22}) can be experessed as

$$\frac{\boldsymbol{E_{11}}}{\boldsymbol{E_m}} = \frac{\mathbf{1}}{\mathbf{1} + \boldsymbol{\emptyset_p}(\boldsymbol{A_1} + \mathbf{2}\boldsymbol{\nu_m}\boldsymbol{A_2})/\boldsymbol{A}} \tag{B1}$$

$$\frac{E_{22}}{E_m} = \frac{1}{1 + \emptyset_p(-2\nu_m A_3 + (1-\nu_m)A_4 + (1+\nu_m)A_5 A)/2A} \tag{B2}$$

where ν_m is the Poisson's ratio of polymer matrices and the A_i (i =1-5) are the functions of Eshelby's tensors as given below:

$$\boldsymbol{A_1 = D_1(B_4 + B_5) - 2B_2} \tag{B3}$$

$$A_2 = (1 + D_1)B_2 - (B_4 + B_5) \tag{B4}$$

$$A_3 = B_1 - D_1 B_3 \tag{B5}$$

$$A_4 = (1 + D_1)B_1 - 2B_3 \tag{B6}$$

$$A_5 = (1 - D_1)/(B_4 - B_5) \tag{B7}$$

$$A_6 = 2B_2 B_3 - B_1(B_4 + B_5) \tag{B8}$$

where D_1, D_2 and D_3 are functions of Lame constant of matrix and nanofillers in the following expressions:

$$\boldsymbol{D_1 = 1 + 2\left(\mu_f - \mu_m\right)/\left(\lambda_f - \lambda_m\right)} \tag{B9}$$

$$D_2 = (\lambda_m + 2\mu_m)/\left(\lambda_f - \lambda_m\right) \tag{B10}$$

$$D_3 = \lambda_m/\left(\lambda_f - \lambda_m\right) \tag{B11}$$

$$\lambda o = \frac{Ev}{(1+v)(1-2v)} \tag{B12}$$

$$\mu = \frac{E}{2(1+v)} \tag{B13}$$

where λo and μ are the Lame first and second constants, respectively. E and v are elastic modulus and Poisson's ratio. The subscripts f and m represent nanofillers and polymer matrices, respectively. B_j (i =1-5) can be calculated as follows:

$$\boldsymbol{B_1 = \phi_f D_1 + D_2 + (1 - \phi_f)(D_1 S_{1111} + \ 2S_{2211})} \tag{B14}$$

$$B_2 = \phi_f + D_3 + (1-\phi_f)(D_1 S_{1122} + S_{2222} + \ 2S_{2233}) \tag{B15}$$

$$B_3 = \phi_f + D_3 + \left(1-\phi_f\right)[S_{1111} + (1+D_1)S_{2211}] \tag{B16}$$

$$B_4 = \phi_f D_1 + D_2 + \left(1-\phi_f\right)[S_{1122} + D_1 S_{2222} + S_{2233}] \tag{B17}$$

$$B_5 = \phi_f + D_3 + (1-\phi_f)(S_{1122} + S_{2222} + \ D_1 S_{2233}) \tag{B18}$$

$$S_{1111} = \frac{1}{2(1-vo)}\left\{1 - 2vo + \frac{3\alpha^2 - 1}{\alpha^2 - 1} - \left[1 - 2vo + \frac{3\alpha^2}{\alpha^2 - 1}\right] g\right\} \tag{B19}$$

$$S_{2222} = S_{3333} = \frac{3}{8(1-vo)}\frac{\alpha^2}{\alpha^2 - 1} + \frac{1}{4(1-vo)}\left[1 - 2vo - \frac{9}{4(\alpha^2 - 1)}\right] g \tag{B20}$$

$$S_{2233} = \frac{1}{4(1-vo)}\left\{\frac{\alpha^2 - 1}{2(\alpha^2 - 1)} - \left[1 - 2vo + \frac{3}{4(\alpha^2 - 1)}\right] g\right\} \tag{B21}$$

$$S_{2211} = -\frac{1}{2(1-vo)}\frac{\alpha^2}{\alpha^2 - 1} + \frac{1}{4(1-vo)}\left\{\frac{3\alpha^2}{\alpha^2 - 1} - (1 - 2vo)\right\} g \tag{B22}$$

Appendix C: Statement of Contribution of Others

To whom it may concern:

I, **Dr. Yu Dong** has contributed as supervisor, technical advisor and through mentoring to one book chapter and two research papers as part of a PhD thesis preparation for Curtin University by Mohanad Mousa.

I am also listed as co-author of the papers referred to below and did so in my capacity as PhD Supervisor.

List of articles:

- **M. Mousa** and Y. Dong, "Strong Poly (Vinyl Alcohol)(PVA)/Bamboo Charcoal (BC) Nanocomposite Films with Particle Size Effect," *ACS Sustainable Chemistry & Engineering*, vol. 6, no. 1, pp. 467-479, 2017.
- **M. Mousa** and Y. Dong,Novel Three-Dimensional Interphase Characterisation of Polymer Nanocomposites Using Nanoscaled Topography, *Nanotechnology*, vol. 29, no. 38, pp 385701, 2018.
- **M. H. Mousa**, Y. Dong, and I. J. Davies, "Recent advances in bionanocomposites: Preparation, properties, and applications," *International Journal of Polymeric Materials and Polymeric Biomaterials*, vol. 65, no. 5, pp. 225-254,.
- **M. Mousa**, Y. Dong, and I. J. Davies, "Eco-friendly polyvinyl alcohol (PVA)/bamboo charcoal (BC) nanocomposites with superior mechanical and

thermal properties," *Advanced Composite Materials*, In press, doi.org/10.1080/09243046.2017.1407906.

- Mousa, M. and Dong, Y., 2018. Elastic Behavior of Nanophases in Polyvinyl Alcohol (PVA)/Bamboo Charcoal (BC) Nanocomposite Films. *Frontiers in Materials*. 5: 44.

The papers take part of the PhD thesis and first author Mohanad Mousa.

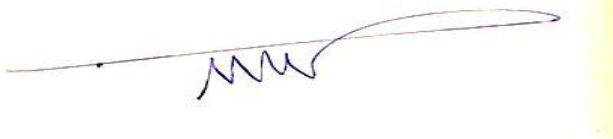

(Supervisor and co-author signature)

Dr. Yu Dong Mohanad Mousa

To whom it may concern:

I, **Dr. Ian J. Davies** has contributed as co-supervisor, manuscript editing to one book chapter and two research papers as part of a PhD thesis preparation for Curtin University by Mohanad Mousa.

I am also listed as co-author of the papers referred to below and did so in my capacity as PhD Supervisor.

List of articles:

- **M. H. Mousa**, Y. Dong, and I. J. Davies, "Recent advances in bionanocomposites: Preparation, properties, and applications," *International Journal of Polymeric Materials and Polymeric Biomaterials*, vol. 65, no. 5, pp. 225-254,.
- **M. Mousa**, Y. Dong, and I. J. Davies, "Eco-friendly polyvinyl alcohol (PVA)/bamboo charcoal (BC) nanocomposites with superior mechanical and thermal properties," *Advanced Composite Materials*, In press, doi.org/10.1080/09243046.2017.1407906.

The papers take part of the PhD thesis and first author Mohanad Mousa.

Co-Supervisor and co-author signature) (Candidate signature)

Dr. Ian J. Davies Mohanad Mousa

Home | Account Info | Help

Title:	Eco-friendly polyvinyl alcohol (PVA)/bamboo charcoal (BC) nanocomposites with superior mechanical and thermal properties
Author:	Mohanad Mousa, Yu Dong, Ian J. Davies
Publication:	Advanced Composite Materials
Publisher:	Taylor & Francis
Date:	Dec 7, 2017

Rights managed by Taylor & Francis

Logged in as:
Mohanad Mousa
Account #:
3000962330
LOGOUT

Thesis/Dissertation Reuse Request

Taylor & Francis is pleased to offer reuses of its content for a thesis or dissertation free of charge contingent on resubmission of permission request if work is published.

BACK | CLOSE WINDOW